Particle-Resolved Simulation of Mono- and Bi-Disperse Fluid-Solid Couette Flows

Oliver Bendjamin Strapasson Scorsim

▶ **To cite this version:**

Oliver Bendjamin Strapasson Scorsim. Particle-Resolved Simulation of Mono- and Bi-Disperse Fluid-Solid Couette Flows. Fluid mechanics [physics.class-ph]. Institut National Polytechnique de Toulouse - INPT, 2021. English. NNT : 2021INPT0110 . tel-04186682

HAL Id: tel-04186682

https://theses.hal.science/tel-04186682v1

Submitted on 24 Aug 2023

HAL is a multi-disciplinary open access archive for the deposit and dissemination of scientific research documents, whether they are published or not. The documents may come from teaching and research institutions in France or abroad, or from public or private research centers.

L'archive ouverte pluridisciplinaire **HAL**, est destinée au dépôt et à la diffusion de documents scientifiques de niveau recherche, publiés ou non, émanant des établissements d'enseignement et de recherche français ou étrangers, des laboratoires publics ou privés.

THÈSE

En vue de l'obtention du

DOCTORAT DE L'UNIVERSITÉ DE TOULOUSE

Délivré par :

Institut National Polytechnique de Toulouse (Toulouse INP)

Discipline ou spécialité :

Dynamique des fluides

Présentée et soutenue par :

M. OLIVER BENDJAMIN STRAPASSON SCORSIM

le mardi 7 décembre 2021

Titre :

Particle-Resolved Simulation of Mono- and Bi-Disperse Fluid-Solid Couette Flows

---

Ecole doctorale :

Mécanique, Energétique, Génie civil, Procédés (MEGeP)

Unité de recherche :

Institut de Mécanique des Fluides de Toulouse (IMFT)

Directeurs de Thèse :

M. OLIVIER SIMONIN

M. PASCAL FEDE

Rapporteurs :

M. ADRIEN TOUTANT, UNIVERSITE DE PERPIGNAN

M. JEAN-PHILIPPE MATAS, UNIVERSITE LYON 1

Membres du jury :

MME IVANA VINKOVIC, UNIVERSITE LYON 1, Présidente

M. JULIEN CHAUCHAT, INP GRENOBLE, Membre

MME MICHELINE ABBAS, TOULOUSE INP, Membre

M. OLIVIER SIMONIN, TOULOUSE INP, Membre

M. PASCAL FEDE, TOULOUSE INP, Membre

M. STÉPHANE VINCENT, UNIVERSITE MARNE LA VALLEE, Membre

Acknowledgement

I am extremely grateful to my advisors Olivier Simonin and Pascal Fede for their valuable guidance, helpful feedback and share of their precious knowledge throughout this thesis project, as well as for the cordial welcome at the Toulouse Institute of Fluid Mechanics.

Moreover, I would like to thank the IMFT staff for contributing with all the necessary resources for this project. Special thanks to the worthy friends at the Institute for providing a pleasant ambiance and the researchers for the fertile scientific atmosphere.

I also wish to acknowledge CINES and CALMIP facilities for providing the high performance computing infrastructure needed for this project. Further, I would like to recognize the assistance received by the personnel of the doctoral institution MEGEP and by INP-Toulouse.

Finally, last but not least, I am grateful to the Brazilian scientific funding agency CAPES for the financial support needed for this work.

Remerciement

Je tiens à exprimer ma plus profonde gratitude à Olivier Simonin, car sa générosité a largement dépassé son rôle de directeur de thèse et l'achèvement de ce travail n'aurait pas eu lieu sans son précieux support. De plus, je ne peux qu'exprimer mon admiration envers ses grandes qualités humaines et son intelligence scientifique hors du commun.

Je remercie Pascal Fede, par l'encadrement à l'IMFT et les discussions importantes qui ont fait avancer la thèse.

Je suis aussi très content d'avoir été accueilli de bras ouverts par la ville de Toulouse qui m'a proportionné des inoubliables rencontres, des amis inestimables ainsi que des expériences exceptionnelles!

Agradecimento

Agradeço a minha família: Marcos, Rori e Marjorie, assim como amigos e pessoas mais que especiais pelo apoio, suporte e amor incondicional.

Sou também grato ao Rigoberto E. M. Morales por ter sido minha primeira referência no mundo dos escoamentos multifásicos.

Abstract

A particle resolved numerical simulation tool, based on the tensorial viscous penalty method, that allows the resolution of the fluid-flow around the moving particles was used to investigate both mono and bi-disperse fluid-particle flow in a Couette configuration, aiming to study the flow, as well as to test, improve and develop macroscopic models, notably leveraging the level of detail contained in the resolved simulations.

A hybrid Eulerian-Lagrangian statistical approach to extract the statistics of the fluid-particle flow is described. The fluid phase is taken into account by a characteristic phase operator that notably allows for the derivation fluid-particle interfacial transport terms. The particles are described by a probability density function, and via the Liouville's formalism, continuum transport equations of the particle phase such as the particle fluctuating kinetic energy are derived. The trailblazing aspect of such methodology is that long duration contacts between particles are allowed. A methodology for the calculation of particle and fluid statistics, as well as the calculation of the coupling terms, are described. In addition, an original method for decomposing the particle-particle interaction terms into source and flux terms are presented.

Mono disperse cases were studied and the effects of the inertia and particle volume fraction were investigated. Several particle and fluid statistics, such as the mean velocity and fluctuating kinetic energy are given and analyzed with respect to the flow physics. Viscous dissipation as well as its spatial and temporal scales are compared to the other relevant scales. Particle kinetic stress as well as the third and fourth order particle velocity fluctuation correlations, are analyzed and tested against available modeling. Relevant transport equations of both the particle and the fluid phase are presented in the form of budgets, highlighting local physical mechanisms, such as production, destruction, as well as fluid-particle and particle-particle interactions. Fluid force modeling both for an single and for an ensemble of particles is revisited. A correlation analysis is performed to inquiry into the mean transverse force in the particle flow. In addition, a Stochastic Langevin approach is used to model fluid force velocity fluctuation correlations, this formalism is tested against our data providing interesting modeling insights.

Bi-dispersion is achieved with lighter and heavier particles with the same diameter. An equivalent Stokes number for the bi-disperse flows are derived and analyzed in the frame of our data. Particle-particle interaction terms are separated into the global contribution of the heavier and the lighter phase, in the fluctuating kinetic energy budget, then those terms are further separated into source and flux terms. Next, an extension for the mean bi-disperse restitution coefficient is presented and then used to test against the momentum collisional flux and kinetic stress source terms, yielding interesting results.

Keywords: particle resolved simulation, fluid-particle flow, Couette, fluid-particle interaction, particle-particle interaction, particle kinetic stress, modeling, bi-disperse, Stokes number, budget analysis, stochastic, Langevin, drag-law, fluid force velocity correlation modeling, collisional modeling, source and flux terms, kinetic theory of granular flow.

Contents

Introduction

Fluid-Particle flows occurs in many environmental and industrial applications. Pollutant dispersion, volcano eruptions and dust storms are examples of those flows, such cases are illustrated in Figure 1. Gas-solid reactors (see Figure 2) such as the fluidized beds, are widely used in the industry because of their excellent mixing properties, which is favorable to promote chemical reactions.

(a)

(b)

(c)

Figure 1: Manifestations of fluid-particle flow (a) Pollutant dispersion. (b) Volcano Eruption. (c) Dust Storm.

Fluidized beds are found, for example, in the petrochemical sector, for the production of olefins or oil cracking [53]. In this type of application, the catalyst particles are suspended into the flow to form a fluidized bed which improves the exchanges between the phases, the temperature control, and therefore optimizes chemical reactions. The nuclear sector also uses fluidized beds for fuel development or reactor core materials, such as for uranium fluorination [124] or zirconium production.

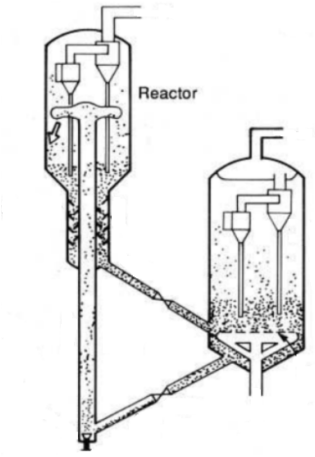

Figure 2: Schematics of an industrial fluidized bed gas-solid reactor

Numerical simulation of fluidized beds has found a great interest in recent years for several reasons. Primarily due to the economic and technological importance and also because it is particularly difficult to perform local measurements in fluid-particle flows. Numerical simulation allows for the possibility to analyze local physical mechanisms, such as inter-particle and fluid-particle interactions. The study and investigation of such phenomena is essential for the scientific progress in the field and consequently to the advancement of industrial reactors.

The numerical simulation of fluidized beds is complex due to the multi-scale phenomena that takes place inside the reactor, such as: turbulent dispersion of the particles, particle-particle interactions, wall-interactions, heat-transfer, mass-transfer, chemical reactions, etc. Until very recently, two approaches coexisted for the numerical simulation of fluidized beds: the Euler-Euler (or more generally the n-Euler) approach [103], also called the multi-fluid approach, and the Euler-Lagrange approach [116]. In these approaches, the fluid flow is modeled by a RANS (Reynolds Averaged Numerical Simulation) or LES (Large Eddy Simulation) approach [20, 77]. With respect to the n-Euler approach, the particulate flow is considered as a continuous phase, whereas for the Euler-Lagrange approach, particle trajectories are tracked and calculated based on the solution of the flow field, which may or may not be coupled to the particle equation of motion.

An example of the numerical simulation of a gas-solid solid fluidized bed reactor using n-Euler methodology is shown at the Figure 3, (adapted from [73]), it can be seen that the solution is continuous even in the maximum zoom, depicted at the right hand side of the figure, where the mesh grid is visible. This is suitable to industrial purposes, where generally average quantities and transfer rates are used to design or numerically evaluate the performance of a reactor at a reasonable CPU cost. In contrast, particle tracking methods, offer more details with respect to the particle trajectories, with the downside of being capable of handling a lower amount of particles, generally several orders of magnitude lower than a real reactor, often due to memory limitations.

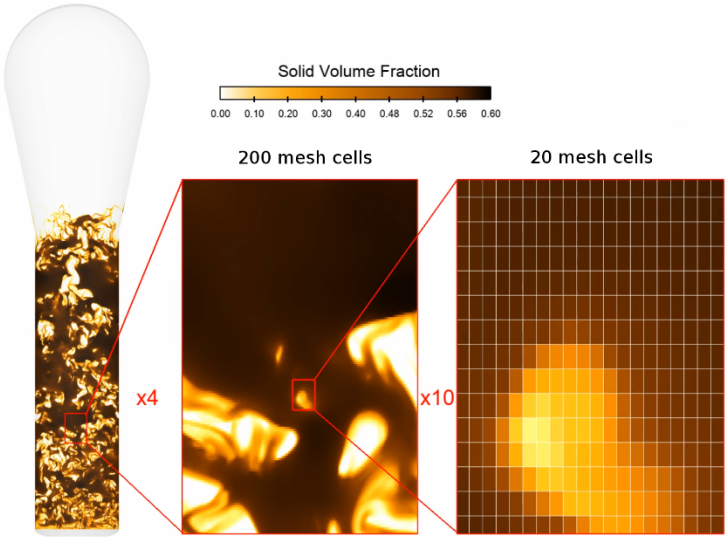

Figure 3: Example of a gas-solid reactor simulation using n-Euler methodology, depicting the continuous solution. Adapted from [73].

In order to improve and test the validity of the models present in n-Euler simulations, data related to local fluid and particle flow, specially at the particle scale, with sufficient time and spacial resolution is needed.

A possibility to acquire data, is with experiments. Several methods are available to for that purpose [19, 108, 110], such as the techniques based on electric and electromagnetic properties [128] , fiber-optics [43], acoustics [97], single point lasers [107], particle image velocimetry (PIV) [23], radioactive tracers [72] and etc. Besides, despite the advancement in measurement techniques however, fluid-particle flow velocity measurements are still challenging [31].

Another possibility to access such data with enough spatial and temporal resolution for statistical purposes, is to perform numerical simulations capable of resolving the fluid flow around the moving particles. In fact, until recently, the computational cost to perform such computations was prohibitive, and the numerical simulation of fluid-particle flow was restricted to n-Euler and Euler-Lagrange techniques. With the progress in computational power, and with CPU resources increasingly available, particle resolved simulations became possible.

Body-fitted approach [48, 49], lattice-Boltzmann method (LBM) [55, 56, 57] and fictitious-domain method [17, 21] are examples of particle resolved methods. A succinct discussion about those methods are given in the chapter 1.

Particularly within the category of the fictitious-domains, a method based on the penalization of the viscous stress tensor is used to solve the fluid flow around finite-sized moving particles [121]. In this method, Navier-Stokes is solved on the whole domain, and fluid like-behavior is obtained where the penalization is not applied, whereas particle-like characteristics, such as rigid body motion, are obtained where the penalization is applied. On the Figure 4 is shown an example of the detail level of the solution around the particles, obtained using the viscous penalty method.

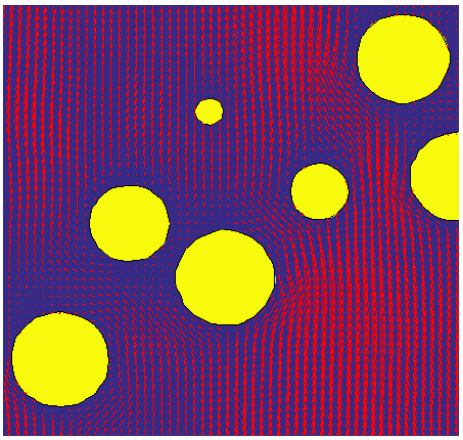

Figure 4: Example of resolved fluid flow around the particles using the tensorial viscous penalty method.

With respect to previous work using this code, we may cite the numerical simulation of particles in isotropic turbulence [13]. Drag force, as well as thermal analysis of an array of motionless spheres [113, 114]. In addition to that, an experiment realized by [23] was numerically simulated by [78], and several statistics were compared against the experimental results. In fact, this code is capable of performing numerical experiments with great precision.

As a result of the high level of detail in particle resolved simulations, a high CPU cost is also needed, and for that reason, usually only small configurations are numerically simulated. Besides, due to the great level of precision, this type of simulation is sometimes referred to as a micro-scale simulation. This is in contrast with n-Euler simulations that are referred as macro-scale simulations.

One might argue that emergent properties occurring in macro-scale are in fact, the result of all the micro-scale interactions. The particle pressure for instance, which is an emergent local property of the particles, is the result of local inter-particle interactions. As a matter of fact, macro-scale simulations, often rely on the modeling of those emergent properties, which can indeed be achieved through the analysis of the micro-scale interactions.

Within the scope of this thesis, we aim to investigate the micro-scale simulations in a Couette (shear-flow) configuration, using the tensorial viscous penalty method based code, in order to test, develop and improve macro-scale models, which are particularly useful either for the scientific progress itself and for industrial applications as well. The study in this manuscript is divided into mono and bi-disperse configurations. Snapshots of those cases are depicted on the Figure 5, on the left a mono-disperse configuration and on the right a bi-disperse configuration.

This manuscript is organized into four main chapters. In the first one, numerical aspects of the code, as well as the description of the cases are presented. In the second one, detailed computation of the statistics for both the fluid and the particle phase are delved into. In chapter three, mono-disperse cases are explored and in chapter four, bi-disperse cases are investigated.

First of all, in chapter 1, a brief discussion about the available numerical

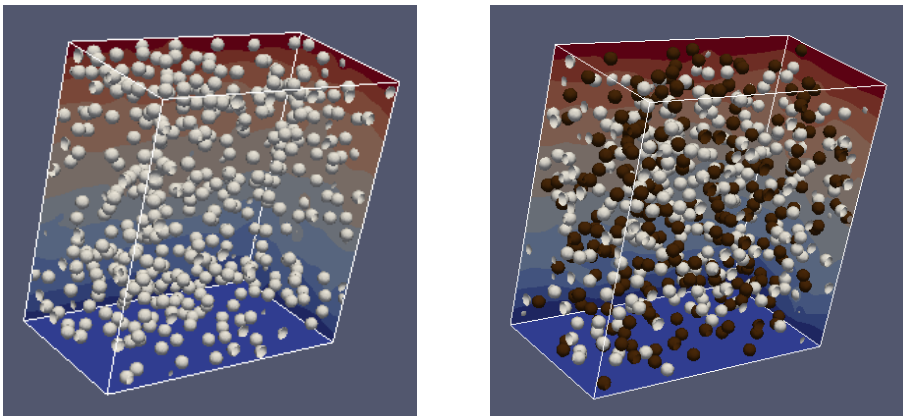

(a) mono-disperse (b) bi-disperse

Figure 5: Snapshot of mono and bi-disperse fluid-particle flow in a Couette configuration.

methods to perform particle resolved simulations of fluid-particle flows, as well as a more detailed discussion of the tensorial viscous penalty method, are presented. Also, it is described how the code deals with near range repulsive forces between the particles. In addition to that, both numerical and physical parameters related to the numerical simulations such as the domain size, number of particles, fluid and particle densities, are given. Finally, details about the procedures to run the simulations are discussed.

On chapter 2, details about how statistics are computed both for the fluid and the particles are described. Statistics of the fluid phase are based upon a characteristic phase operator, which particularly allows for the derivation of the exchange terms associated to the fluid-particle interface occurring in the fluid transport equations. For the particles, we describe a formalism based upon the transport equation of a fine-grained probability density function related to the particles. Moments of that equations are derived, yielding transport equations such as the mean particle velocity and particle fluctuating kinetic energy. Besides, the procedure for the computation of the fluid-particle exchange terms is discussed as well as the link between the two previously presented formalisms. Additionally, an original decomposition of the so-called collision term, or the particle-particle interaction term, present in the particle transport equations, into source and flux like terms, which can be associated with different physical mechanisms.

With respect to chapter 3, the influence of several parameters on particle statistics are investigated on the mono-disperse cases. Particle inertia for instance, characterized through the Stokes number, was linked to an observed macroscopic transition. Also, other parameters such as the mean fluid and particle velocities, as well as the velocity fluctuation correlations of second, third and fourth order are analyzed and related to the physical phenomena. Moreover, scales based on the fluid viscous dissipation are analyzed as a means to investigate the results. Available modeling is also tested against the data and used to comprehend the behavior of the simulation. In addition to that, macroscopic

transport equations, such as the mean-velocity equation, particle and fluid fluctuating kinetic energy equation, are computed from our particle resolved simulation and presented in the form of a budget, indeed highlighting local physics related to fluid-particle and inter-particle interactions, as well as the so-called kinetic terms, such as the diffusive or production terms. Fluid-particle force is discussed both for a single and an ensemble of particles. Moreover, a stochastic anisotropic impulse model based on the Langevin equation is investigated, and used to model force velocity fluctuation correlations, yielding interesting results.

The bi-dispersion of the cases presented in chapter 4 are achieved by changing the particle density, resulting in a group of lighter and heavier particles. Also, an equivalent bi-disperse Stokes number is derived, which permits to evaluate the overall particle mixture inertia. In this chapter, we mainly focus on the particle-particle phenomena. With that in mind, budget analysis of the particle fluctuating kinetic energy of both species are shown with the particle-particle interaction term decomposed into a contribution due to the lighter particles and another due to the heavier ones, which shines a light into the global mechanisms of transfer from one particle species to the other. Furthermore, still related to that, those terms are decomposed into the source and flux terms, which can more precisely measure different effects related to the collision, such as dissipation, redistribution and production of fluctuating kinetic energy. Moreover, a comparison of the resultant source and flux terms against available models is performed. Related to that, an extension of the average restitution coefficient taking into account the bi-dispersion is presented.

The pioneer aspect of this work, aside from the physical and mathematical developments and inquiries, is that resolved simulations are used to quantitatively test and develop fluid-particle and particle-particle models in the frame of the kinetic theory of granular flow, as well as to better comprehend both microscopic and macroscopic phenomena related to the fluid-particle flow.

Chapter 1

Numerical Simulation

Contents

1.1 Resolved methods for fluid particle flow

In this section we discuss about the available methods to resolve the fluid flow around moderately dense fluid-particle flows. Specifically, we are interested in the case where the fluid is incompressible ($\nabla \cdot \mathbf{u}_\mathrm{f} = 0$) and obeys the Newton viscous law, which is governed by the Navier-Stokes equations.

$$\rho_\mathrm{f} \left(\frac{\partial u_{\mathrm{f},i}}{\partial t} + u_{\mathrm{f},j} \frac{\partial u_{\mathrm{f},i}}{\partial x_j} \right) = -\frac{\partial p_\mathrm{f}}{\partial x_i} - \mu_\mathrm{f} \frac{\partial^2 u_{\mathrm{f},i}}{\partial {x_j}^2} + \rho S_i \tag{1.1}$$

where ρ_f, $\boldsymbol{u}_\mathrm{f}$, p_f, and $\boldsymbol{S}$, stand respectively for the density, velocity, pressure and a body force. In the next sections we succinctly discuss about available numerical methods used for the mentioned purpose.

1.1.1 Body-fitted approach

The body-fitted approach is based on the mesh grids that only exists in the fluid domain. An example of such mesh grid is depicted by Figure 1.1.

When the particles inclusions do not move, than mesh generation is only created once. If the objects are free to move inside the flow field, then an adaptive mesh has to be used [8], that is: the grid should take into account the movement of the objects and the solution should be also be projected onto the new mesh. Which can be very computational intensive, and consequently a time-consuming task. A problem with such procedure is that the quality of the solution is relatively sensitive to numerical set up of the parameters [9].

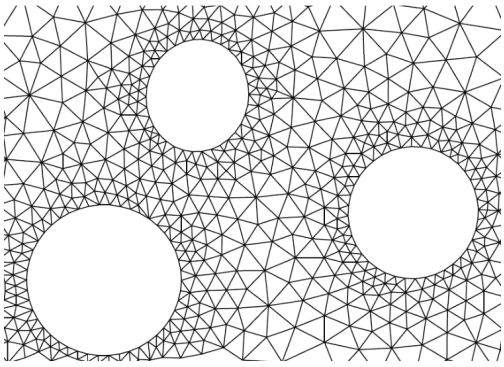

Figure 1.1: Example of a body-fitted, non-structured mesh [65].

The approaches in which the mesh follows the particles in a Lagrangian manner are called Arbitrary Lagrangian Eulerian (ALE). This approach has been used to study some configurations, such as the Poiseuille flow of solid-liquid particles [48] and sedimentation of spheres [49]. Further studies include the simulation of 2D rigid particles in a viscous incompressible fluid in a bi-periodic domain [65] and finally the analysis of the apparent viscosity in a 2D configuration was analyzed using this technique [60].

1.1.2 Lattice Boltzmann Method

The Lattice Boltzmann method (LBM) is a weakly compressible flow solver based on the kinetic theory of gases and the evolution of a molecular distribution function on a lattice. The propagation of information among the lattices involves a collision stage, where the related distribution function relaxes towards the equilibrium in a given time-scale [66]. In other words, from simple and local update rules based on molecule interactions, continuum flow quantities can be obtained. The simplicity of implementation and the versatility of its formulation has caused this methods to have a rapid expansion in usage among the researchers [2].

Numerical simulation of fluid-particle flows with LBM can be achieved by representing the particle boundaries as walls, over which molecular collisions (in the frame of LBM) take place. The global resulting force applied by the fluid onto the particle can then be calculated. This is then used to transport the particles in a Lagrangian manner.

Several studies using LBM can be found in the literature, such as the first investigations made by [55, 56, 57] and the simulation of ordered and random arrays of flow past spheres studies [45],[46]. The drag, lift and moment coefficients of differently shaped fixed single particles have been calculated in the work of [47]. An inspection of the LBM method for DNS of solid-liquid suspensions were done by [30]. More recently we note the work of [88] where a coupled discrete element method is used to simulate fluid-particle flows. Also, numerical simulation of particles in a channel has been studied by [33].

1.1.3 Fictitious Domain Methods

Fictitious domain methods provide a resolved simulation of particles freely suspended in a flow while avoiding the challenges of body-fitted approaches. In this method, a fixed computational mesh is specified for the whole domain, including the volume occupied by the particles, the methods are set so that the (fictitious) fluid defined inside each particle location mathematically responds with particle like-behavior. In some methods, forces are applied to the body surface (immersed boundary methods) or applied throughout the particle volume (immersed body methods) to achieve particle motion behavior [21, 22, 28, 66].

One of the pioneer studies using the immersed boundary method were [81, 82], in which cardiac dynamics and the related blood flow are studied. The distinguishing feature of that method is that the entire simulation was carried out on a Cartesian grid, which did not conform to the geometry of the heart, and a novel procedure was performed for imposing the effect of the immersed boundary on the flow. [69]. In addition, we can cite the work of [61, 62], [63] and [117, 118, 119] .

Another way to apply rigid body motion to a fictions domain is the tensorial viscous penalty method [17, 121, 123] in which the stress tensor is penalized to impose solid behavior inside the particle volume. This method is the one used in this thesis, and it is going to be further detailed in the next section.

1.2 Tensorial Viscous Penalty Method

The Tensorial Viscous Penalty Method, is based on the separation of the fluid stresses into four different contributions, which was first proposed by [17]. First, we write the fluid stress tensor, assuming Newtonian behavior, as follows:

$$\sigma_{\mathrm{f},ij} = -p\delta_{ij} + \lambda\nabla\cdot\mathbf{u}_{\mathrm{f}}\delta_{ij} + 2\mu D_{ij} \tag{1.2}$$

Where λ and μ are respectively the compression and shearing viscosities. The deformation rate stands for $D_{ij} = \frac{1}{2}\left(\frac{\partial u_{\mathrm{f},i}}{\partial x_j} + \frac{\partial u_{\mathrm{f},j}}{\partial x_i}\right)$. The velocity gradient can be decomposed into a symmetric (D_{ij}) and a anti-symmetric part (A_{ij}).

$$\frac{\partial u_{\mathrm{f},i}}{\partial x_j} = \underbrace{\frac{1}{2}\left(\frac{\partial u_{\mathrm{f},i}}{\partial x_j} + \frac{\partial u_{\mathrm{f},j}}{\partial x_i}\right)}_{D_{ij}} + \underbrace{\frac{1}{2}\left(\frac{\partial u_{\mathrm{f},i}}{\partial x_j} - \frac{\partial u_{\mathrm{f},j}}{\partial x_i}\right)}_{A_{ij}} \tag{1.3}$$

Combining Eq. (1.3) with Eq. (1.2), we obtain:

$$\sigma_{\mathrm{f},ij} = -p\delta_{ij} + \lambda\nabla\cdot\mathbf{u}_{\mathrm{f}}\delta_{ij} + 2\mu\left(\frac{\partial u_{\mathrm{f},i}}{\partial x_j} - A_{ij}\right) \tag{1.4}$$

Which can thus be turned into the following form in Cartesian coordinates:

$$\begin{aligned}
\underline{\underline{\sigma_{\mathrm{f}}}} \;=\; & \begin{bmatrix} -p+\lambda\nabla\cdot\mathbf{u}_{\mathrm{f}} & 0 & 0 \\ 0 & -p+\lambda\nabla\cdot\mathbf{u}_{\mathrm{f}} & 0 \\ 0 & 0 & -p+\lambda\nabla\cdot\mathbf{u}_{\mathrm{f}} \end{bmatrix} + \kappa \underbrace{\begin{bmatrix} \frac{\partial u_{\mathrm{f},x}}{\partial x} & 0 & 0 \\ 0 & \frac{\partial u_{\mathrm{f},y}}{\partial y} & 0 \\ 0 & 0 & \frac{\partial u_{\mathrm{f},z}}{\partial z} \end{bmatrix}}_{\underline{\underline{\Lambda}}} \\
+ \; & \zeta \underbrace{\begin{bmatrix} 0 & \frac{\partial u_{\mathrm{f},x}}{\partial y} & \frac{\partial u_{\mathrm{f},x}}{\partial z} \\ \frac{\partial u_{\mathrm{f},y}}{\partial x} & 0 & \frac{\partial u_{\mathrm{f},y}}{\partial z} \\ \frac{\partial u_{\mathrm{f},z}}{\partial x} & \frac{\partial u_{\mathrm{f},z}}{\partial y} & 0 \end{bmatrix}}_{\underline{\underline{\Theta}}} - \eta \underbrace{\begin{bmatrix} 0 & \frac{\partial u_{\mathrm{f},x}}{\partial y} - \frac{\partial u_{\mathrm{f},y}}{\partial x} & \frac{\partial u_{\mathrm{f},x}}{\partial z} - \frac{\partial u_{\mathrm{f},z}}{\partial x} \\ \frac{\partial u_{\mathrm{f},y}}{\partial x} - \frac{\partial u_{\mathrm{f},x}}{\partial y} & 0 & \frac{\partial u_{\mathrm{f},y}}{\partial z} - \frac{\partial u_{\mathrm{f},z}}{\partial y} \\ \frac{\partial u_{\mathrm{f},z}}{\partial x} - \frac{\partial u_{\mathrm{f},x}}{\partial z} & \frac{\partial u_{\mathrm{f},z}}{\partial y} - \frac{\partial u_{\mathrm{f},y}}{\partial z} & 0 \end{bmatrix}}_{\underline{\underline{\Gamma}}}
\end{aligned} \tag{1.5}$$

Comparing Eq. (1.5) with Eq. (1.4), we note that the following equalities must held: $2\mu = \kappa = \zeta = 2\eta$ in order to describe the so called Newtonian fluid behavior. Analyzing the terms of Eq. (1.5), we can identify:

- κ stands for the elongation viscosity
- ζ stands for the tearing viscosity
- η stands for the rotation viscosity

Also, λ can be seen as a dilation viscosity. Considering that, the decomposition of the stress tensor can then be written with the four main contributions as follows:

$$\sigma_{\mathrm{f},ij} = (-p + \lambda \nabla \cdot \mathbf{u}_\mathrm{f})\, \delta_{ij} + \kappa \Lambda_{ij} + \zeta \Theta_{ij} - \eta \Gamma_{ij} \tag{1.6}$$

The main advantage to write the stress tensor in this particular form is that it eases the implementation of the penalization method. Actually, the stresses can be independently imposed when acting on the different viscosities. [86].

In order to impose solid or fluid behavior, each mesh grid must be identified as such (fluid or particle). A color function, is used to accomplish this task. Figure 1.2 illustrates the color function. In this case, we note that the fluid domain is characterized by $C = 0$, whereas $C = 1$ is used to identify the particles. As a matter of fact, solid behavior is obtained when $\eta \gg 1$, $\kappa = 2\eta$ and $\zeta = 2\eta$.

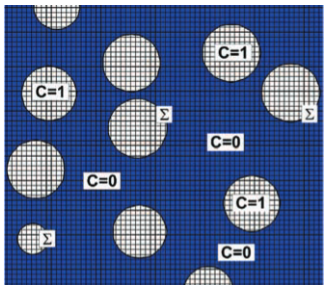

Figure 1.2: Color function C. $C = 1$ for the particles and $C = 0$ for the fluid [121]

This method, although formally equivalent to the previous viscous penalty methods in a continuous point of view [125], in a discrete manner the approaches are different [13]. Indeed, a more accurate description of fluid-solid interface is obtained when the method described in this section is used [121].

Concluding, the key point of the method, is that it permits to solve Navier Stokes in the whole domain, including particle and fluid location, in fact, particle-like behavior with rigid body motion occurs only where the penalized is applied. One can clearly see in Eq. (1.2), that when the viscosity tends to infinity ($\mu \to \infty$), than the absolute values of D_{ij} should vanish, so the stress tensor can assume a finite value. Thus explaining why rigid body motion is achieved when locally penalizing the viscosity, as $|D_{ij}| = 0$ is characteristic of rigid body motion. Naturally, where the penalization is not applied, fluid-like behavior occurs.

1.2.1 Augmented Lagrangian Method

In order to solve the velocity-pressure coupling in with the tensorial viscous penalty method presented in the last section, the Augmented Lagrangian method is used. This method was first introduced by [37], and it consists in solving an optimization problem with an Uzawa algorithm [120]. The adapted

form of the algorithm [86], which takes into account the tensorial decomposition described in the last section, is schematically described below:

$$
\begin{array}{l}
\text{Initial guess:} \\
\left(\mathbf{u}_{\mathrm{f}}^{*,0}, p^{*,0}, \underline{\underline{\mathbf{LG}_2}}^{*,0}, \underline{\underline{\mathbf{LG}_3}}^{*,0}, \underline{\underline{\mathbf{LG}_4}}^{*,0}\right) = \left(\mathbf{u}_{\mathrm{f}}^{n}, p^{n}, \underline{\underline{\mathbf{LG}_2}}^{n}, \underline{\underline{\mathbf{LG}_3}}^{n}, \underline{\underline{\mathbf{LG}_4}}^{n}\right) \\
\\
\text{While } |\nabla \cdot \mathbf{u}_{\mathrm{f}}^{*,k}| > \epsilon \;\; ; \;\; \text{cycling over } k \qquad (1.7) \\
\left\{
\begin{array}{l}
\text{Solve the system for: } \mathbf{u}_{\mathrm{f}}^{*,k} \\
\rho\left(\frac{f\left(\mathbf{u}_{\mathrm{f}}^{*,k}, \mathbf{u}_{\mathrm{f}}^{n}, \mathbf{u}_{\mathrm{f}}^{n-1}\right)}{\Delta t} + \mathbf{u}_{\mathrm{f}}^{*,k-1} \cdot \nabla \mathbf{u}_{\mathrm{f}}^{*,k}\right) = \rho \mathbf{S} \\
+\nabla\left(r \nabla \cdot \mathbf{u}_{\mathrm{f}}^{*,k}\right) - \nabla \cdot \left[\kappa \underline{\underline{\mathbf{\Lambda}}}\left(\mathbf{u}_{\mathrm{f}}^{*,k}\right) + \zeta \underline{\underline{\mathbf{\Theta}}}\left(\mathbf{u}_{\mathrm{f}}^{*,k}\right) + \eta \underline{\underline{\mathbf{\Gamma}}}\left(\mathbf{u}_{\mathrm{f}}^{*,k}\right)\right] \\
-\nabla p^{*,k-1} + \nabla \cdot \left[\underline{\underline{\mathbf{LG}_2}}^{*,k-1} + \underline{\underline{\mathbf{LG}_3}}^{*,k-1} + \underline{\underline{\mathbf{LG}_4}}^{*,k-1}\right] \\
\\
\text{Augmented Lagrangian iteration:} \\
\quad p^{*,k} = p^{*,k-1} - r \nabla \cdot \mathbf{u}^{*,k} \\
\underline{\underline{\mathbf{LG}_2}}^{k} = \underline{\underline{\mathbf{LG}_2}}^{k-1} - \kappa \underline{\underline{\mathbf{\Lambda}}}\left(\mathbf{u}^{*,k}\right) \\
\underline{\underline{\mathbf{LG}_3}}^{k} = \underline{\underline{\mathbf{LG}_3}}^{k-1} - \zeta \underline{\underline{\mathbf{\Theta}}}\left(\mathbf{u}^{*,k}\right) \\
\underline{\underline{\mathbf{LG}_4}}^{k} = \underline{\underline{\mathbf{LG}_4}}^{k-1} - \eta \underline{\underline{\mathbf{\Gamma}}}\left(\mathbf{u}^{*,k}\right)
\end{array}
\right. \\
\\
\text{Solution:} \\
\left(\mathbf{u}_{\mathrm{f}}^{n+1}, p^{n+1}, \underline{\underline{\mathbf{LG}_2}}^{n+1}, \underline{\underline{\mathbf{LG}_3}}^{n+1}, \underline{\underline{\mathbf{LG}_4}}^{n+1}\right) = \left(\mathbf{u}_{\mathrm{f}}^{*,k}, p^{*,k}, \underline{\underline{\mathbf{LG}_2}}^{*,k}, \underline{\underline{\mathbf{LG}_3}}^{*,k}, \underline{\underline{\mathbf{LG}_4}}^{*,k}\right)
\end{array}
$$

Where $\left(\mathbf{u}_{\mathrm{f}}^{*,k}, p^{*,k}\right)$ are the velocity and pressure fields to be solved, and k is an Augmented Lagrangian iterative index, and n is the index representing the time, so $(\mathbf{u}_{\mathrm{f}}^{n}, p^{n})$ is the obtained solution at the time index n, and ϵ is a numerical threshold controlling the constraint. In the same way, $\left(\underline{\underline{\mathbf{LG}_2}}^{*,k}, \underline{\underline{\mathbf{LG}_3}}^{*,k}, \underline{\underline{\mathbf{LG}_4}}^{*,k}\right)$ are the tensorial viscous stresses, related to each viscosity to be solved.

The field $\mathbf{S}$ relates to the body forces, which may contain gravity and local repulsion forces due to particle interaction, which are further detailed in the section 1.3. In the standard Augmented Lagrangian Method, a fixed parameter r is used. As shown by [122], if the value of r is locally adapted, than the system of equations should be locally correctly solved. On the other hand, if the value of r is too high, than it act as a penalty term, inducing the numerical solution to satisfy only the divergence free ($\nabla \cdot \mathbf{u}_{\mathrm{f}} = 0$) condition. When dealing with multimaterial simulations, such as fluid-particle simulation, local properties, such as density or viscosity, may vary depending on whether it is the particle or a fluid mesh. Thus a single value of r parameter is not suitable for multimaterial flows simulation.

A solution to this problem was proposed by [122], where the value of $r = r(M,t)$ locally depends on the space position M and the time t. This method is called Adaptative Augmented Lagrangian. Within this methodology, the value of $r(M,t)$ is insured to be two or three orders of magnitude higher than the most important term in the conservation equation. Thus insuring the solution quality for all the phases.

1.2.2 Mesh Grid

The spatial discretization scheme of the mesh grid is shown by Figure 1.3 below. In the center of the volume element, a pressure node is present. Velocity nodes are found in the faces and viscosity nodes are found at the corners.

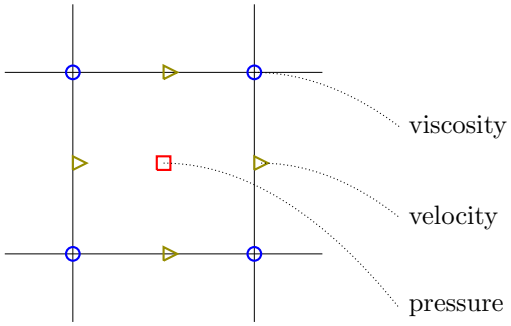

Figure 1.3: Mesh Grid

1.2.3 Particle Transport

The Lagrangian particle transport is accomplished by:

$$\begin{aligned} \tilde{\mathbf{x}}_{\mathrm{p}}^{n+\frac{1}{2}} &= \mathbf{x}_{\mathrm{p}}^{n} + \frac{\Delta t}{2}\mathbf{u}_{\mathrm{p}}^{n} \\ \tilde{\mathbf{u}}_{\mathrm{p}}^{n+\frac{1}{2}} &= \frac{3}{2}\mathbf{u}_{\mathrm{p}}^{n} - \frac{1}{2}\mathbf{u}_{\mathrm{p}}^{n-1} \end{aligned}$$

The estimated positions and velocities are then used to calculate the interaction forces between the particles, that in fact, depend on the relative velocity and position of each pair of particles. The calculation of forces is detailed in the section 1.3. Then, the calculated forces are projected as body forces into the system of (1.7), specifically at the term $\mathbf{S}$, where each concerned particles is located. When the solution of the Augmented Lagrangian Method is achieved, that is: $\left(\mathbf{u}^{n+1}, p^{n+1}\right)$, the velocity of the particles are interpolated to obtain a unique rigid body motion velocity $\mathbf{u}_{\mathrm{p}}^{n+1}$ for each particle.

The actual particle velocity at the time index $n+1/2$ is calculated, to compute the particle position at the time $n+1$.

$$\mathbf{u}_{\mathrm{p}}^{n+\frac{1}{2}} = \frac{\mathbf{u}_{\mathrm{p}}^{n+1} + \mathbf{u}_{\mathrm{p}}^{n}}{2} \tag{1.8}$$

$$\mathbf{x}_{\mathrm{p}}^{n+1} = \mathbf{x}_{\mathrm{p}}^{n} + \mathbf{u}_{\mathrm{p}}^{n+\frac{1}{2}}\Delta t \tag{1.9}$$

Knowing the center of mass position of all the particles ($\mathbf{x}_{\mathrm{p}}^{n+1}$), the color function can be actualized and the related values of density, viscosity and etc, can be projected into the mesh grid, more details at [121].

In other IBM methods, the particle velocity is deduced from the resulting force after the integration of the stresses into the particle boundary. The problem, is that due to the steep gradient of properties in the vicinity zone of the

particle boundary, the quality of the solution may be undermined in these zones, and so, it turns out that the resulting calculated force may not be very accurate, and as a consequence the particle velocity may not be accurate as well. This may threat the overall fluid-particle dynamics. Higher order spatial interpolation methods may be used to enhance the quality of the integration, but this can be specially difficult when dealing with dense flows, where particles are very close to each other. Also, such interpolation methods may be very CPU intensive.

As opposed those other IBM methods, in the method used in this thesis, the velocity of the particles is directly computed from the solution of Eq. (1.7). Thus being free of the constraints of using the fluid solution in the particle boundary. Which is a great advantage of the method used in this thesis.

1.2.4 Code Optimization

Investigating the performance of the code for the cases in this thesis, specially when dealing with large simulations, it has been noticed that its performance could be significantly improved. For instance, for the case M6, (described by the Table 1.2 and further studied in Chapter 3), the so called wall-time, which is the time to complete one time step by the code was about 35.5s. From that, 8s was used to solve Navier Stokes by the Lagrangian Augmented Method and the rest to perform other tasks, such as the velocity interpolation and convection of the particles. Those other tasks consuming about 27s.

Further analyzing the code, we profiled the most CPU intensive parts of the code for those other tasks. We note that 20s were used to perform the particle velocity interpolation and 7s to for the particle projection in the mesh.

Messaging Optimization

After a comprehensive scrutiny of the code into the velocity interpolation part, it was noticed that the enormous amount of time into this part was due to the colossal volume of message exchange among the processors. More precisely, in a particular piece of code, the operation "MPISUM" (function to perform a sum in parallel mode) were called a number of times N_{calls} that was proportional to the number of particles and processors, so:

$$N_{\text{calls}} \quad \alpha \quad N_{\text{particles}}\, N_{\text{processors}}\, N_d^3 \tag{1.10}$$

where N_d is the dimension of the problem (3 for 3D). Thus, this problem only appeared when performing large simulations with a lot of particles and simulations with high parallelism, which were the case of all the simulations of this thesis.

Inquiring the code structure, it was noticed that it was possible to reduce all of the parallel operations into a single one (due to the linearity of the operation), thus requiring only one message to be sent. After the modification, the time needed to conclude this task was greatly improved, without any change in the accuracy.

Connectivity Mesh

The lack of performance in the projection of the particles was due to the fact that the code was designed in a non-structured way, but in reality only structured Cartesian meshes were used in the thesis.

In order to solve this problem a matrix linking non-structured points to a structured grid was implemented. Thus permitting to easily perform operations in a structured way. Greatly enhancing the code performance.

Global Improvement

With the previous optimization's, the total wall-time to perform a time step passed from 35.5s to 8.5s. The time needed to solve Navier-Stokes was unaltered, since the solver was untouched. The other tasks however, evolved from 27.5s to 0.5s per time-step iteration. From that gain, 89% was due to the messaging optimization improvement.

This boost in the code performance allowed the simulation of otherwise non-viable simulations in this thesis. In reality, the simulations performed in this thesis were very costly and were in fact only possible due to those improvements. It is also clear that the bigger the simulation, the higher the performance gain, thus benefiting future users of the code.

1.3 Inter-particle Interaction

In this section, it is shown how inter-particle interaction is handled within the code. First a dry collision model is detailed and then a lubrication model is presented as well.

The time scale involved into the collision duration is generally several orders of magnitude smaller than the other scales of the flow field, such as the hydrodynamic scale for example. Consequently, it is impractical to constraint the time-step to collision related time scales. To tackle the problem, the collision force is applied during several hydrodynamic based time-steps in a way that the correct amount of momentum is transferred during the interaction between the particles.

1.3.1 Soft-sphere model

The soft-sphere model, consisting in a mechanical system with a spring and a dashpot, where the particles are allowed to overlap, is the one used to account for particle-interactions. Figure 1.4 shows the scheme of the model. Particle a with mass m_a and radius r_a, and position $\mathbf{x}_a$ collides with the particle b, with the properties: m_b, r_b and $\mathbf{x}_b$. Also, δ_n is the normal overlap between the particles, and $d\eta_n/dt$ is the normal relative velocity between the particles.

The equation of motion for the particle a is given as follows:

$$m_a \frac{d^2\mathbf{x}_a}{dt^2} = \mathbf{F}_{b\to a} = \left(-k_n\delta_n - \eta\frac{d\delta_n}{dt}\right)\mathbf{n}_{ab} \tag{1.11}$$

where $\mathbf{n}_{ab} = (\mathbf{x}_b - \mathbf{x}_a)/|\mathbf{x}_b - \mathbf{x}_a|$. One can also note that the following relation, involving the normal overlap, reads:

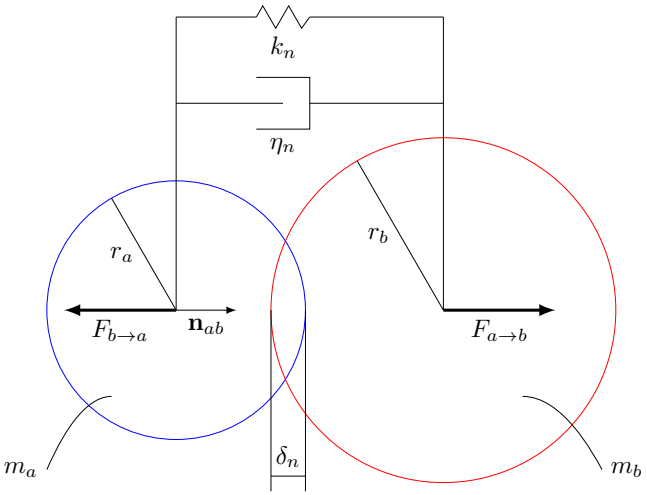

Figure 1.4: Spring dashpot scheme for the particle-particle collision modeling.

$$\delta_n = \max\left(0, r_a + r_b - |\mathbf{x}_a - \mathbf{x}_b|\right) \tag{1.12}$$

A similar equation of motion for the particle b can be easily developed, observing the fact that $\mathbf{F}_{a\to b} = -\mathbf{F}_{b\to a}$. One can easily find that the values of k_n and η_n should be the following:

$$k_n = m_{ef}\frac{\pi^2 + ln^2(e_d)}{(N_c\Delta t)^2} \tag{1.13}$$

$$\eta = -\frac{2\ m_{ef}\ ln(e_d)}{N_c\Delta t} \tag{1.14}$$

where $m_{ef} = (m_b m_a)/(m_b + m_a)$ and e_d is the dry collision coefficient, and should be comprised between 0 and 1. Zero corresponding for total inelastic collision and one for a collision without energy loss.

The numerical value of e_d is previously defined in our simulations. The choice of N_c depends onto two factors: first, if N_c is too small than, the applied force could not be correctly integrated in time, due to a coarse discretization of the force in time. If N_c is too big, than the overlap between the particles may be too big. One can easily show that for the case of perfectly elastic collisions ($e_d = 1$), the maximum overlap is:

$$\delta_{n,max} = \frac{u_{r0}N_c\Delta t}{\pi} \tag{1.15}$$

where $u_{r0} = d\delta_n/dt$ is the normal relative velocity at the instant of the impact. Thus the maximal overlap is directly proportional to N_c. Considering that the time step is given by a CFL number: $\frac{\Delta t}{\Delta x}U_\mathrm{f} = 0.3$, and that the hydrodynamic reference velocity is at the order of magnitude of the initial relative velocity $U_\mathrm{f} \approx u_{r0}$, and assuming that $d_\mathrm{p}/\Delta x = 12$ than, we found that:

$$\frac{\delta_{n,max}}{d_\mathrm{p}} \approx 0.008 N_c \tag{1.16}$$

It has been demonstrated that N_c ranging from 5 to 10 is the optimal value for the collision duration [13]. And thus the value of $N_c = 8$ is the one retained in our simulations, which gives an estimation of $\delta_{n,max}/d_\mathrm{p} \approx 0.06$, which is a reasonable amount of overlap in the simulation.

1.3.2 Lubrication correction

A combined soft-sphere model with an additional sub-grid force, to take into account the non-resolved hydrodynamic interaction at a near distance were proposed by [15]. The idea behind the model is to add a body force to the particles interacting at a given near distance, so that the force that the particles undergo is exact.

The main advantage of the use of those combined models is that they do not restrict the numerical simulations to extremely small time steps and mesh sizes. As explained before, the soft-sphere model allow the use time-steps constrained by hydrodynamic time-related scales, and not by extremely small collision related time scales. Analogously, the sub-grid force is added so the mesh size is not restrictively small to capture the correct force emerging from the complex interactions at a very near distance. One should take into account that those simulations are already very costly in CPU hours. In that sense, strongly diminishing the time-step or the mesh size would totally make the simulations unfeasible.

In order to take into account this non-resolved force in the code used in this thesis [14] has proposed a model that is described along the following lines. Basically, a force given by Eq. (1.17), is activated in selected zones, to account for the sub-grid correction.

$$F_L = -6\pi\mu_f \frac{d_\mathrm{p}}{2} u_n \left[\lambda\left(\varepsilon\right) - \lambda\left(\varepsilon_{al}\right)\right] \tag{1.17}$$

Where $u_n = d\delta_n/dt$ is the relative velocity, and $\varepsilon = 2|\mathbf{d}|/d_\mathrm{p}$ is the dimensionless distance between them. And depending on whether the collision take place between two particles, then Eq. (1.18) should be used, further if the collision is with the wall than, Eq. (1.19) is the suitable one.

$$\lambda_\mathrm{pp}\left(\varepsilon\right) = \frac{1}{4\varepsilon} - \frac{9}{40}\log\left(\varepsilon\right) - \frac{3}{112}\varepsilon\log\left(\varepsilon\right) + 0.995 + \left(\varepsilon\right) \tag{1.18}$$

$$\lambda_\mathrm{pw}\left(\varepsilon\right) = \frac{1}{\varepsilon} - \frac{1}{5}\log\left(\varepsilon\right) - \frac{1}{21}\varepsilon\log\left(\varepsilon\right) + 0.971 + \left(\varepsilon\right) \tag{1.19}$$

Figure 1.5 shows how both the sub-grid model and the dry collision model are activated together.

The lubrication force, is activated at ϵ_{al} and varies continually as a function of ϵ until it reaches the value ϵ_1. From ϵ_1 to $\epsilon = 0$ the lubrication force remains with the calculated value of ϵ_1. After overlap, that is: from $\epsilon = 0$ to ϵ_2, the dry collision model, explained at the last section, takes place and varies continually, while lubrication force still maintains the computed value at ϵ_1. From ϵ_2 and further, only the dry collision model is used. More details can be found at [14].

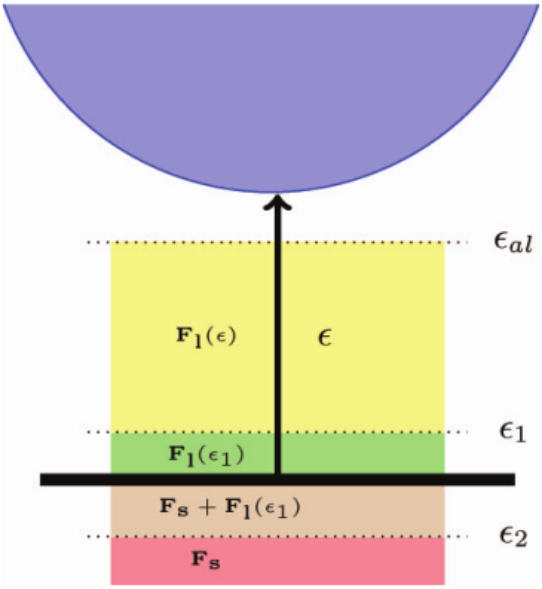

Figure 1.5: Scheme of the force activation for the model proposed by [14].

1.4 Mono and Bi-disperse Couette configuration

1.4.1 Mono-disperse

Monodiperse fluid-particle numerical simulations have been performed in 3D Couette configuration in order to investigate fluid-particle and particle-particle interactions. Figure 1.6 gives a schematic of the simulation case. The computation domain is a box of length $H_x = H$, $H_y = H$ and $H_z = H/2$. In the stream-wise direction (x-direction) and span-wise (z-direction) periodic boundary conditions are applied. In the y-direction (wall-normal direction) two moving walls with no-slip boundary conditions for the fluid phase take place. For the particles, free-slip wall boundary condition is imposed.

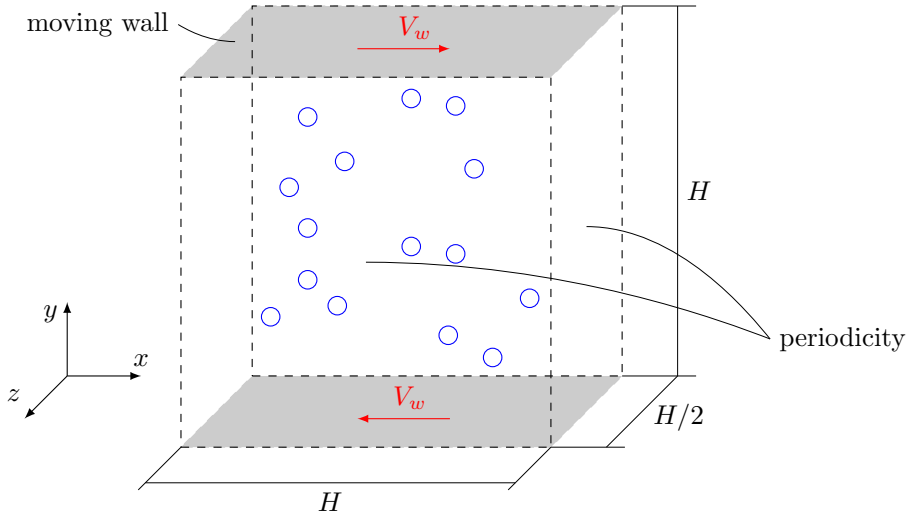

Figure 1.6: Schematic view of the simulation case: Couette configuration.

Six mono-dispersed cases have been performed. Table 1.1 gives the fluid, particle and domain size properties and Table 1.2 gives the simulation parameters of the investigated cases. The parameters, V_w and N_p are respectively the wall velocity and the total number of particles inside the domain. The bulk Stokes number $\mathrm{St}_\mathrm{p,b}$, which characterizes particle inertia with respect to the viscous forces, is defined as follows:

$$\mathrm{St}_\mathrm{p,b} = \tau_\mathrm{p} \frac{2V_w}{H} \tag{1.20}$$

Where the particle response time is $\tau_\mathrm{p} = \rho_\mathrm{p} d_\mathrm{p}^2 / 18\mu_\mathrm{f}$. For all the monodisperse cases, the value is $\tau_\mathrm{p} = 0.526s$. The bulk particle volume fraction is given by $\alpha_\mathrm{p,b} = (N_\mathrm{p}\pi d_\mathrm{p}^3/6)/H_x H_y H_z$. The particle diameter to mesh size ratio is $d_\mathrm{p}/\Delta x = 12$, with $\Delta x = \Delta y = \Delta z$, and the time step is based on the Courant–Friedrichs–Lewy number of CFL = 0.3.

The effects of particle inertia and particle volume fraction are respectively analyzed by investigating the two sets of bulk Stokes number, $St_\mathrm{p,b} = \{15, 30\}$ and the three sets of particle bulk volume fraction $\alpha_\mathrm{p,b} = \{5\%, 15\%, 30\%\}$.

Table 1.1: Fluid and particle material properties

particle diameter	d_p	6 mm
particle density	ρ_p	1000 kg/m^3
fluid density	ρ_f	10 kg/m^3
fluid viscosity	μ_f	3.8 mPa.s
domain dimension	$\mathrm{H}_x = \mathrm{H}_y = 2\mathrm{H}_z = 20d_\mathrm{p}$	12 cm

Table 1.2: Physical parameters of the mono-disperse simulations

CASE	V_w $[\frac{\mathrm{m}}{\mathrm{s}}]$	$\mathrm{N_p}$	$\mathrm{St_{p,b}}$	$\alpha_{\mathrm{p,b}}$
M1	1.71	382	15	5%
M2	1.71	1146	15	15%
M3	1.71	2292	15	30%
M4	3.42	382	30	5%
M5	3.42	1146	30	15%
M6	3.42	2292	30	30%

1.4.2 Bi-disperse

Five cases have been performed in order to investigate bi-disperse fluid-particle behavior at the 3D Couette case. Table 1.3 gives the fluid, particle and domain size properties and Table 1.4 gives the simulation parameters of all the cases. The particle diameter to mesh size ratio is $d_p/\Delta x = 8$ (where $d_\mathrm{p} = d_\mathrm{q}$ and $\Delta x = \Delta y = \Delta z$) and the time step is based on the Courant–Friedrichs–Lewy number of CFL = 0.3.

Table 1.3: Fluid and particle material properties

particle diameter	$d_\mathrm{p} = d_\mathrm{q}$	6 mm
p-particle density	ρ_p	1000 kg/m^3
q-particle density	ρ_q	2000 kg/m^3
fluid density	ρ_f	10 kg/m^3
fluid viscosity	μ_f	3.8 mPa.s
domain dimension	$\mathrm{H}_x = \mathrm{H}_y = 2\mathrm{H}_z = 20d_\mathrm{p}$	12 cm

Table 1.4: Physical parameters of the bi-disperse simulations

CASE	V_w $[\frac{\mathrm{m}}{\mathrm{s}}]$	$\mathrm{N_p}$	$\mathrm{N_q}$	$\mathrm{St_{p,b}}$	$\mathrm{St_{q,b}}$	$\alpha_{\mathrm{p,b}}$	$\alpha_{\mathrm{q,b}}$
B0	0.85	256	256	7.5	15	3.3%	3.3%
B1	1.71	381	76	15	30	5%	1%
B2	1.71	256	256	15	30	3.3%	3.3%
B3	1.71	76	381	15	30	1%	5%
B4	3.42	256	256	30	60	3.3%	3.3%

Using the values of Table 1.3, it can be calculated that: $\tau_\mathrm{p} = 0.526s$ and $\tau_\mathrm{q} = 1.05s$. The values of $\mathrm{St_{p,b}}$ and $\mathrm{St_{q,b}}$ given by Table 1.4 are respectively

the bulk Stokes number of the p-particles and q-particles, calculated as if they were alone in the domain. It is shown in the chapter 4, how to calculate an equivalent bulk bi-disperse Stokes number (St_b^*) taking into account the mixture of particles. In fact, cases B0 to B4 are organized from the least to highest inertial case. This is further discussed in the bi-disperse chapter.

1.5 Simulation procedure

The procedures for the numerical simulations are as follows. At the initial time step ($t = 0$ s), the particles are uniformly and randomly distributed inside the domain without overlapping.

In this manuscript, it is focused on the steady-state particle statistics. And due to that, it is important to establish when the steady-state is in fact reached. For that purpose, the temporal evolution of the total kinetic energy of the particles and the bulk collision frequency are measured. In fact, when the total kinetic energy of the particles reaches a plateau and the collision frequency is constant, statistical convergence is assumed for the purposes of this manuscript. In fact, a posteriori tests showed that this is the case.

The temporal evolution of the total kinetic energy of the two classes of particles, for the case B3 is given by Figure 1.7. It can be seen that near the end of the simulation, a constant value of the kinetic energy is established. Clearly, the more simulation time, the better are the statistics, however, one should bear in mind that the simulation cost is very high, and as such, a good compromise between simulation cost and duration should be achieved. The simulation times used in our simulations provided enough statistical realization data for the purposes of this manuscript.

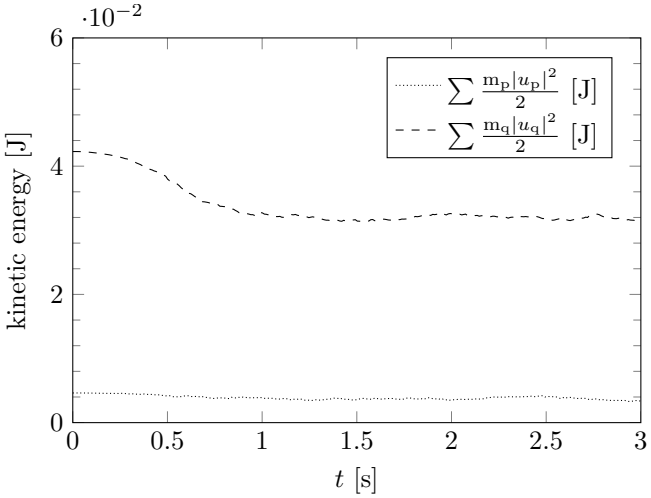

Figure 1.7: Temporal evolution of the total kinetic energy of the particles for the case B3.

Another important parameter to verify the steadiness of the particle flow, is the bulk collision frequency, it can be measured by taking the derivative of the cumulative number of contacts K inside the domain. Every time a particle

begins an interaction with another one, two contacts are formed, and consequently summed to K. The relationship between the collision frequency f_c and the cumulative number is the following one:

$$f_c = \frac{1}{2}\frac{dK}{dt} \tag{1.21}$$

The temporal evolution of K, for the case B3, is shown by Figure 1.8. We note a small transient time in the beginning of the simulation, followed by a linear evolution of K. A linear fit of the data near the end of the time is shown by a red dashed line.

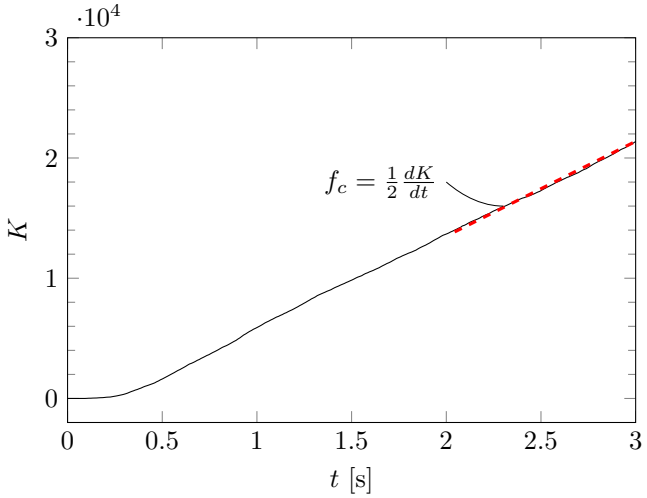

Figure 1.8: Temporal evolution of the cumulative number of contacts K for the case B3. The red dashed line is a linear fit near the end of the simulation time.

Chapter 2

Hybrid Eulerian-Lagrangian statistical approach

Contents

2.1 Introduction

In this section we present a hybrid statistical approach to analyze both the fluid and particle phases [71, 130]. First we present general statistical properties related to the averaging process, and the notion of ensemble average of a random variable is introduced. After that, the Eulerian formalism used to obtain averaged equations of the fluid phase taking into account the interfacial transfers, based on the so-called phase-operator, is shown.

The particle phase is described by a fine-grained probability density function, and based on the Liouville's formalism we originally show an approach that naturally allows for particle interactions with any arbitrary duration, in this manner the Bolztmann assumption of instantaneous collisions are not needed. In addition to that, we show the related transport equations of macroscopic variables such as mean particle velocity and particle fluctuating kinetic energy. Next, we show how to compute the fluid-particle transfers in both the Eulerian fluid frame and the particle Lagrangian frame, and also the relationship between them. Finally, at the end of this chapter, we give an original method for computing the source and flux terms of the particle-particle collisions contribution.

2.2 Average properties

The formulation of average quantities is related to the definition of the average operator $\langle\cdot\rangle$, which must satisfy some properties. Those conditions are usually referred as the Reynolds axioms [84]. Considering the random variables $\mathscr{H}$ and $\mathscr{G}$, the properties can be written as:

$$\langle \mathscr{H} + \mathscr{G} \rangle = \langle \mathscr{H} \rangle + \langle \mathscr{G} \rangle \tag{2.1}$$

$$\langle a\mathscr{H} \rangle = a \langle \mathscr{H} \rangle \quad \text{, if } a = \text{cte} \tag{2.2}$$

$$\langle a \rangle = a \quad \text{, if } a = \text{cte} \tag{2.3}$$

$$\langle \langle \mathscr{H} \rangle \mathscr{G} \rangle = \langle \mathscr{H} \rangle \langle \mathscr{G} \rangle \tag{2.4}$$

$$\left\langle \frac{\partial \mathscr{H}}{\partial t} \right\rangle = \frac{\partial \langle \mathscr{H} \rangle}{\partial t} \tag{2.5}$$

$$\left\langle \frac{\partial \mathscr{H}}{\partial x_j} \right\rangle = \frac{\partial \langle \mathscr{H} \rangle}{\partial x_j} \tag{2.6}$$

Also, it is common to separate into the mean and the fluctuation in the following manner: $\mathscr{H} = \langle \mathscr{H} \rangle + \mathscr{H}'$, with $\mathscr{H}'$ being the fluctuation. Using the relationships (2.1) and (2.4) in such a decomposition, it directly follows that the average of a fluctuating quantity is null: $\langle \mathscr{H}' \rangle = 0$.

A very useful average in fluid mechanics is the so-called ensemble average, which is defined as follows:

$$\langle \mathscr{H} \rangle = \lim_{\mathbb{N}_r \to \infty} \sum_{r=1}^{\mathbb{N}_r} \mathscr{H}^{(r)} \tag{2.7}$$

Where $\mathbb{N}_r$ is the number of identical macroscopic realizations which obey the same statistical laws, but correspond to different local instantaneous values

of the random values. In this case $\mathscr{H}^{(r)}$ corresponds to the value of the random variable of the realization r. In practice the sum presented by Eq. (2.7), under certain conditions, can be expressed in an equivalent integral form [70], with spatial averages given by Eq. (2.8) used in homogeneous configurations and temporal integrals in the form of Eq. (2.9) used in statistically stationary systems.

$$\langle \mathscr{H} \rangle = \lim_{V \to \infty} \frac{1}{V} \int_V \mathscr{H} \, d\boldsymbol{x} \tag{2.8}$$

$$\langle \mathscr{H} \rangle = \lim_{\Delta t \to \infty} \frac{1}{\Delta t} \int_t^{t+\Delta t} \mathscr{H} \, d\tau \tag{2.9}$$

In ergodic systems [84], both of those averages should yield the same results, and can be indistinguishably used. Under that circumstance, a spatio-temporal average, can be used. Such an average is given by Eq. (2.10).

$$\langle \mathscr{H} \rangle = \lim_{V \to \infty} \lim_{\Delta t \to \infty} \frac{1}{V} \frac{1}{\Delta t} \int_t^{t+\Delta t} \int_V \mathscr{H} \, d\boldsymbol{x} d\tau \tag{2.10}$$

In the following of this chapter more details related to the averages for the fluid and the particle phase are given.

2.3 Fluid-phase Eulerian averaging

2.3.1 Single phase equations

The transport equations in terms of single phase fluid flow, related to the conservation of mass and momentum are respectively given by Eqs. (2.11) and (2.19).

$$\frac{\partial \rho_{\mathrm{f}}}{\partial t} + \frac{\partial \left(\rho_{\mathrm{f}} u_{\mathrm{f},j}\right)}{\partial x_j} = 0 \tag{2.11}$$

$$\frac{\partial \left(\rho_{\mathrm{f}} u_{\mathrm{f},i}\right)}{\partial t} + \frac{\partial \left(\rho_{\mathrm{f}} u_{\mathrm{f},i} u_{\mathrm{f},j}\right)}{\partial x_j} = \frac{\partial \sigma_{\mathrm{f},ij}}{\partial x_j} + \rho_{\mathrm{f}} g_i \tag{2.12}$$

Where $\sigma_{\mathrm{f},ij} = -p_{\mathrm{f}}\delta_{ij} + \tau_{\mathrm{f},ij}$ is the stress tensor, p_{f} is the fluid pressure, δ_{ij} is the Kronecker delta, and $\tau_{\mathrm{f},ij}$ accounts for the viscous part of the tensor. Besides, in the case of a Newtonian fluid, it is given by $\tau_{\mathrm{f},ij} = 2\mu_{\mathrm{f}} D_{ij} + \lambda_{\mathrm{f}} \frac{\partial u_{\mathrm{f},m}}{\partial x_m}\delta_{ij}$, with μ_{f} and λ_{f} being the dynamic viscosity coefficients, and the deformation tensor is given by $D_{ij} = \frac{1}{2}\left(\frac{\partial u_{\mathrm{f},i}}{\partial x_j} + \frac{\partial u_{\mathrm{f},j}}{\partial x_i}\right)$. In addition, g_i, is the acceleration of gravity, which is not present in our simulations.

2.3.2 Multi-phase flow formalism

In this section we establish local and instantaneous equations for the fluid phase, with constant density ρ_{f}, taking into account the interfacial transfers with other phases. In order to derive such equations, [51], [50] and [29], a characteristic phase operator χ_{f} is used, which is defined as follows:

$$\chi_{\mathrm{f}}(\mathbf{M}, t) = \begin{cases} 1, & \text{if } \mathbf{M} \text{ is inside the fluid phase at the time } t \\ 0, & \text{otherwise} \end{cases} \tag{2.13}$$

Where $\mathbf{M}$ is an arbitrary point in space. This function is a 3D generalization of the Heaviside function, and in the sense of distributions, this function has the following properties:

$$\frac{\partial \chi_{\mathrm{f}}}{\partial t} + w_j \frac{\partial \chi_{\mathrm{f}}}{\partial x_j} = 0 \tag{2.14}$$

$$\frac{\partial \chi_{\mathrm{f}}}{\partial x_j} = n_{\mathrm{p},j}\delta_{\mathrm{fp}} \tag{2.15}$$

Where $\boldsymbol{w}$ is the local propagation velocity of the interface, $\boldsymbol{n}_{\mathrm{p}}$ is the unit vector normal to the fluid-particle interface δ_{fp} and pointing outward the particle phase, as depicted by Figure 2.1, and δ_{fp} is the Dirac's delta distribution associated to the fluid particle interface.

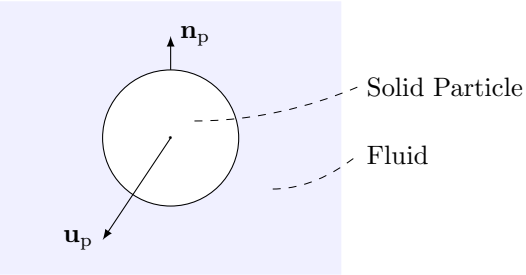

Figure 2.1: Normal unity vector $\boldsymbol{n}_\mathrm{p}$ at a given arbitrary point at the fluid-particle interface.

In order to obtain a local and instantaneous equation for the mass conservation for the fluid phase that takes into account inter-facial transfers, the single phase equation for mass conservation, Eq. (2.11), is multiplied by the phase operator χ_f, and combined with the properties of the phase operator, given by Eqs. (2.14) & (2.15), which yields:

$$\frac{\partial\left(\rho_\mathrm{f}\chi_\mathrm{f}\right)}{\partial t}+\frac{\partial\left(\rho_\mathrm{f}u_{\mathrm{f},j}\chi_\mathrm{f}\right)}{\partial x_j}=\rho_\mathrm{f}\left(u_{\mathrm{f},j}-w_j\right)n_{\mathrm{p},j}\delta_\mathrm{fp} \tag{2.16}$$

In our case, since there is no mass transfer, the term on the right-hand side of the equation above is null, and thus the fluid velocity at the fluid-particle interface coincide with the propagation velocity of the interface.

Averaged fluid mass balance

Applying the ensemble average on Eq. (2.16), gives:

$$\frac{\partial\left(\alpha_\mathrm{f}\rho_\mathrm{f}\right)}{\partial t}+\frac{\partial\left(\alpha_\mathrm{f}\rho_\mathrm{f}U_{\mathrm{f},j}\right)}{\partial x_j}=0 \tag{2.17}$$

Where $\alpha_\mathrm{f}=\langle\chi_\mathrm{f}\rangle$ is the fluid volume fraction. Additionally, we define the phase average, consistent with our case with constant fluid density, as the ratio of the ensemble averages in the following manner:

$$\langle\cdot\rangle_\mathrm{f}=\frac{\langle\,\cdot\,\chi_\mathrm{f}\rangle}{\langle\chi_\mathrm{f}\rangle} \tag{2.18}$$

With this definition, the mean fluid velocity, present in Eq. (2.17), is given by: $U_{\mathrm{f},i}=\langle u_{\mathrm{f},i}\rangle_\mathrm{f}$

Averaged fluid momentum balance

Following a similar procedure, the averaged fluid equation of the mean fluid velocity, taking into account interfacial transfers, is given as:

$$\frac{\partial\left(\alpha_{\mathrm{f}}\rho_{\mathrm{f}}U_{\mathrm{f},i}\right)}{\partial t}+\frac{\partial\left(\alpha_{\mathrm{f}}\rho_{\mathrm{f}}U_{\mathrm{f},i}U_{\mathrm{f},j}\right)}{\partial x_j} = -\frac{\partial\left(\alpha_{\mathrm{f}}P_{\mathrm{f}}\right)}{\partial x_i}+\frac{\partial}{\partial x_j}\left(\alpha_{\mathrm{f}}\left\langle\tau_{\mathrm{f},ij}\right\rangle_{\mathrm{f}}-\alpha_{\mathrm{f}}\rho_{\mathrm{f}}R_{\mathrm{f},ij}\right) +\alpha_{\mathrm{f}}\rho_{\mathrm{f}}g_i+I_{\mathrm{p}\to\mathrm{f},i} \tag{2.19}$$

Where $P_{\mathrm{f}}=\left\langle p_{\mathrm{f}}\right\rangle_{\mathrm{f}}$ is the mean pressure, $R_{\mathrm{f},ij}=\left\langle u'_{\mathrm{f},i}u'_{\mathrm{f},j}\right\rangle_{\mathrm{f}}$ is the Reynolds stress tensor. Also, the term due to the interfacial momentum transfer is:

$$I_{\mathrm{p}\to\mathrm{f},i}=-\left\langle\sigma_{\mathrm{f},ij}n_{\mathrm{p},j}\delta_{\mathrm{fp}}\right\rangle+\left\langle\rho_{\mathrm{f}}u_{\mathrm{f},i}\left(u_{\mathrm{f},j}-w_{\mathrm{f},j}\right)n_{\mathrm{p},j}\delta_{\mathrm{fp}}\right\rangle \tag{2.20}$$

The second term on the right-hand side becomes null without mass transfer. Regarding the right-hand side of the averaged mean fluid velocity balance, it can be respectively found a term due to the mean pressure gradient, a term resulting from the competition between the viscous stresses and the Reynolds stresses, one term due to the body forces in the fluid and finally a term due to the exchange of momentum via interaction with the particle interfaces.

Averaged fluid fluctuating kinetic energy balance

The averaged transport equation for the fluid fluctuating kinetic energy $k_{\mathrm{f}}=R_{\mathrm{f},ii}/2$ is obtained in a similar manner, averaging the instantaneous kinetic energy equation and subtracting from the mean kinetic energy equation, which gives the equation below:

$$\begin{aligned}\frac{\partial\left(\alpha_{\mathrm{f}}\rho_{\mathrm{f}}k_{\mathrm{f}}\right)}{\partial t}+\frac{\partial\left(\alpha_{\mathrm{f}}\rho_{\mathrm{f}}k_{\mathrm{f}}U_{\mathrm{f},j}\right)}{\partial x_j} &= -\alpha_{\mathrm{f}}\rho_{\mathrm{f}}R_{\mathrm{f},ij}\frac{\partial U_{\mathrm{f},i}}{\partial x_j}-\alpha_{\mathrm{f}}\left\langle\tau'_{\mathrm{f},ij}\frac{\partial u'_{\mathrm{f},i}}{\partial x_j}\right\rangle_{\mathrm{f}} \\ &\quad -\frac{\partial}{\partial x_j}\left[\frac{\alpha_{\mathrm{f}}\rho_{\mathrm{f}}}{2}S_{\mathrm{f},iij}+\alpha_{\mathrm{f}}\left\langle p'_{\mathrm{f}}u'_{\mathrm{f},j}\right\rangle_{\mathrm{f}}-\alpha_{\mathrm{f}}\left\langle\tau'_{\mathrm{f},ij}u'_{\mathrm{f},i}\right\rangle_{\mathrm{f}}\right] \\ &\quad +\Pi^{k_{\mathrm{f}}}_{\mathrm{p}\to\mathrm{f}}\end{aligned} \tag{2.21}$$

On the right-hand side of the equation, the first term is related to the production of fluctuating kinetic energy associated to the mean shear of the fluid velocity, which is a term related to the transfer of mean to the fluctuating motion. The second term is the dissipation of k_{f} due to internal fluid friction. Next, on the second line, three diffusive terms are found, the first one is related to the triple fluid velocity correlation, which represents the transport of fluctuant kinetic energy by the velocity fluctuation, the second to the correlation between the pressure and the velocity fluctuations, and finally a term related to viscous diffusion. The last term is related to the exchange due to the interaction with the particles, and it is given by:

$$\Pi^{k_{\mathrm{f}}}_{\mathrm{p}\to\mathrm{f}}=-\left\langle\sigma_{\mathrm{f},ij}u'_{\mathrm{f},i}n_{\mathrm{p},j}\delta_{\mathrm{fp}}\right\rangle+\left\langle\frac{1}{2}\rho_{\mathrm{f}}u'_{\mathrm{f},i}u'_{\mathrm{f},j}\left(u_{\mathrm{f},j}-w_j\right)n_{\mathrm{p},j}\delta_{\mathrm{fp}}\right\rangle \tag{2.22}$$

Similarly to the other interfacial terms, only the first term on the right-hand side of the equation above is non-null in our simulations.

2.4 Particle-phase Lagrangian averaging

2.4.1 Probability density function approach

The strong analogy between the thermal motion of molecules and the random motion of particles in turbulent two-phase flow has led several authors to use the kinetic theory approach to describe the particle statistics and and derive continuum equations for the dispersed phase [16], [71], [87], [129] and [102].

As already stated at the beginning of the chapter, generally in the kinetic theory, the Boltzmann assumption of instantaneous collision is used. In this section, we nonetheless describe an approach based on the Liouville's formalism that allows for particle-particle interaction with any arbitrary duration, and could be extended to other interaction types such as electromagnetic ones.

Let $f_{\mathrm{p}}\left(\boldsymbol{c}_{\mathrm{p}}, \boldsymbol{x}, t\right)$ be a one particle probability density function, related to an ensemble of particles with the same mass m_{p} and diameter d_{p}, such that the expression given by the Eq. (2.23) represents the probable mean number of particles whose particle center $\boldsymbol{x}_{\mathrm{p}}(t) \in [\boldsymbol{x}, \boldsymbol{x} + \delta\boldsymbol{x}[$ and particle translational velocity $\boldsymbol{u}_{\mathrm{p}}(t) \in [\boldsymbol{c}_{\mathrm{p}}, \boldsymbol{c}_{\mathrm{p}} + \delta\boldsymbol{c}_{\mathrm{p}}[$.

$$f_{\mathrm{p}}\left(\boldsymbol{c}_{\mathrm{p}}, \boldsymbol{x}, t\right) \delta\boldsymbol{c}_{\mathrm{p}} \delta\boldsymbol{x} \tag{2.23}$$

The function f_{p}, obeying the properties described above [87], can be written as:

$$f_{\mathrm{p}}\left(\boldsymbol{c}_{\mathrm{p}}, \boldsymbol{x}, t\right) = \lim_{\mathbb{N}_r \to \infty} \frac{1}{\mathbb{N}_r} \sum_{r=1}^{\mathbb{N}_r} \left[\sum_{n=1}^{N_{\mathrm{p}}^{(r)}} \delta\left(\boldsymbol{c}_{\mathrm{p}} - \boldsymbol{u}_{\mathrm{p}}^{(n,r)}(t)\right) \delta\left(\boldsymbol{x} - \boldsymbol{x}_{\mathrm{p}}^{(n,r)}(t)\right) \right] \tag{2.24}$$

Where $\mathbb{N}_r$ is the number of realization of the particulate flow and, $N_{\mathrm{p}}^{(r)}$ is the number of particles related to each realization. Also, $\boldsymbol{u}_{\mathrm{p}}^{(n,r)}(t)$, $\boldsymbol{x}_{\mathrm{p}}^{(n,r)}(t)$ are respectively the translational velocity and center position of a particle n, at a time t, of the realization r. From the definition, it follows that the particle number density n_{p}, or the number of particles per unit volume, can be found by integrating f_{p} over the velocity space, reads:

$$n_{\mathrm{p}}(\boldsymbol{x}, t) \quad = \quad \int f_{\mathrm{p}}\left(\boldsymbol{c}_{\mathrm{p}}, \boldsymbol{x}, t\right) d\boldsymbol{c}_{\mathrm{p}} \tag{2.25}$$

In the case of a mixture of two particle species differing by its mass, one probability density function can be attributed to each particle species. With f_{p} for the particles of mass m_{p} and f_{q} for the ones with mass m_{q}. In the following, we describe the equations for the p-particles associated with the probability density function f_{p}. The same equations for the q-particles can be obtained in a similar fashion.

Let $\mathscr{H}$ be a function attached to each particle, we denote the conditional average according to the instantaneous particle properties with the following notation:

$$\langle \mathscr{H} | \boldsymbol{c}_\mathrm{p}, \boldsymbol{x}, t \rangle = \langle \mathscr{H} \left(\boldsymbol{u}_\mathrm{p}, \boldsymbol{x}_\mathrm{p}; t \right) | \boldsymbol{u}_\mathrm{p}(t) = \boldsymbol{c}_\mathrm{p}, \boldsymbol{x}_\mathrm{p}(t) = \boldsymbol{x} \rangle \tag{2.26}$$

Which by definition [105]:

$$\begin{aligned} &\langle \mathscr{H} | \boldsymbol{c}_\mathrm{p}, \boldsymbol{x}, t \rangle \, f_\mathrm{p} \left(\boldsymbol{c}_\mathrm{p}, \boldsymbol{x}, t \right) = \\ &\lim_{\mathbb{N}_r \to \infty} \frac{1}{\mathbb{N}_r} \sum_{r=1}^{\mathbb{N}_r} \left[\sum_{n=1}^{N_\mathrm{p}^{(r)}} \mathscr{H}^{(r)} \left(\boldsymbol{c}_\mathrm{p}, \boldsymbol{x}, t \right) \delta \left(\boldsymbol{c}_\mathrm{p} - \boldsymbol{u}_\mathrm{p}^{(n,r)}(t) \right) \delta \left(\boldsymbol{x} - \boldsymbol{x}_\mathrm{p}^{(n,r)}(t) \right) \right] \end{aligned} \tag{2.27}$$

Using the definitions given above, the mean value of $\mathscr{H}$ is given as follows:

$$n_\mathrm{p} \langle \mathscr{H} \rangle \left(\boldsymbol{x}, t \right) = \int \langle \mathscr{H} | \boldsymbol{c}_\mathrm{p}, \boldsymbol{x}, t \rangle \, f_\mathrm{p} \left(\boldsymbol{c}_\mathrm{p}, \boldsymbol{x}, t \right) d\boldsymbol{c}_\mathrm{p} \tag{2.28}$$

Related to the p-particles, the most used statistical variables in this thesis are given below:

$$\begin{aligned} U_{\mathrm{p},i} &= \langle u_{\mathrm{p},i} \rangle & (2.29) \\ R_{\mathrm{p},ij} &= \left\langle u'_{\mathrm{p},i} u'_{\mathrm{p},j} \right\rangle & (2.30) \\ S_{\mathrm{p},ijk} &= \left\langle u'_{\mathrm{p},i} u'_{\mathrm{p},j} u'_{\mathrm{p},k} \right\rangle & (2.31) \\ Q_{\mathrm{p},ijkl} &= \left\langle u'_{\mathrm{p},i} u'_{\mathrm{p},j} u'_{\mathrm{p},k} u'_{\mathrm{p},l} \right\rangle & (2.32) \end{aligned}$$

Where $u'_{\mathrm{p},i} = u_{\mathrm{p},i} - \langle u_{\mathrm{p},i} \rangle$, is the particle velocity fluctuation. The physical meaning of such variables are discussed throughout the next chapters. Another important variable is the particle fluctuating kinetic energy, and it is defined as the trace of the particle kinetic stress tensor, divided by two:

$$q_\mathrm{p}^2 = \frac{R_{\mathrm{p},ii}}{2} \tag{2.33}$$

The transport equation of f_p is known as the Liouville equation, and can be written in its most general form [87, 129] as:

$$\frac{\partial f_\mathrm{p}}{\partial t} + \frac{\partial}{\partial x_i} \left[c_{\mathrm{p},i} f_\mathrm{p} \right] + \frac{\partial}{\partial c_{\mathrm{p},i}} \left[\left\langle \frac{d u_{\mathrm{p},i}}{dt} | \boldsymbol{c}_\mathrm{p}, \boldsymbol{x}, t \right\rangle f_\mathrm{p} \right] = 0 \tag{2.34}$$

Substantially, the particle acceleration is a result of the effect of all the various forces acting on the particle as written in Eq. (2.35). The first term on the right-hand side is the force due to the interaction with the fluid phase. The second and third terms are respectively associated with the total repulsive force due to the ensemble of p-particles and q-particles. Finally, the fourth term represents exterior forces acting through distance, such as gravity or electrical forces, which are not present in our study.

$$m_{\mathrm{p}} \frac{d\boldsymbol{u}_{\mathrm{p}}}{dt} = \mathbf{F}_{\mathrm{f}\to\mathrm{p}} + \sum_{\mathrm{p'}\neq\mathrm{p}} \mathbf{F}_{\mathrm{p'}\to\mathrm{p}} + \sum_{\mathrm{q}} \mathbf{F}_{\mathrm{q}\to\mathrm{p}} + \mathbf{F}_{\mathrm{B}\to\mathrm{p}} \tag{2.35}$$

Substituting Eq.(2.35) into Eq.(2.34), and rearranging the terms related to the particle-particle interaction, and body forces on the right-hand side of the equality, a common version of this equation can be found, where the effect of the particle-particle interactions are written simply in the form $\frac{\partial f_{\mathrm{p}}}{\partial t}|_{\mathrm{coll}}$.

$$\begin{aligned}\frac{\partial f_{\mathrm{p}}}{\partial t} + \frac{\partial}{\partial x_i}\left[c_{\mathrm{p},i} f_{\mathrm{p}}\right] + \frac{\partial}{\partial c_{\mathrm{p},i}}\left[\left\langle \frac{F_{\mathrm{f}\to\mathrm{p},i}}{m_{\mathrm{p}}} \mid \mathbf{c}_{\mathrm{p}} \right\rangle f_{\mathrm{p}}\right] + \frac{\partial}{\partial c_{\mathrm{p},i}}\left[\left\langle \frac{F_{\mathrm{B}\to\mathrm{p},i}}{m_{\mathrm{p}}} \mid \mathbf{c}_{\mathrm{p}} \right\rangle f_{\mathrm{p}}\right] \\ = \underbrace{-\frac{\partial}{\partial c_{\mathrm{p},i}}\left[\left\langle \sum_{\mathrm{p'}\neq\mathrm{p}} \frac{F_{\mathrm{p'}\to\mathrm{p},i}}{m_{\mathrm{p}}} \mid \mathbf{c}_{\mathrm{p}} \right\rangle f_{\mathrm{p}}\right] - \frac{\partial}{\partial c_{\mathrm{p},i}}\left[\left\langle \sum_{\mathrm{q}} \frac{F_{\mathrm{q}\to\mathrm{p},i}}{m_{\mathrm{p}}} \mid \mathbf{c}_{\mathrm{p}} \right\rangle f_{\mathrm{p}}\right]}_{\frac{\partial f_{\mathrm{p}}}{\partial t}|_{\mathrm{coll}}}\end{aligned} \tag{2.36}$$

In the frame of our bi-disperse simulations, see section 1.4.2, we consider each class of particle having their own probability density transport equation. In this way, Eq. (2.34), is written for the class of particles p, and the same equation, but with the index q, is to be referred to the transport equation of the class of particles q. Note that there is a coupling between both transport equations due to the interaction forces from one class of particles to the other.

2.4.2 Moment equations

Assuming that $\mathscr{H}$ is a function of the particle translational velocity, and considering an ensemble of p-particles with the same given mass m_{p}, the transport equation, Eq. (2.34), can then be multiplied by $\mathscr{H}$ and integrated though the velocity space, [18], to yield:

$$\begin{aligned}\frac{\partial}{\partial t}\left(n_{\mathrm{p}} m_{\mathrm{p}} \left\langle \mathscr{H} \right\rangle\right) + \frac{\partial}{\partial x_j}\left(n_{\mathrm{p}} m_{\mathrm{p}} \left\langle \mathscr{H} \right\rangle U_{\mathrm{p},j}\right) = -\frac{\partial}{\partial x_j}\left(n_{\mathrm{p}} m_{\mathrm{p}} \left\langle u'_{\mathrm{p},j} \mathscr{H} \right\rangle\right) \\ + n_{\mathrm{p}} \left\langle m_{\mathrm{p}} \frac{du_{\mathrm{p},j}}{dt} \frac{\partial \mathscr{H}}{\partial u_{\mathrm{p},j}} \right\rangle\end{aligned} \tag{2.37}$$

Particle number density equation

Substituting $\mathscr{H} = 1$, the transport equation of the p-particle number density n_{p} is written:

$$\frac{\partial}{\partial t}\left(n_{\mathrm{p}} m_{\mathrm{p}}\right) + \frac{\partial}{\partial x_i}\left(n_{\mathrm{p}} m_{\mathrm{p}} U_{\mathrm{p},i}\right) = 0 \tag{2.38}$$

Particle mean velocity equation

The transport equation of the mean p-particle velocity, can be obtained by substituting $\mathscr{H} = u_{\mathrm{p},i}$, which in combination with Eq. (2.35) and Eq. (2.38), is written:

$$n_{\mathrm{p}} m_{\mathrm{p}} \left(\frac{\partial U_{\mathrm{p},i}}{\partial t} + U_{\mathrm{p},j} \frac{\partial U_{\mathrm{p},i}}{\partial x_j} \right) = -\frac{\partial \left(n_{\mathrm{p}} m_{\mathrm{p}} R_{\mathrm{p},ij} \right)}{\partial x_j} + n_{\mathrm{p}} \left\langle F_{\mathrm{f}\to\mathrm{p},i} \right\rangle + n_{\mathrm{p}} \left\langle F_{\mathrm{B}\to\mathrm{p},i} \right\rangle + \mathbb{C}_{\mathrm{p}\to\mathrm{p}}(m_{\mathrm{p}} u_{\mathrm{p},i}) + \mathbb{C}_{\mathrm{q}\to\mathrm{p}}(m_{\mathrm{p}} u_{\mathrm{p},i}) \quad (2.39)$$

Where, in accordance with Eq. (2.35), there are two particle-particle terms, one due to the interaction p-particles and another due to the q-particles $\mathbb{C}_{\mathrm{p}\to\mathrm{p}}(m_{\mathrm{p}} u_{\mathrm{p},i}) = n_{\mathrm{p}} \left\langle F_{\mathrm{p}'\to\mathrm{p},i} \right\rangle$, and $\mathbb{C}_{\mathrm{q}\to\mathrm{p}}(m_{\mathrm{p}} u_{\mathrm{p},i}) = n_{\mathrm{p}} \left\langle F_{\mathrm{q}\to\mathrm{p},i} \right\rangle$. Related to the fluid-particle interaction term, we denote $n_{\mathrm{p}} \left\langle F_{\mathrm{f}\to\mathrm{p},i} \right\rangle = I_{\mathrm{f}\to\mathrm{p},i}$. The terms on the right-hand side of the Eq. (2.39) respectively represent: a kinetic momentum transport term by velocity fluctuation, a fluid-particle interaction term, a body-force term and the last two terms are the particle-particle interaction terms.

Particle kinetic stress equation

Substituting $\mathscr{H} = u_{\mathrm{p},i} u_{\mathrm{p},j}$, and combining with Eq. (2.38), Eq. (2.39) and Eq. (2.35), the transport equation of the particle kinetic stress, is written:

$$\begin{aligned} n_{\mathrm{p}} m_{\mathrm{p}} \left(\frac{\partial R_{\mathrm{p},ij}}{\partial t} + U_{\mathrm{p},k} \frac{\partial R_{\mathrm{p},ij}}{\partial x_k} \right) = & -\frac{\partial \left(n_{\mathrm{p}} m_{\mathrm{p}} S_{\mathrm{p},ijk} \right)}{\partial x_k} \\ & - n_{\mathrm{p}} m_{\mathrm{p}} \left[R_{\mathrm{p},ik} \frac{\partial U_{\mathrm{p},j}}{\partial x_k} - R_{\mathrm{p},jk} \frac{\partial U_{\mathrm{p},i}}{\partial x_k} \right] \\ & + n_{\mathrm{p}} \left\langle F_{\mathrm{f}\to\mathrm{p},k} \left[\delta_{k,i} u'_{\mathrm{p},j} + \delta_{k,j} u'_{\mathrm{p},i} \right] \right\rangle \\ & + \mathbb{C}_{\mathrm{p}\to\mathrm{p}}(m_{\mathrm{p}} u'_{\mathrm{p},i} u'_{\mathrm{p},j}) + \mathbb{C}_{\mathrm{q}\to\mathrm{p}}(m_{\mathrm{p}} u'_{\mathrm{p},i} u'_{\mathrm{p},j}) \\ & + n_{\mathrm{p}} \left\langle F_{\mathrm{B}\to\mathrm{p},k} \left[\delta_{k,i} u'_{\mathrm{p},j} + \delta_{k,j} u'_{\mathrm{p},i} \right] \right\rangle \quad (2.40) \end{aligned}$$

Where $\mathbb{C}_{\mathrm{p}\to\mathrm{p}}(m_{\mathrm{p}} u'_{\mathrm{p},i} u'_{\mathrm{p},j}) = n_{\mathrm{p}} \left\langle F_{\mathrm{p}'\to\mathrm{p},k} \left[\delta_{k,i} u'_{\mathrm{p},j} + \delta_{k,j} u'_{\mathrm{p},i} \right] \right\rangle$, and analogously $\mathbb{C}_{\mathrm{q}\to\mathrm{p}}(m_{\mathrm{p}} u'_{\mathrm{p},i} u'_{\mathrm{p},j}) = n_{\mathrm{p}} \left\langle F_{\mathrm{q}\to\mathrm{p},k} \left[\delta_{k,i} u'_{\mathrm{p},j} + \delta_{k,j} u'_{\mathrm{p},i} \right] \right\rangle$. On the right-hand side of the equation above, it can be respectively found at each line: a kinetic transport term by the velocity fluctuation, a production term by the mean particle velocity shear, a fluid-particle interaction term, two particle-particle interaction terms and a body force related term.

Particle fluctuating kinetic energy equation

The transport equation of the particle fluctuating kinetic energy can be obtained by taking the trace of the particle kinetic stress equation:

$$n_{\mathrm{p}} m_{\mathrm{p}} \left(\frac{\partial q_{\mathrm{p}}^2}{\partial t} + U_{\mathrm{p},j} \frac{\partial q_{\mathrm{p}}^2}{\partial x_j} \right) = -\frac{1}{2} \frac{\partial \left(n_{\mathrm{p}} m_{\mathrm{p}} S_{\mathrm{p},iij} \right)}{\partial x_j} - n_{\mathrm{p}} m_{\mathrm{p}} R_{\mathrm{p},ij} \frac{\partial U_{\mathrm{p},i}}{\partial x_j}$$
$$+ n_{\mathrm{p}} \left\langle F_{\mathrm{f}\to\mathrm{p},i} u'_{\mathrm{p},i} \right\rangle + \mathbb{C}_{\mathrm{p}\to\mathrm{p}}\left(\frac{m_{\mathrm{p}} u'_{\mathrm{p},i} u'_{\mathrm{p},i}}{2} \right) + \mathbb{C}_{\mathrm{q}\to\mathrm{p}}\left(\frac{m_{\mathrm{p}} u'_{\mathrm{p},i} u'_{\mathrm{p},i}}{2} \right) + n_{\mathrm{p}} \left\langle F_{\mathrm{B}\to\mathrm{p},i} u'_{\mathrm{p},i} \right\rangle \quad (2.41)$$

The terms on the right-hand side of this equation are similar to those of the particle kinetic stress equation, since only a contraction of the indexes was performed. Also, we denote the term fluid-particle $n_{\mathrm{p}} \left\langle F_{\mathrm{f}\to\mathrm{p},i} u'_{\mathrm{p},i} \right\rangle = \Pi^{q_{\mathrm{p}}^2}_{\mathrm{f}\to\mathrm{p}}$.

2.5 Computation of the statistics

2.5.1 Particle statistics

In order to compute the statistics, first the domain is divided into slices such as the one depicted by Figure 2.2, due to the homogeneity in the xz plane in our simulation, which is caused by the infinite domain in this plane due to the periodic boundary conditions both in stream-wise and span-wise directions. The slices are defined in such a way that the coordinate in the wall-normal direction of the j-th slice is y_j, and the thickness of each slice is ΔH. Considering that, any particle whose center of mass obeys the following relationship $y_\mathrm{p} \in [y_j - \Delta H/2, y_j + \Delta H/2]$ is considered inside the j-th slice.

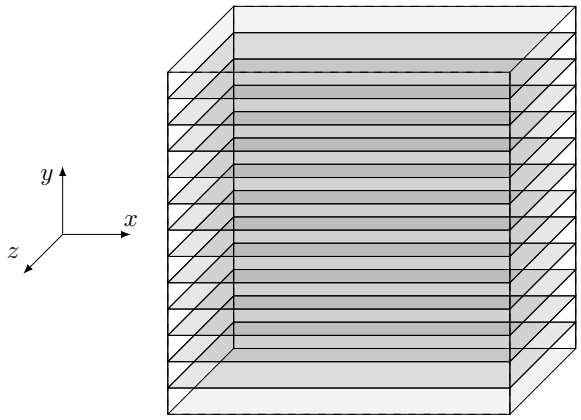

Figure 2.2: Division of the computational domain into slices.

Furthermore, taking into consideration that the flow is statistically converged in the time range $t \in [t_i, t_f]$. A spatio-temporal cumulative function of a variable $\mathscr{H}$ is defined in the following manner:

$$\mathrm{CUMUL}[\ \mathscr{H}\ ] \ = \sum_{\substack{y_\mathrm{p} \in [y_j - \Delta H/2, y_j + \Delta H/2] \\ t \in [t_i, t_f]}} \mathscr{H} \tag{2.42}$$

This is in fact a cumulative sum whose particle centers are inside the slice for all the realizations associated with the statistically converged time-steps. Note that we assumed a ergodic hypothesis, which in practice is related to the fact that both the spatial and temporal statistics produce the same result. The average value of $\mathscr{H}$, which is a function only of the slice coordinate, is calculated as follows:

$$< \mathscr{H} > = \ \frac{\mathrm{CUMUL}[\ \mathscr{H}\ ]}{\mathrm{CUMUL}[\ 1\ ]} \tag{2.43}$$

All of the fluctuating statistics can be easily calculated using non-fluctuating statistics. For instance, the average of the velocity fluctuation product can be written as:

$$< u'_{\mathrm{p},i} u'_{\mathrm{p},j} > = < u_{\mathrm{p},i} u_{\mathrm{p},j} > - < u_{\mathrm{p},i} >< u_{\mathrm{p},j} > \tag{2.44}$$

The particle number density, n_{p}, or the mean number of particle centers in a given volume (slice volume in our case), is calculated as follows:

$$n_{\mathrm{p}} = \frac{\mathrm{CUMUL}[\ 1\ ]}{N_t H_x H_z \Delta H} \tag{2.45}$$

Where N_t is the number of time-steps between t_i and t_f. And H_x and H_z are respectively the domain length and depth, given by Table 1.1.

The choice of the slice thickness is based upon the following arguments: In order to have a good converged statistical value, one has to have enough statistical events, nonetheless our resolved simulations are very expensive in CPU cost, and thus the number of statistical events are limited. In that sense, the larger the size of the slice, the greater the number of statistical events. On the other hand, to posses good spatial resolution in the wall normal direction, that is, to be able to capture the gradients in the y-direction the resolution should be small, and consequently the slice size should be small. For our cases, we have found that ten to thirty divisions presented approximately the same results.

2.5.2 Fluid statistics

To perform fluid statistics a similar procedure is used, the only difference however is that the cumulation of a fluid variable φ is performed at a given wall-normal coordinate, that coincides with the available position of the velocity solution on the mesh grid, reads:

$$\mathrm{CUMUL}_{\mathrm{f}}[\ \varphi\ ] = \sum_{\substack{y_{\mathrm{f}}=y_{\mathrm{mesh}} \\ t\in[t_i,t_f]}} \varphi \tag{2.46}$$

In fact, the function on the left-hand side of Eq. (2.46), only depends on that coordinate.

In order to perform phase averages in the fluid flow zone, the phase operator, which can be expressed by means of the color function, as: $\chi_{\mathrm{f}} = 1 - C$, is used to compute the phase-average of a fluid variable φ, as follows:

$$< \varphi >_{\mathrm{f}} = \frac{\mathrm{CUMUL}_{\mathrm{f}}[\ \varphi\chi_{\mathrm{f}}\ ]}{\mathrm{CUMUL}_{\mathrm{f}}[\ \chi_{\mathrm{f}}\ ]} \tag{2.47}$$

This formula is related to the definition given by Eq. (2.18). Details on the computation of the interfacial terms of equations (2.19) and (2.21) are given in the next section.

2.6 Computation of fluid-particle exchange terms

2.6.1 Fluid to Particle transfer

From the results of our resolved simulations, it is possible to compute the individual acceleration, for each particle, at all time. Also, all forces related to particle-particle interactions are also known in all time-steps, see section 1.3. In our case no body forces are present. With that information, using Eq. (2.35), the fluid force applied at each particle at all time-steps can be computed as follows:

$$\mathbf{F}_{\mathrm{f}\to\mathrm{p}} = m_{\mathrm{p}}\frac{d\boldsymbol{u}_{\mathrm{p}}}{dt} - \sum_{\mathrm{p'}\neq\mathrm{p}}\mathbf{F}_{\mathrm{p'}\to\mathrm{p}} - \sum_{\mathrm{q}}\mathbf{F}_{\mathrm{q}\to\mathrm{p}} \tag{2.48}$$

The fluid force applied to the particle could also be obtained by the integration of the fluid stress tensor in the whole surface of the particle whose center belongs to the averaging volume. Note that, in such an integration, while the surface of the particle may be slightly outside the averaging volume, the center on the other hand, must be contained within the averaging volume. This is due to the fact that even tough the forces are applied in the surface of the particle, the resulting force is in fact applied in the center mass of the particle, which is where all the other transported variables by the particle are defined.

Obtaining the fluid force by Eq. (2.48) is however much more convenient, since it avoids the need for numerical interpolation schemes near the surface of the particle to compute the surface integral.

With these data from the fluid force for all particles, at all time-steps, the computation of the transfer terms are then performed using Eq. 2.43. Related to the mean particle velocity and fluctuating kinetic energy equation, the transfer of momentum from the fluid to particles and the source term of particle fluctuating kinetic energy were denoted in the text as follows:

$$I_{\mathrm{f}\to\mathrm{p},i} = n_{\mathrm{p}}\left\langle F_{\mathrm{f}\to\mathrm{p},i}\right\rangle \tag{2.49}$$

$$\Pi^{q_{\mathrm{p}}^2}_{\mathrm{f}\to\mathrm{p}} = n_{\mathrm{p}}\left\langle F_{\mathrm{f}\to\mathrm{p},i}u'_{\mathrm{p},i}\right\rangle \tag{2.50}$$

2.6.2 Particle to Fluid transfer

According to the section 2.3.2, the interfacial momentum transfer to the fluid phase, for our case, is given by the expression $I_{\mathrm{p}\to\mathrm{f},i} = -\langle\sigma_{ij}n_{\mathrm{p},j}\delta_{\mathrm{fp}}\rangle$. This average is directly related to the interfaces present in the fluid phase, and not necessarily to the whole surface of a given particle. This is depicted in Figure 2.3, which indicates in thicker lines the surfaces upon with the average in question is performed.

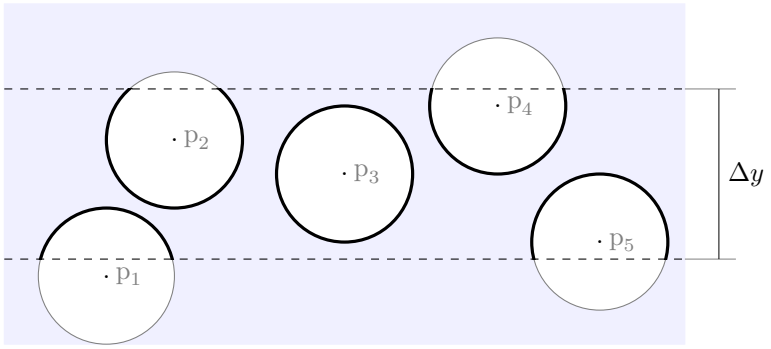

Figure 2.3: Particles inside control volume used for averaging. Thicker lines inside the control volume represent surfaces to be taken into account for the interfacial transfer terms related to the control volume delimited by Δy.

The averaged momentum interfacial term can be calculated as:

$$\langle \sigma_{ij} n_{\mathrm{p},j} \delta_{\mathrm{fp}} \rangle = \frac{1}{N_t} \sum_{r=1}^{N_t} \left[\sum_{n=1}^{N_\mathrm{p}} \int_{S_\mathrm{in}^{(n,r)}} \sigma_{\mathrm{f},ij} n_{\mathrm{p},j} dS \right] \tag{2.51}$$

Where N_t is the number of simulation time-steps used in the averaging and $S_\mathrm{in}^{(n,r)}$ is the surface inside the associated control volume of the n-th particle, for a given realization r, related to a simulation time-step. From Eq. (2.51), it can be seen that, in the limiting case where all the particles are always inside the averaging control volume, or in other words, the particle surfaces are never outside the control volume, corresponding to the case of homogeneous flow, then the equality rigorously holds true:

$$I_{\mathrm{p}\to\mathrm{f},i} = -I_{\mathrm{f}\to\mathrm{p},i} \tag{2.52}$$

In slightly inhomogeneous flow, where the interfaces are roughly evenly distributed inside the control volume, in average the equality given by Eq. (2.52) is approximately true, since the surface integration from one particle may be compensated by another particle in the control volume. For instance, in Figure 2.3, the integration of surface related to particle p_5 is approximately compensated by the surface of particle p_4. Over several realizations, the results approximately balances out.

On the most general case, the effect of partially included particles in the control volume must be taken into account by the a correction term, which is represented by the second term on the right-hand side of the equation below, more details on [130].

$$I_{\mathrm{p}\to\mathrm{f},i} = -I_{\mathrm{f}\to\mathrm{p},i} + \frac{\partial \theta_{\mathrm{pf},ij}}{\partial x_j} \tag{2.53}$$

With respect to the interfacial term associated with the fluid fluctuating kinetic energy $\Pi_{\mathrm{p}\to\mathrm{f}}^{k_\mathrm{f}} = -\left\langle \sigma_{ij} u'_{\mathrm{f},i} n_{\mathrm{p},j} \delta_{\mathrm{fp}} \right\rangle$, the fluid fluctuating velocity in the

surface of the particle intervenes in the average, which can be written as a function of the center of mass, translational velocity of the particle $\boldsymbol{u}_\mathrm{p}$, and its rotation vector $\boldsymbol{\omega}_\mathrm{p}$, reads:

$$\boldsymbol{u}'_\mathrm{f}(\boldsymbol{x}_\mathrm{fp}(t),t) = \underbrace{\boldsymbol{u}_\mathrm{p}(t) + \boldsymbol{\omega}_\mathrm{p}(t) \times (\boldsymbol{x}_\mathrm{fp}(t) - \boldsymbol{x}_\mathrm{p}(t))}_{\boldsymbol{u}_\mathrm{f}} - \boldsymbol{U}_\mathrm{f}(\boldsymbol{x}_\mathrm{fp}(t),t) \tag{2.54}$$

Where $(\boldsymbol{x}_\mathrm{fp} - \boldsymbol{x}_\mathrm{p})$ is the vector pointing from the origin of the particle center, $\boldsymbol{x}_\mathrm{p}$, to a given point, $\boldsymbol{x}_\mathrm{fp}$, in its surface. Using Eq. (2.54), the average $\left\langle \sigma_{\mathrm{f},ij} u'_{\mathrm{f},i} n_{\mathrm{p},j} \delta_\mathrm{fp} \right\rangle$ can then be written as:

$$\begin{aligned} \left\langle \sigma_{\mathrm{f},ij} u'_{\mathrm{f},i} n_{\mathrm{p},j} \delta_\mathrm{fp} \right\rangle &= \left\langle \sigma_{\mathrm{f},ij} u'_{\mathrm{p},i} n_{\mathrm{p},j} \delta_\mathrm{fp} \right\rangle + (U_{\mathrm{p},i} - U_{\mathrm{f},i}) \left\langle \sigma_{\mathrm{f},ij} n_{\mathrm{p},j} \delta_\mathrm{fp} \right\rangle \\ &\quad + \left\langle \sigma_{\mathrm{f},ij} \varepsilon_{ikl} \omega_{\mathrm{p},k} \left(x_{\mathrm{fp},l} - x_{\mathrm{p},l} \right) n_{\mathrm{p},j} \delta_\mathrm{fp} \right\rangle \end{aligned} \tag{2.55}$$

Where ε_{ikl} is the Levi-Civita tensor, used to the write the cross product within the frame of the Einstein index notation. With respect to the first term on the right-hand side, analogously to the term in Eq. (2.53), can be written as:

$$-\left\langle \sigma_{\mathrm{f},ij} u'_{\mathrm{p},i} n_{\mathrm{p},j} \delta_\mathrm{fp} \right\rangle = -\Pi^{q_\mathrm{p}^2}_{\mathrm{p}\to\mathrm{f}} + \frac{\partial \theta_{\mathrm{pf},i}}{\partial x_i} \tag{2.56}$$

The last term of Eq. (2.55) is related to the rate of energy transfer to the particle rotation due to the fluid interaction. To verify so, first consider the torque applied by the fluid on a given particle, with surface S_p:

$$T_{\mathrm{f}\to\mathrm{p},i} = \int_{S_\mathrm{p}} \varepsilon_{ijk} \left(x_{\mathrm{fp},j} - x_{\mathrm{p},j} \right) \sigma_{\mathrm{f},kl} n_{\mathrm{p},l} dS \tag{2.57}$$

And a source term, from the perspective of the particles, related to particle rotation is: $\Upsilon_{\mathrm{f}\to\mathrm{p}} = n_\mathrm{p} \left\langle T_{\mathrm{p}\to\mathrm{f},i} \omega_{\mathrm{p},i} \right\rangle$. Similarly to Eq. (2.53) & Eq. (2.56), it can be shown that:

$$-\left\langle \sigma_{\mathrm{f},ij} \varepsilon_{ikl} \omega_{\mathrm{p},k} \left(x_{\mathrm{fp},l} - x_{\mathrm{p},l} \right) n_{\mathrm{p},j} \delta_\mathrm{fp} \right\rangle = -\Upsilon_{\mathrm{f}\to\mathrm{p}} + \frac{\partial \Xi_{\mathrm{pf},i}}{\partial x_i} \tag{2.58}$$

Finally, combining the equation above, the expression for the source term, due to interfacial transfer, of the fluid fluctuating kinetic energy as follows:

$$\begin{aligned} \Pi^{k_\mathrm{f}}_{\mathrm{p}\to\mathrm{f}} &= -\Pi^{q_\mathrm{p}^2}_{\mathrm{p}\to\mathrm{f}} + \frac{\partial \theta_{\mathrm{pf},i}}{\partial x_j} + (U_{\mathrm{p},i} - U_{\mathrm{f},i}) \left(-I_{\mathrm{f}\to\mathrm{p},i} + \frac{\partial \theta_{\mathrm{pf},ij}}{\partial x_j} \right) \\ &\quad -\Upsilon_{\mathrm{f}\to\mathrm{p}} + \frac{\partial \Xi_{\mathrm{pf},i}}{\partial x_i} \end{aligned} \tag{2.59}$$

The first two terms on the right-hand side are related to the direct transfer of fluctuating motion from one phase to the other, the third is related to fluctuating motion produced by the mean relative motion between the phases and finally the last one is due to the rate of energy transfer involved in the rotation. This formula is an extension of the formula given by [106] to the case of finite-sized particles.

2.7 Decomposition of the collision term

In this section an original method for decomposing the particle-particle interaction terms into source and flux terms is presented. Also, again, contrarily to the kinetic theory of granular flow, we do not assume instantaneous collisions, in fact, the method allows for contacts of long duration. Besides, it is a general formulation that only assumes force interactions between the particles. This formulation however has a correspondence with the kinetic theory formulation of the collision term decomposition into a source and a collision flux term [26], which is theoretically based upon the limited development of the so-called collision integral in a Taylor series [18]. The modeling aspects of it are further explored in section 4.4.

Notably in this section, the mathematical formalism related to the decomposition of the particle-particle interaction term associated to the particle mean velocity equation and those related to second order physics, particle kinetic stress and particle fluctuating kinetic energy are presented. Furthermore, two different methods for computing the terms are discussed.

The first one is more intuitive because it clearly separates the contributions of source and flux terms respectively in relation to internal and external particle-particle forces, while the second one is more consistent with respect to the uniqueness of flux terms.

2.7.1 Internal and external force separation

Consider a given control volume V, associated to j-th slice in the form of Figure 2.2, centered in the y_j coordinate and with thickness Δy, where two different species of particles, p and q, interact with each other throughout collision forces, see Figure 2.4. We denote Ω_p and Ω_q respectively as the ensemble of p-particles and q-particles whose center or mass are inside V. In addition $\partial\Omega_\mathrm{p}$ and $\partial\Omega_\mathrm{q}$ are respectively defined as the ensemble of p-particles and q-particles such as that their center of mass are outside V and are interacting with some particle inside V. We denote also, $\partial\Omega_\mathrm{p}^+$ as the ensemble of $\partial\Omega_\mathrm{p}$ that are in the top of V, and $\partial\Omega_\mathrm{p}^-$ the ones from $\partial\Omega_\mathrm{p}$ that are below V. A similar definition can be made for the q-particles as well.

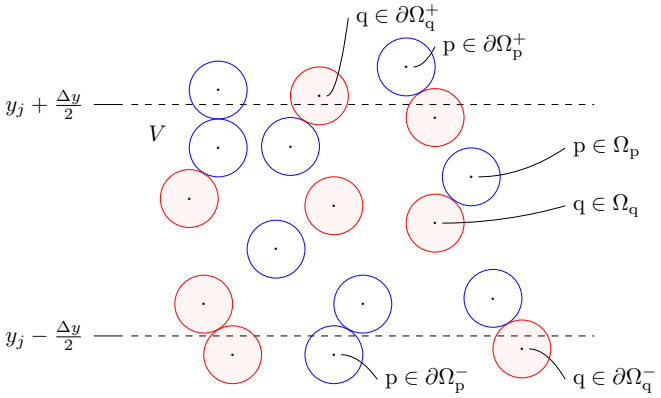

Figure 2.4: Particles interacting in a given slice domain V.

First order

The total force per unit volume, acting on the ensemble of p-particles inside V due to the q-particles, reads:

$$\mathbb{C}_{\mathrm{q}\to\mathrm{p}}\left(m_{\mathrm{p}}u_{\mathrm{p},i}\right) \;=\; n_{\mathrm{p}}\left\langle F_{\mathrm{q}\to\mathrm{p},i}\right\rangle \;=\; \frac{1}{V}\sum_{\substack{\mathrm{q}\in\Omega_{\mathrm{q}}\cup\partial\Omega_{\mathrm{q}}\\ \mathrm{p}\in\Omega_{\mathrm{p}}}} F_{\mathrm{q}\to\mathrm{p},i} \tag{2.60}$$

The sum presented on the right-hand side of Eq. (2.60), may be separated into two contributions, one due to the internal forces, and another one due to the external forces :

$$\frac{1}{V}\sum_{\substack{\mathrm{q}\in\Omega_{\mathrm{q}}\cup\partial\Omega_{\mathrm{q}}\\ \mathrm{p}\in\Omega_{\mathrm{p}}}} F_{\mathrm{q}\to\mathrm{p},i} \;=\; \underbrace{\frac{1}{V}\sum_{\substack{\mathrm{q}\in\Omega_{\mathrm{q}}\\ \mathrm{p}\in\Omega_{\mathrm{p}}}} F_{\mathrm{q}\to\mathrm{p},i}}_{\text{internal forces}} + \underbrace{\frac{1}{V}\sum_{\substack{\mathrm{q}\in\partial\Omega_{\mathrm{q}}\\ \mathrm{p}\in\Omega_{\mathrm{p}}}} F_{\mathrm{q}\to\mathrm{p},i}}_{\text{external forces}} \tag{2.61}$$

The first term on the right-hand side of Eq. (2.61), representing the internal interacting forces, is denoted as:

$$\chi_{\mathrm{qp},i} = \frac{1}{V}\sum_{\substack{\mathrm{q}\in\Omega_{\mathrm{q}}\\ \mathrm{p}\in\Omega_{\mathrm{p}}}} F_{\mathrm{q}\to\mathrm{p},i} \tag{2.62}$$

It directly follows from the definition above that $\chi_{\mathrm{qp},i}+\chi_{\mathrm{pq},i}=0$. Note that in the particular case of the transfer from the same particle species to itself, it gives $\chi_{\mathrm{pp},i}=0$ or $\chi_{\mathrm{qq},i}=0$, as expected.

We denote the total force per unit area, acting on interior particles from exterior particles, crossing the boundary in the upper part of the domain as $\theta^{+}_{\mathrm{qp},iy}$ and in the lower part of the domain as $\theta^{-}_{\mathrm{qp},iy}$. They can be respectively written by Eq. (2.63) & Eq. (2.64).

$$\theta^{+}_{\mathrm{qp},iy}\left(y_j+\frac{\Delta y}{2}\right) = \frac{1}{A}\sum_{\substack{\mathrm{q}\in\partial\Omega^{+}_{\mathrm{q}}\\ \mathrm{p}\in\Omega_{\mathrm{p}}}} F_{\mathrm{q}\to\mathrm{p},i} \tag{2.63}$$

$$\theta^{-}_{\mathrm{qp},iy}\left(y_j-\frac{\Delta y}{2}\right) = -\frac{1}{A}\sum_{\substack{\mathrm{q}\in\partial\Omega^{-}_{\mathrm{q}}\\ \mathrm{p}\in\Omega_{\mathrm{p}}}} F_{\mathrm{q}\to\mathrm{p},i} \tag{2.64}$$

It can be shown that contribution due to the exterior forces in Eq. (2.61), can be written as function of Eq. (2.63) & Eq. (2.64) as follows.

$$\frac{1}{V}\sum_{\substack{\mathrm{q}\in\partial\Omega_{\mathrm{q}}\\ \mathrm{p}\in\Omega_{\mathrm{p}}}} F_{\mathrm{q}\to\mathrm{p},i} = \frac{A}{V}\left[\theta^{+}_{\mathrm{qp},iy}\left(y_j+\frac{\Delta y}{2}\right)-\theta^{-}_{\mathrm{qp},iy}\left(y_j-\frac{\Delta y}{2}\right)\right] \tag{2.65}$$

Combining Eq. (2.60) & Eq. 2.61 & (2.62) & Eq. (2.65), and noting that $V = A\Delta y$, we obtain:

$$\mathbb{C}_{\mathrm{q}\to\mathrm{p}}\left(m_{\mathrm{p}}u_{\mathrm{p},i}\right) \;=\; n_{\mathrm{p}}\left\langle F_{\mathrm{q}\to\mathrm{p},i}\right\rangle \;=\; \chi_{\mathrm{qp},i} + \frac{\Delta\theta_{\mathrm{qp},iy}}{\Delta y} \tag{2.66}$$

In the equation above, it is assumed that the ratio of the upper minus the bottom fluxes to the domain thickness can be assigned to the gradient of a tensor $\theta_{\mathrm{qp},iy}$. A discussion about the uniqueness of such a tensor is given in the end of this section and in section 2.7.2 as well.

Second order

In order to make the decomposition of collision terms present in the transport equation of the particle kinetic stress, Eq. (2.40) and particle fluctuating kinetic energy, Eq. (2.41), into source and flux related terms. We first consider the identity below:

$$n_{\mathrm{p}}\left\langle F_{\mathrm{q}\to\mathrm{p},i}u'_{\mathrm{p},j}\right\rangle = n_{\mathrm{p}}\left\langle F_{\mathrm{q}\to\mathrm{p},i}u_{\mathrm{p},j}\right\rangle - n_{\mathrm{p}}\left\langle F_{\mathrm{q}\to\mathrm{p},i}\right\rangle\left\langle u_{\mathrm{p},j}\right\rangle \tag{2.67}$$

The second term on the right-hand side of the equation above, can be directly computed from Eq. (2.66). With respect to the first term on the right-hand side, with the purpose of getting source and flux related terms. We separate it into internal and external contributions as well:

$$\begin{aligned} n_{\mathrm{p}}\left\langle F_{\mathrm{q}\to\mathrm{p},i}u_{\mathrm{p},j}\right\rangle &= \frac{1}{V}\sum_{\substack{\mathrm{q}\in\Omega_{\mathrm{q}}\cup\partial\Omega_{\mathrm{q}}\\ \mathrm{p}\in\Omega_{\mathrm{p}}}} F_{\mathrm{q}\to\mathrm{p},i}u_{\mathrm{p},j} \\ &= \underbrace{\frac{1}{V}\sum_{\substack{\mathrm{q}\in\Omega_{\mathrm{q}}\\ \mathrm{p}\in\Omega_{\mathrm{p}}}} F_{\mathrm{q}\to\mathrm{p},i}u_{\mathrm{p},j}}_{\text{internal forces}} + \underbrace{\frac{1}{V}\sum_{\substack{\mathrm{q}\in\partial\Omega_{\mathrm{q}}\\ \mathrm{p}\in\Omega_{\mathrm{p}}}} F_{\mathrm{q}\to\mathrm{p},i}u_{\mathrm{p},j}}_{\text{external forces}} \end{aligned} \tag{2.68}$$

The first term of Eq. (2.68) is defined as the second order hat source term:

$$\hat{\chi}_{\mathrm{qp},ij} = \frac{1}{V}\sum_{\substack{\mathrm{q}\in\Omega_{\mathrm{q}}\\ \mathrm{p}\in\Omega_{\mathrm{p}}}} F_{\mathrm{q}\to\mathrm{p},i}u_{\mathrm{p},j} \tag{2.69}$$

A force applied to a given object multiplied to the velocity of such object can be linked to a power transfer. In the equation above the terms are associated to the rate of change of total particle energy due to internal particle interactions.

Moreover, similarly to the definitions of Eq. 2.63 and Eq. 2.64, we denote the terms $\hat{\theta}^{+}_{\mathrm{qp},ijy}$ and $\hat{\theta}^{-}_{\mathrm{qp},ijy}$, as the terms associated to the power transfer from exterior forces, respectively from the upper part and the lower part, that are applied to internal particles as:

$$\hat{\theta}^{+}_{\mathrm{qp},ijy}\left(y_j+\frac{\Delta y}{2}\right)=\frac{1}{A}\sum_{\substack{\mathrm{q}\in\partial\Omega^{+}_{\mathrm{q}}\\ \mathrm{p}\in\Omega_{\mathrm{p}}}}F_{\mathrm{q}\to\mathrm{p},i}u_{\mathrm{p},j} \tag{2.70}$$

$$\hat{\theta}^{-}_{\mathrm{qp},ijy}\left(y_j-\frac{\Delta y}{2}\right)=-\frac{1}{A}\sum_{\substack{\mathrm{q}\in\partial\Omega^{-}_{\mathrm{q}}\\ \mathrm{p}\in\Omega_{\mathrm{p}}}}F_{\mathrm{q}\to\mathrm{p},i}u_{\mathrm{p},j} \tag{2.71}$$

Similarly to Eq. 2.65, the last term of Eq. 2.68, associated to the external forces, can written as function of the two terms defined above as:

$$\frac{1}{V}\sum_{\substack{\mathrm{q}\in\partial\Omega_{\mathrm{q}}\\ \mathrm{p}\in\Omega_{\mathrm{p}}}}F_{\mathrm{q}\to\mathrm{p},i}u_{\mathrm{p},j}=\frac{\theta^{+}_{\mathrm{qp},ijy}\left(y_j+\frac{\Delta y}{2}\right)-\theta^{-}_{\mathrm{qp},ijy}\left(y_j-\frac{\Delta y}{2}\right)}{\Delta y} \tag{2.72}$$

Combining Eq. (2.72), (2.69) and (2.68), and assuming the expression above can be written as a gradient of a tensor, leads to:

$$n_{\mathrm{p}}\left\langle F_{\mathrm{q}\to\mathrm{p},i}u_{\mathrm{p},j}\right\rangle=\hat{\chi}_{\mathrm{qp},ij}+\frac{\Delta\hat{\theta}_{\mathrm{qp},ijy}}{\Delta y} \tag{2.73}$$

In order to derive the transport terms related to force velocity fluctuation correlations, we define the following variables based on hat variables:

$$\chi_{\mathrm{qp},ij}=\hat{\chi}_{\mathrm{qp},ij}+\hat{\chi}_{\mathrm{qp},ji}-U_{\mathrm{p},i}\chi_{\mathrm{qp},j}-U_{\mathrm{p},j}\chi_{\mathrm{qp},i} \tag{2.74}$$

$$\theta_{\mathrm{qp},ijy}=\hat{\theta}_{\mathrm{qp},ijy}+\hat{\theta}_{\mathrm{qp},jiy}-U_{\mathrm{p},i}\theta_{\mathrm{qp},jy}-U_{\mathrm{p},j}\theta_{\mathrm{qp},iy} \tag{2.75}$$

Note for instance that, in the particular case of the contracted term of the interaction of the p-species with itself, then $\chi_{\mathrm{pp},ii}=2\hat{\chi}_{\mathrm{pp},ii}$, or twice the internal rate of energy dissipation through inelastic collisions.

Substituting Eq. (2.74), (2.75), (2.73) and (2.66) into (2.67) we obtain:

$$\begin{aligned}\mathbb{C}_{\mathrm{q}\to\mathrm{p}}\left(m_{\mathrm{p}}u'_{\mathrm{p},i}u'_{\mathrm{p},j}\right) &= n_{\mathrm{p}}\left\langle F_{\mathrm{q}\to\mathrm{p},i}u'_{\mathrm{p},j}\right\rangle+n_{\mathrm{p}}\left\langle F_{\mathrm{q}\to\mathrm{p},j}u'_{\mathrm{p},i}\right\rangle \\ &= \underbrace{\chi_{\mathrm{qp},ij}}_{\text{source}}+\underbrace{\frac{\Delta\theta_{\mathrm{qp},ijy}}{\Delta y}}_{\text{transport}}+\underbrace{\theta_{\mathrm{qp},iy}\frac{\Delta U_{\mathrm{p},j}}{\Delta y}+\theta_{\mathrm{qp},jy}\frac{\Delta U_{\mathrm{p},i}}{\Delta y}}_{\text{production}}\end{aligned} \tag{2.76}$$

In this manner the particle-particle interaction term, present in the transport equation of the particle kinetic stress is decomposed in three main groups. Two related to collision fluxes and one source term. Generally, those fluxes related terms are more relevant when the particle flow is denser, which is the case of our moderately dense simulations.

The source term, is related to local dynamics, such as energy transfer from one direction to another through particle-interaction or, as already mentioned, to the energy dissipation due to inelastic collisions. The last identified group in Eq. (2.76), is the production of particle kinetic stress due to particle-particle interactions. Note that while the kinetic production is associated to the product of the particle kinetic stress and the mean particle velocity gradient, the production by collision is the product of the collision flux times the mean velocity gradient. According to the kinetic theory of granular flows, collisional flux becomes more important than kinetic stress for dense particle flows : the transport of momentum by particle interaction is dominant compared to that by fluctuating velocity. Consequently, collisional production also becomes more important than the one by kinetic stress for dense particle flows.

Discussion about the flux definition

Within the frame of continuous media assumption, such as continuous fluid mechanics or even solid mechanics, the definitions of source and flux terms, related to forces, are generally pretty straightforward. This is due to the fact that several variables can be assigned to a given point in space, such as stress tensor, velocity and etc. With that in mind, its trivial to, for instance, uniquely assign a force (stress-tensor) to a surface and multiply it by a velocity if needed.

In our case however, since the particle sizes are comparable to the characteristic size of the domain, as depicted by Figure 2.4, in order for particle-particle interaction force to cross a given surface, the particles should be at different sides of that given surface. In that manner, even though the force can be assigned to a given surface, the positions and velocities of those particles are most likely assigned to other instantaneous positions. And from that peculiarity stems some issues regarding the definitions of the fluxes just previously presented.

Concerning the flux of force per unit area given by Eq. 2.63 and Eq. 2.64, there are two outcomes. The first, when we look into the flux related to a given particle species with itself, such as p with itself, from the action-reaction principle it results that: $\theta^{+}_{\mathrm{pp},iy}\left(y_j + \frac{\Delta y}{2}\right) = -\theta^{-}_{\mathrm{pp},iy}\left(y_j + \frac{\Delta y}{2}\right)$ and from that equivalence a unique flux tensor can then be easily defined in a surface. The second outcome is related to the interaction of different particle species. In such case we have that $\theta^{+}_{\mathrm{qp},iy}\left(y_j + \frac{\Delta y}{2}\right) \neq -\theta^{-}_{\mathrm{qp},iy}\left(y_j + \frac{\Delta y}{2}\right)$. The unequal sign in this case is related to the fact that in the left-hand-side the expression accounts for q-particles applying force to p-particles "from above" whereas in the right-hand-side it is the opposite. A possible equality in this case is when the indexes are inverted $\theta^{+}_{\mathrm{qp},iy}\left(y_j + \frac{\Delta y}{2}\right) = -\theta^{-}_{\mathrm{pq},iy}\left(y_j + \frac{\Delta y}{2}\right)$.

Related to the power transfer term from exterior forces, no obvious relationships can be directly established between $\hat{\theta}^{+}_{\mathrm{qp},ijy}$ and $\hat{\theta}^{-}_{\mathrm{qp},ijy}$, which is ultimately linked to the fact that this term is mathematically constructed to be a force from a particle q, coming from one side times the velocity of particle p, on the other side, this specific constraint makes impractical to establish a precise relationship between the terms.

In order to solve the issues discusses in this section, we propose an alternative separation of the force terms which finally lead to a unique definition of the fluxes that solves the problems discussed so-far. The method is further detailed in the next section.

2.7.2 Alternative method for the separation

Having in mind the problems related to the definition of the flux terms exposed in the end of last section, here we propose an alternative method that solves the exposed problems by cleverly separating the force terms in a way that, despite the finite-size of the particles, results in well-defined and unique flux terms definitions.

Moreover, the form of the terms presented in this alternative approach, are equivalent to the form of the collision terms in the frame of the kinetic theory for a mixture of two species of particles, which was given by [26], and also found in [35].

First of all, the total force per unit volume acting on the ensemble of p-particles inside V due to q-particles, see Eq. 2.60, are instead separated as follows:

$$\begin{aligned}\frac{1}{V}\sum_{\substack{\mathrm{q}\in\Omega_\mathrm{q}\cup\partial\Omega_\mathrm{q}\\ \mathrm{p}\in\Omega_\mathrm{p}}} F_{\mathrm{q}\to\mathrm{p},i} \;=\; & \underbrace{\frac{1}{2}\left[\frac{1}{V}\sum_{\substack{\mathrm{q}\in\Omega_\mathrm{q}\cup\partial\Omega_\mathrm{q}\\ \mathrm{p}\in\Omega_\mathrm{p}}} F_{\mathrm{q}\to\mathrm{p},i} + \frac{1}{V}\sum_{\substack{\mathrm{q}\in\Omega_\mathrm{q}\\ \mathrm{p}\in\Omega_\mathrm{p}\cup\partial\Omega_\mathrm{p}}} F_{\mathrm{q}\to\mathrm{p},i}\right]}_{\text{source related}} \\ & + \underbrace{\frac{1}{2}\left[\frac{1}{V}\sum_{\substack{\mathrm{q}\in\Omega_\mathrm{q}\\ \mathrm{p}\in\Omega_\mathrm{p}}} F_{\mathrm{q}\to\mathrm{p},i} - \frac{1}{V}\sum_{\substack{\mathrm{q}\in\Omega_\mathrm{q}\\ \mathrm{p}\in\partial\Omega_\mathrm{p}}} F_{\mathrm{q}\to\mathrm{p},i}\right]}_{\text{flux related}}\end{aligned} \tag{2.77}$$

First order

The source term, related to the momentum equation is alternatively defined as the first term on the right-hand side of Eq. 2.77. This term represents the sum of the forces acting on all particles belonging to an interacting pair of which one or the other (or both) belong to the control volume.

$$\chi_{\mathrm{qp},i} \;=\; \frac{1}{2}\left[\frac{1}{V}\sum_{\substack{\mathrm{q}\in\Omega_\mathrm{q}\cup\partial\Omega_\mathrm{q}\\ \mathrm{p}\in\Omega_\mathrm{p}}} F_{\mathrm{q}\to\mathrm{p},i} + \frac{1}{V}\sum_{\substack{\mathrm{q}\in\Omega_\mathrm{q}\\ \mathrm{p}\in\Omega_\mathrm{p}\cup\partial\Omega_\mathrm{p}}} F_{\mathrm{q}\to\mathrm{p},i}\right] \tag{2.78}$$

Regarding the flux related to the momentum 'crossing' the surfaces in the upper and lower boundaries, are alternatively defined as:

$$\theta^{+}_{\mathrm{qp},iy}\left(y_j+\frac{\Delta y}{2}\right) = \frac{1}{2}\left[\frac{1}{A}\sum_{\substack{\mathrm{q}\in\partial\Omega^{+}_{\mathrm{q}}\\ \mathrm{p}\in\Omega_{\mathrm{p}}}} F_{\mathrm{q}\to\mathrm{p},i} - \frac{1}{A}\sum_{\substack{\mathrm{q}\in\Omega_{\mathrm{q}}\\ \mathrm{p}\in\partial\Omega^{+}_{\mathrm{p}}}} F_{\mathrm{q}\to\mathrm{p},i}\right] \tag{2.79}$$

$$\theta^{-}_{\mathrm{qp},iy}\left(y-\frac{\Delta y}{2}\right) = -\frac{1}{2}\left[\frac{1}{A}\sum_{\substack{\mathrm{q}\in\partial\Omega^{-}_{\mathrm{q}}\\ \mathrm{p}\in\Omega_{\mathrm{p}}}} F_{\mathrm{q}\to\mathrm{p},i} - \frac{1}{A}\sum_{\substack{\mathrm{q}\in\Omega_{\mathrm{q}}\\ \mathrm{p}\in\partial\Omega^{-}_{\mathrm{p}}}} F_{\mathrm{q}\to\mathrm{p},i}\right] \tag{2.80}$$

Note however in this case that since the fluxes are defined in a symmetrical way due to the sum of two terms in the right-hand-side, it can be easily shown that the following relationship holds true:

$$\theta_{\mathrm{qp},iy}\left(y+\frac{\Delta y}{2}\right) = \theta^{+}_{\mathrm{qp},iy}\left(y+\frac{\Delta y}{2}\right) = -\theta^{-}_{\mathrm{qp},iy}\left(y+\frac{\Delta y}{2}\right) \tag{2.81}$$

With those definitions, the following relationship can be rigorously written.

$$\frac{1}{2}\left[\frac{1}{V}\sum_{\substack{\mathrm{q}\in\partial\Omega_{\mathrm{q}}\\ \mathrm{p}\in\Omega_{\mathrm{p}}}} F_{\mathrm{q}\to\mathrm{p},i} - \frac{1}{V}\sum_{\substack{\mathrm{q}\in\Omega_{\mathrm{q}}\\ \mathrm{p}\in\partial\Omega_{\mathrm{p}}}} F_{\mathrm{q}\to\mathrm{p},i}\right] = \frac{\Delta\theta_{\mathrm{qp},iy}}{\Delta y} \tag{2.82}$$

Using the alternative definitions of $\chi_{\mathrm{qp},i}$ and $\theta_{\mathrm{qp},ij}$, given in this section, Eq. (2.66) holds true as well.

Second order

Similarly for second order relationships, the alternative definition for source hat term is:

$$\hat{\chi}_{\mathrm{qp},ij} = \frac{1}{2}\left[\frac{1}{V}\sum_{\substack{\mathrm{q}\in\Omega_{\mathrm{q}}\cup\partial\Omega_{\mathrm{q}}\\ \mathrm{p}\in\Omega_{\mathrm{p}}}} F_{\mathrm{q}\to\mathrm{p},i}u_{\mathrm{p},j} + \frac{1}{V}\sum_{\substack{\mathrm{q}\in\Omega_{\mathrm{q}}\\ \mathrm{p}\in\Omega_{\mathrm{p}}\cup\partial\Omega_{\mathrm{p}}}} F_{\mathrm{q}\to\mathrm{p},i}u_{\mathrm{p},j}\right] \tag{2.83}$$

And for the alternative collision flux definition is written as follows:

$$\hat{\theta}^{+}_{\mathrm{qp},ijy}\left(y+\frac{\Delta y}{2}\right) = \frac{1}{2}\left[\frac{1}{A}\sum_{\substack{\mathrm{q}\in\partial\Omega^{+}_{\mathrm{q}}\\ \mathrm{p}\in\Omega_{\mathrm{p}}}} F_{\mathrm{q}\to\mathrm{p},i}u_{\mathrm{p},j} - \frac{1}{A}\sum_{\substack{\mathrm{q}\in\Omega_{\mathrm{q}}\\ \mathrm{p}\in\partial\Omega^{+}_{\mathrm{p}}}} F_{\mathrm{q}\to\mathrm{p},i}u_{\mathrm{p},j}\right] \tag{2.84}$$

$$\hat{\theta}^{-}_{\mathrm{qp},ijy}\left(y-\frac{\Delta y}{2}\right) = -\frac{1}{2}\left[\frac{1}{A}\sum_{\substack{\mathrm{q}\in\partial\Omega^{-}_{\mathrm{q}}\\ \mathrm{p}\in\Omega_{\mathrm{p}}}} F_{\mathrm{q}\to\mathrm{p},i}u_{\mathrm{p},j} - \frac{1}{A}\sum_{\substack{\mathrm{q}\in\Omega_{\mathrm{q}}\\ \mathrm{p}\in\partial\Omega^{-}_{\mathrm{p}}}} F_{\mathrm{q}\to\mathrm{p},i}u_{\mathrm{p},j}\right] \tag{2.85}$$

Using such definition, the collision flux $\hat{\theta}_{\mathrm{qp},ijy}$ is also now uniquely defined in a given surface, reads:

$$\hat{\theta}^{+}_{\mathrm{qp},ijy}\left(y+\frac{\Delta y}{2}\right)=-\hat{\theta}^{-}_{\mathrm{qp},ijy}\left(y+\frac{\Delta y}{2}\right)=\hat{\theta}_{\mathrm{qp},ijy}\left(y+\frac{\Delta y}{2}\right) \tag{2.86}$$

Which permits to directly associate it with a function gradient, as follows:

$$\frac{\Delta\hat{\theta}_{\mathrm{qp},ijy}}{\Delta y}=\frac{1}{2}\left[\frac{1}{V}\sum_{\substack{\mathrm{q}\in\partial\Omega_{\mathrm{q}}\\ \mathrm{p}\in\Omega_{\mathrm{p}}}}F_{\mathrm{q}\to\mathrm{p},i}u_{\mathrm{p},j}-\frac{1}{V}\sum_{\substack{\mathrm{q}\in\Omega_{\mathrm{q}}\\ \mathrm{p}\in\partial\Omega_{\mathrm{p}}}}F_{\mathrm{q}\to\mathrm{p},i}u_{\mathrm{p},j}\right] \tag{2.87}$$

It can be shown that using the definitions presented so far, Eq. (2.73) is verified. And since it is the case, Eq. (2.74), (2.75) and (2.76) remain consistent as well.

Numerical comparison between the methods

Concerning the difference from both methods of decomposition. A posteriori results have shown that they lead to very close results, but are not identical, especially concerning the second-order collisional fluxes.

This is probably related to the fact that the complementary symmetrical results added in this alternative method are very close, in average, to the unilateral results from the "internal versus external" method.

Chapter 3

Mono-disperse Flow

Contents

3.1 Introduction

In this chapter, six cases of mono-disperse fluid-particle flows are deeply investigated. Material properties and numerical parameters of the simulations are given in the section 1.4.1.

First, we show the macroscopic behavior of the particles, and notably the transition observed related to the bulk Stokes number. We show important parameters of the particle laden flow such as the particle number density, mean velocities and fluctuating kinetic energies.

An investigation of the fluid phase and higher order moments such as the Reynolds stresses, and the viscous dissipation effects in the domain are analyzed. We study the scales of the pseudo turbulence in our cases, and its consequences on the macroscopic behavior of the fluid-particle flow. Additionally we show a budget of the fluid fluctuating kinetic energy, which depicts local phenomena related to the transport of that variable.

The separate terms of the transport equation governing the velocity correlations, given in section 2.4, such as mean particle velocity, fluctuating kinetic energy and kinetic stress tensor, are extracted from the simulations and presented as a budget of the corresponding equation.

Fluid force modeling both for a single and for an ensemble of particles is revisited. A correlation analysis is performed to inquiry into the mean transverse force in the particle flow. In addition, a Stochastic Langevin approach is used to model fluid force velocity fluctuation correlations. This formalism is tested against our data providing interesting modeling insights.

3.2 Macroscopic behavior

From Table 1.2, we note that the cases are divided into two classes of bulk Stokes number. Cases M1 to M3, have their bulk Stokes number equal to 15, and the cases M4 to M6, have their bulk Stokes number equal to 30. Since, the bulk Stokes number is a measure of the particle inertia, we may classify the first group as the one with the smallest inertia, and the other one with relatively higher inertia. It actually has a huge implication into the macroscopic behavior of the fluid-particle flow. This is seen by Figure 3.1 and 3.2, where instantaneous snapshots of the mono-disperse cases, at the converged steady-state, are shown.

Interestingly, cases with the smaller inertia show an accumulation of the particles near the centre of the domain. Whereas the group with higher inertia tend to accumulate more towards the wall. Thus exhibiting a transition depending on the bulk Stokes number. Therefore, we assume that there must be a range of bulk Stokes number where the transition must lie.

$$15 < \mathrm{St}_{b,\mathrm{transition}} < 30 \tag{3.1}$$

A similar transition is also observed for the bi-disperse simulations in chapter 4 where an appropriate definition of the Stokes number for bi-disperse cases yields transitional values contained in the same range as shown above.

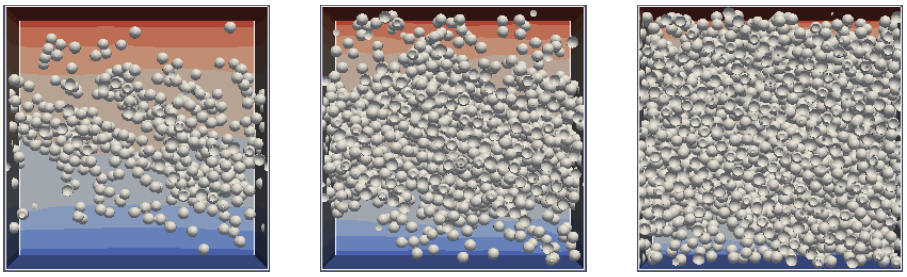

(a) M1 (b) M2 (c) M3

(d) M4 (e) M5 (f) M6

Figure 3.1: Front view of instantaneous snapshots of the particles. The contours represent the magnitude of the fluid velocity. Cases M1 to M3 correspond to $St_\mathrm{b} = 15$ and cases M4 to M6 to $St_\mathrm{b} = 30$.

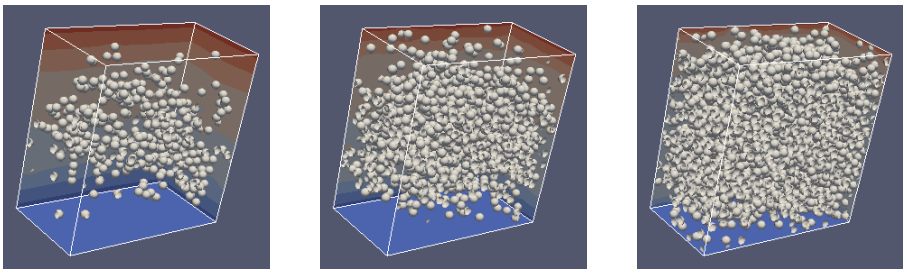

(a) M1 (b) M2 (c) M3

(d) M4 (e) M5 (f) M6

Figure 3.2: 3D view of instantaneous snapshots of the particles. The contours represent the magnitude of the fluid velocity. Cases M1 to M3 correspond to $St_\mathrm{b} = 15$ and cases M4 to M6 to $St_\mathrm{b} = 30$.

3.2.1 Particle number density

The particle number density, n_p, defined by Eq. (2.45) is a way of characterizing the accumulation of particles seen in the snapshots presented before. The values of n_p for all the mono-disperse cases are shown by Figure 3.3. The values are normalized by $n_{\mathrm{p},b}$, which is the ratio of the total number of particles in the domain to the total domain volume to the the total domain volume.

For the cases with lower inertia, M1 to M3, the particle number density profiles on Figure 3.3(a) shows that the maximum particle density number is located at the centre of the domain. Whereas the for the cases M4 to M6, a minimum is observed at the centre. Interestingly, all of the cases on Figure. 3.3(b) approximately follow the same curve.

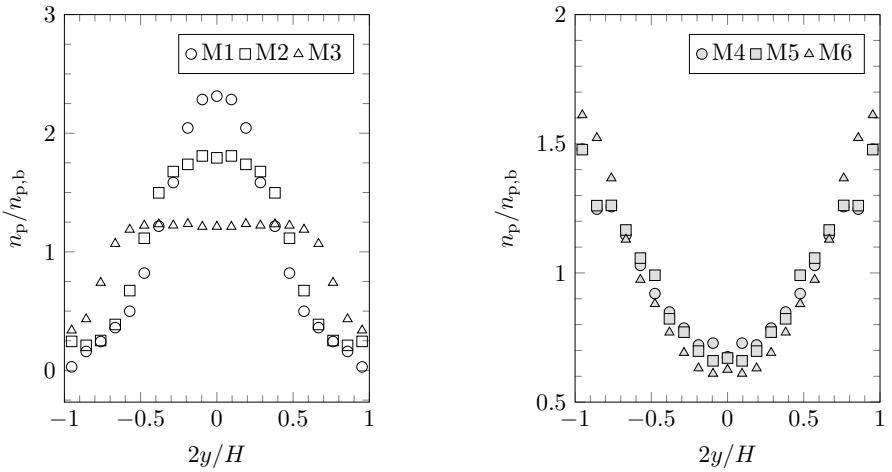

(a) (b)

Figure 3.3: Particle number density.

Another commonly used variable is the particle volume fraction. It can be calculated as follows:

$$\alpha_\mathrm{p} = n_\mathrm{p}\pi d_\mathrm{p}^3/6 \tag{3.2}$$

Figure 3.4 shows the values of α_p for all the cases. We see that the cases can reach dense particle packing, up to 37% for the case M3 on the Fig. 3.4(a). And up to 48%, at Figure 3.4(b), near the walls for the case M6.

The complete change in macroscopic behavior from the cases with $\mathrm{St}_b = 15$ to $\mathrm{St}_b = 30$ where the profiles of n_p, change from concave to convex, is investigated in the following sections. Specially in section 3.5 where terms of the transport equations, given at the section 2.4 are measured, giving insights in local physics.

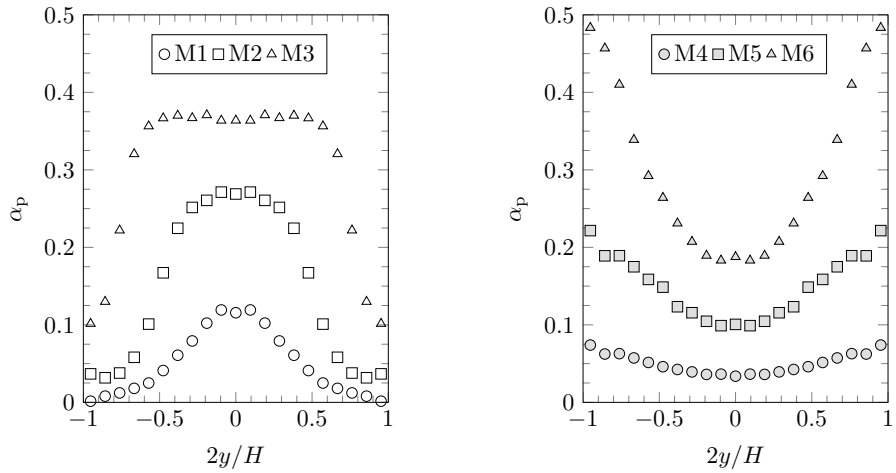

(a) (b)

Figure 3.4: Particle volume fraction.

3.2.2 Fluid and particle mean velocities

Instantaneous snapshots of the flow field are given by Figure 3.5. Similar to contour plots, ten discrete shades/colors are used for better visualization. We note that the flow is relatively more ordered for cases M1 to M3 compared to M4 to M6.

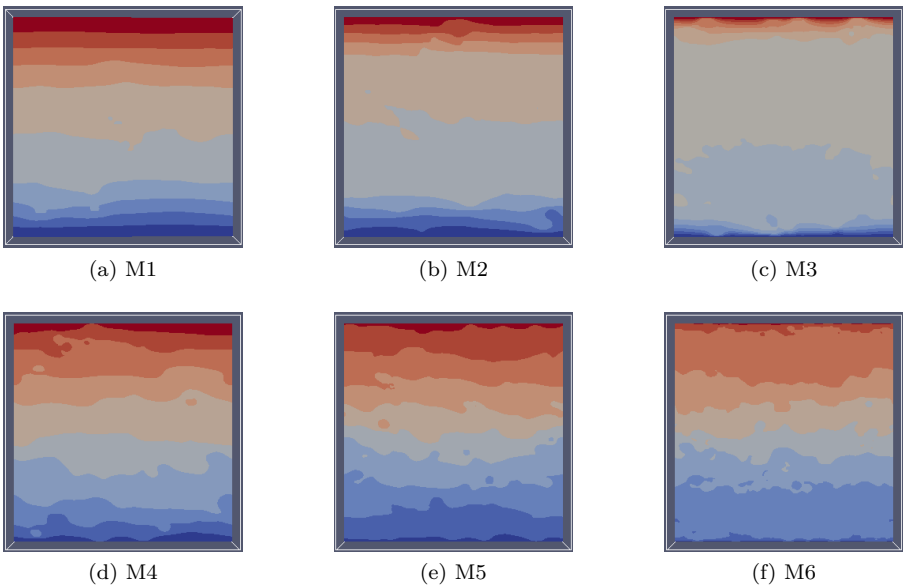

(a) M1 (b) M2 (c) M3

(d) M4 (e) M5 (f) M6

Figure 3.5: Instantaneous stream-wise fluid velocity.

Mean particle and fluid velocity in the stream-wise direction calculated according to the procedures described in the section 2.5 for the cases M1 to M3 are shown by Figure 3.6. We note that mean particle and fluid velocities are very close. It can be seen that the particle velocity does not attain, in average, more than sixty percent of the wall velocity. Also, we note that the stream-wise velocity is almost linear near the centre of the domain coinciding with the region of maximum particle volume fraction as depicted by Figure 3.4(a).

Regarding the cases M4 to M6, the values are given by Figure 3.7. All those three cases show an approximately linear mean velocity gradient across the whole domain. Fluid and particle mean velocities are very close as well. Also, all three cases seem to fall into the same normalized velocity profile. The only difference being the deviation near the wall for the case M6.

The other components of mean velocity in the wall-normal and span-wise directions, not shown, are null both for the fluid and the particles.

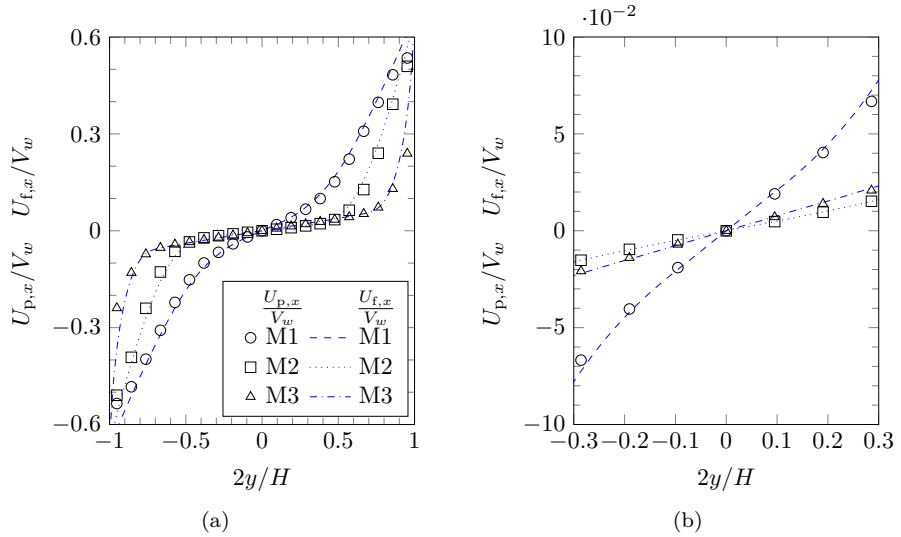

Figure 3.6: Fluid and particle stream-wise velocity for the cases M1, M2 and M3 for (a) all domain (b) zoom on the core of the flow.

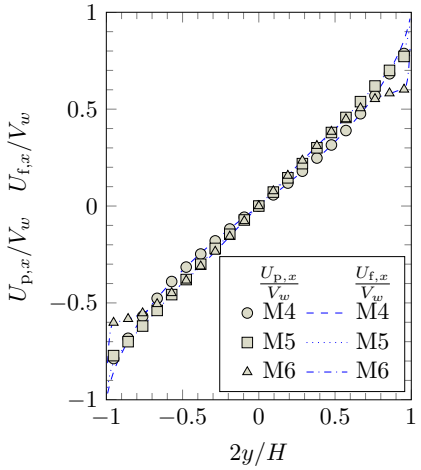

Figure 3.7: Fluid and particle stream-wise velocity for the cases M4, M5 and M6.

Based on the macroscopic relative velocity $\boldsymbol{V}_r = \boldsymbol{U}_\mathrm{p} - \boldsymbol{U}_\mathrm{f}$, the particle Reynolds number $Re_\mathrm{p} = |\boldsymbol{V}_r| d_\mathrm{p}/\nu_\mathrm{f}$ can be evaluated. The values for all the cases are given by Figure 3.8 where we can observe that the particle Reynolds number are relatively small for all the cases.

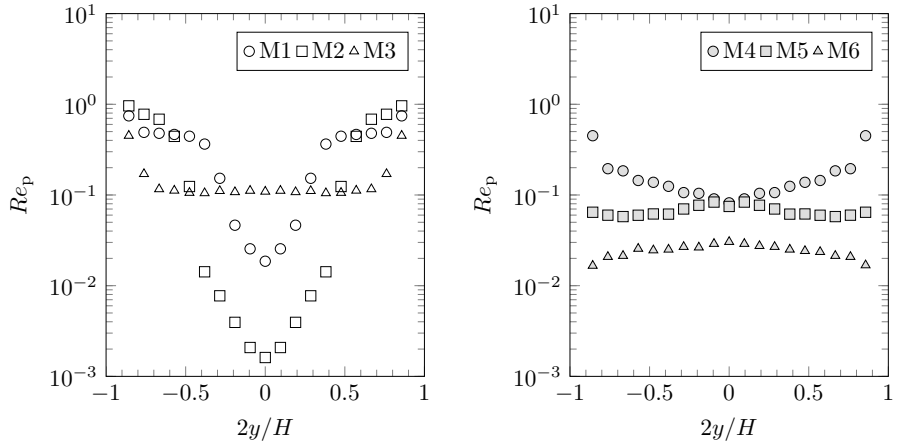

(a) (b)

Figure 3.8: Particle Reynolds number.

3.2.3 Fluid and particle fluctuating kinetic energies

Cases M1 to M6 were previously numerically simulated without particles, and yielded no fluid fluctuating motion. As pointed out by [64], the planar Couette flow is linearly stable for all the single phase Reynolds numbers [89]. In mono-disperse cases the main cause of the fluid fluctuating motion is the interaction with the particles. This is further detailed and explored in section 3.3 notably in the budget of the transport equation of the fluid fluctuating kinetic energy, where it will be shown that the dominant effect producing fluid fluctuating kinetic energy is the interaction with the particles. Moreover, the characteristic length and time-scales of such fluctuations are investigated as well.

As opposed to pure single phase turbulence, the fluctuating motion of the fluid in our case is called pseudo-turbulence [68], because it is due feed-back loop between both phases.

Figure 3.9 shows the magnitude of the particle fluctuating kinetic energy q_{p}^2 alongside to the fluid fluctuating kinetic energy k_{f}, in a logarithmic scale, for visualization sake. On the left hand side, from top to bottom, cases M1 to M3 are shown, and on the right hand side, also from top to bottom, cases M4 to M6. The cases with smaller inertia show a minimum on the centre of the domain, whereas the cases with higher inertia a maximum is found at the centre.

Interestingly, comparing Figures 3.9 and 3.3, it can be seen that the regions of maximum velocity variance locally coexists with the regions of minimum particle number density and vice-versa. This phenomenon is similar to what [4] have observed and it will be further detailed in section 3.5.

Regarding the regions near the walls for the cases with lower inertia M1 to M3 we note that augmenting the particle volume fraction tend to bring both values closer with the values closer in the limiting case of higher α_{p} at Figure 3.9(e). This is probably related to the fact that higher particle volume fraction tends to exert more influence on the fluid motion thus equalizing more its values. Near the centre, a non-trivial relationship is observed.

With respect to the cases with high inertia, a larger gap between particle and fluid velocity variance is observed specially near the centre of the domain.

The ratio of the fluctuating kinetic energies, q_{p}^2/k_f, for all the mono-disperse cases are given as a function of the particle volume fraction by Figure 3.10. The values are taken at the centre of the core flow. We note that the fluctuating kinetic energy of the particles are larger than that of the fluid for all the cases. That is different from the gravity driven flows in [23], [78] and [3], where the fluid fluctuations are larger than those of the particles.

This is due to the fact that the mechanisms of fluctuating motion creation are different in both cases. Generally, in gravity driven flows as the particles falls, a considerable amount of mean slip occurs between the phases, and substantially the difference in mean motion creates large scale fluctuations that retroactively entrain the particle agitation.

In our configuration, the fluid fluctuations are mainly created by the interaction with the fluctuating motion of the particles that are produced by the mean particle velocity shear, analysis of the transport equations both for the fluid and for the particles in the section 3.5. Besides, as will be explained in section 3.3.4, for our cases, the scales of the fluid fluctuation are much smaller than the particle diameter, hence not directly entraining the particle fluctuating motion due to the scale separation.

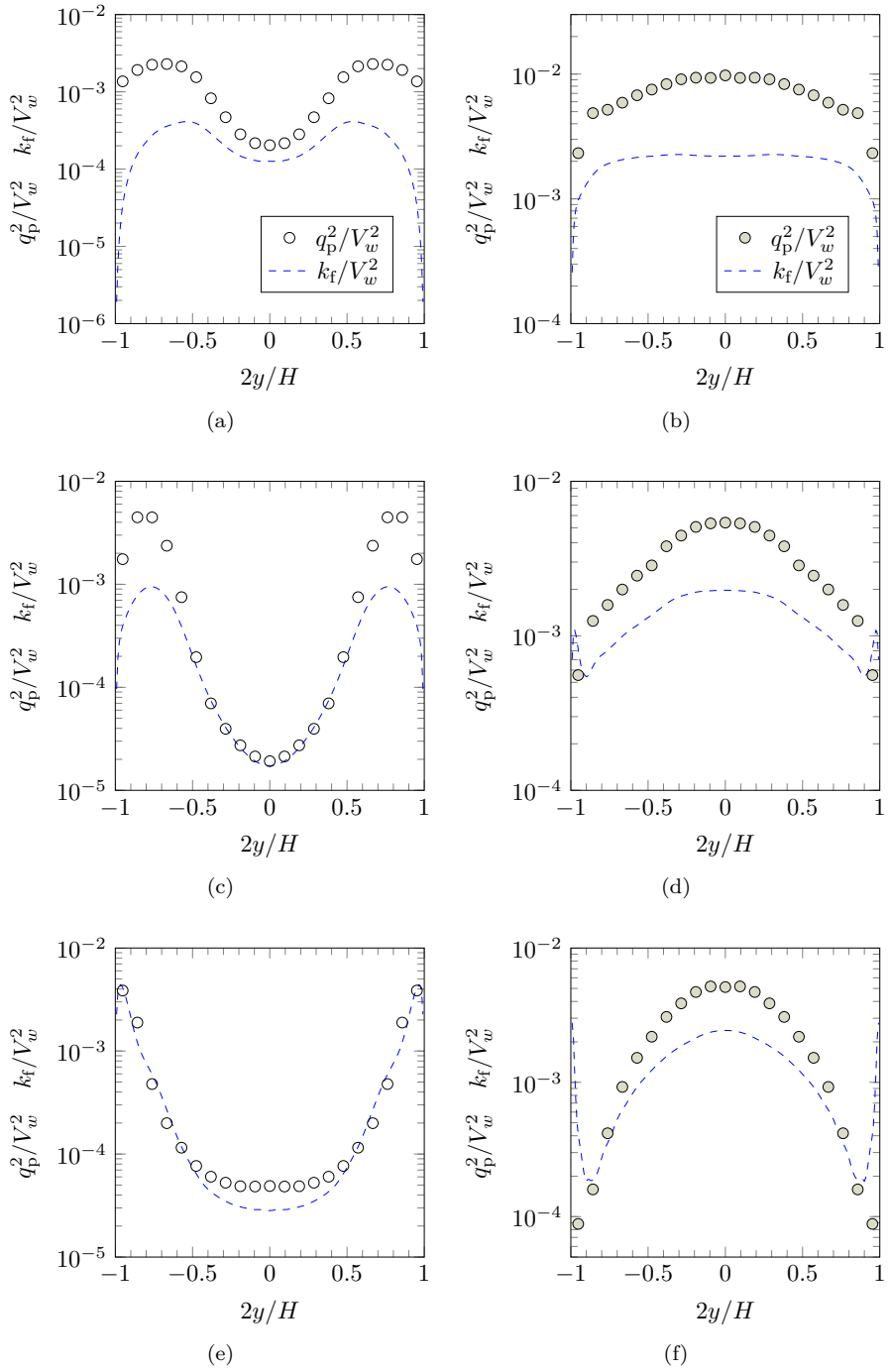

Figure 3.9: Comparison of the particle fluctuating kinetic energy and the fluid fluctuating kinetic energy, for the cases (a) M1, (b) M4, (c) M2, (d) M5, (e) M3 and (f) M6.

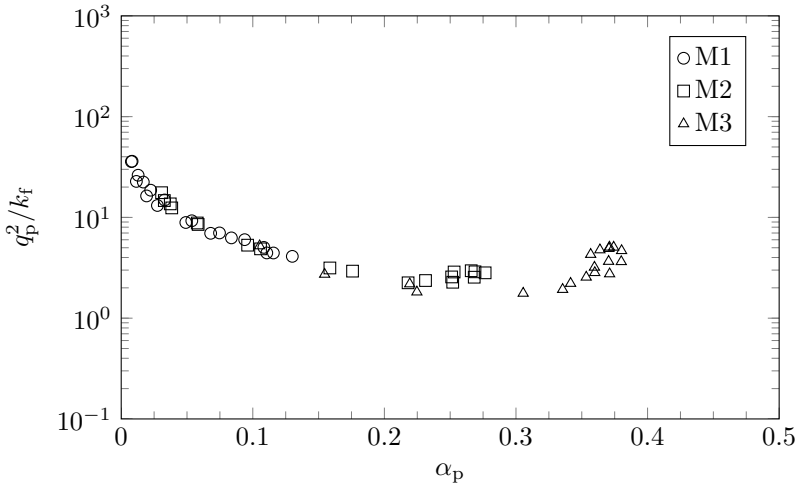

(a)

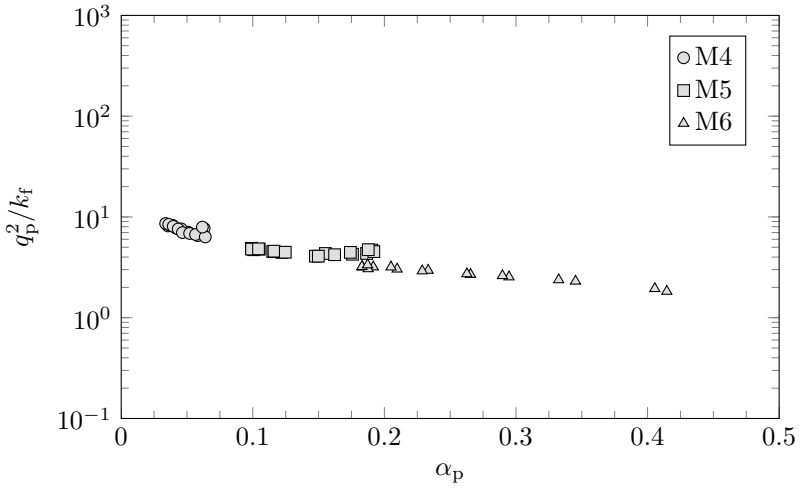

(b)

Figure 3.10: Particle and fluid fluctuating kinetic energy with respect to the particle volume fraction for the cases of low inertia (a) and high inertia (b).

3.3 Fluid statistics and higher order moments

In this section we analyze relevant fluid statistics. Details on the computation of the statistical variables are given in the section 2.5.2.

3.3.1 Pressure

Mean fluid pressure P_f for all the cases are shown by Figure 3.11. In the figure, the mean value is superposed with a fitting curve on the centre of the core flow. The pressure is fitted by a polynomial of second order. Similar curves are found for the other cases. The data shows that the fluid pressure is higher in the regions of larger particle volume fraction.

This procedure of interpolation is performed for all the cases, and the quadratic coefficient of the interpolation for all the cases are given in Table 3.1. As expected negative coefficients are found for the cases with low inertia and the opposite for the other cases. Indicating a negative slope of the pressure gradient for the cases M1 to M3 and a positive one for cases M4 to M6.

For the cases with small inertia, the gradients show an inverse relationship with the particle volume fraction meaning that higher volume fractions give smaller gradients. On another hand, the opposite is found for the cases with higher inertia where higher volume fractions actually have larger gradients.

Table 3.1: Quadratic fit coefficient: ax^2.

Case	M1	M2	M3	M4	M5	M6
a	-27.1	-15.1	-7.5	65.1	92.2	97.2

It will be shown in section 3.6 that the magnitude of the forces generated by those gradients in the particles are negligible when comparing other dominant forces in the particle-laden flow.

$$\left|\frac{1}{\rho_\mathrm{p}}\frac{\partial P_\mathrm{f}}{\partial y}\right| \ll \left|\left\langle \frac{F_{\mathrm{f}\to\mathrm{p},y}}{m_\mathrm{p}} \right\rangle\right| \tag{3.3}$$

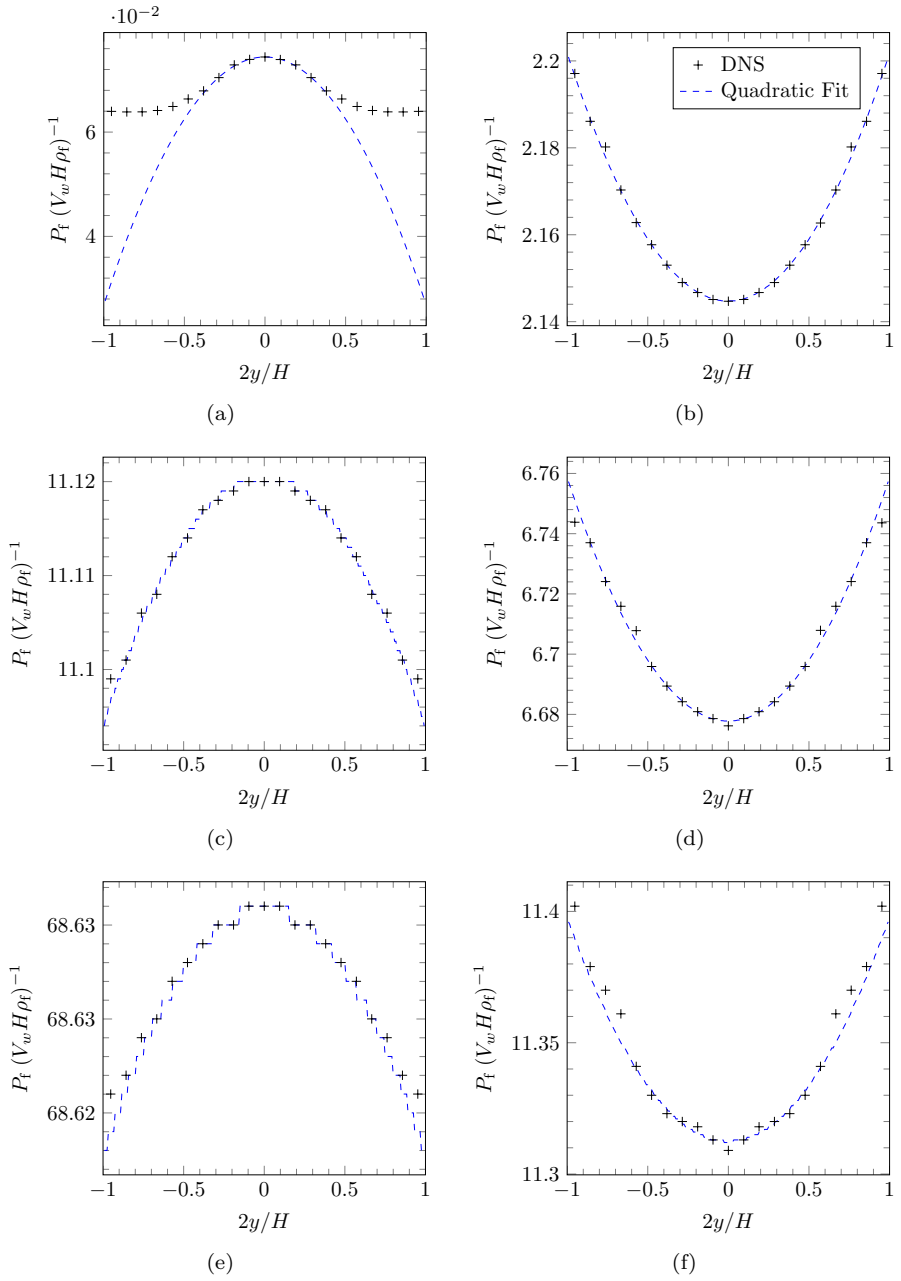

Figure 3.11: Fluid pressure with a quadratic fit for the cases (a) M1, (b) M4, (c) M2, (d) M5, (e) M3 and (e) M6.

3.3.2 Reynolds stresses

The Reynolds stress defined as the tensor $R_{\mathrm{f},ij} = \left\langle u'_{\mathrm{f},i} u'_{\mathrm{f},j} \right\rangle$ is a pertinent statistical variable related to fluid fluctuating motion. In fact, diagonal components are related to the variance or fluctuating motion in the principal direction while off-diagonal components are related to the shear. According to [84], those stresses play a crucial role in the equations for the mean fluid velocity field. In fact, those terms appear as apparent stresses in the momentum balance of the mean fluid velocity. Pope, also states that while viscous stresses ultimately come from momentum transfer at the molecular level, the Reynolds stresses stems from the momentum transfer by the fluctuating velocity field. The Reynolds stresses also appear in the transport equation of the fluid fluctuant kinetic energy, see section 2.3.

Diagonal components of the Reynolds stress tensor are given by Figure 3.12. For sake of comparison and visualization, the figures are given in a semi-log scale with the same limits. For all the cases, we note that $R_{\mathrm{f},xx}$ is the larger one among the diagonal components while the the other directions are closer together and smaller. Analogously to the results by Figure 3.9, a convex shape is found for the cases with smaller inertia and a concave shape for the cases with higher inertia.

A way of measuring the difference between the diagonal components is the Reynolds stress anisotropy tensor given by Eq. (3.4). The closer this components are to zero, the closer the system is to an isotropic state.

$$a_{\mathrm{f},ij} = \frac{R_{\mathrm{f},ij}}{\frac{2}{3}k_{\mathrm{f}}} - \delta_{ij} \tag{3.4}$$

Values of the anisotropy tensor $a_{\mathrm{f},xx}$, are given in Table 3.2. Values are given on the centre of the core flow. We note that the values of the cases with small inertia augment little with the particle volume fraction, and are close to one, meaning that the diagonal Reynolds stress related to the stream-wise direction is approximately one hundred percent larger than the average diagonal components, thus meaning a huge anisotropy for those cases.

Concerning the cases with high inertia the anisotropy coefficient shown in Table 3.2. We observe that the values are smaller in comparison and diminish with the augmentation of the particle volume fraction.

Table 3.2: Anisotropy of the Reynolds Stress at the centre of the domain.

Case	M1	M2	M3	M4	M5	M6
$a_{\mathrm{f},xx}$	1.04	1.06	1.10	0.77	0.54	0.33

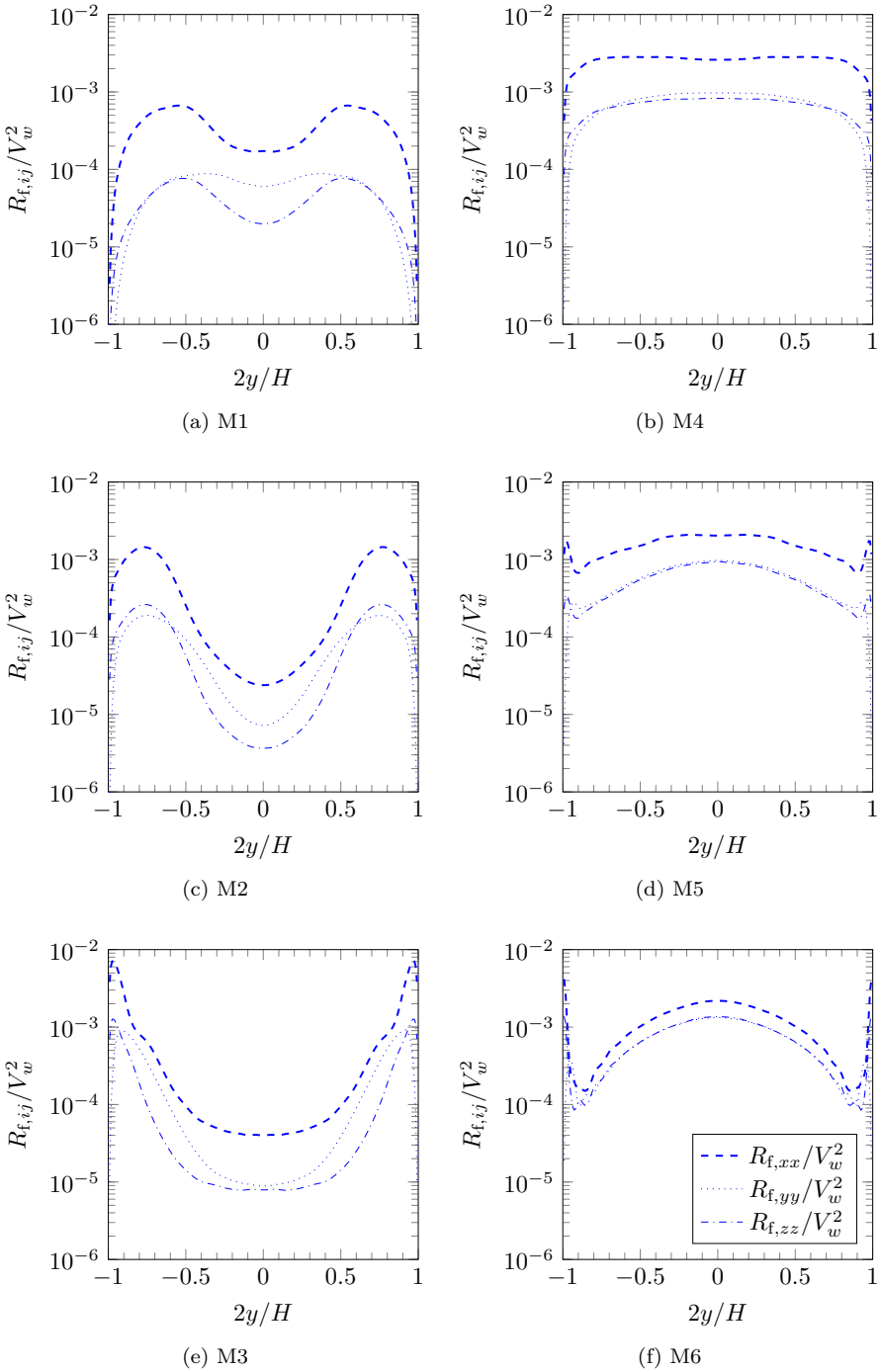

(a) M1 (b) M4

(c) M2 (d) M5

(e) M3 (f) M6

Figure 3.12: Fluid Reynolds stresses $R_{\mathrm{f},ij}$.

Regarding the shear kinetic stresses, the only non-null, non diagonal term, is the component $R_{\mathrm{f},xy}$. In fact, this is related to the fact that the only relevant mean shear is the one in the stream-wise direction across the wall normal direction $\partial U_{\mathrm{f},x}/\partial y$. From Figure 3.13, we note that the shear kinetic stresses in the centre of the core flow increases with the particle volume fraction for a given bulk Stokes number.

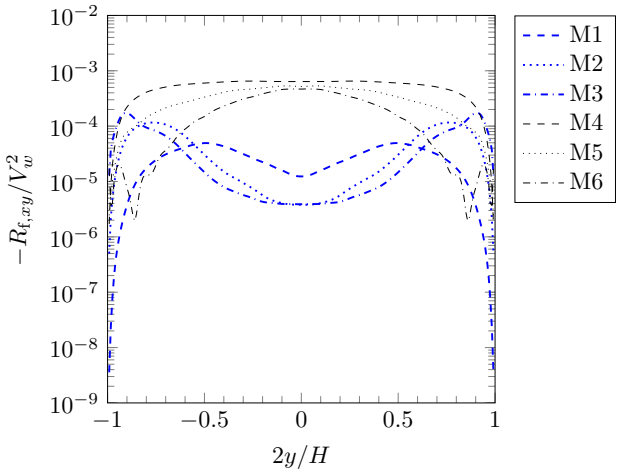

Figure 3.13: Shear kinetic stress $R_{\mathrm{f},xy}$ for the cases.

3.3.3 Viscous dissipation

In the transport equation of the average fluid kinetic energy and fluid fluctuating kinetic energy, the dissipation terms are important terms to characterize the dissipation rate of fluid energy due to internal fluid friction. For a Newtonian fluid, the dissipation of the average fluid kinetic energy ϵ_{M} and the fluctuating kinetic energy ϵ are given by:

$$\epsilon_{\mathrm{M}} = \left\langle \nu_{\mathrm{f}} \left(\frac{\partial u_{\mathrm{f},i}}{\partial x_j} + \frac{\partial u_{\mathrm{f},j}}{\partial x_i} \right) \frac{\partial u_{\mathrm{f},i}}{\partial x_j} \right\rangle_{\mathrm{f}} \tag{3.5}$$

$$\epsilon = \left\langle \nu_{\mathrm{f}} \left(\frac{\partial u'_{\mathrm{f},i}}{\partial x_j} + \frac{\partial u'_{\mathrm{f},j}}{\partial x_i} \right) \frac{\partial u'_{\mathrm{f},i}}{\partial x_j} \right\rangle_{\mathrm{f}} \tag{3.6}$$

The values for both the dissipation of the mean fluid kinetic energy and the fluid fluctuating kinetic energy are given by Figure 3.14. The values are multiplied by $H^2/(V_w^2\nu_\mathrm{f})$ for normalization sake.

With respect to both ϵ_M and ϵ, for the cases with high inertia, we observe a direct relationship of the particle volume fraction and the dissipation at the centre on the core flow that is the higher the particle concentration the larger is the viscous dissipation in that zone. For the cases with low inertia a non linear relationship is observed with the particle volume fraction, with a minimum of dissipation for M2 in the centre.

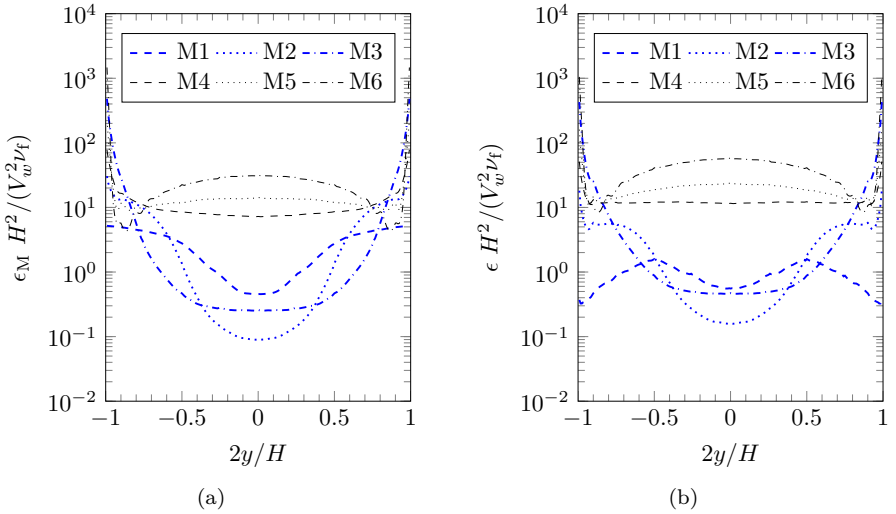

Figure 3.14: Viscous dissipation of the (a) average fluid kinetic energy and (b) fluctuating kinetic energy.

Instantaneous snapshots of the viscous dissipation of the fluid kinetic energy, with a logarithmic scaling are given by Figure 3.15. For values refer to the graphs on Figure 3.14(a). Figures on the top are related to the cases accumulating near the centre, and on the bottom related to particles more near the walls (see Figure 3.1). It can be seen that the accumulation of particles near the centre for cases M1 to M3 creates a zone of small viscous dissipation inside the particle "cocoon". For the cases M4 to M6, we note a more even distribution of the viscous dissipation across the plane.

For those cases with higher inertia particles are able to give enough energy in a given rate to the fluid to sustain fluid dissipation and agitation of both phases, thus having a more active behavior, creating an ignited state, whereas for the cases with lower inertia, particles do not attain the required energy state levels, and are more likely to be shut down by the fluid. In fact, by being quenched by the fluid they do have enough collisions and consequently do not create enough particle pressure to repel each other, causing them to collapse near the centre, this is further explored in section 3.5.

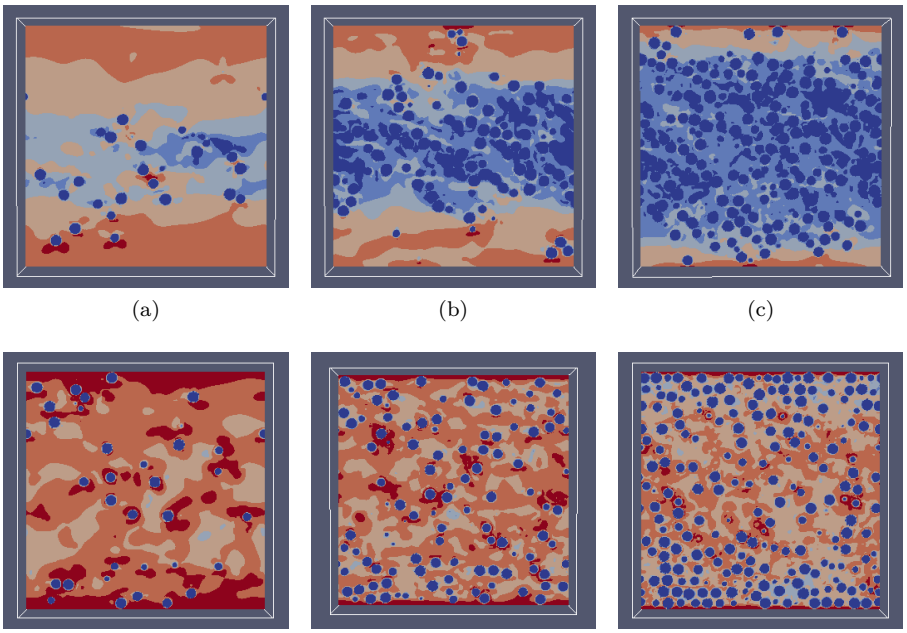

Figure 3.15: Snapshot of the instantaneous viscous dissipation in logarithm scale. Red color represents maximum dissipation and blue color minimum dissipation. (a) M1, (b) M2, (c) M3, (d) M4, (e) M5 and (f) M6.

3.3.4 Scales of the pseudo-turbulence

From the viscous dissipation of the fluctuant kinetic energy ϵ and fluid fluctuant kinetic energy k_f it is possible to establish a characteristic length: l_{k_f} and time scale: τ_{k_f}, of the pseudo-turbulence, as follows:

$$l_{k_\mathrm{f}} = \frac{k_\mathrm{f}^{3/2}}{\epsilon} \tag{3.7}$$

$$\tau_{k_\mathrm{f}} = \frac{k_\mathrm{f}}{\epsilon} \tag{3.8}$$

First of all, Figure 3.16(a) compares the characteristic length scale of the pseudo-turbulence to the diameter of the particles. We note that for all the cases the particle diameter is much larger than the characteristic length scale of the fluid fluctuations and this is more pronounced for the cases with higher inertia.

Another parameter of interest is to quantify the relationship of the characteristic length scale of the fluctuations to the length scale of the interstices between the particles. Eq. (3.9) gives an estimation for the interstice length scale, reads:

$$l_\mathrm{inter} = d_\mathrm{p} \left(\frac{\pi}{6} \frac{1-\alpha_\mathrm{p}}{\alpha_\mathrm{p}} \right)^{1/3} \tag{3.9}$$

Figure 3.16(b) shows that the value of the ratio $l_{\text{inter}}/l_{k_\text{f}}$ is relatively large for all the cases indicating that the pseudo-turbulent length scales are confined between the particles.

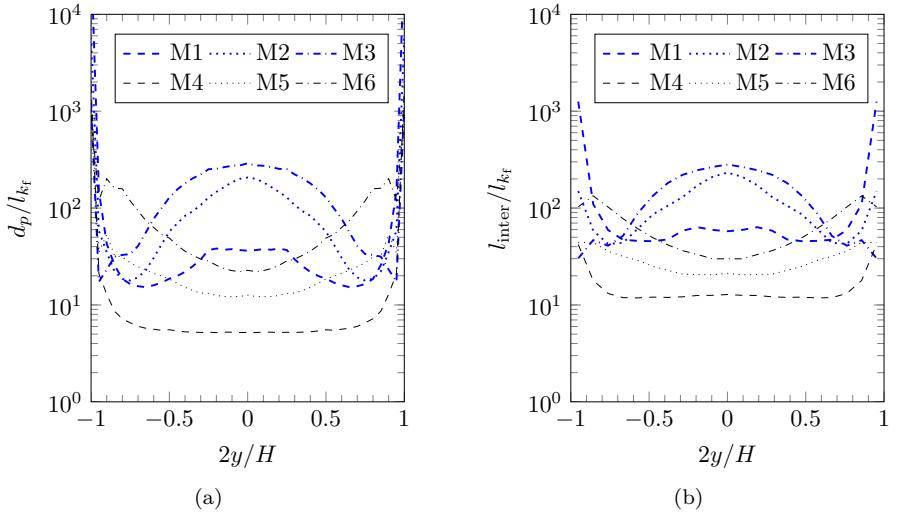

Figure 3.16: Comparison of the characteristic length scales of the pseudo-turbulence to the (a) particle diameter and (b) characteristic interstice length scale between the particles.

With respect to the characteristic time-scale given by Eq. (3.8) it can be compared to the particle response time, τ_p. In this thesis, we characterize the Stokes number as the particle response time with respect to the shear response time. However it is also possible to characterize the particle response time to the characteristic time-scale of the fluid fluctuations by the ratio $\tau_\text{p}/\tau_{k_\text{f}}$. The values for the cases are depicted by Figure 3.17. We note that the particle response time is indeed much larger than the time-scales of the pseudo-turbulence.

The data clearly indicates that the length scales of the pseudo-turbulence are very small and are confined between the particles in their interstices, with a time-scale much smaller than the particle response time. Indicating that there is probably not an strong inverse coupling from the fluid to the particles with respect to the fluctuating motion. In essence, as the fluid passes through the particles a fast and small wake is created in the interstices. Since both the time and length scales are not comparable to that of the particles, fluid fluctuation cannot directly affect the fluctuating motion of the particles. In fact, given the scales of the pseudo-turbulence it is possible that those fluctuations may only affect the particles through the modification of the boundary layer close to the particles.

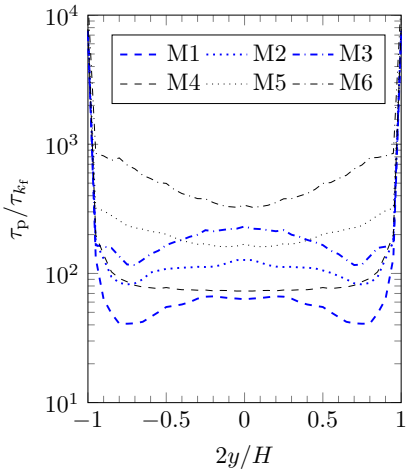

Figure 3.17: Comparison of the characteristic time-scale of the pseudo-turbulence to the particle response time.

3.4 Particle statistics and higher order moments

In this section, steady-state statistics from the mono-disperse case are analyzed. The procedure for calculating those statistics are detailed in the section 2.5. Results are normalized using constant values related to the Couette configuration, such as the wall-velocity V_w, the bulk particle number density $n_{\mathrm{p,b}}$, and the bulk Stokes number $\mathrm{St}_{\mathrm{p,b}}$. Those values are given in Table 1.2.

3.4.1 Local Stokes

The bulk Stokes number, St_b, previously defined by Eq. (1.20) is based on constant parameters defined before the numerical simulation, and as such do not actually depend on simulation results. However, this non-dimensional number, has proven to be a relevant characteristic number to predict the threshold of the macroscopic transition observed for the mono-disperse cases, and also for the bi-disperse cases in the Chapter 4.

In our simulations, we observe gradients of several variables across the domain. Considering that it is also interesting to investigate the actual local Stokes number. Comparing the particle response time to the local characteristic timescale of the shear. To do so, we estimate its value by means of the following formula:

$$\mathrm{St}_{\mathrm{p}} = \frac{\rho_{\mathrm{p}} d_{\mathrm{p}}^2}{18\mu_{\mathrm{f}}} \frac{\partial U_{\mathrm{p},x}}{\partial y} \tag{3.10}$$

Figure 3.18 shows the local Stokes normalized by the bulk Stokes number. Thus giving an idea of the deviation of the local Stokes number from the bulk one. Inspecting the cases M1 to M3, see Figure 3.18(a), we verify that their local Stokes number in the central region of the domain are much smaller than their bulk Stokes number. The case M2 for example exhibits a central local value of about $St_{\mathrm{p}} \approx 0.8$. For the cases M4 to M6, see Figure 3.18(b), it shows a local Stokes number value relatively closer to the bulk one. The case M4 for instance shows a value of $St_{\mathrm{p}} \approx 24$ in the central region. Under those circumstances, it can be seen that the difference in particle inertia is actually much greater than the simple difference from bulk Stokes numbers. Regarding the cases M2 and M4, that are equally charged in particles, $\alpha_{\mathrm{p},b} = 15\%$, local Stokes number is about thirty times bigger at the centre for the case M4.

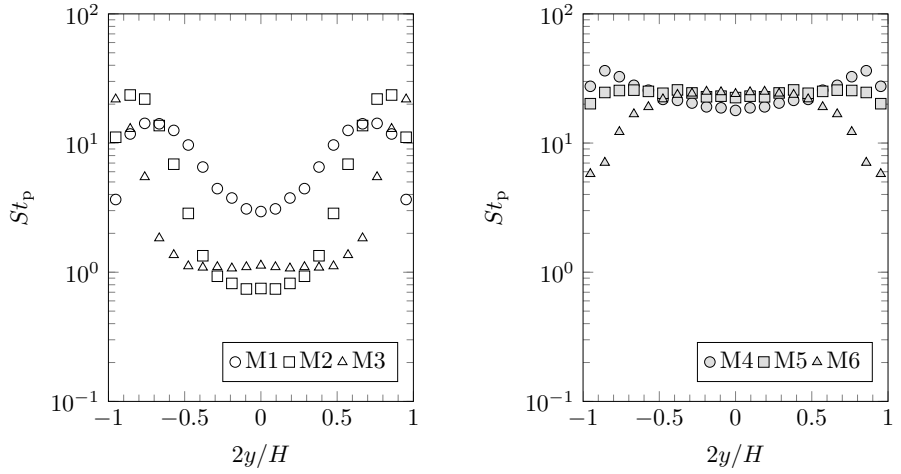

Figure 3.18: Local Stokes normalized by the bulk Stokes number. (a) Smaller inertia, cases M1 to M3. (b) Higher inertia, cases M4 to M6.

3.4.2 Quenched and Ignited states

The transition between the quenched and ignited state in a simple-shear fluid-particle flow have been originally investigated by [115] and later by [79, 93]. According to Tsao and Koch, two qualitatively different steady states are possible: an ignited state, where the variance of the particle velocity is very large, and a quenched state, where most of the particles follows the local mean fluid velocity.

Further, it is stated that most of the collisions in the quenched state are shear induced, meaning that particles are mostly dragged by the mean fluid flow and the particle velocity difference due to the shear may cause them to collide whereas for the ignited state, particles typically fly from one collision to another with little perturbation by the fluid.

In the study of Tsao and Koch a linear gradient of fluid velocity is set in a viscous fluid, and the presence of particles do not affect the fluid flow. Only particles are affected by the pre-established simple shear which is not the case in our resolved simulations where particles affect the fluid, and vice-versa in a very complex manner.

Even though the conditions are not exactly the same, both the study of Tsao and Koch and our simulations are in accordance with the fact that the Stokes number is the dominant factor controlling the transition, with cases M1 to M3 classified as quenched and M4 to M6 as ignited.

Regarding the transition, Tsao and Koch argue that increasing the Stokes number or the particle volume fraction. The particle agitation in the quenched state would grow toward a point where it might transition to the ignited state. With that in mind, if the shear induced variance is greater than an unstable value of particle agitation, than the imposed shear would cause enough fluctuations to take the system towards the ignited state. Related to that, and after some

analysis, the authors put forward the fact that the transition may be estimated with: $St^3\alpha_\mathrm{p} \sim O(1)$. This latter estimation indicates that the Stokes number influence grows quicker than the particle volume fraction. That is indeed what our data suggest, that is, in our parameter range, the particle volume fraction do not seem to have an impact on the transition possibly because the Stokes number effect is much more dominant.

With a collision oriented point of view, continuing the work of Tsao and Koch, [79] established a non dimensional number T^*_p, characterizing the importance of shear induced and variance induced collisions, see Eq.(3.11). With the quenched state located in the limit where $T^*_\mathrm{p} \ll 1$, that is, when the collisions by the mean shear effect are dominant. The ignited state represented by $T^*_\mathrm{p} \gg 1$, which is when the agitation is the main mechanism causing collisions.

$$T^*_\mathrm{p} = \frac{2}{3} q^2_\mathrm{p} / \left(\frac{d_\mathrm{p}}{2} \frac{\partial U_{\mathrm{p},x}}{\partial y} \right)^2 \tag{3.11}$$

Figure 3.19 shows local values of the non-dimensional number T^*_p for the mono-disperse cases. We note that none of our cases lies into the definitions given above, that is, neither of them can be classified in a category where clearly T^*_p is very small or much greater than one. One reason for that is that possibly the cases are too close to the transition.

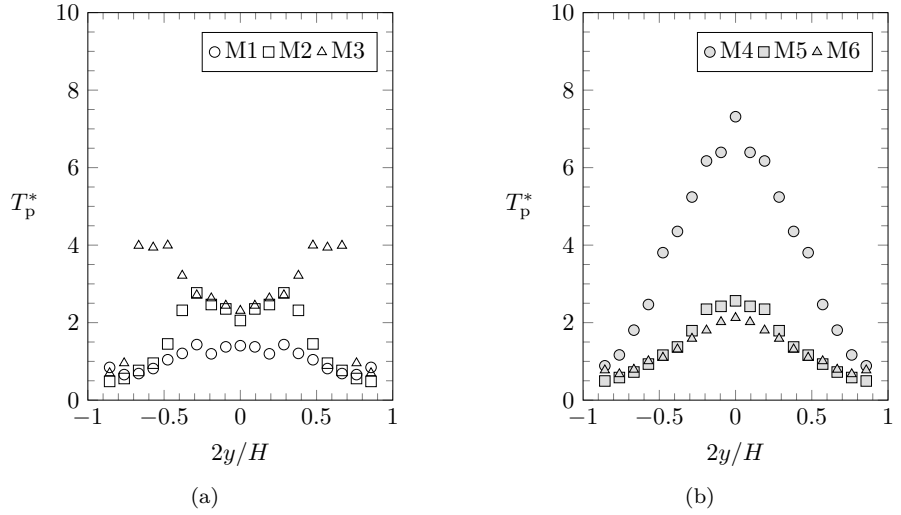

Figure 3.19: Dimensionless number T^*_p comparing agitation and the mean shear for: (a) cases M1 to M3. (b) cases M4 to M6.

3.4.3 Particle kinetic stress tensor

The particle kinetic stress or velocity correlation tensor $R_{\mathrm{p},ij} = \left\langle u'_{\mathrm{p},i} u'_{\mathrm{p},j} \right\rangle$ introduced at the section 2.4 is a symmetric second order tensor with the particle velocity fluctuation correlations in its components.

In our configuration, it is expected to have particle velocity variance in all of the three principal directions, thus implying in non-zero diagonal terms. Moreover, since the configuration has periodic boundaries in the stream-wise (x)-direction and span-wise (z)- direction, we also expect the only non-zero shear component to be in the xy plane. Indeed this is what we observe for all the cases.

With respect to the cases M4 to M6, Figure 3.20 shows the values of all six components of the particle kinetic stress tensor. For all the cases, $R_{\mathrm{p},xx}$ is larger than $R_{\mathrm{p},yy}$ and $R_{\mathrm{p},zz}$. These two components are found nearly equal in all investigated cases. As explained in details in section 3.5, the particle velocity fluctuation is produced in the stream-wise direction, and then part of that fluctuating energy is redistributed through the same physical mechanism to the wall normal and span-wise directions, thus explaining higher values of $R_{\mathrm{p},xx}$.

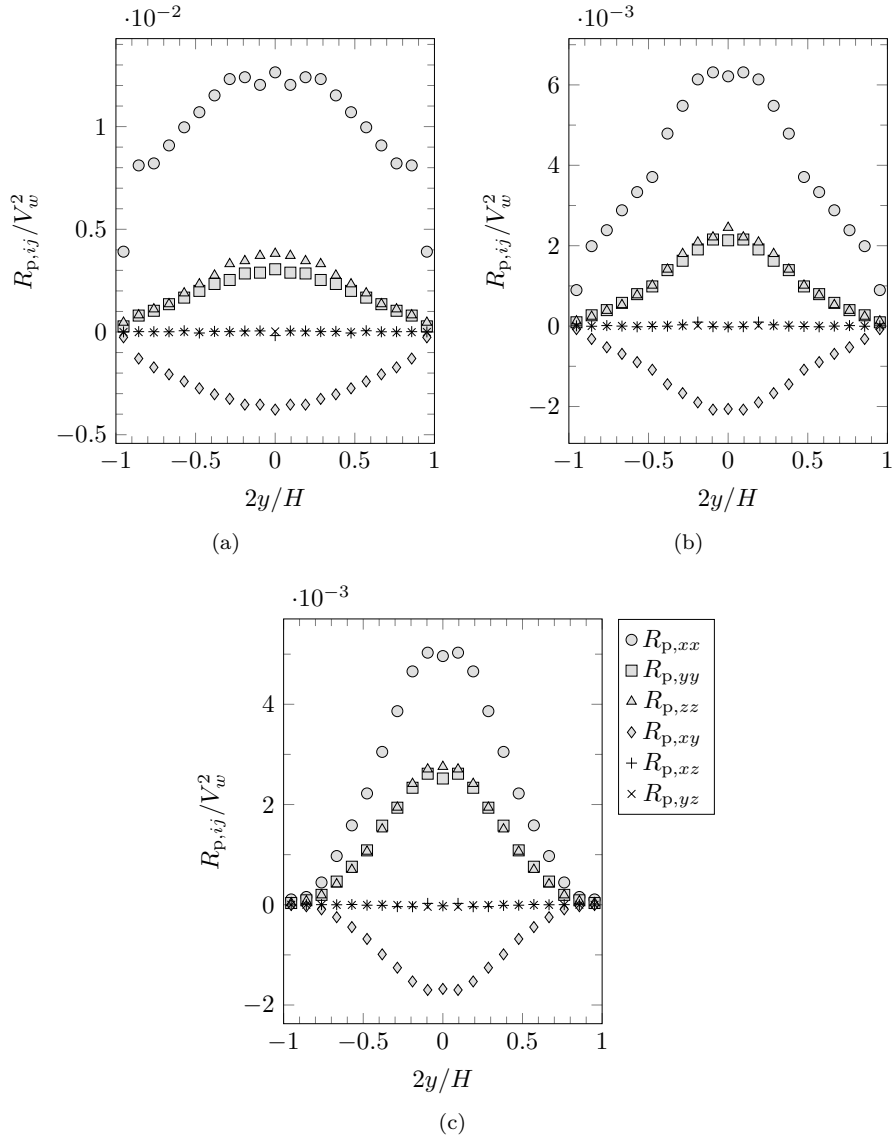

Figure 3.20: Particle kinetic stress for (a) M4; (b) M5; (c) M6.

Particle-particle interactions are responsible for this mechanism of fluctuating energy transfer from one direction to the others. As a consequence, particle kinetic stress tensor approaches a more isotropic state as this mechanism of redistribution is stronger. This is actually know as the isotropization effect [4] and it is expected to be more important in collision driven flows. The anisotopy tensor, $a_{\mathrm{p},ij}$, is a way of measuring the degree of deviation from an isotropic state of particle kinetic stress tensor and it is defined as follows:

$$a_{\mathrm{p},ij} = \frac{R_{\mathrm{p},ij}}{\frac{2}{3}q_{\mathrm{p}}^2} - \delta_{ij} \tag{3.12}$$

The value of the diagonal term $R_{\mathrm{p},xx}$ of the anisotropy tensor is shown by Figure 3.21. The degree of anisotropy diminishes from case M4 to M6. Which corresponds to an augmentation of total particle volume fraction in the Couette configuration, thus augmenting the interaction among the particles causing the inter-particle redistribution mechanism to be more efficient [59].

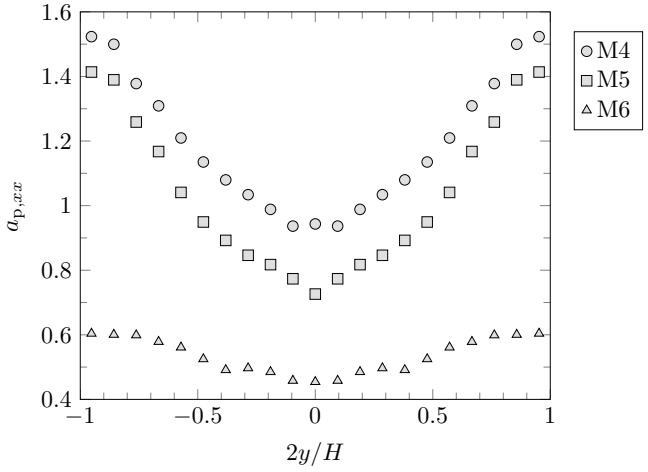

Figure 3.21: First diagonal anisotropy component: $a_{\mathrm{p},xx}$.

With respect to the cases M1 to M3, a huge variation on the order of magnitude of the diagonal terms of the particle kinetic stresses values occurs across the domain. For that reason Figure 3.22 uses a logarithmic scale. Similarly to fore-mentioned cases, stream-wise direction shows the highest fluctuating motion and in the other orthogonal directions smaller values are observed. Also, $R_{\mathrm{p},zz}$ is slightly lower than $R_{\mathrm{p},zz}$ in the centre region.

Shear kinetic stresses for the case M2, in the center region of the domain, are given by Figure 3.23(a). As expected, with the only non-zero value being the $R_{\mathrm{p},xy}$, which is the case for all our Couette cases. The negative sign of this particle kinetic shear stress is in fact due to the sign of the velocity gradient. The values of $R_{\mathrm{p},xy}$ for the cases M1, M2 and M3 are given by Figure 3.23(b). Note that the values in this latter figure are multiplied by minus one as indicated in vertical axis label for visualization sake in log scale.

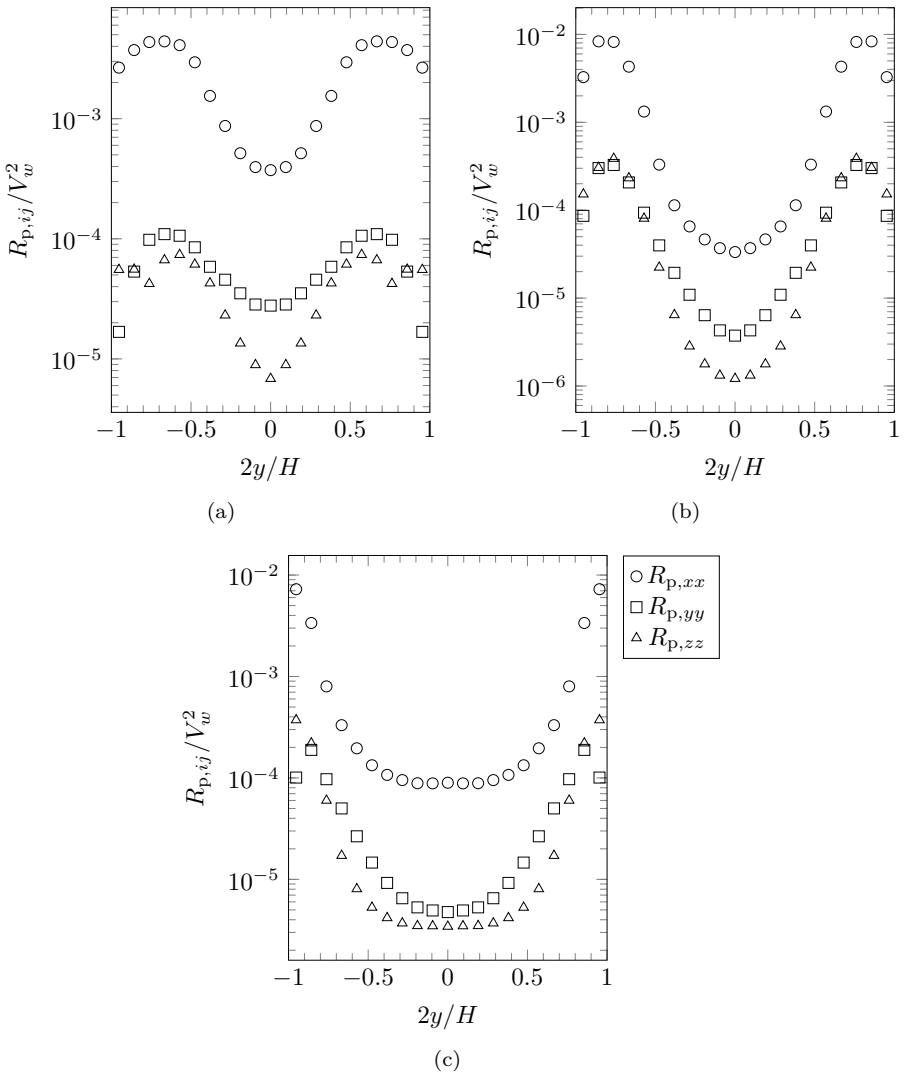

Figure 3.22: Particle kinetic stress for (a) M1; (b) M2; (c) M3.

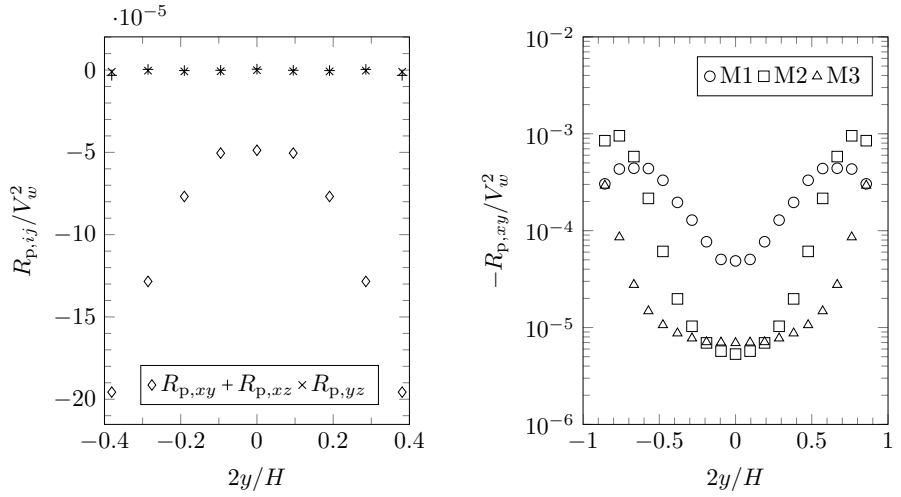

Figure 3.23: Particle shear kinetic stresses. (a) all components in the centre, for the case M2. (b) $-R_{\mathrm{p},xy}$ for the cases M1, M2 and M3.

In the frame of the kinetic theory of particulate flow, the particle kinetic stress tensor can be modeled using the Boussinesq approximation with an eddy-viscosity closure model, written as follows:

$$R_{\mathrm{p},ij} = \frac{2}{3} q_{\mathrm{p}}^2 \delta_{ij} - \nu_{\mathrm{p}}^{kin} \left(\frac{\partial U_{\mathrm{p},i}}{\partial x_j} + \frac{\partial U_{\mathrm{p},j}}{\partial x_i} - \frac{2}{3} q_{\mathrm{p}}^2 \delta_{ij} \frac{\partial U_{\mathrm{p},m}}{\partial x_m} \right) \tag{3.13}$$

Where ν_{p}^{kin} is the particle kinetic viscosity depending on the fluctuating kinetic energy and time-scales related to the fluid-particle interaction and particle-particle interactions. It can be directly calculated by Eq. (3.13) through the substitution of the shear kinetic stress $R_{\mathrm{p},xy}$. The values of the kinetic viscosity are given by Figure 3.24. Related to the magnitude, we observe that they are larger for the cases with higher inertia. Also, we note a clear inverse relationship with the volume fraction. With the largest kinetic viscosity being the one with the smallest volume fraction.

The kinetic viscosity in the regime dominated by the transport of momentum by the particle fluctuating velocity may be given as the product of a characteristic length scale, or mixing-length, and of the fluctuant velocity intensity.

$$\nu_{\mathrm{p}}^{kin} = l^{\nu} \sqrt{\frac{2}{3} q_{\mathrm{p}}^2} \tag{3.14}$$

Where l^{ν} represents the mean free path in the frame of kinetic theory of rapid granular flows. In the fluid-particle flow, the interaction with the fluid may reduce this length scale by friction or, in contrast, increase it due to the transport by large scales of the fluid turbulent motion.

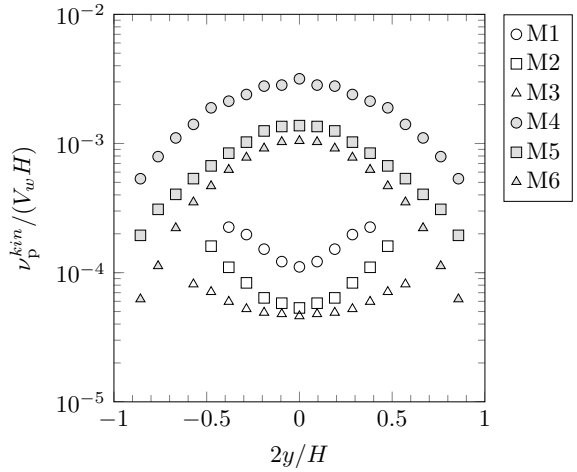

Figure 3.24: Kinetic viscosity for the mono disperse cases.

The values of l^ν, in the center of the core flow, are given by Figure 3.25, we note that this characteristic kinetic mixing length is larger for the cases of high inertia. According to [95], we can define a Knudsen number as the ratio of this length scale with the channel width H. The values of this parameter coincide with the data shown by Figure 3.25. We note that the order of magnitude of the kinetic viscosity based Knudsen number, is about $\sim 10^{-4}$. Since this value is small, it indicates that our cases are close to a local equilibrium.

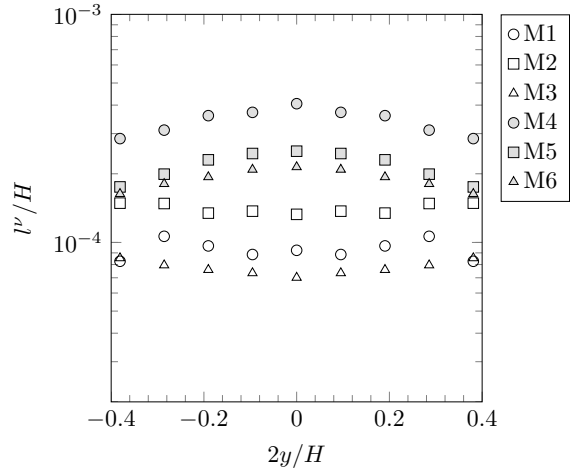

Figure 3.25: Non dimensional mixing length or Knudsen number.

Following [103], the kinetic viscosity can be modeled by the expression below:

$$\nu_{\mathrm{p}}^{kin} = \left[\nu_{\mathrm{fp}}^{t} + \frac{\tau_{\mathrm{fp}}^{F}}{2}\frac{2}{3}q_{\mathrm{p}}^{2}\left(1+\alpha_{\mathrm{p}}g_0\Phi_c\right)\right]\left(1+\frac{\tau_{\mathrm{fp}}^{F}}{2}\frac{\sigma_c}{\tau_{\mathrm{p}}^{c}}\right)^{-1} \tag{3.15}$$

Where τ_{fp}^{F} and τ_{p}^{c} are respectively the time-scales related to fluid-particle interactions and collisions. In addition, ν_{fp}^{t} represents the particle momentum transport by the fluid turbulence, and σ_c and Φ_c are parameters depending on the elastic normal restitution coefficient e_c. Note however that in the limit where $\tau_{\mathrm{p}}^{c} << \tau_{\mathrm{fp}}^{F}$, then Eq. (3.15) asymptotically gives as proportional to the collision time scale and the particle agitation:

$$\nu_{\mathrm{p}}^{kin} = \tau_{\mathrm{p}}^{c}\frac{2}{3}q_{\mathrm{p}}^{2}\frac{\left(1+\alpha_{\mathrm{p}}g_0\Phi_c\right)}{\sigma_c} \tag{3.16}$$

With the factor multiplying the right-hand side of the q_{p}^{2}, being generally in the order of magnitude of one or slightly larger.

The time-scale related to collisions, as given by the kinetic theory [18], is given by Eq. 3.17.

$$\tau_{\mathrm{p}}^{c} = \left[g_0 n_{\mathrm{p}}\pi d_{\mathrm{p}}^{2}\sqrt{\frac{16}{3}\frac{2q_{\mathrm{p}}^{2}}{\pi}}\right]^{-1} \tag{3.17}$$

Under the assumptions of the derivation of Eq. (3.16), a comparison of the time-scale formed by $\tau_{\mathrm{p}}^{\nu} = \nu_{\mathrm{p}}^{kin}/\frac{2}{3}q_{\mathrm{p}}^{2}$ and τ_{p}^{c} given by Eq. (3.17) is performed, and shown by Figure 3.26, the values are given in centre of the domain to avoid wall-effect phenomena interference.

With respect to the cases with the small bulk Stokes number, at Figure 3.26(a), interestingly, it can be seen that for both cases M2 and M3, the time-scales are very close, that is $\tau_{\mathrm{p}}^{\nu} \sim \tau_{\mathrm{p}}^{c}$, which seems to indicate that the collisions probably have a dominant effect. The smallest time-scale is the one controlling the particle flow and in this case the collision time-scale is possibly the smallest one. For the case M1, the gap between the values is bigger which might indicate that for this case another phenomena is taking place, such as a more pronounced fluid effect for example, which would invalidate the assumptions under which Eq. (3.16) is derived, thus explaining the gap, since the formula would no longer be applicable. The effect of the factor depending on α_{p}, g_0, σ_c and Φ_c, on Eq. (3.16), could not explain the gap since it would only augment it even more.

With respect to the cases with the larger bulk Stokes number, at Figure 3.26(b), we observe that for the case with the higher volume fraction, case M6, both time-scales are close to one another, whereas for the cases M5 and M4, the difference is more accentuated, being more distant for the case with the smallest particle volume fraction, which again may be an indication of a greater effect of the fluid in lower volume fractions and a dominant effect of the collision in the case with the higher volume fraction.

Analyzing the change from case M6 to M5, the diminution of the particle volume fraction may possibly have caused a more predominant growth in influence of the fluid in comparison with that of the collisions in case M5 relative to M6. Which might probably have directly led case M5 to a state where the assumption of $\tau_{\mathrm{p}}^{c} << \tau_{\mathrm{fp}}^{F}$ is no longer valid. For the cases with small inertia this "transition" may possibly have been delayed to a lower volume fraction, being between case M2 and M1.

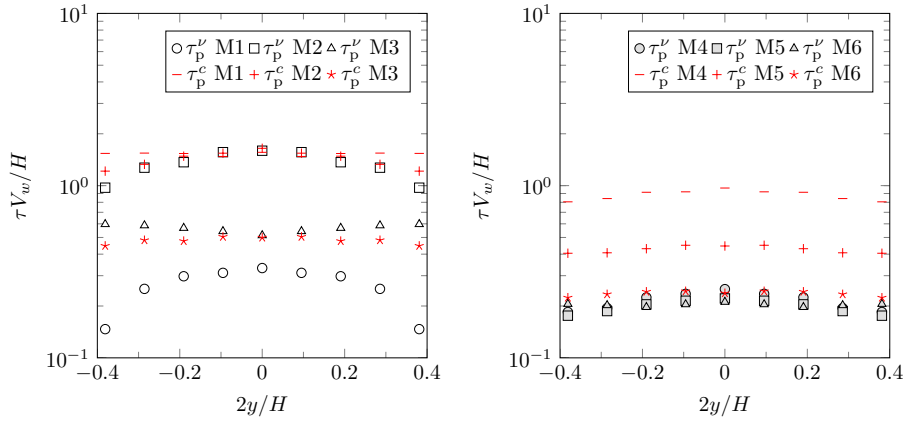

Figure 3.26: Kinetic viscosity time-scale and kinetic theory collision time-scale.

3.4.4 Third-order correlation

The particle third order correlation tensor $S_{\mathrm{p},ijk} = \left\langle u'_{\mathrm{p},i} u'_{\mathrm{p},j} u'_{\mathrm{p},k} \right\rangle$, introduced at the section 2.4, is a tensor with rank three of the velocity fluctuations. This third order correlation tensor appears in the transport equation of the particle kinetic stress tensor components and represents the kinetic transport by the particle velocity fluctuation [94, 99].

The triple correlation gradient term in the kinetic stress transport equation is a diffusive term which represents the transport of the second-order velocity correlations by the particle velocity fluctuation. The contraction of this tensor, is the transport term of the particle kinetic energy. In the configuration studied here, the term in any $R_{\mathrm{p},ij}$ equation is written $\frac{\partial(n_{\mathrm{p}} S_{\mathrm{p},ijk})}{\partial y}$ and represents the transport of the kinetic stress $R_{\mathrm{p},ij}$ across the domain.

All of the non null triple correlations are shown by Figure 3.27 for the cases M4 to M6. It can be seen that they are anti-symmetric with respect to the centre of the domain, which is mainly due to the boundary conditions of the configuration. Values obtained for the cases M1 to M3 are shown by Figure 3.28. For sake of visualization, the data are presented close to the centre, which coincides to highest concentration of particles for those cases. Also note that all of the triple correlations containing an odd moment of z-velocity components are null, thus not shown.

We observe that the sign of the correlations change with the bulk Stokes number transition. For instance, the triple correlation $S_{\mathrm{p},xxx}$ is positive in the

upper part of the domain for the cases M4 to M6, and negative for the cases M1 to M3. In fact, this inverse relationship related to the sign, occurs for all our non-null triple correlations.

The variation of the sign from the lower part to the upper part of the domain or more precisely the slope of the triple correlation times the particle number density is particularly important because it is directly associated to the diffusive term of Eq. (2.40).

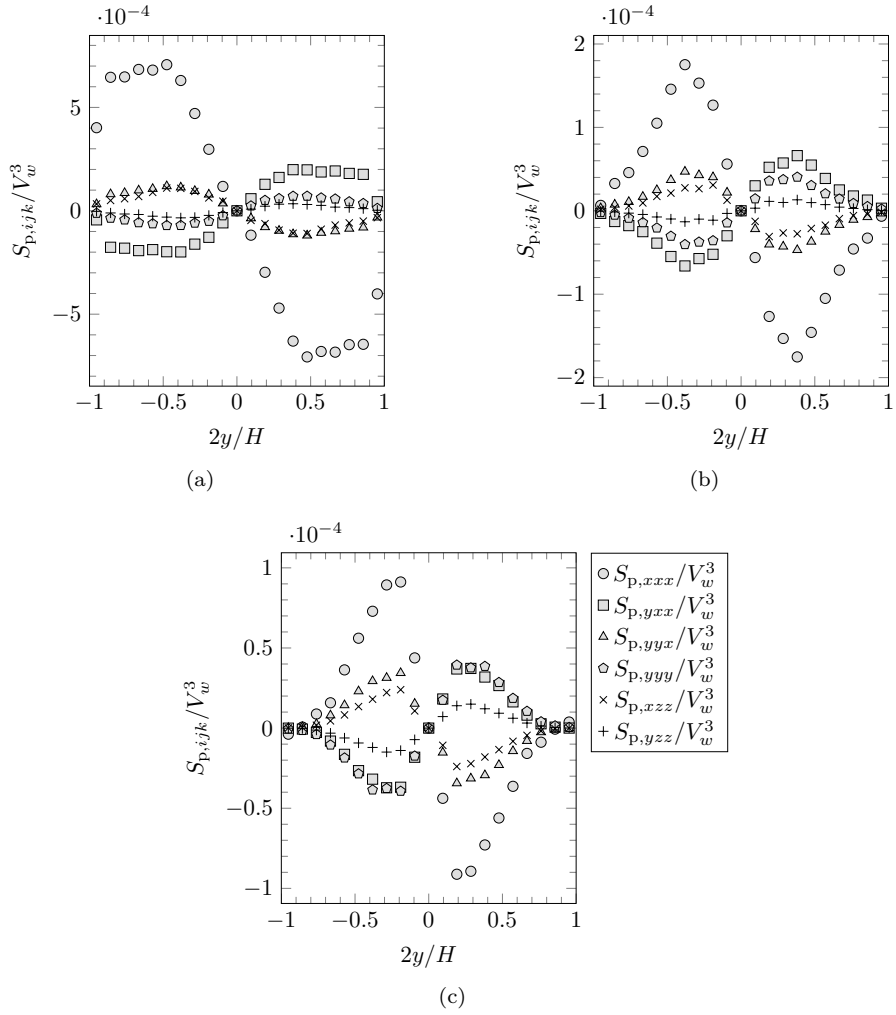

Figure 3.27: Triple correlation for the cases (a) M4, (b) M5 and (c) M6.

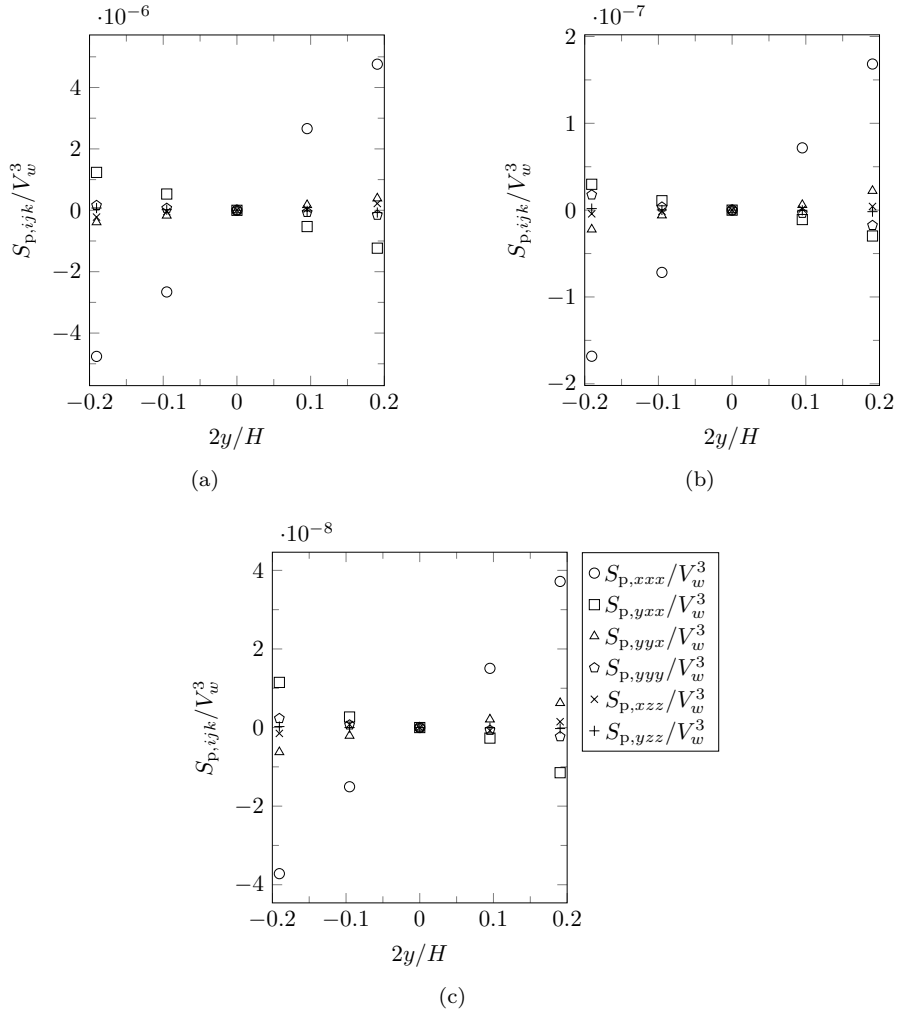

Figure 3.28: Triple correlation for the cases (a) M1, (b) M2 and (c) M3.

In the framework of Grad's approach, based on the third-order expansion of the distribution function as Hermite polynomials, the thirteen-moment model is derived from the full twenty-moment model, by assuming Eq. (3.18), which gives the triple correlation tensor $S_{\mathrm{p},ijk}$ as a function of its contracted forms $S_{\mathrm{p},ijj}$. For more details refer to [40].

$$S_{\mathrm{p},ijk} = \frac{1}{5}\left(S_{\mathrm{p},inn}\delta_{jk} + S_{\mathrm{p},jnn}\delta_{ki} + S_{\mathrm{p},knn}\delta_{ij}\right) \tag{3.18}$$

In order to test this approximation, an a priori test of the model equation is carried out for the correlations $S_{\mathrm{p},xxx}$, $S_{\mathrm{p},xyy}$ and $S_{\mathrm{p},xzz}$. The formula for the first one is given by Eq. (3.19). With respect to the second and third ones, even though they are different, they both share the same formula for the approximation, which is given by Eq. (3.20). The comparison for the cases is presented in Figure 3.29. Absolute values are plotted with the purpose of fitting

them on a logarithmic scale. An overall agreement is observed for the correlation $S_{\mathrm{p},xxx}$, and a slightly overestimation for the other ones, which are: $S_{\mathrm{p},xyy}$ and $S_{\mathrm{p},xzz}$.

$$S_{\mathrm{p},xxx} = \frac{3}{5}\left(S_{\mathrm{p},xxx} + S_{\mathrm{p},xyy} + S_{\mathrm{p},xzz}\right) \tag{3.19}$$

$$S_{\mathrm{p},xyy} = \frac{1}{5}\left(S_{\mathrm{p},xxx} + S_{\mathrm{p},xyy} + S_{\mathrm{p},xzz}\right) = S_{\mathrm{p},xzz} \tag{3.20}$$

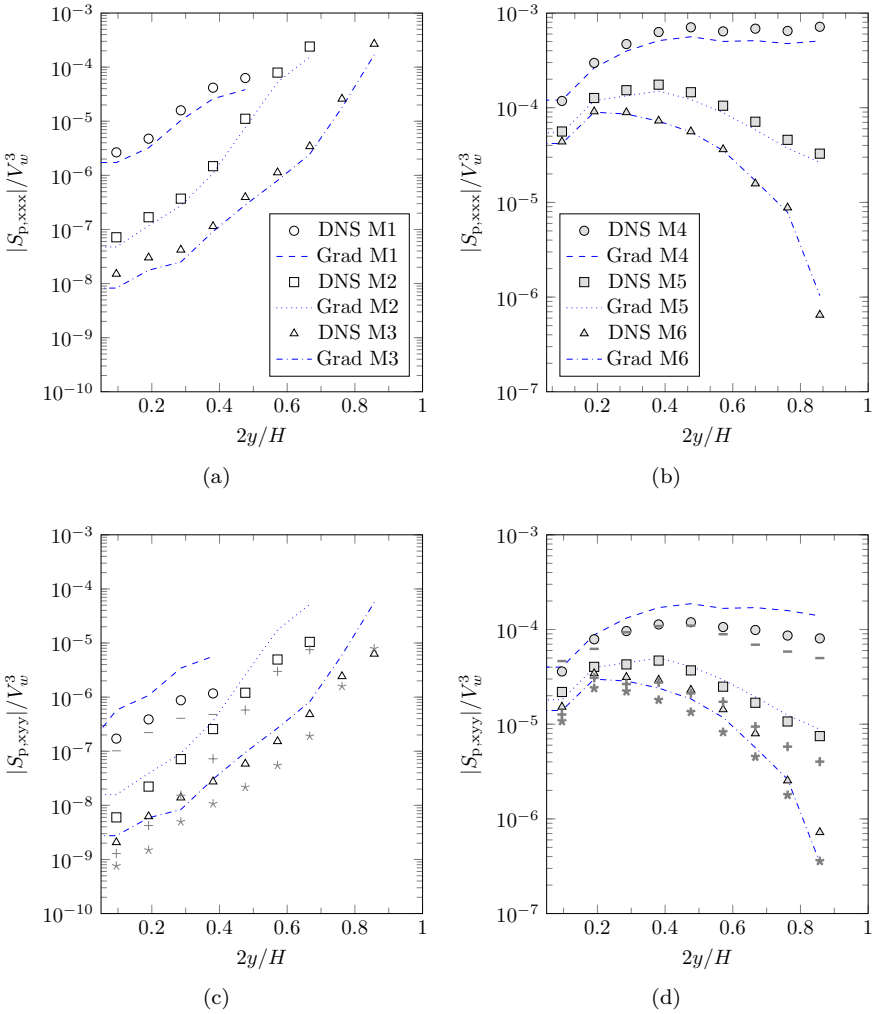

Figure 3.29: Third-order correlation comparison with the thirteen moment Grad approximation. Additional symbols for $S_{\mathrm{p},xzz}$, on the figures (c) and (d), are as follows: M1 (_); M2 (+); M3 (⋆); M4 (_); M5 (+); M6 (⋆).

In the framework of the modeling and simulation of particle kinetic stress using second-order moment transport equations a gradient approximation has been derived for the triple velocity correlation by [44, 99, 101]. The proposed modeling approach was developed in the frame of the kinetic theory of particulate flows and inspired by the work of [27, 42]. The gradient model reads:

$$S_{\mathrm{p},ijk} = -K_{in}^{kin}\frac{\partial R_{\mathrm{p},jk}}{\partial x_n} - K_{jn}^{kin}\frac{\partial R_{\mathrm{p},ki}}{\partial x_n} - K_{kn}^{kin}\frac{\partial R_{\mathrm{p},ij}}{\partial x_n} \tag{3.21}$$

Where K_{ij}^{kin} is the dispersion tensor. Under the assumption that the fluid-particle correlation is null meaning that the particles are not dragged by the fluctuation motion of the fluid. Then the dispersion tensor can be given as proportional to the kinetic stress tensor and to a characteristic time with this latter being dependent on the drag and the collisions effects, see [103].

The first validation of this modeling with results from Lagrangian simulation of particles in a turbulent vertical channel can be found in [94, 95]. In our configuration, mostly due to the boundary layers, the relevant coefficients are K_{xy}^{kin} and K_{yy}^{kin}. As a matter of fact, those can be directly computed by means of Eqs. (3.22) and (3.23), reads:

$$S_{\mathrm{p},xxx} = -3K_{xy}^{kin}\frac{\partial R_{\mathrm{p},xx}}{\partial y} \tag{3.22}$$

$$S_{\mathrm{p},yyy} = -3K_{yy}^{kin}\frac{\partial R_{\mathrm{p},yy}}{\partial y} \tag{3.23}$$

Calculated values of K_{xy}^{kin} and K_{yy}^{kin} are respectively given by Figure 3.30.

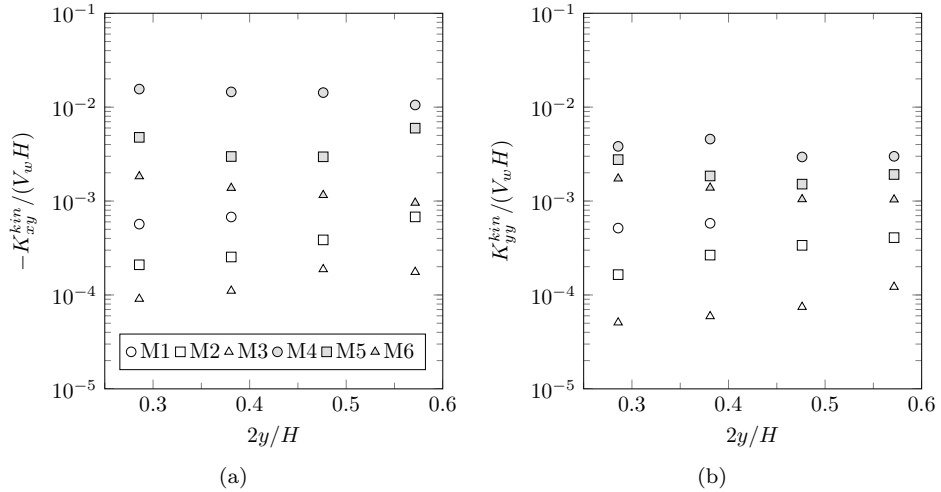

Figure 3.30: Relevant components of the dispersion tensor, related to the triple correlation gradient model.

In order to verify whether the gradient approximation is consistent, then the use of those latter computed coefficients should predict correct values of other

arbitrary triple correlation depending on those components of the dispersion tensor. To test this assumption, we predict the values of the following triple correlations: $S_{\mathrm{p},yxx}$, $S_{\mathrm{p},xyy}$, $S_{\mathrm{p},yzz}$ and $S_{\mathrm{p},xzz}$. The formulas related to those correlations are given by Eqs. 3.24 to 3.27. using the components of the dispersion tensor computed with Eqs. (3.22) and (3.23) and shown by Figure 3.30.

$$S_{\mathrm{p},yxx} = -2K_{xy}^{kin}\frac{\partial R_{\mathrm{p},xy}}{\partial y} - K_{yy}^{kin}\frac{\partial R_{\mathrm{p},xx}}{\partial y} \tag{3.24}$$

$$S_{\mathrm{p},xyy} = -K_{xy}^{kin}\frac{\partial R_{\mathrm{p},yy}}{\partial y} - 2K_{yy}^{kin}\frac{\partial R_{\mathrm{p},xy}}{\partial y} \tag{3.25}$$

$$S_{\mathrm{p},yzz} = -K_{yy}^{kin}\frac{\partial R_{\mathrm{p},zz}}{\partial y} \tag{3.26}$$

$$S_{\mathrm{p},xzz} = -K_{xy}^{kin}\frac{\partial R_{\mathrm{p},zz}}{\partial y} \tag{3.27}$$

The predictions for all the cases are given by Figure 3.31 and 3.32. Since both the values given by the model and the results of the DNS agree for all four different triple correlations, indicating that the gradient model looks satisfactory. The fact that both the kinetic viscous mixing length, and the diffusion mixing length, discussed latter on this section, are small is an indication that the cases are close to a local equilibrium, and [95] has shown that when this is the case, then the gradient model is likely to work.

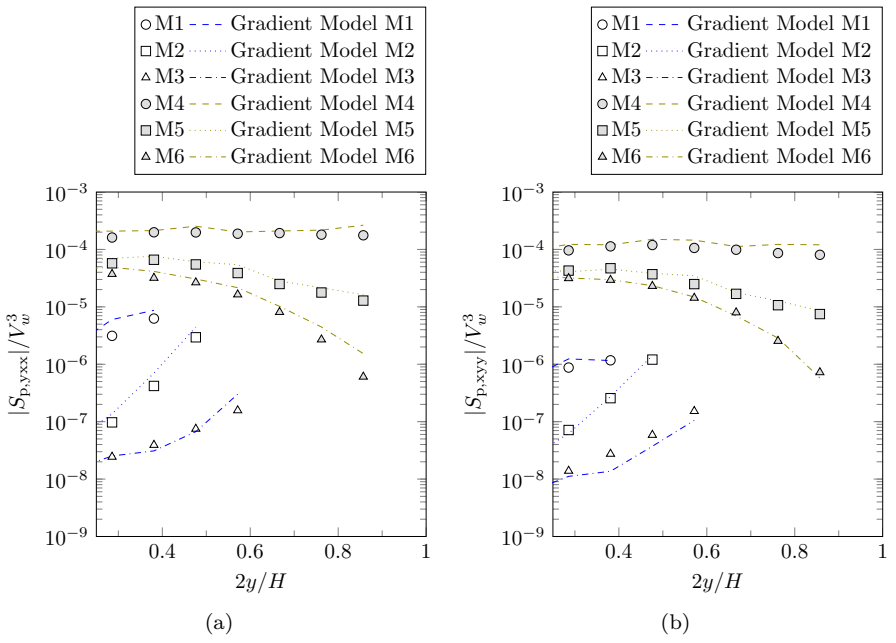

Figure 3.31: Consistency of the prediction of the third-order correlations by using the gradient model.

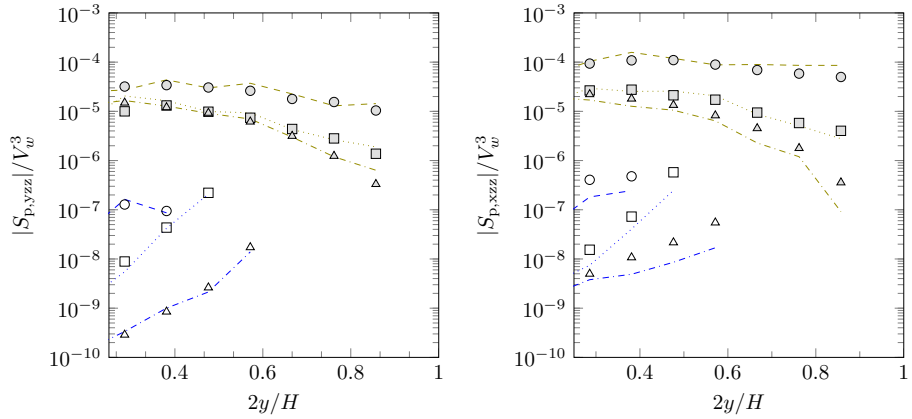

Figure 3.32: Consistency of the prediction of the third-order correlations by using the gradient model. Legends are the same as Figure 3.31.

With respect to the order of magnitude of the normalized dispersion tensor components, given by Figure 3.30, we note that they range between 10^{-2} to 10^{-4}. Also we note that K_{xy}^{kin} is negative and K_{yy}^{kin} positive. The first one is plotted with a minus sign in order to fit it onto a log scale. Absolute values of K_{xy}^{kin} seem to be slightly lower than K_{yy}^{kin}. Regarding the tendency, similarly to the kinetic viscosity, values for the most inertial cases are systematic larger in comparison with those with smaller inertia. In addition, an inverse relationship between the particle volume fraction and the dispersion tensor components is also found. Indeed, the cases with small volume fraction values are the ones with the largest dispersion tensor components for a given bulk Stokes number

Following [95, 103], in the case of a fluid-particle flow without the turbulence effect, the dispersion tensor may be written as function of the particle kinetic stress and a characteristic dispersion time-scale which results from the competition of the drag and collisions in the particle flow, reads:

$$K_{ij}^{kin} = \left[R_{\mathrm{pf},ij} \frac{\tau_{\mathrm{fp}}^t}{\sigma_q} + \frac{5}{9} \tau_{\mathrm{fp}}^F R_{\mathrm{p},ij} \left(1 + \alpha_{\mathrm{p}} g_0 \Psi_c\right) \right] \left(1 + \frac{5}{9} \tau_{\mathrm{fp}}^F \frac{\xi_c}{\tau_{\mathrm{p}}^c} \right)^{-1} \tag{3.28}$$

Where σ_q and Ψ_c are adjustable constant parameters of the model. Similarly to the kinetic viscosity, the equation above in the limit where $\tau_{\mathrm{p}}^c << \tau_{\mathrm{fp}}^F$, gives:

$$K_{ij}^{kin} = \tau_{\mathrm{p}}^c R_{\mathrm{p},ij} \frac{\left(1 + \alpha_{\mathrm{p}} g_0 \Psi_c\right)}{\xi_c} \tag{3.29}$$

The values of the diffusion time-scale τ_{p}^K, calculated through the equation above by substituting the dispersion tensor and the corresponding particle kinetic stress component, are given by Figure 3.33. We also observe that the values do not show a clear dependence on the volume fraction for the cases with small inertia, similarly to what has been shown for the viscosity time-scale by

Figure 3.26(a). In addition, the values for the cases with small inertia are bigger than those with high inertia. With respect to the order of magnitude, we observe that they are approximately $\sim 10^1$ times bigger than the kinetic viscous time-scale.

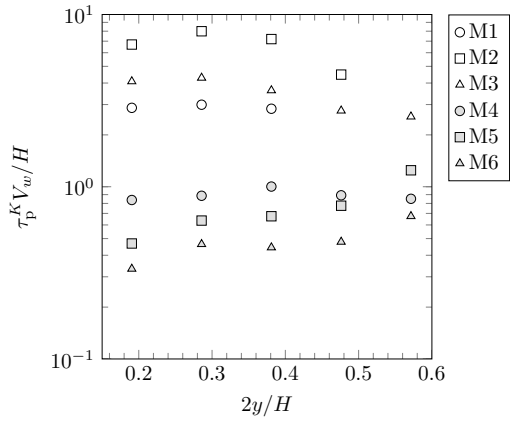

Figure 3.33: Diffusion characteristic time-scale.

A useful non-dimensional number related to both ν_{p}^{kin} and K_{ij}^{kin} is the Schmidt number. It is defined as the ratio of the kinetic viscosity to the dispersion tensor. It characterizes the relative importance of both the kinetic viscous and kinetic diffusion phenomena. For our cases, Sc varies from 0.1 to 1. Meaning that the transport of particle agitation is more efficient than the momentum transport.

Related to the diffusion time-scale, a Knudsen number based on the corresponding mixing length scale can be calculated as $\tau_{\mathrm{p}}^K \sqrt{\frac{2}{3} q_{\mathrm{p}}^2}/H$, the order of magnitude of this non-dimensional length is larger than that of the kinetic viscosity but it remains well below one. This has a direct implication for the gradient model as already discussed in this section.

3.4.5 Fourth-order correlation

The particle fourth-order correlation, $Q_{\mathrm{p},mnij} = \left\langle u'_{\mathrm{p},m} u'_{\mathrm{p},n} u'_{\mathrm{p},i} u'_{\mathrm{p},j} \right\rangle$, is introduced in section 2.4. Some authors proposed formulas for those correlations, notably [40] and [95, 101]. With the second one being the formula linking fourth order moments, to second order moments for an anisotropic Gaussian distribution. Their formulas, are respectively given by Eq. 3.30 and 3.31.

$$\begin{aligned} Q^{\mathrm{Grad}}_{\mathrm{p},mnij} &= \frac{2}{3} q_{\mathrm{p}}^2 [R_{\mathrm{p},ij}\delta_{mn} + R_{\mathrm{p},im}\delta_{jn} + R_{\mathrm{p},in}\delta_{jm} \\ &\quad + R_{\mathrm{p},jm}\delta_{in} + R_{\mathrm{p},jn}\delta_{im} + R_{\mathrm{p},mn}\delta_{ij}] \\ &\quad - \frac{4}{9} \left[q_{\mathrm{p}}^2\right]^2 [\delta_{ij}\delta_{mn} + \delta_{im}\delta_{jn} + \delta_{in}\delta_{jm}] \end{aligned} \tag{3.30}$$

$$Q^{\mathrm{Gauss}}_{\mathrm{p},mnij} = R_{\mathrm{p},ij}R_{\mathrm{p},mn} + R_{\mathrm{p},im}R_{\mathrm{p},jn} + R_{\mathrm{p},in}R_{\mathrm{p},jm} \tag{3.31}$$

A comparison of several components of the fourth-order correlation against both the formulas presented above is given by Figure 3.34. Figure 3.34(a) shows that the Gaussian approximation gives satisfactory results whereas the Grad's approximation is only good for two out of the five correlations shown. This is in agreement of what has been found by [11], related to the better accuracy of the Gaussian approximation.

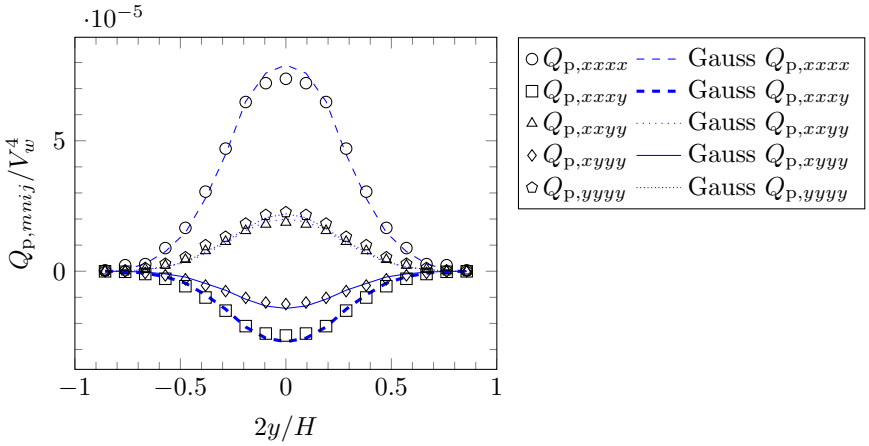

(a)

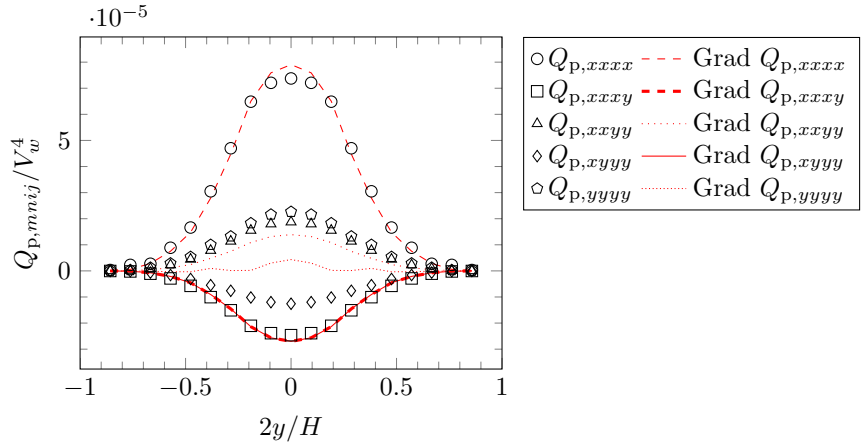

(b)

Figure 3.34: Comparison of formulas for the approximation of the fourth-order correlation for the case M6. (a) Gauss (b) Grad.

A comparison of the fourth order correlation with the gaussian formula is given by Figure 3.35 for all the cases. For those cases only positive values are shown, in order to fit in a semi-log scale. A satisfactory agreement is found for all the cases.

The good results of the fourth-order correlation comparison in junction with the results shown in the last section for the gradient model for the triple correlation are in agreement with the fact that both the Knudsen number based on the mixing length scale of kinetic transport of momentum (viscosity) and velocity variance (diffusivity) are very small.

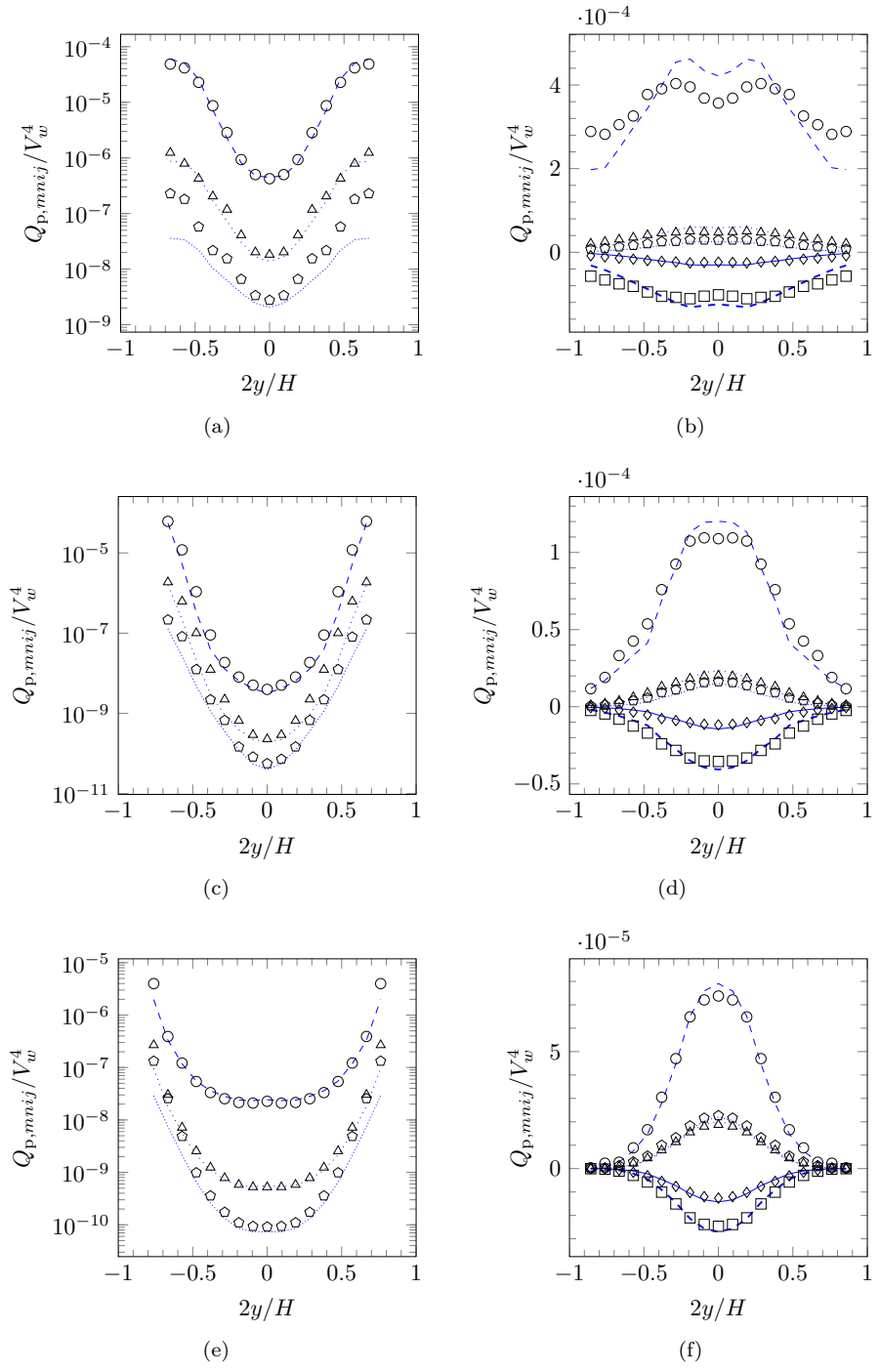

Figure 3.35: Comparison of the fourth-order correlations with the Gaussian approximation for the cases (a) M1, (b) M2, (c) M3, (d) M4, (e) M5 and (e) M6. For the symbols refer to Figure. 3.34(a).

3.5 Budget analysis

In this section, the terms for the fluid and particle transport equations, respectively given in sections 2.3 and 2.4, are directly measured from our resolved simulations. The results are presented in the form of budget highlighting local physical phenomenon. For the fluid, we show the budget of the fluid fluctuating kinetic energy and for the particles we show first and second order budgets which are respectively related to the forces and the particle kinetic stresses, or fluctuating kinetic energy of the particles.

3.5.1 Mean particle velocity budget

The transport equation of the mean particle velocity, given by Eq. (2.39), is rewritten for our mono-disperse cases on Eq. (3.32). It is composed of three main terms: a diffusive term, called D, which is separated into $D1$ and $D2$; a fluid interaction term, called F; and a particle-particle interaction term, called C_{pp}. The first one, D, is related to an effective force which is due to gradients in the particle kinetic stresses and particle number density, the second F, is simply due to the action of the fluid flow into the particles, also called the drag. Finally, the third term, is due to an average transfer of linear momentum to the particles due to particle-particle interaction.

$$\frac{\partial U_{\mathrm{p},i}}{\partial t} = \overbrace{\underbrace{-\frac{\partial R_{\mathrm{p},iy}}{\partial y}}_{D1} \underbrace{-\frac{R_{\mathrm{p},iy}}{n_{\mathrm{p}}}\frac{\partial n_{\mathrm{p}}}{\partial y}}_{D2}}^{D} + \underbrace{\left\langle \frac{F_{\mathrm{f}\to\mathrm{p},i}}{m_{\mathrm{p}}} \right\rangle}_{F} + \underbrace{\left\langle \frac{F_{\mathrm{p}'\to\mathrm{p},i}}{m_{\mathrm{p}}} \right\rangle}_{C_{\mathrm{pp}}} \tag{3.32}$$

The mean velocity budgets in the stream-wise and wall-normal directions for all the cases are given by Figures 3.36 to 3.39. The values are normalized by H/V_w^2. Besides, for sake of simplicity, the general names for the terms cited above are used in the legends, such as: $D1$, $D2$, F and C_{pp}. The budgets on the span-wise direction are not shown, since the particle laden flow is homogeneous in this direction.

Regarding the stream-wise velocity budgets for the cases M1 to M3, on Figure 3.36, the budgets are shown in the center of the core flow, for better visualization. With respect to the fluid, we observe that it drags the particles forward into the stream-wise direction, since it is positive on the upper part of the domain, and negative on the lower part. Also we observe that this effect is largely diminished in the zones of higher particle volume fraction. In addition, we note that a negative slope related to the particle-particle interaction term, which is due to the gradient of the collisional flux explained on the section 2.7. This force goes in the opposite direction as the mean fluid force, it is greatly diminished in the zones of higher volume fraction. Related to the diffusive forces we note that $D1$ has the sign of the fluid term and $D2$ to the particle-particle term. The budget says that the fluid is dragging the particles forward, and the collision flux gradient through particle-particle interaction, and the diffusive terms are balancing it.

Still on the stream-wise direction, a different scenario is found for the cases with higher inertia, on the Figure 3.37. Contrary to the other cases, the fluid

term is the dominant ones for the cases with high inertia. In fact, the particle-particle interaction term and the diffusive terms are the most important ones. Regarding the particle-particle interaction term, we note that it has a positive slope, meaning that it is a mechanism pushing forward the particles in the stream-wise direction. It is also interesting to note that as the particle volume fraction augments, this term became more dominant, which can be seen by comparing Figures 3.37, which makes sense, since the collision flux tends to be larger in the cases with larger volume fraction. The fact that the slope of the particle-particle term is positive for the cases with higher inertia and the inverse for the cases with low inertia, is among other reasons related to the fact that the collision flux depend on the particle number density, and since their shape change from cases with low and high inertia (see Figure 3.3), notably from concave to convex, the gradient of the collision flux, which is responsible for the this particle-particle term, as a consequence, change as well (A deeper investigation and validation of the collision term separation is given on the next chapter for the bi-solid cases). Similarly, it is found that the diffusive term $D2$ have the same sign of the particle-particle term, whereas $D1$ the opposite. Fundamentally, there is a balance between the particle-particle interaction term and the diffusive terms.

The budgets for the mean wall-normal velocity are also shown at the centre of the core flow for the cases with low inertia, see Figure 3.38. Particularly for the case M1, we note that the fluid term is pushing the particles towards the centre. In contrast, for the cases M2 and M3 this force seems very small in the core flow. A deeper analysis of this force is given in the section 3.6, where it is shown that the pressure gradient is not responsible for this force, and it is more compatible with a lift force. The particle-particle interaction term acts to expel the particles outwards the centre of the core flow. The fore-mentioned terms are then balanced by the diffusive terms.

With respect to the cases of high inertia, still on the wall-normal direction, the budgets are given by Figure 3.39. Similarly to the low-inertia cases, the fluid term is also pushing the particles towards the centre of the core-flow. In addition, the particle-particle term also have a mean effect of pushing particles outwards the centre. Analogously to the budget in the stream-wise direction for the same cases, the diffusive terms are very dominant in the budget.

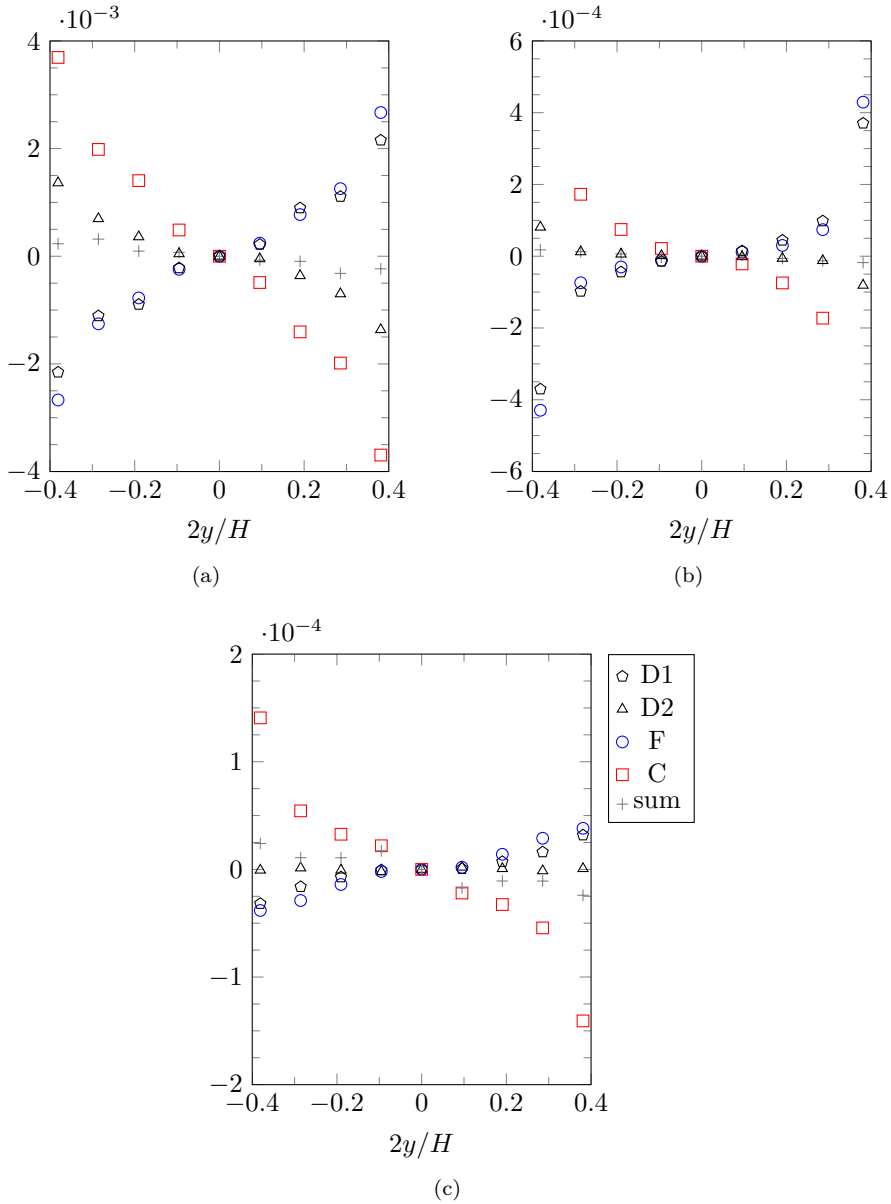

Figure 3.36: Budget analysis of the particle momentum in the stream-wise direction for the cases M1 (a), M2 (b) and M3 (c). All terms are dimensionless by dividing with H/V_w^2.

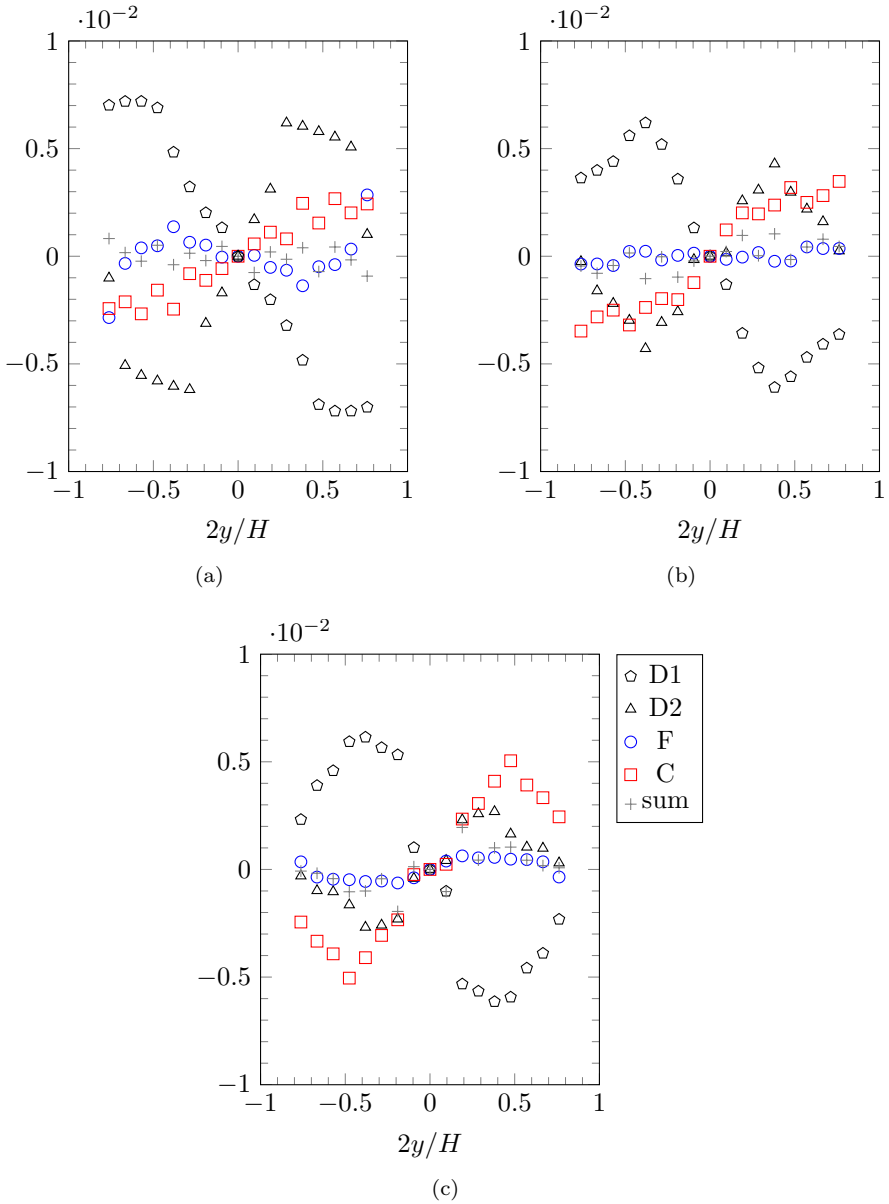

Figure 3.37: Budget analysis of the particle momentum in the stream-wise direction for the cases M4 (a), M5 (b) and M6 (c). All terms are dimensionless by dividing with H/V_w^2.

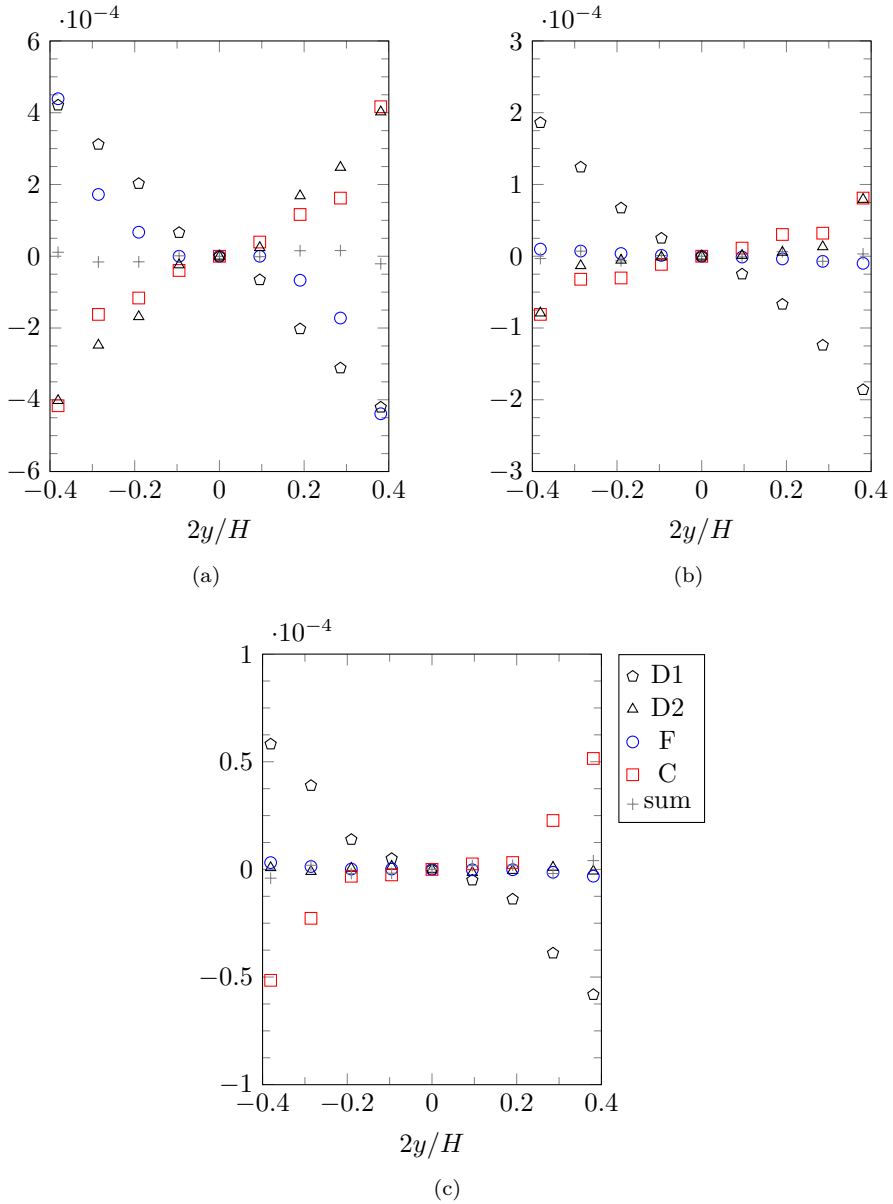

Figure 3.38: Budget analysis of the particle momentum in the wall-normal direction for the cases M1 (a), M2 (b) and M3 (c). All terms are dimensionless by dividing with H/V_w^2.

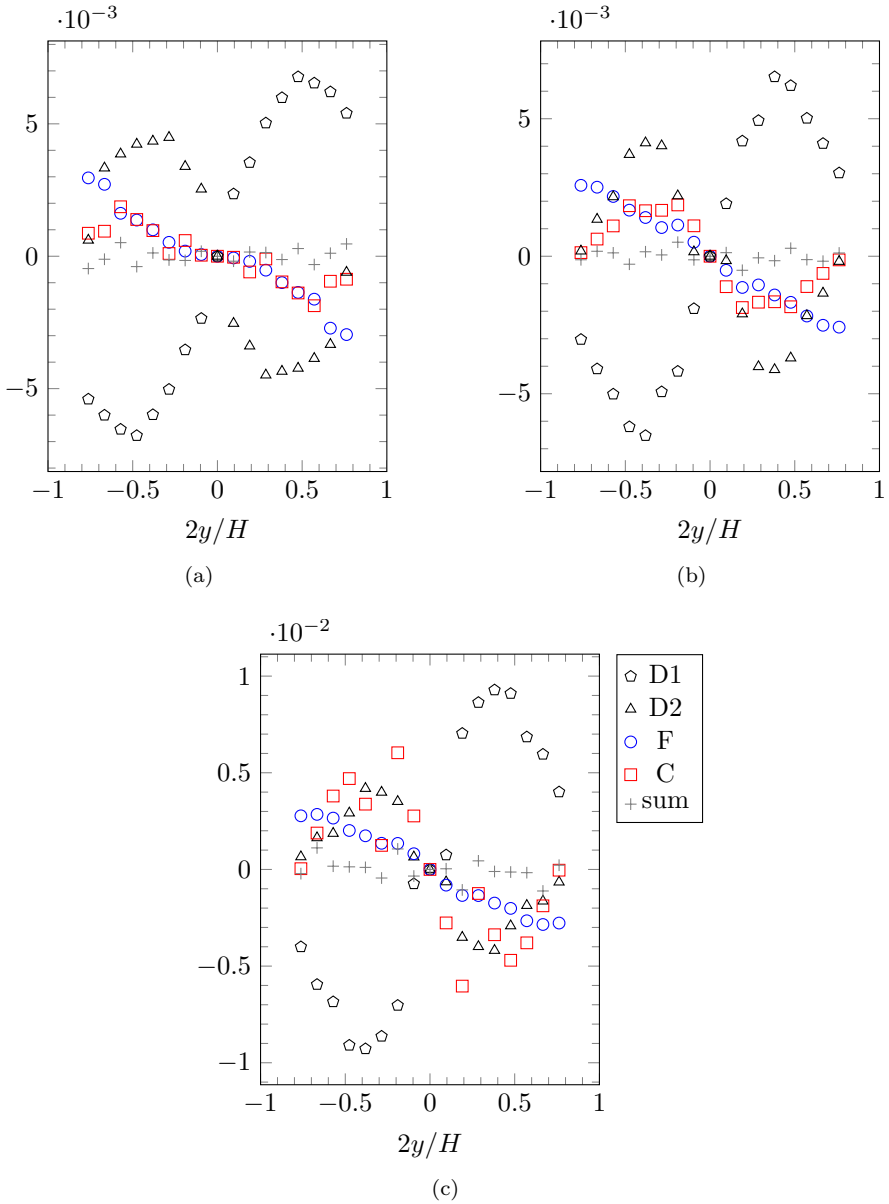

Figure 3.39: Budget analysis of the particle momentum in the wall-normal direction for the cases M4 (a), M5 (b) and M6 (c). All terms are dimensionless by dividing with H/V_w^2.

3.5.2 Fluid fluctuating kinetic energy budget

Assuming a null particle velocity in wall-normal and span-wise direction, and non-null gradients only with respect to the wall-normal direction, the fluid fluctuating kinetic energy transport equation, Eq. (2.21), can be rewritten as:

$$\begin{aligned}\alpha_{\mathrm{f}}\rho_{\mathrm{f}}\frac{\partial k_{\mathrm{f}}}{\partial t} &= -\frac{\partial}{\partial y}\left[\alpha_{\mathrm{f}}\left\langle p' u'_{\mathrm{f},y}\right\rangle_{\mathrm{f}}\right] - \frac{\rho_{\mathrm{f}}}{2}\frac{\partial}{\partial y}\left[\alpha_{\mathrm{f}} S_{\mathrm{f},iiy}\right] \\ &\quad +\alpha_{\mathrm{f}}\rho_{\mathrm{f}}\left[\nu_{\mathrm{f}}\left(\frac{\partial^2 k_{\mathrm{f}}}{\partial y^2}+\frac{\partial^2 R_{\mathrm{f},yy}}{\partial y^2}\right)+\frac{\nu_{\mathrm{f}}}{\alpha_{\mathrm{f}}}\frac{\partial \alpha_{\mathrm{f}}}{\partial y}\left(\frac{\partial k_{\mathrm{f}}}{\partial y}+\frac{\partial R_{\mathrm{f},yy}}{\partial y}\right)\right] \\ &\quad -\alpha_{\mathrm{f}}\rho_{\mathrm{f}} R_{\mathrm{f},ij}\frac{\partial U_{\mathrm{f},i}}{\partial x_j} - \alpha_{\mathrm{f}}\rho_{\mathrm{f}}\epsilon + \Pi^{k_{\mathrm{f}}}_{\mathrm{f}\to\mathrm{p}}\end{aligned} \tag{3.33}$$

On the right-hand side of the equation above we found three diffusive terms: one due to pressure effects, one due to turbulent transport, and another due to viscous effects. Additionally, the fourth term is the production by the mean fluid shear velocity, the fifth is the viscous dissipation of the fluctuating kinetic energy due to internal friction, which is discussed on the sections 3.3.4 and 3.3.3. Finally, the last term is the term related to the interfacial exchange due to the presence of particles in the fluid phase, and from section 2.6.2 it is rewritten are as:

$$\begin{aligned}\Pi^{k_{\mathrm{f}}}_{\mathrm{p}\to\mathrm{f}} &= \underbrace{-\Pi^{q_{\mathrm{p}}^2}_{\mathrm{f}\to\mathrm{p}}+\frac{\partial \theta_{\mathrm{pf},i}}{\partial x_j}}_{\text{due to particle variance}} + \underbrace{(U_{\mathrm{p},i}-U_{\mathrm{f},i})\left(-I_{\mathrm{f}\to\mathrm{p},i}+\frac{\partial \theta_{\mathrm{pf},ij}}{\partial x_j}\right)}_{\text{due to mean slip}} \\ &\quad \underbrace{-\Upsilon_{\mathrm{f}\to\mathrm{p}}+\frac{\partial \Xi_{\mathrm{pf},i}}{\partial x_i}}_{\text{due to rotation}}\end{aligned} \tag{3.34}$$

As indicated by the brackets in the equation above, three main mechanisms can be found in the exchange term above, and depending on the sign they can act as a source or a sink effect. The first group, due to particle variance, is directly related to the creation or destruction of fluid variance by means of the interaction with the particle velocity variance. Or, in other words, how the fluctuating kinetic energy of the particles affects the fluctuating kinetic energy of the fluid phase. As already explained in section 2.6.2, the second term is due to inhomogeneous flow effects. The second mechanisms is due to the mean slip between the phase, and it is linked to the transfer of mean motion between the phases to the fluid variance. Finally, the third one is related to the transfer of fluid fluctuating kinetic energy to the particle rotation.

The mean-slip mechanism is particularly important in gravity driven flows, such as in [3]. The description by which the fluid variance are generated by this mechanism has been discussed in section 3.2.3. In the case of our resolved simulations, we will show in the next paragraphs that it is not a relevant mechanism.

Neglecting the gradient terms due to the inhomogeneous flow, and comparing the effect due to the particle variance to the mean slip mechanism on the right-hand side of Eq. (3.34), we found that the dominant mechanism by far in our

case is the production of fluid variance by the interaction with the particle variance. For that reason, we neglect the mean-slip term. In that sense, in our case the term $\Pi^{k_\mathrm{f}}_{\mathrm{p}\to\mathrm{f}}$ may approximately assume the following form:

$$\Pi^{k_\mathrm{f}}_{\mathrm{p}\to\mathrm{f}} \simeq -\Pi^{q^2_\mathrm{p}}_{\mathrm{f}\to\mathrm{p}} - \Upsilon_{\mathrm{f}\to\mathrm{p}} \tag{3.35}$$

Both terms can be computed from Lagrangian statistics using the methodology given in the section 2.7. Nonetheless, rotation data was not available for the computation of this term.

The budgets of the fluid fluctuating kinetic energy, k_f, according to the transport Eq. (3.33), and with the exchange term computed by $\Pi^{k_\mathrm{f}}_{\mathrm{p}\to\mathrm{f}} \simeq -\Pi^{q^2_\mathrm{p}}_{\mathrm{f}\to\mathrm{p}}$, for the cases M1, M2 and M3 are given by Figure 3.40. In those figures, all the transport terms with the exception of the diffusive term due to the pressure velocity fluctuations are given.

The results show that the diffusive terms, and the production by the mean fluid shear velocity are negligible. The budget basically consists in an balance by the production of fluid velocity variance by the interaction with the particles, and a destruction by the fluid viscous dissipation. Note that while the interfacial exchange term is computed in the particle grid, the others are on the fluid grid. Besides, the fact that the budgets are nearly closed, indicate that the approximation for $\Pi^{k_\mathrm{f}}_{\mathrm{f}\to\mathrm{p}}$ is likely adequate for the analyzed cases.

From the analysis of the scales of the fluid fluctuating motion in the section 3.3.4, it is known that the fluid fluctuating scales are smaller than both the particle size and the characteristic length on the intersticial volume between the particles. Those results indicate that the fluctuations in the fluid flow probably stem from small wakes generated by the passage of the fluid past the particles.

The budgets for the cases with high inertia are given by Figure 3.41, according to Eq. (3.33), and similarly, the interfacial term is computed as: $\Pi^{k_\mathrm{f}}_{\mathrm{p}\to\mathrm{f}} \simeq -\Pi^{q^2_\mathrm{p}}_{\mathrm{f}\to\mathrm{p}}$. The budgets also show that the dominant terms are the viscous dissipation and the inter-phase exchange term. The budgets are nevertheless positive, which is probably related to the fact that the rotation term $-\Upsilon_{\mathrm{f}\to\mathrm{p}}$, in Eq. (3.35) is missing to balance it, this would indicate that energy is being drawn from the fluid to rotate the particles, and thus would be a negative contribution in the term due to the particles, and would possibly balance the budget.

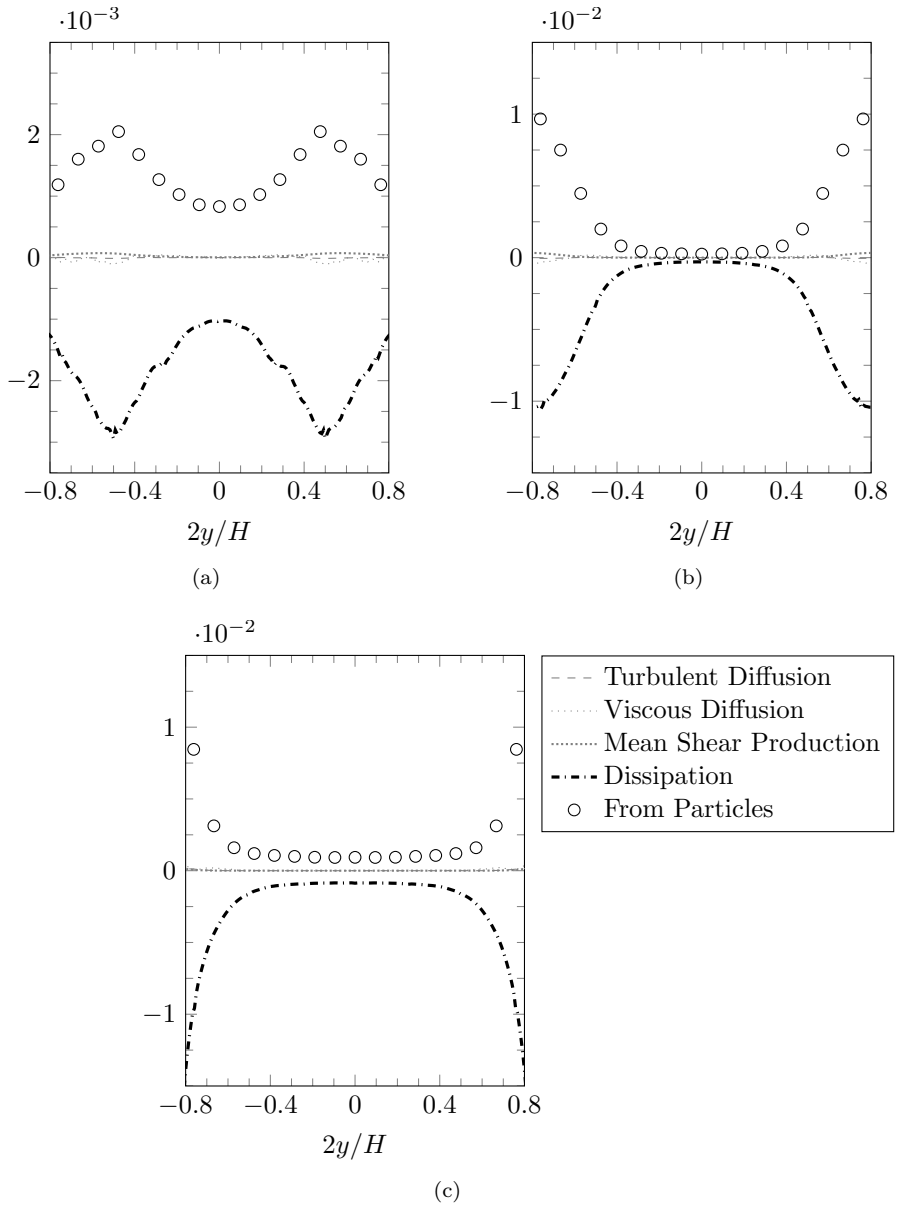

Figure 3.40: Fluid fluctuating kinetic energy budget for the cases M1 (a), M2 (b) and M3 (c). All terms are dimensionless by dividing with H/V_w^3.

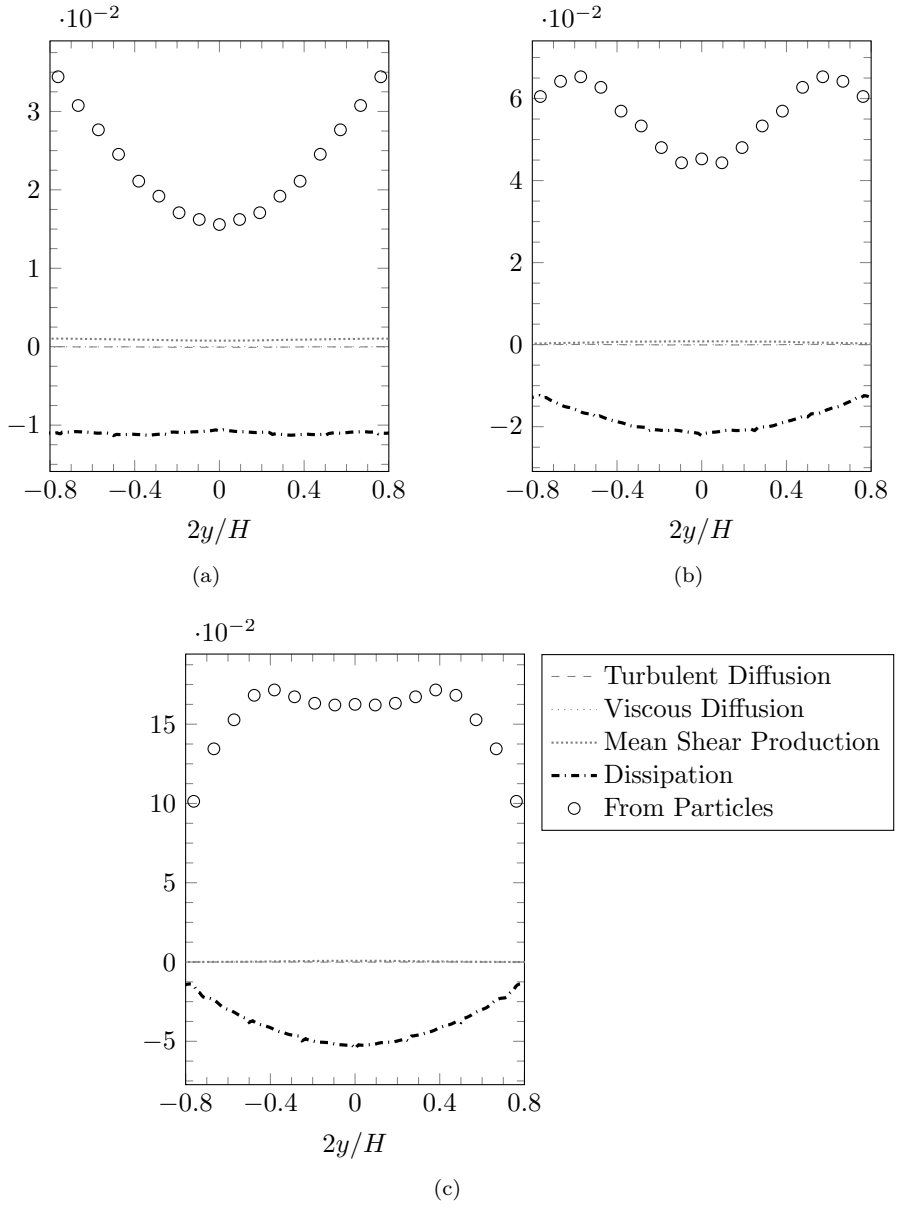

Figure 3.41: Fluid fluctuating kinetic energy budget for the cases M4 (a), M5 (b) and M6 (c). All terms are dimensionless by dividing with H/V_w^3.

3.5.3 Particle fluctuating kinetic energy budget

The transport equation of the particle fluctuating kinetic energy can be obtained from the particle kinetic stress equation, and it was given by Eq. (2.41). For our configuration with the mono-disperse cases, can be written as follows:

$$\frac{\partial q_{\mathrm{p}}^2}{\partial t} = \underbrace{-\frac{1}{2n_{\mathrm{p}}}\frac{\partial\left(n_{\mathrm{p}}S_{\mathrm{p},iiy}\right)}{\partial y}}_{D} \underbrace{-R_{\mathrm{p},xy}\frac{\partial U_{\mathrm{p},x}}{\partial y}}_{P} + \underbrace{\left\langle \frac{F_{\mathrm{f}\to\mathrm{p},i}}{m_{\mathrm{p}}}u'_{\mathrm{p},i}\right\rangle}_{F} + \underbrace{\left\langle \frac{F_{\mathrm{p}'\to\mathrm{p},i}}{m_{\mathrm{p}}}u'_{\mathrm{p},i}\right\rangle}_{C_{\mathrm{pp}}} \quad (3.36)$$

Note that the budget is composed of four main terms: terms: a diffusive, D, a production term by the mean shear, P, a particle-fluid term, F, and finally an inter-particle collision term, C_{pp}. The separation of the terms in the budget is an important tool to understant local physical phenomena related to the production, transport or dissipation of the particle variance.

First, we show the budgets of q_{p}^2 for the cases with high inertia on the Figure 3.42. It is interesting to note that the main mechanisms of particle fluctuating kinetic energy creation are the production by the mean shear and the particle-particle interaction term. The later, is in fact related to the third term on the right-hand side of Eq. (2.76), which is directly proportional to the collision flux and the mean shear as well. Note that as the particle volume fraction augments, from Figure 3.42(a) to Figure 3.42(c), the production due to the particle-particle interaction becomes more dominant. This results from the fact that the collision flux on the case with higher volume fraction becomes more important.

We observe that the main mechanism of particle fluctuating energy dissipation is the friction with the fluid-phase, as observed in all the budgets. In addition, we note that diffusive term is slightly negative at the centre of the core flow and slightly positive near the wall, indicating a diffusive transport from the centre towards the walls. The order of magnitude of the diffusive term however is very small, with a almost negligible effect on the budgets. Also, the sum of the terms is near zero, demonstrating that the budget is closed.

With respect to the cases of small inertia, the budgets are given on the Figure 3.43. Similarly to the cases with high inertia, both the production by the mean shear and the particle-particle interaction are the main effects of creation of particle fluctuating kinetic energy. The levels of production however are much smaller. Note that while the order of magnitude of the non-dimensional budgets for the high inertia is 10^{-3}, the budgets for the low inertia are in the order of about $10^{-4} \sim 10^{-5}$. This is one of the main reasons related to the macroscopic transition observed from cases with low to high inertia. In fact, there is a competition between the action of the fluid pushing the particles to the center, and the agitation of the particles that counterbalances this effect. The cases with small inertia are not able to produce enough particle fluctuating kinetic energy and for that reason there is a collapse of the particles near the center of the core flow.

Moreover, this is precisely the reason why the Stokes number, defined in relation to the characteristic time-scale of the mean-shear, is a pertinent non-dimensional number characterizing the transition. Indeed, both the kinetic production and the collisional production are proportional to the mean shear. With

higher Stokes numbers relating to higher productions of particle fluctuating kinetic energy and the inverse for the lower Stokes numbers.

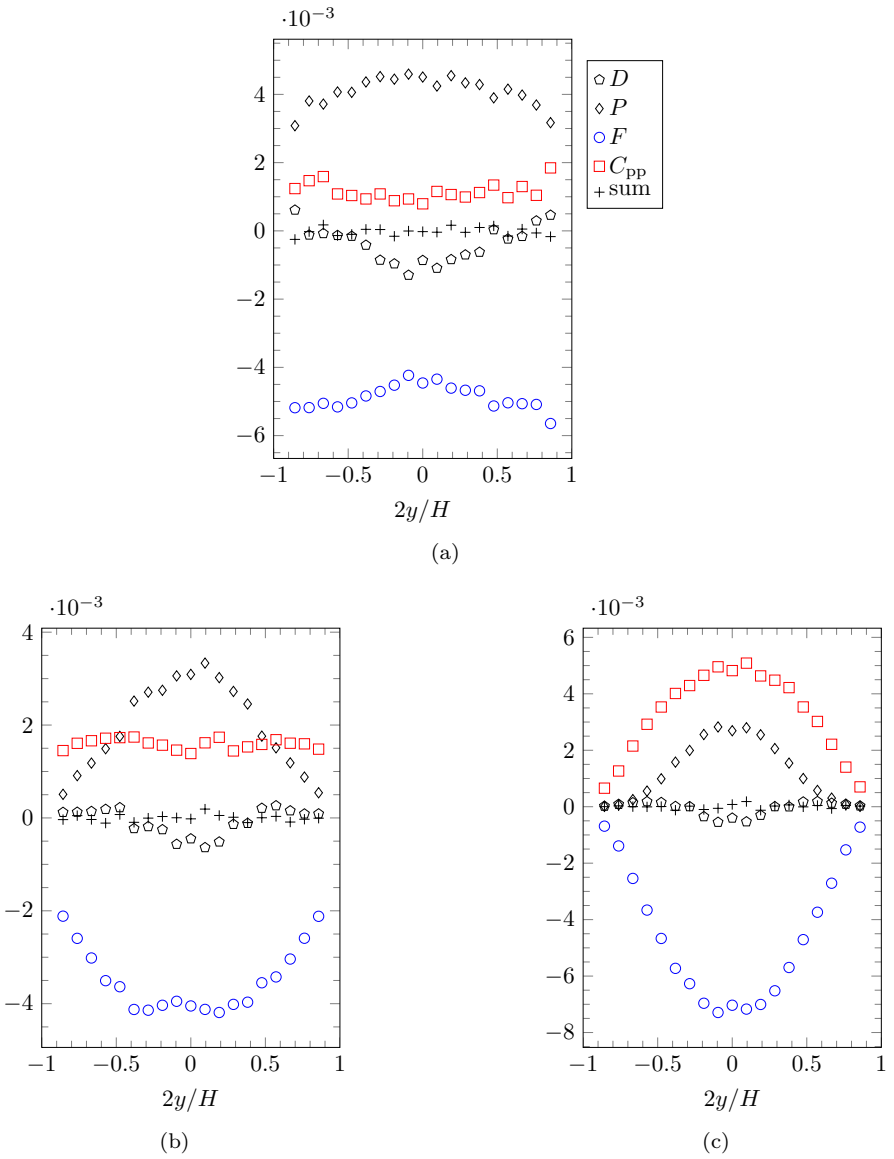

Figure 3.42: Particle fluctuating kinetic energy budget: q_{p}^2, for the cases M4 (a), M5 (b) and M6 (c). All terms are dimensionless by dividing with H/V_w^3.

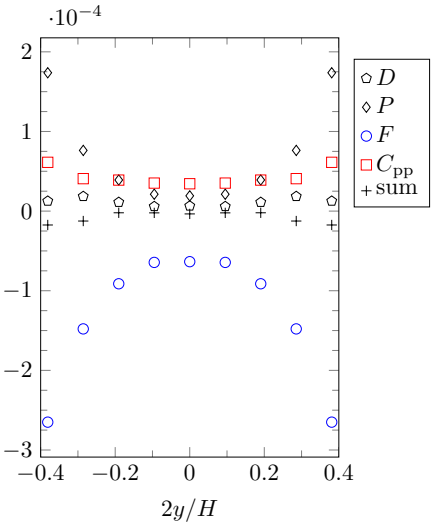

(a)

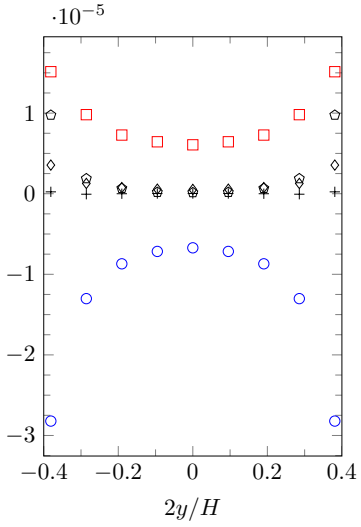

(b)

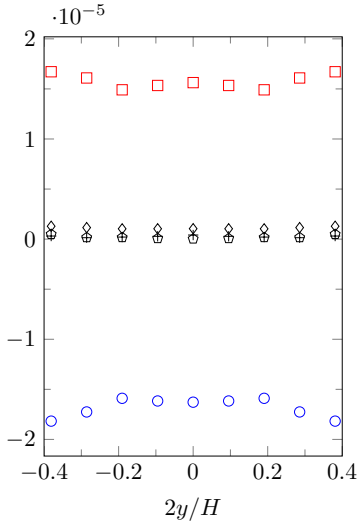

(c)

Figure 3.43: Particle fluctuating kinetic energy budget: q_{p}^2, for the cases M1 (a), M2 (b) and M3 (c). All terms are dimensionless by dividing with H/V_w^3.

3.5.4 Particle kinetic stress budget

Diagonal components of the Particle kinetic stresses

The transport equation of the particle kinetic stress, for the mono-disperse cases are given by Eq. (2.40). Analogously to the transport equation of q_{p}^2 in the last subsection, four main terms are found on the budget.

$$\frac{\partial R_{\mathrm{p},ij}}{\partial t} = \underbrace{-\frac{1}{n_{\mathrm{p}}}\frac{\partial\left(n_{\mathrm{p}}S_{\mathrm{p},ijy}\right)}{\partial y}}_{D} \underbrace{-R_{\mathrm{p},iy}\frac{\partial U_{\mathrm{p},j}}{\partial y} - R_{\mathrm{p},jy}\frac{\partial U_{\mathrm{p},i}}{\partial y}}_{P} \underbrace{+\left\langle\frac{F_{\mathrm{f}\to\mathrm{p},i}}{m_{\mathrm{p}}}u'_{\mathrm{p},j}\right\rangle + \left\langle\frac{F_{\mathrm{f}\to\mathrm{p},j}}{m_{\mathrm{p}}}u'_{\mathrm{p},i}\right\rangle}_{F} \underbrace{+\left\langle\frac{F_{\mathrm{p}'\to\mathrm{p},i}}{m_{\mathrm{p}}}u'_{\mathrm{p},j}\right\rangle + \left\langle\frac{F_{\mathrm{p}'\to\mathrm{p},j}}{m_{\mathrm{p}}}u'_{\mathrm{p},i}\right\rangle}_{C_{\mathrm{pp}}}$$

In the previous subsection, the balance of q_{p}^2 revealed local physics related to the production and dissipation of the total fluctuating energy of the particles. In this subsection, we analyze the budgets of the diagonal terms of the particle kinetic stress tensor, which can elucidate the mechanisms of fluctuating energy creation and destruction in each particular direction, as well as the fluctuating energy transfer from one direction to another. First, we analyze the budgets for the cases with high inertia and then for all the cases with small inertia.

To begin, the budgets of the case M4 are given by Figure 3.44. Regarding the production term, we show that the only direction under which there is a production of variance by the mean shear, P, is on the stream-wise direction, see Figure 3.44(a). This is due to the fact that the only non null gradient of mean velocity $\partial U_{\mathrm{p},x}/\partial y$ is on that direction.

With respect to the particle-particle interaction term, C_{pp}, we note that it is negative for the budget of particle kinetic stress tensor $R_{\mathrm{p},xx}$ and positive for the other two $R_{\mathrm{p},yy}$ and $R_{\mathrm{p},zz}$. This indicates that globally, there is transfer of particle fluctuating kinetic energy from the stream-wise direction to the other directions, that is, wall-normal and span-wise directions. In fact the collision term is a result of the sum of the effects shown in Eq. (2.76). In the stream-wise direction, probably the dominant effect is the one related to the redistribution term, being dominantly negative due to the drain of fluctuating energy by the other directions. This drainage in the stream-wise is then redistributed to the other orthogonal directions, via the same redistribution collisional effect, with this being then the only production mechanisms in those directions. This redistribution mechanisms has also been observed by [4], and may be called an isotropization effect, since it brings the diagonal terms of the particle kinetic stresses closer to an isotropic state.

Analogously to the budget of the particle fluctuating kinetic energy, a slightly negative diffusive term, D, in the centre of the core flow, is indicating a transport of the particles from the centre towards the walls. The fluid term, F, is negative in all the budgets, indicating dissipation through fluid friction of the other production mechanisms.

The budgets show that the fluctuating kinetic energy is mainly created in the stream-wise direction via the mean shear production mechanism and then redistributed to the other direction via particle-particle interactions, and a those effects are counterbalanced by the fluid friction.

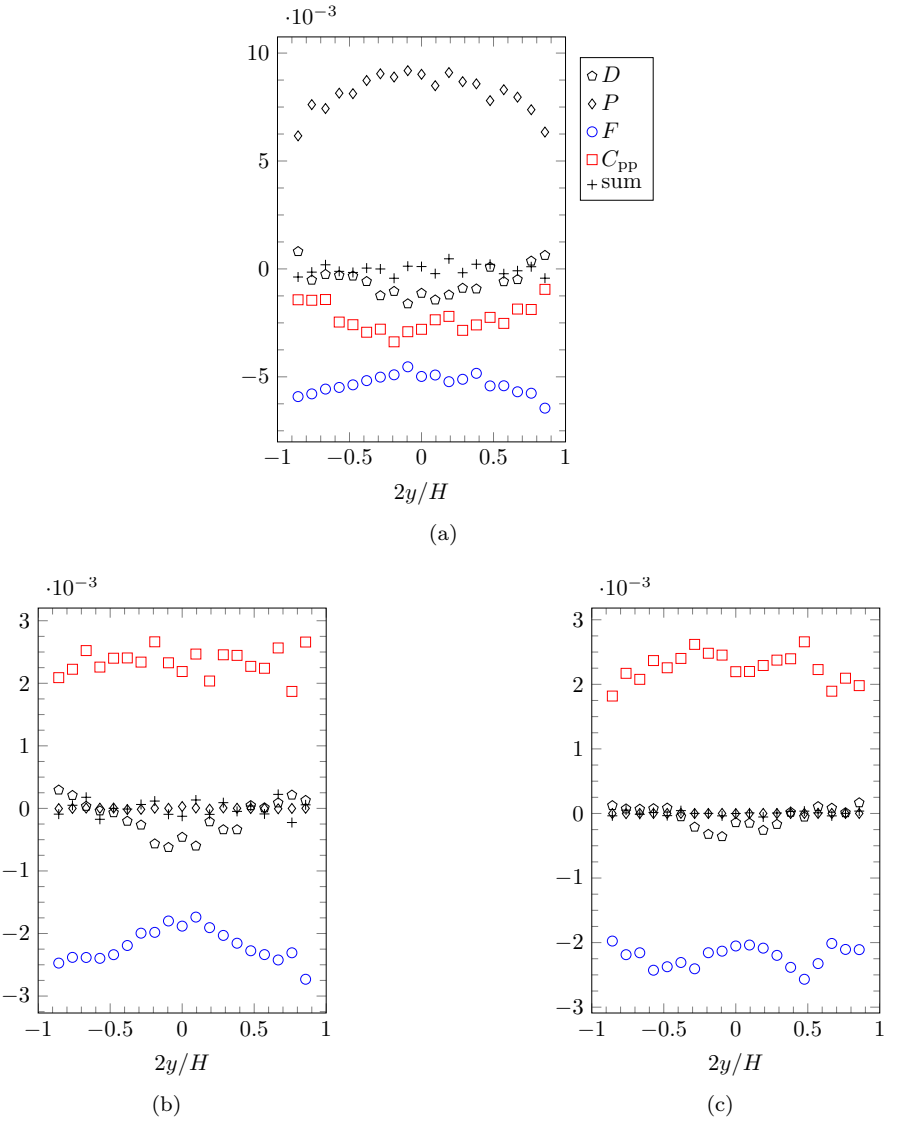

Figure 3.44: Budgets of the diagonal terms of the particle kinetic stress tensor for the case M4. $R_{\mathrm{p},xx}$ (a), $R_{\mathrm{p},yy}$ (b) and $R_{\mathrm{p},zz}$ (c).

Remaining on the group with relatively higher inertia, the other denser cases, M5 and M6, have similar budgets for the diagonal particle kinetic stresses. They are respectively shown by Figure 3.45 and 3.46. The only difference is on the budgets of $R_{\mathrm{p},xx}$, where the collision term, C_{pp}, exhibits positive values near the wall for the case M5, see Figure 3.45(a), and in the whole domain for the case M6, see Figure 3.46(a). This is related to the fact that the collision production, precisely the third term in Eq. (2.76), becomes more dominant than the redistribution component in the zones of higher particle volume fraction, which is the case in the cited zones.

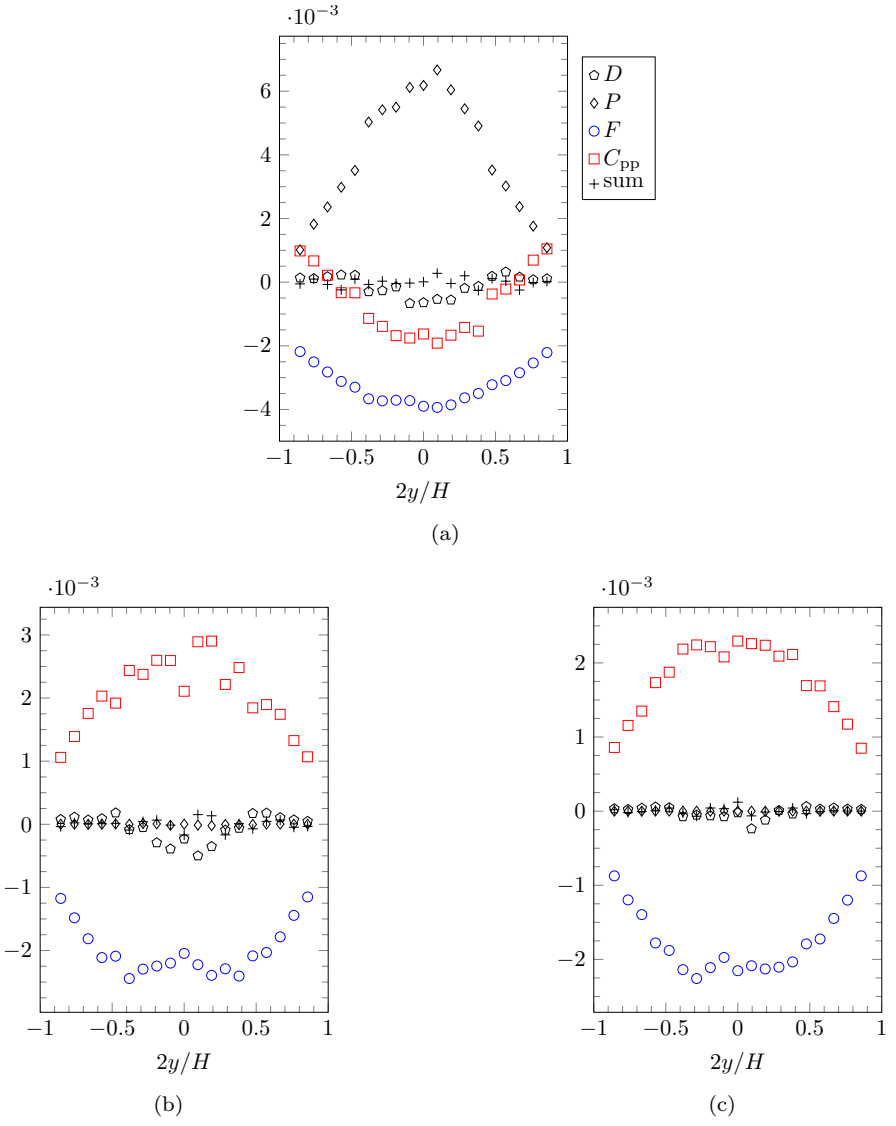

Figure 3.45: Budgets of the diagonal terms of the particle kinetic stress tensor for the case M5. $R_{\mathrm{p},xx}$ (a), $R_{\mathrm{p},yy}$ (b) and $R_{\mathrm{p},zz}$ (c).

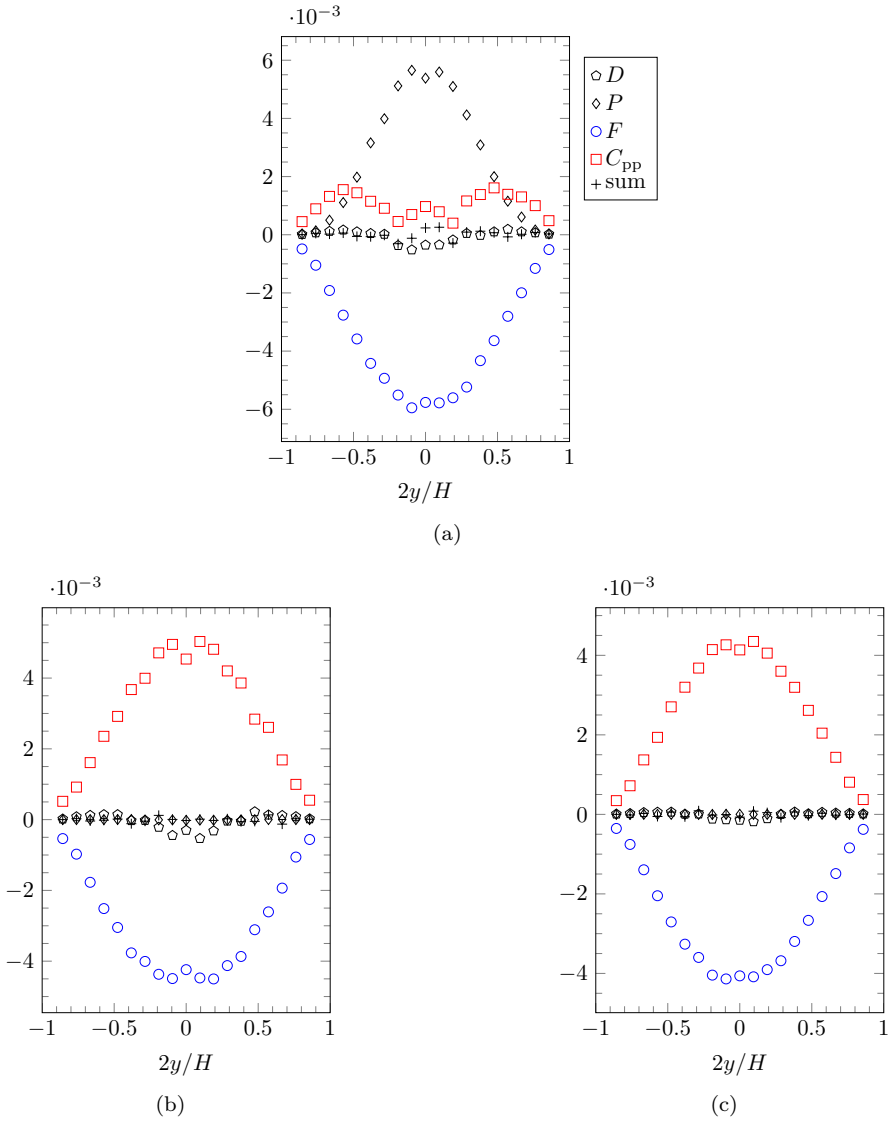

Figure 3.46: Budgets of the diagonal terms of the particle kinetic stress tensor for the case M6. $R_{\mathrm{p},xx}$ (a), $R_{\mathrm{p},yy}$ (b) and $R_{\mathrm{p},zz}$ (c).

With respect to the cases M1, M2 and M3, similarly to the q_{p}^2 budget, the figures are shown in the centre of the core flow. The budgets for the case M1, are given by Figure 3.47. Similarly to the other cases discussed before in the text, the production by the mean shear is, as expected, only present in the budget related to the stream-wise direction. Also, the fluid term is negative for all the components, due to the dissipation via fluid friction. The diffusive term, although very small, is slightly positive near the center of the core flow which is the opposite of the cases with higher inertia, indicating that there is a diffusive transport of particle kinetic stress towards the center of the core flow. Besides a similar redistribution mechanism to the wall-normal and span-wise direction via the particle-particle interactions is observed as well.

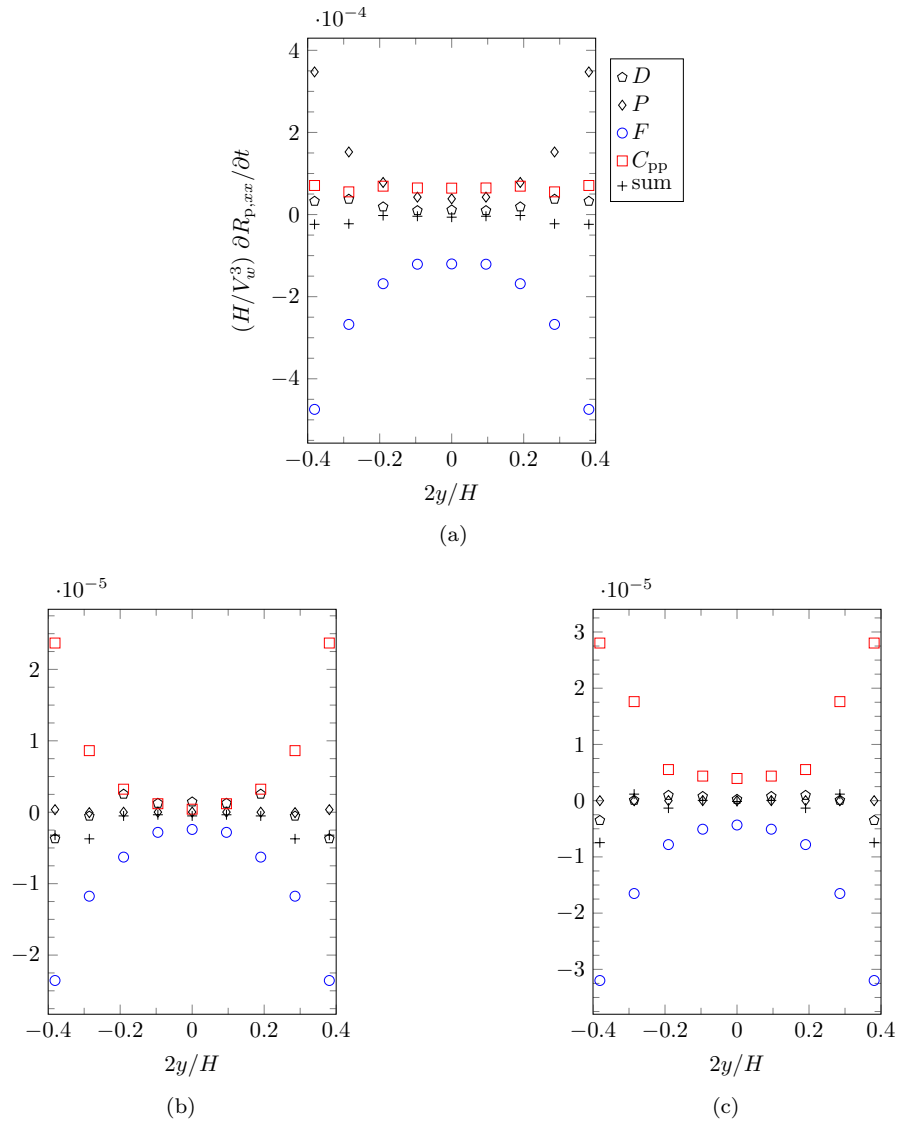

Figure 3.47: Budgets of the diagonal terms of the particle kinetic stress tensor for the case M1. $R_{\mathrm{p},xx}$ (a), $R_{\mathrm{p},yy}$ (b) and $R_{\mathrm{p},zz}$ (c).

Regarding the cases M2 and M3, the graphs for those budgets are respectively depicted by Figure 3.48 and 3.49. A similar behavior, particle-particle interaction terms are more dominant with respect to the others, for the same reasons as explained for the cases with high inertia.

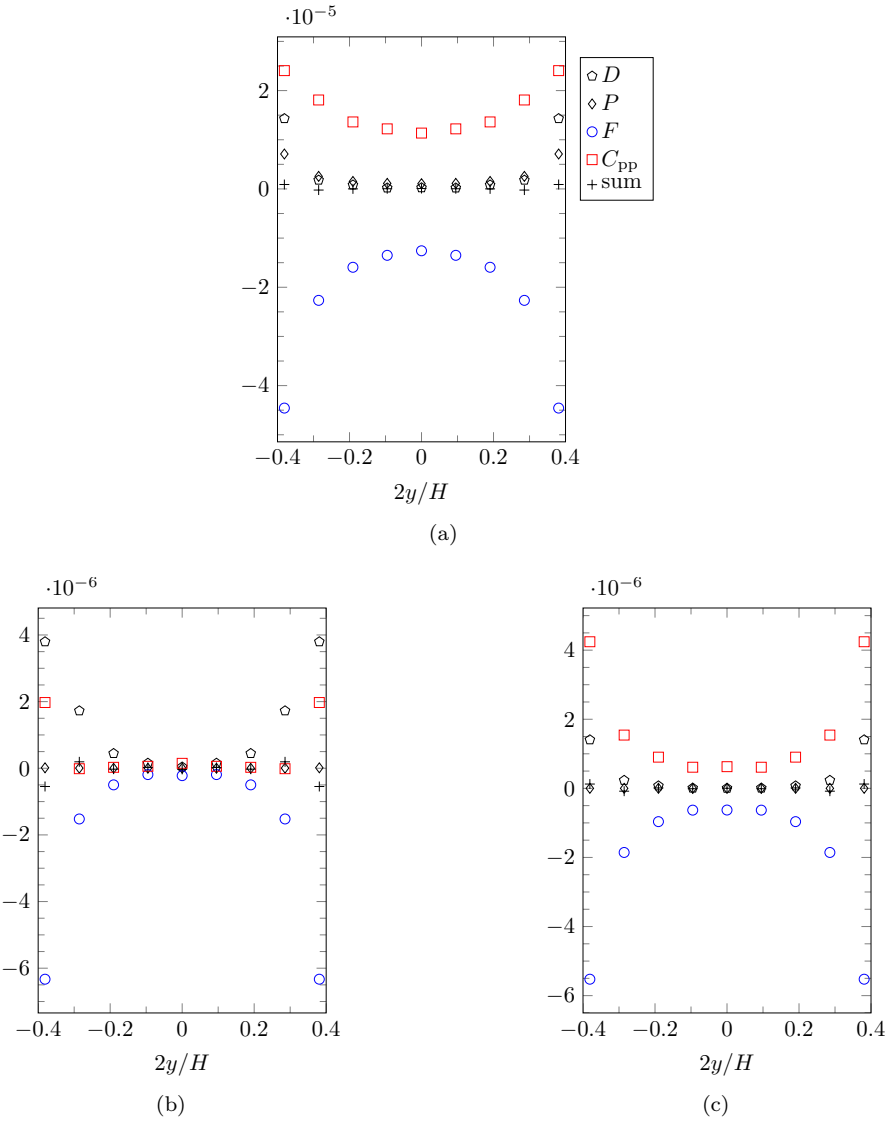

Figure 3.48: Budgets of the diagonal terms of the particle kinetic stress tensor for the case M2. $R_{\mathrm{p},xx}$ (a), $R_{\mathrm{p},yy}$ (b) and $R_{\mathrm{p},zz}$ (c).

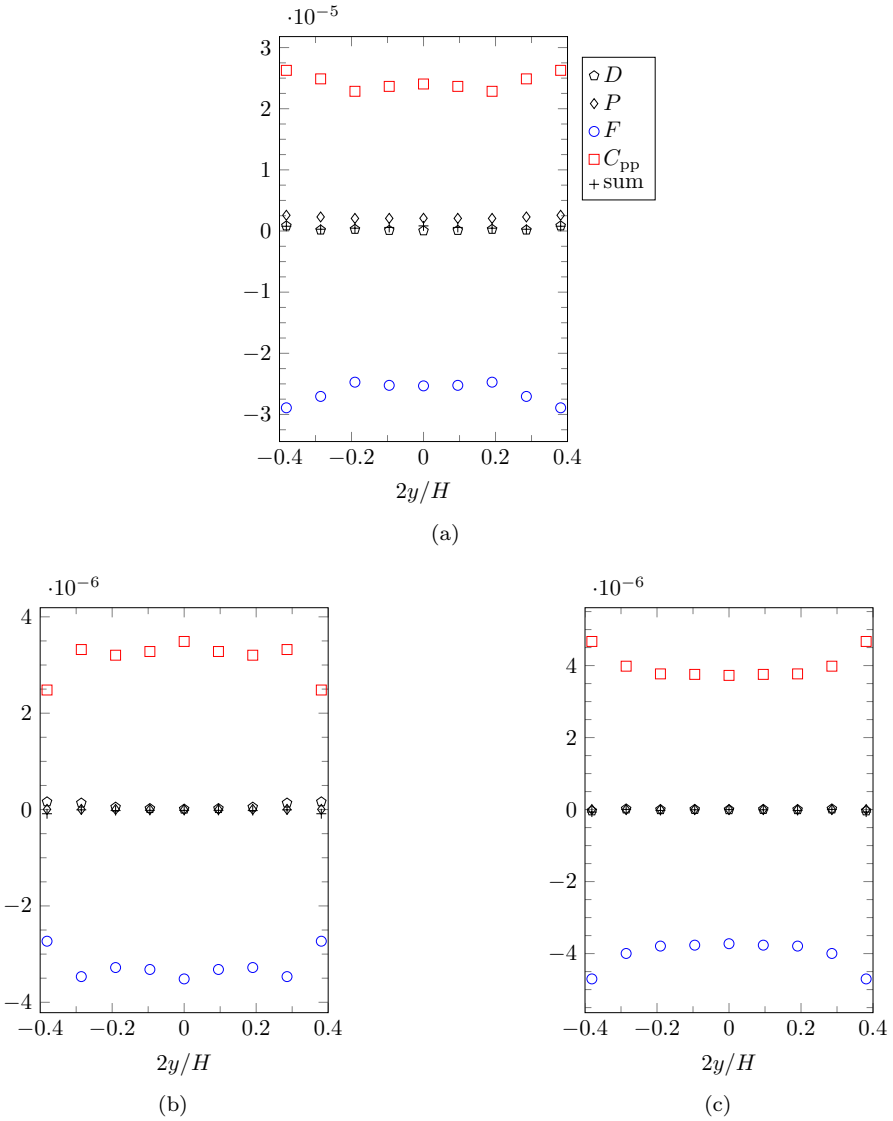

Figure 3.49: Budgets of the diagonal terms of the particle kinetic stress tensor for the case M3. $R_{\mathrm{p},xx}$ (a), $R_{\mathrm{p},yy}$ (b) and $R_{\mathrm{p},zz}$ (c).

Particle shear kinetic stress budget

The transport equations for the particle shear kinetic stresses for our monodisperse cases are also given by Eq. (3.37). In our cases, the only non zero particle kinetic shear stress, is the component: $R_{\mathrm{p},xy}$.

The budgets of $R_{\mathrm{p},xy}$, for the cases M4, M5 and M6 are given by Figure 3.50. On the contrary to the other presented budgets, since $R_{\mathrm{p},xy}$ is negative the productions terms are negative on this budget and positive terms are the destruction terms. Essentially, while production terms are simply the mechanisms leading to the creation of the shear kinetic stresses, the destruction terms can be also perceived as terms that favors the homogenization of the particle flow, since they are pushing the system back, to a state without shear stresses.

We note that the production by the mean shear is the main cause of particle kinetic shear stress creation. Furthermore, in all the cases, the fluid term, is the one mainly stopping the creation of that shear stress through the action of friction. Besides, we note that the diffusive term, has an homogenization effect near the centre for all the cases. Regarding the term due to particle-particle interaction, we note that it mostly brings the system closer to the homogeneous state in the center of the core flow, and some production is observed near the walls for the cases M5 and M6, which is due to the fact that the collision flux is much larger in these zones due to the higher particle volume fraction in these zones. Related to that, we will further discuss in the next chapter the fact that some terms in decomposition of the partile-particle term, see Eq. (2.76), bring the system closer to an isotropic state, whereas others do not.

With respect to the cases of low inertia, the budgets are shown by Figure 3.51. Similarly to the previous cases, the fluid term is the main physical mechanism of shear kinetic stress destruction through friction. Regarding the production of shear kinetic stress on the other hand, there is a transition between a mean shear production dominated regime in case M1, to a production by inter-particle interaction in case M3. This is simply due to the fact that the collision flux becomes dominant against the kinetic production by the mean shear, similarly to what happens in other budgets, where there is a competition between these two production terms.

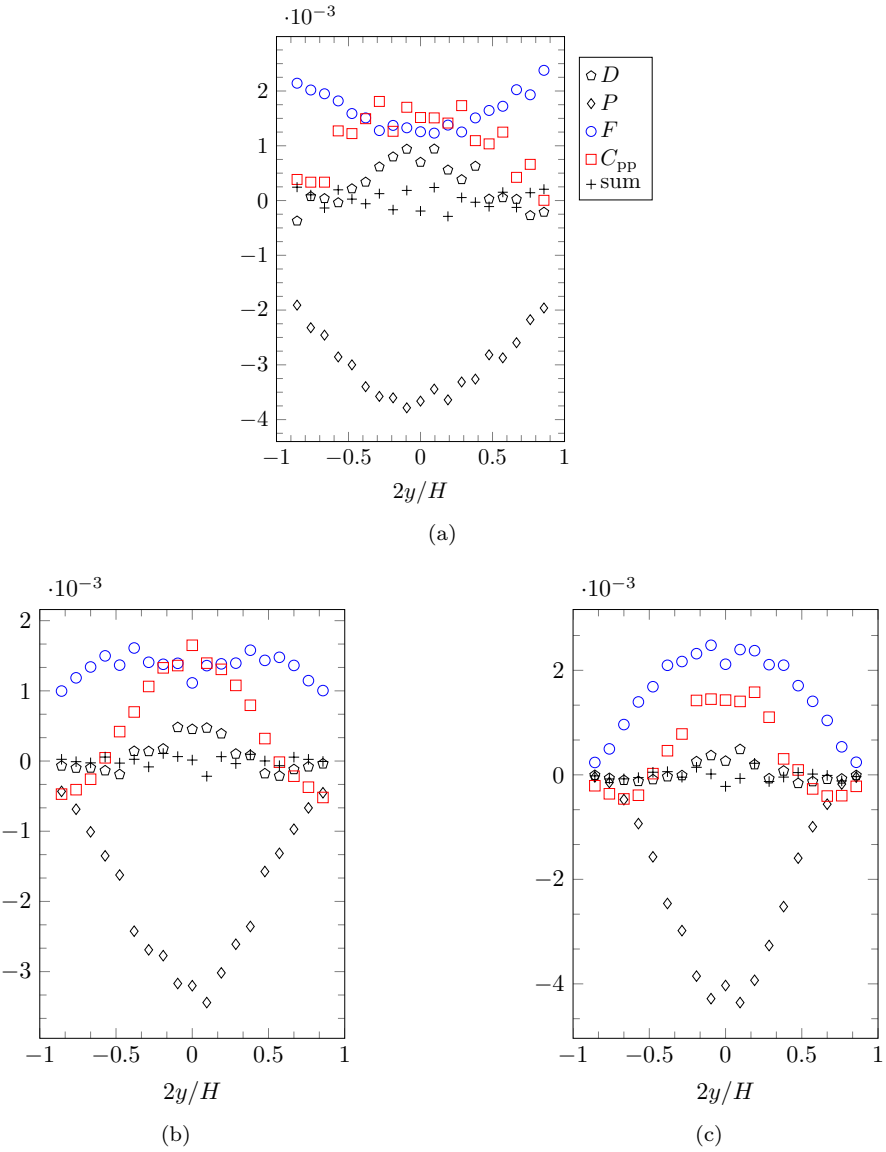

Figure 3.50: Particle shear kinetic stress budget: $R_{\mathrm{p},xy}$, for the case (a) M4, (b) M5 and (c) M6.

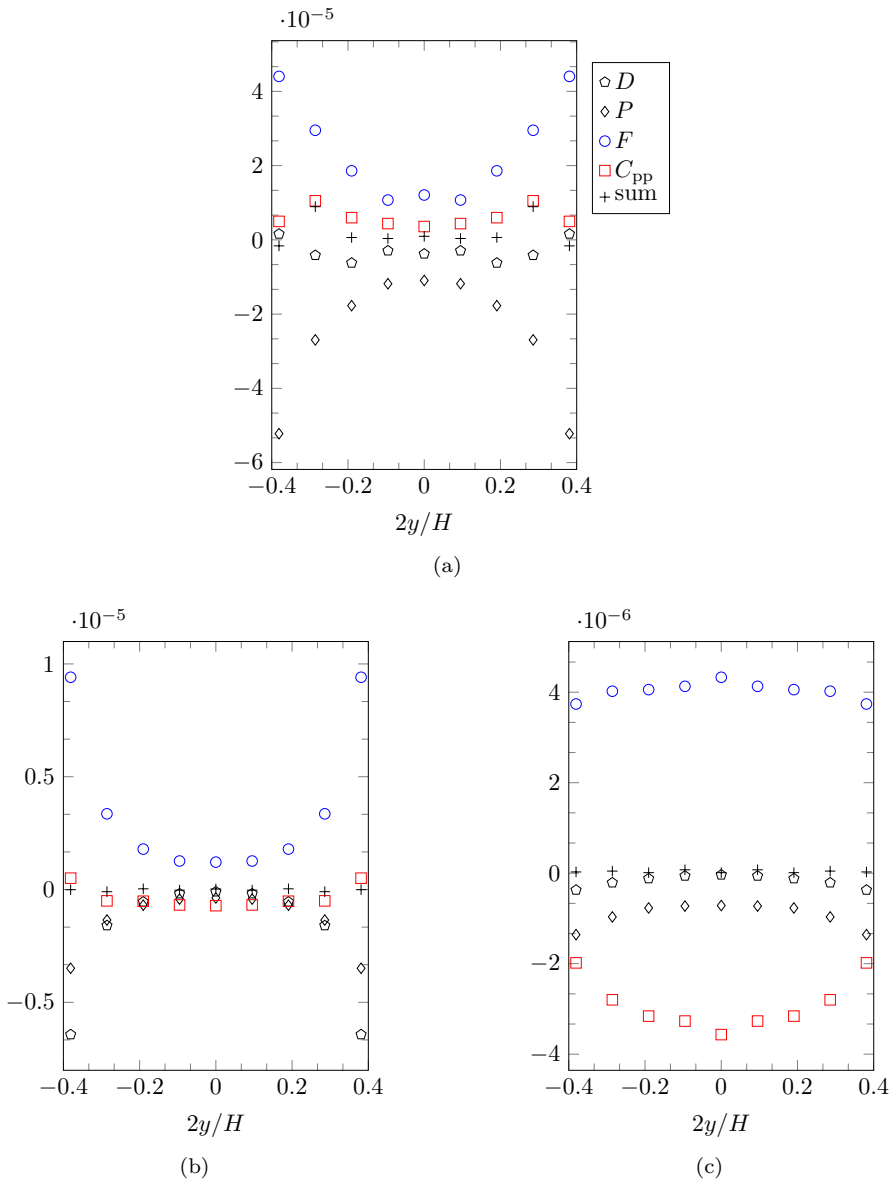

Figure 3.51: Particle shear kinetic stress budget: $R_{\mathrm{p},xy}$, for the case (a) M1, (b) M2 and (c) M3.

3.6 Fluid-Particle interaction modeling

The force on a particle immersed in a viscous fluid can be calculated by means of the integration of the viscous stress tensor $\sigma_{\mathrm{f},ij}$, at the surface of the particle S_p, with a unity vector $n_{\mathrm{p},j}$ pointing outwards the surface, as follows:

$$F_{\mathrm{f}\to\mathrm{p},i} = \int_{S_\mathrm{p}} \sigma_{\mathrm{f},ij} n_{\mathrm{p},j} dS \tag{3.37}$$

In order to compute such integral, the numerical simulation need to be resolved enough. In some types of fluid-particle simulation approaches however, the characteristic mesh size is not resolved enough or even larger than the particle diameter, and for that reason, there is a need for modeling of that force. This is the case in the point-particle approach simulations [52], where the particle diameter is smaller than the characteristic mesh size. We can also cite the case of DEM/CFD approach [74], where the mesh is generally two to three times the size of the particle diameter. In the next sections we discuss the ways of modeling this force.

3.6.1 Instantaneous fluid force on an isolated particle

Several authors investigated the derivation of an analytic expression for the force. One of the first studies, was performed by Stokes, who derived an expression for the drag past a sphere in a creeping flow [109]. Next, particle motion in a fluid were also investigated by [6, 12, 76], and later studied by [24] and [75], followed by [67] and [39], who compiled the latest developments at the time and performed a derivation of the equation of motion of particles, at small Reynolds numbers in non-homogeneous flow.

For the derivation, the authors consider an undisturbed fluid flow field $\breve{\boldsymbol{u}}_\mathrm{f}$, and the solution of the fluid flow due to the perturbation of a single particle with center position $\boldsymbol{x}_\mathrm{p}$, moving with velocity $\boldsymbol{u}_\mathrm{p}$. With that in mind, the authors derive an equation for the fluid force $\boldsymbol{F}_{\mathrm{f}\to\mathrm{p}}$ on a particle in non-homogeneous flow, relating the undisturbed fluid flow field and the Lagrangian variables of the particle. The authors also define $\boldsymbol{v}_r = \boldsymbol{u}_\mathrm{p} - \breve{\boldsymbol{u}}_\mathrm{f}$, as being the relative velocity of the particle to the undisturbed flow field. So provided that the particle Reynolds number $Re_\mathrm{p} = \rho_\mathrm{p} d_\mathrm{p} |\boldsymbol{v}_r| / \mu_\mathrm{f}$ is small and under the condition that the particle size is smaller than the fluid scales. The derived equation writes as:

$$\begin{aligned} \boldsymbol{F}_{\mathrm{f}\to\mathrm{p}} = & \underbrace{-\frac{m_\mathrm{p}}{\rho_\mathrm{p}}\left(-\nabla p + \nabla\cdot\underline{\underline{\boldsymbol{\sigma}_\mathrm{f}}}\right)}_{\text{undisturbed contribution}} \underbrace{-\frac{18\mu_\mathrm{f}}{\rho_\mathrm{p} d_\mathrm{p}^2} m_\mathrm{p} \boldsymbol{v}_r}_{\text{drag force}} \\ & \underbrace{-\frac{1}{2} m_\mathrm{f} \frac{d\boldsymbol{v}_r}{dt}}_{\text{added mass force}} \underbrace{-9\sqrt{\frac{\rho_\mathrm{f}\mu_\mathrm{f}}{\pi}} \frac{m_\mathrm{p}}{\rho_\mathrm{p} d_\mathrm{p}} \left(\int_0^t \frac{\frac{d\boldsymbol{v}_r}{dt}}{(t-t^*)} dt^* \right)}_{\text{history force}} \end{aligned} \tag{3.38}$$

Where m_f is the added fluid mass, for a sphere it may be calculated as $m_\mathrm{f} = \rho_\mathrm{f} \pi d_\mathrm{p}^3 / 12$. Regarding the terms in Eq. (3.38), the first term is associated with the undisturbed fluid flow contribution, whereas the other three terms are

due to the particle perturbation in the fluid flow. The first term can also be linked with buoyancy effects. The drag term is due to the fluid friction caused by relative motion between the fluid and the particle. The third term relates to added mass effects and finally the last term is related to the history of the particle motion, also known as Basset force.

Considering a spherical particle, with mass mass is $m_\mathrm{p} = \rho_\mathrm{p}\pi d_\mathrm{p}^3/6$, in the limit where the particle density ρ_p is much larger than the fluid density ρ_f, it can be shown that the only relevant term in Eq. (3.38) is the drag term:

$$\boldsymbol{F}_{\mathrm{f}\to\mathrm{p}} = -3\mu_\mathrm{f}\pi d_\mathrm{p}\boldsymbol{v}_r \tag{3.39}$$

This force is generally used as normalization factor when dealing with fluid forces in particles. Since it coincides with the solution obtained by Stokes, it is also sometimes called by his name. Besides, for a sphere, the resistant force contrary to the direction of the relative velocity can be referred with the drag coefficient C_D, as follows:

$$C_D = \frac{|\boldsymbol{F}_{\mathrm{f}\to\mathrm{p}} \cdot \boldsymbol{n}_r|}{\pi d_\mathrm{p}^2 \rho_\mathrm{f} |\boldsymbol{v}_r|^2/8} \tag{3.40}$$

Where $\boldsymbol{n}_r = \boldsymbol{v}_r/|\boldsymbol{v}_r|$ is the direction of the relative velocity. For a sphere, it can be easily shown that, within the conditions of validity of Eq. (3.39), the drag coefficient becomes $C_D^\mathrm{St} = 24/\mathrm{Re}_\mathrm{p}$.

Figure 3.52, adapted from [25], depicts the experimental results for the drag coefficient of a spherical particle as function of the Reynolds number. The symbols are the experimental values. Note that, the straight line corresponding to the drag coefficient in the limiting case of the Stokes solution is a good approximation only for small Reynolds numbers. The red dashed curve corresponds to the fit correlation established by [96]. This approximation is valid for $Re_\mathrm{p} < 10^3$. The regime that follows, at the blue dotted line, corresponds to a plateau of approximately $C_D \sim 0.44$, and it is called the Newton regime. Near the end, follows a substantial drop in the drag coefficient near $Re_\mathrm{p} \sim 10^5$.

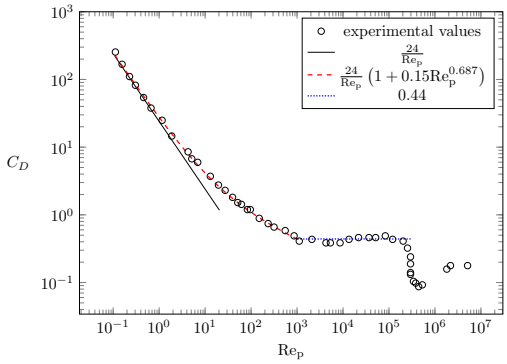

Figure 3.52: Drag coefficient for a spherical particle as function of the particle Reynolds number. Adapted from [25].

It is also known that spinning balls moving in a viscous fluid experience a transverse force. In sports such as soccer and tennis, this force usually is

associated with curved trajectories of the ball. This lift force is denoted Magnus force due to the experimental observations of that force in rotating cylinders made by Magnus [5]. In very large particle Reynolds number, the lift force is due to flow separation whereas in the range of low Reynolds numbers, the lift is mainly generated by the pressure difference on opposite sides of the spinning particle [131]. For the latter case, this force has been theoretically calculated by [90], as follows:

$$\boldsymbol{F}_L^{\text{Magnus}} = \frac{\pi d_\text{p}^3 \rho_\text{f}}{8} \boldsymbol{\omega}_\text{p} \times \boldsymbol{v}_r \tag{3.41}$$

For a freely rotating particle, [92] pointed out that the particle angular velocity can be approximated by half of the local mean fluid shear velocity. Moreover, Saffman showed that for a sphere in a linear unbounded shear flow, in the limit of small Reynolds numbers, in addition to the Magnus lift that is related to particle rotation, another term related to the fact that the particle is immersed in a fluid shear takes place, which in the first order writes [54, 126]:

$$\boldsymbol{F}_L^{\text{Saff}} \quad = \quad -1.61 \rho_\text{f} d_\text{p}^2 \boldsymbol{v}_r \ \text{sign}\left(\dot{\gamma}\right) \sqrt{|\dot{\gamma}| \, \nu_\text{f}} \tag{3.42}$$

Where $\dot{\gamma}$ is the gradient of mean fluid velocity, or mean fluid shear. The function sign is equal to sign of the function argument, thus being either one or minus one. For a particle moving in the x-direction, with a shear augmenting in the y direction, if $\boldsymbol{v}_r$ is negative, then the force is in y direction, whereas if the $\boldsymbol{v}_r$ is positive, then force is in the opposite direction.

Similarly to the drag coefficient, the lift force can also be put in terms of a lift coefficient C_L which is defined as the lift force divided by $\pi d_\text{p}^2 \rho_\text{f} |\boldsymbol{v}_r|^2/8$. The lift coefficient is generally expressed as a function of the particle Reynolds number, a non-dimensional shear number $Sr \ = \ \dot{\gamma} d_\text{p} / \left|\boldsymbol{v}_r\right|$, and a dimensionless distance to the wall in confined situations. A recent review on the lift coefficients can be found in [98].

3.6.2 Mean fluid-particle force on an ensemble of particles

The assumptions under which the equations of last section were derived rely on the definition of an undisturbed fluid flow field and the presence of an isolated particle. In fact [67] stated that the particle should be far isolated from other particles and other disturbances, such as the wall, in order to be in the exact frame under which Eq. (3.38) was derived. Otherwise the equation is no-longer valid. In addition to that, the definition of the relative velocity itself is closely tied to the assumption of an undisturbed fluid flow.

In the case where there are an ensemble of particles in a relatively close distance to one another, the notion of an undisturbed flow field is not clear, since several particles are perturbing the flow field simultaneously. In our simulations, the volume fraction ranges from about 2% to 47%, see Figure 3.4, hence the average distances between particles in such volume fractions range from about one to two diameters away from each other.

Fixed array of particles

In order to access and study the drag in the frame of an ensemble of particles, direct numerical simulations of a fluid flow past a fixed array of spheres have been performed, see for example [7, 111] and [114]. With such simulations, it is possible to analyze the mean force and its dependence notably as a function of the particle Reynolds number, often based on the macroscopic relative velocity, and the local particle volume fraction. Using dimensional analysis, the average force in an isotropic and statically homogeneous distribution of particles can be written in a general manner as follows:

$$\langle \boldsymbol{F}_{\mathrm{f}\to\mathrm{p}} \rangle = -3\pi\mu_{\mathrm{f}} d_{\mathrm{p}} \alpha_{\mathrm{f}} \boldsymbol{V}_r \tilde{F}^*_{\mathrm{f}\to\mathrm{p}} \left(\tilde{\boldsymbol{n}}_r, \alpha_{\mathrm{f}}, Re_{\mathrm{p}}, \nabla \tilde{P}_{\mathrm{f}}, St_{\mathrm{p}} \right) \tag{3.43}$$

Where $\tilde{F}^*_{\mathrm{f}\to\mathrm{p}}$ is a non-dimensional force function, $\boldsymbol{V}_r = \boldsymbol{U}_{\mathrm{p}} - \boldsymbol{U}_{\mathrm{f}}$ is the mean macroscopic relative velocity, $\tilde{\boldsymbol{n}}_r = \boldsymbol{V}_r / |\boldsymbol{V}_r|$ is the unity vector aligned with $\boldsymbol{V}_r$. The Reynolds number based on the average relative velocity is $Re_{\mathrm{p}} = |\boldsymbol{V}_r| d_{\mathrm{p}} \rho_{\mathrm{f}} / \mu_{\mathrm{f}}$, the non-dimensional pressure gradient is written as $\nabla \tilde{P}_{\mathrm{f}} = \nabla P_{\mathrm{f}} / \left[\mu_{\mathrm{f}} |\boldsymbol{V}_r| / d_{\mathrm{p}}^2 \right]$ and finally the Stokes number based on the average relative velocity is $St_{\mathrm{p}} = |\boldsymbol{V}_r| d_{\mathrm{p}} \rho_{\mathrm{p}} / \mu_{\mathrm{f}}$.

Supposing that the gradient contribution could be linearly separated from the general form of Eq. (3.43), we can write:

$$\langle \boldsymbol{F}_{\mathrm{f}\to\mathrm{p}} \rangle = -3\pi\mu_{\mathrm{f}} d_{\mathrm{p}} \alpha_{\mathrm{f}} \boldsymbol{V}_r F^*_{\mathrm{f}\to\mathrm{p}} \left(\alpha_{\mathrm{f}}, Re_{\mathrm{p}}, St_{\mathrm{p}} \right) - \frac{\pi d_{\mathrm{p}}^3}{6} \frac{\nabla P_{\mathrm{f}}}{\rho_{\mathrm{f}}} \tag{3.44}$$

In the case where the ensemble of particles are dense, randomly distributed through space, and weakly agitated by the pseudo-turbulence generated by the wake past the particles, with relatively high inertia, there is a link between the average forces measured in an array of randomly fixed particles and the non-dimensional force function as follows:

$$F^*_{\mathrm{f}\to\mathrm{p}||} \left(\alpha_{\mathrm{f}}, Re_{\mathrm{p}} \right) = \frac{-1}{3\pi\mu_{\mathrm{f}} d_{\mathrm{p}} \alpha_{\mathrm{f}} |\boldsymbol{V}_r|} \left[\langle \boldsymbol{F}_{\mathrm{f}\to\mathrm{p}} \rangle + \frac{\pi d_{\mathrm{p}}^3}{6} \frac{\nabla P_{\mathrm{f}}}{\rho_{\mathrm{f}}} \right] \cdot \boldsymbol{n}_r \tag{3.45}$$

Note that $F^*_{\mathrm{f}\to\mathrm{p}||}$ is used to denote the part of non-dimensional force function that is related to the force parallel to the mean macroscopic velocity, and since the particles do not move on the fixed array, the Stokes number do not play a role in this limiting case. Correlations extracted from direct numerical simulations of fixed array of particles can be found in [7, 111]. Additionally, based on experimental results correlations, the following authors [32, 127] also proposed correlations. The formulas associated with those authors are summarized in the Table 3.3:

Table 3.3: Non-dimensional force as a function of α_{f} and $Re^*_{\mathrm{p}} = \alpha_{\mathrm{f}} Re_{\mathrm{p}}$.

Author	Normalized drag law ($F^*_{\mathrm{f}\to\mathrm{p}\vert\vert}$)
Wen & Yu	$F^*_{\mathrm{f}\to\mathrm{p}\vert\vert} = \left(1 + 0.15 {Re^*_{\mathrm{p}}}^{0.687}\right) \alpha_{\mathrm{f}}^{-3.65}$
Ergun	$F^*_{\mathrm{f}\to\mathrm{p}\vert\vert} = \frac{150}{18}\frac{1-\alpha_{\mathrm{f}}}{\alpha_{\mathrm{f}}^2} + \frac{7}{4}\frac{1}{18}\frac{Re^*_{\mathrm{p}}}{\alpha_{\mathrm{f}}^2}$
Beetstra et al.	$F^*_{\mathrm{f}\to\mathrm{p}\vert\vert} = \frac{10\left(1-\alpha_{\mathrm{f}}\right)}{\alpha_{\mathrm{f}}^2} + \alpha_{\mathrm{f}}^2\left(1 + 1.5\sqrt{1-\alpha_{\mathrm{f}}}\right) + \frac{0.413 Re^*_{\mathrm{p}}}{24\alpha_{\mathrm{f}}^2}\left[\frac{\alpha_{\mathrm{f}}^{-1} + 3\left(1-\alpha_{\mathrm{f}}\right)\alpha_{\mathrm{f}} + 8.4 {Re^*_{\mathrm{p}}}^{-0.343}}{1 + 10^{3(1-\alpha_{\mathrm{f}})} {Re^*_{\mathrm{p}}}^{-0.5-2(1-\alpha_{\mathrm{f}})}}\right]$
Tenneti et al.	$F^*_{\mathrm{f}\to\mathrm{p}\vert\vert} = F_{\mathrm{isol}}\alpha_{\mathrm{f}}^{-3} + F_1 + F_2$ $F_{\mathrm{isol}} = \left(1 + 0.15 {Re^*_{\mathrm{p}}}^{0.687}\right)$ $F_1 = \frac{5.81\left(1-\alpha_{\mathrm{f}}\right)}{\alpha_{\mathrm{f}}^3} + 0.48\frac{\left(1-\alpha_{\mathrm{f}}\right)^{\frac{1}{3}}}{\alpha_{\mathrm{f}}^4}$ $F_2 = \left(1-\alpha_{\mathrm{f}}\right)^3 Re^*_{\mathrm{p}}\left[0.95 + \frac{0.61\left(1-\alpha_{\mathrm{f}}\right)^3}{\alpha_{\mathrm{f}}^2}\right]$

Moving Particles

Direct numerical simulations of the fluid flow around moving particles have also been performed to analyze the mean fluid-particle forces. We may cite for instance [91] who investigated the role of the Stokes number on the drag. In addition, [78] analyzed a fluidized bed and evaluated the validity of a fludization law, which indirectly relates to the fluid friction. A study of fludized bed is also present in [34]. An analysis in the framework of suspension stresses in a Couette flow can also be found in [85].

A question arising in the framework of moving particles, is whether the particle Reynolds number should be based on the mean macroscopic relative velocity $\boldsymbol{V}_r$, which was already given in Figure 3.8, or the average of $\boldsymbol{v}_r = \boldsymbol{u}_\mathrm{p} - \boldsymbol{U}_\mathrm{f}$, which is the instantaneous relative velocity of the particle to the mean macroscopic fluid flow. In fact, the average of the latter can be evaluated through the expression below:

$$\langle |\boldsymbol{v}_\mathrm{r}| \rangle = \sqrt{\langle \boldsymbol{v}_r \cdot \boldsymbol{v}_r \rangle} = \sqrt{\boldsymbol{V}_r \cdot \boldsymbol{V}_r + 2q_\mathrm{p}^2} \tag{3.46}$$

The advantage of this form is that it contains the particle fluctuating kinetic energy in addition to the mean macroscopic flow difference. The values of the particle Reynolds number are given by Figure 3.53. We note that the computation of the Reynolds number in this manner is greater than the other evaluation.

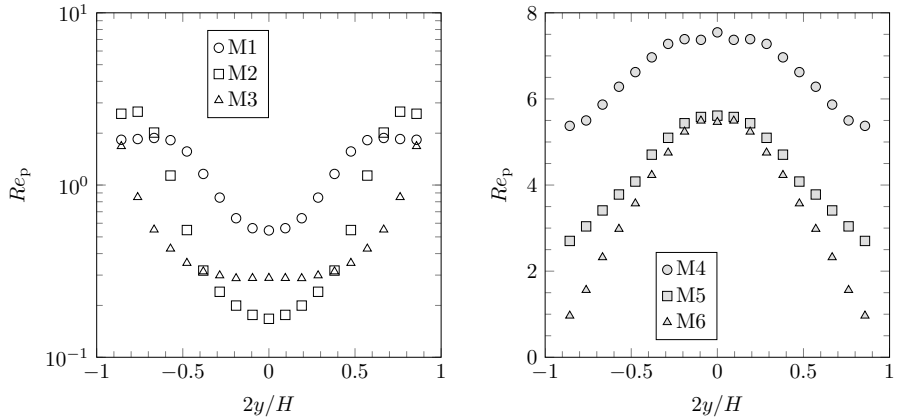

Figure 3.53: Particle Reynolds number calculated as $Re_\mathrm{p} = \langle |\boldsymbol{v}_r| \rangle \, d_\mathrm{p}/\nu_\mathrm{f}$.

In order to have an idea of the non-dimensional force function, see Table 3.3, with the local parameters of the Couette cases, we give the values of $F^*_{\mathrm{f}\to\mathrm{p}||}$, for the cases M2 and M5 on Figure 3.54. Figures on the left are computed with the particle Reynolds number based on the $\boldsymbol{V}_r$ and figures on the right, based on $\langle |\boldsymbol{v}_\mathrm{r}| \rangle$. We note that for the case M2, the values almost did not changed from left to right, whereas for the case M5 a slightly augmentation is observed when the particle agitation is taken into account on the expression. Similar results are observed for the other cases.

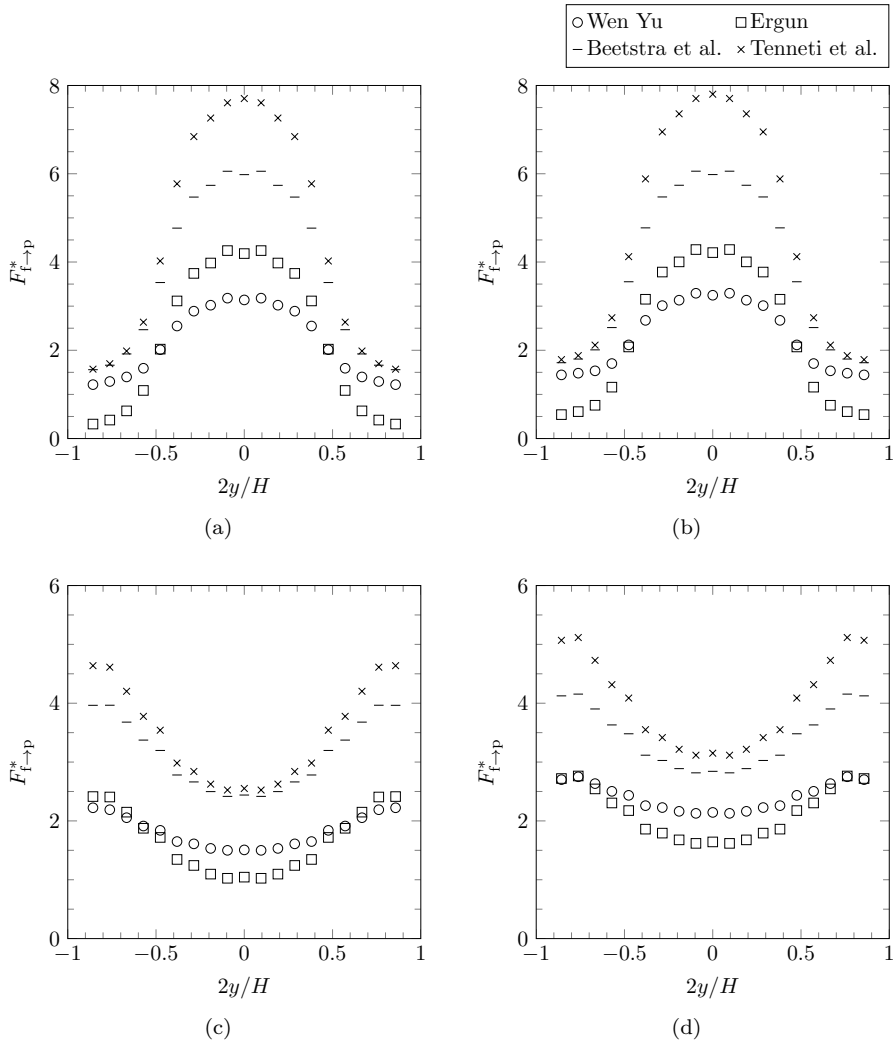

Figure 3.54: Sensitivity of the non-dimensional force functions. Figures (a) and (b) correspond to M2; and (c) and (d) to M5. Figures on the left are computed with $Re^*_{\mathrm{p}} = \alpha_{\mathrm{f}}|\boldsymbol{V}_r|d_{\mathrm{p}}/\nu_{\mathrm{f}}$; whereas those on the right: $Re^*_{\mathrm{p}} = \alpha_{\mathrm{f}}\langle|\boldsymbol{v}_r|\rangle\, d_{\mathrm{p}}/\nu_{\mathrm{f}}$.

Mean transverse force in the Couette cases

In our mono-disperse Couette cases, we observe a transverse force, in the wall-normal direction, that points towards the centre of the core flow. This force is more predominant in the budgets of the cases of high inertia, see Figure 3.39. And is only relevant in the budget of the case M1, for the cases of low inertia, as it is notably observed in Figure 3.38(a).

To begin with the analysis, the mean transverse force for those cases is compared with the force that would be generated due to the pressure gradient. It can be found that this force is negligible because it is some orders of magnitude smaller than the mean transverse force, hence, the pressure gradient does not explain the data:

$$\left| \frac{1}{\rho_\mathrm{p}} \frac{\partial P_\mathrm{f}}{\partial y} \right| \ll \left| \left\langle \frac{F_{\mathrm{f}\to\mathrm{p},y}}{m_\mathrm{p}} \right\rangle \right| \tag{3.47}$$

Another possible candidates for the mean transverse would be either a Magnus and a Saffman lift force. The expressions related to those effects, for an isolated particle, are respectively given by Eq. (3.41) and (3.42). In our case, there is, an ensemble of particles influencing each other, so it is likely that the neighboring particles would have an influence on those formulas. Even though this influence exists, it is possible that formulas taking into account those effects would still be proportional to the same variables, such as the relative velocity for example. In fact, considering that the particle angular velocity proportional to the mean fluid shear, the Magnus lift would be proportional to $V_{r,x}\partial U_{\mathrm{f},x}/\partial y$, and the Saffman lift would be proportional to $V_{r,x}\sqrt{\partial U_{\mathrm{f},x}/\partial y}$.

In order to test the relevance of these parameters, we perform a correlation analysis of the mean transverse force against those variables as well as other relevant parameters such as the particle volume fraction gradient. To do so, the Pearson correlation coefficient is used. The correlation is such that, when the norm of the correlation is close to one, the two data-sets are highly correlated and when it is close to zero it is not correlated. Table 3.4 gives the correlation values of the mean transverse force with the variables shown in the first row, for each Couette case. The correlation is computed with the data in the center of the core flow: $-0.6 < 2y/H < 0.6$, to avoid wall effects. Correlations with the norm larger than 0.9, are shown with bold text.

With respect to the cases with small inertia, we note that only the case M1, which is in fact the only one that shows a relevant transverse force in the budget of wall normal velocity, is highly correlated to relative velocity, as well as the relative velocity and the product of it to either the mean fluid shear or its square root. Moreover, regarding the cases with high inertia, interestingly, we note that the results are highly correlated to the gradient of the volume fraction.

The results seem to indicate that transverse force observed for the case M1 has a different physical origin than the one on the cases M4, M5 and M6. It is probably related to the mean relative velocity, whereas for the cases of high inertia, the gradient of particle volume fraction, which may possibly cause the flow field to be altered in such a way that it produces a equivalent lift force.

Table 3.4: Correlation coefficient between the given variable and the mean transverse force $\langle F_{\mathrm{f}\to\mathrm{p},y}\rangle$ for the mono-disperse cases.

Case	$\frac{\partial \alpha_\mathrm{p}}{\partial y}$	α_p	$V_{r,x}$	$\lvert V_{r,x}\rvert^2$	$V_{r,x}\frac{\partial U_{\mathrm{f},x}}{\partial y}$	$V_{r,x}\sqrt{\frac{\partial U_{\mathrm{f},x}}{\partial y}}$	$\frac{\partial U_{\mathrm{f},y}}{\partial y}$
M1	0.60	0.12	**0.95**	-0.33	**0.98**	**0.97**	-0.06
M2	-0.58	-0.37	-0.02	0.35	0.10	0.05	0.36
M3	-0.62	0.65	-0.66	0.59	-0.63	-0.66	-0.63
M4	**-0.94**	-0.10	-0.39	-0.35	-0.36	-0.38	0.01
M5	**-0.91**	-0.07	-0.37	0.54	-0.39	-0.38	-0.05
M6	**-0.95**	0.06	-0.84	-0.30	-0.83	-0.84	-0.05

Since the results showed a high correlation with both the Saffman and Magnus lift, we give on Figure 3.55, a comparison of the mean transverse force against the lift formulas given by Eqs. (3.41) and (3.42), using the relative macroscopic velocity $\boldsymbol{V}_r$ and the particle angular velocity as: $|\omega_\mathrm{p}| = |\dot{\gamma}/2|$. In addition, the force due to the pressure gradient is shown as well. We note that even tough the order of magnitude of the Saffman force is correct, it has nonetheless an opposite sign.

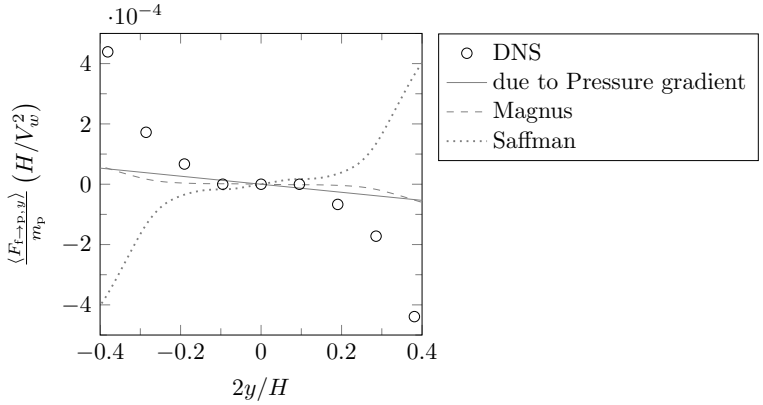

Figure 3.55: Transverse force comparison for the case M1.

Regarding the cases of high inertia, due to the high correlation with the gradient of particle volume fraction, we evaluated a simple coefficient of proportionality relying the data in the following form $C_\alpha = \left\langle \frac{F_{\mathrm{f}\to\mathrm{p},y}}{m_\mathrm{p}} \right\rangle / \frac{\partial \alpha_\mathrm{p}}{\partial y}$.

We observed that this coefficient is approximately constant for a given case among those with high inertia. The mean values of C_α are given in Table 3.5. Both the cases M5 and M6 have approximately the same coefficient whereas the case M4 is the larger one.

Table 3.5: Coefficient C_α.

Case	M4	M5	M6
C_α/V_w^2	$-1.3\ 10^{-2}$	$-4.3\ 10^{-3}$	$-4.3\ 10^{-3}$

A comparison of the mean transverse force with the predictions of the other forces, alongside the fitted model associated with a constant coefficient of proportionality, is given by Figure 3.56. It can be observed that the force due to the pressure gradient is very small. Also, the other lift expressions are negligible as well. It is interesting to note that a constant coefficient of proportionality is enough to give the good tendency of the data which seem to be an indication that indeed the phenomena behind the transverse force for the cases of high inertia comes from the alteration of the fluid flow due to the gradient of particle volume fraction.

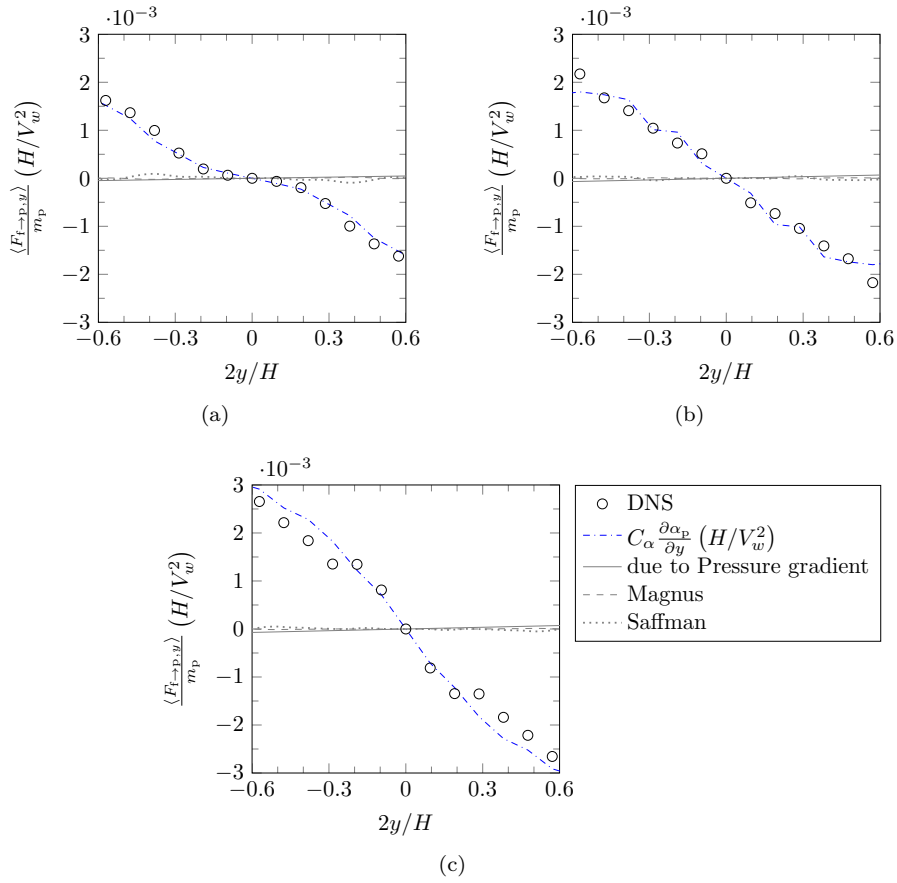

Figure 3.56: Transverse force comparison for the case (a) M4, (b) M5 and (c) M6.

In the presented analysis, we do not particularly relied on available lift coefficient expressions due to the fact that in our case the relative velocity is very small which makes difficult to access the dimensionless shear number needed in the formulas.

3.6.3 Fluid force and particle velocity fluctuation correlation

In order to describe the change in the linear momentum of a given particle, due the instantaneous impulse of the fluid force, a Langevin equation can be used [38, 112]. The equation writes as follows:

$$m_{\mathrm{p}} du_{\mathrm{p},i} = F_{\mathrm{f}\to\mathrm{p},i} dt = \langle F_{\mathrm{f}\to\mathrm{p},i} \rangle (\boldsymbol{x}, t)\, dt - A_{F,im} u'_{\mathrm{p},m} dt + m_{\mathrm{p}} B^*_{F,im} dW_m \quad (3.48)$$

The first term on the right-hand side of Eq. (3.48) represents the impulse related to the mean force, the second term is associated with the velocity fluctuations, with $A_{F,ij}$ being the linear fluid-particle force tensor and finally the third term is a stochastic term linked to a Wiener process increment $d\boldsymbol{W}$, with B^*_{ij} being the dispersion fluid-particle force tensor, or simply drift tensor. Equation above is similar to the one presented by Garzo et al., the only difference being that in our case, the mean force is directly given by the mean force field expression.

In terms of probability distribution function equations, Eq. (3.48) is formally equivalent to the relationship below [58, 83]:

$$\begin{aligned} \langle F_{\mathrm{f}\to\mathrm{p},i} | \boldsymbol{u}_{\mathrm{p}}(t) = \boldsymbol{c}_{\mathrm{p}}, \boldsymbol{x}_{\mathrm{p}}(t) = \boldsymbol{x} \rangle\, f_{\mathrm{p}}(\boldsymbol{c}_{\mathrm{p}}, \boldsymbol{x}, t) \quad &= \quad \langle F_{\mathrm{f}\to\mathrm{p},i} \rangle (\boldsymbol{x}, t)\, f_{\mathrm{p}}(\boldsymbol{c}_{\mathrm{p}}, \boldsymbol{x}, t) \\ &\quad - A_{F,im} \left[c_{\mathrm{p},m} - U_{\mathrm{p},m} \right] f_{\mathrm{p}}(\boldsymbol{c}_{\mathrm{p}}, \boldsymbol{x}, t) \\ &\quad - B_{F,im} \frac{\partial f_{\mathrm{p}}(\boldsymbol{c}_{\mathrm{p}}, \boldsymbol{x}, t)}{\partial c_{\mathrm{p},m}} \end{aligned} \quad (3.49)$$

With $B_{F,ij} = m_{\mathrm{p}} B^*_{F,im} B^*_{F,jm}/2$. Assuming that the linear force tensor and the related dispersion force tensor are only functions of the spatial coordinate and time: $A_{F,ij} = A_{F,ij}(\boldsymbol{x}, t)$ and $B_{F,ij} = B_{F,ij}(\boldsymbol{x}, t)$, and using the relationship given by Eq. (2.28), an integration of both sides of Eq. (3.49) over the velocity space, yields the trivial relationship given by Eq. (3.50). Note that the integration of the second and third terms of the right-hand side of Eq. 3.49 over the velocity space are null.

$$n_{\mathrm{p}} \langle F_{\mathrm{f}\to\mathrm{p},i} \rangle = n_{\mathrm{p}} \langle F_{\mathrm{f}\to\mathrm{p},i} \rangle \quad (3.50)$$

Analogously, multiplying Eq. (3.49) by $[c_{\mathrm{p},j} - U_{\mathrm{p},j}]$ and integrating over the velocity space, a relationship involving the correlation between the fluid force and the velocity fluctuation can be obtained as follows:

$$n_{\mathrm{p}} \left\langle F_{\mathrm{f}\to\mathrm{p},i} u'_{\mathrm{p},j} \right\rangle \quad = \quad -n_{\mathrm{p}} A_{F,im} R_{\mathrm{p},mj} + n_{\mathrm{p}} B_{F,ij} \quad (3.51)$$

Using a similar procedure, but multiplying Eq. (3.49) by the second order velocity fluctuation $[c_{\mathrm{p},j} - U_{\mathrm{p},j}]\,[c_{\mathrm{p},k} - U_{\mathrm{p},k}]$, the correlation between the fluid force and the double velocity fluctuation, after integration, gives:

$$n_{\mathrm{p}} \left\langle F_{\mathrm{f}\to\mathrm{p},i} u'_{\mathrm{p},j} u'_{\mathrm{p},k} \right\rangle \quad = \quad n_{\mathrm{p}} \langle F_{\mathrm{f}\to\mathrm{p},i} \rangle R_{\mathrm{p},jk} - n_{\mathrm{p}} A_{F,im} S_{\mathrm{p},mjk} \quad (3.52)$$

Simonin's 1991 approach

In this section we present a model proposed by [100], which can be framed as a particular case of the model discussed in the previous subsection. In such model the instantaneous force that a particle undergoes is assumed to be in the same direction of the relative velocity. It can be written as follows:

$$\boldsymbol{F}_{\mathrm{f}\to\mathrm{p}} = \quad -3\pi\mu_{\mathrm{f}} d_{\mathrm{p}} \alpha_{\mathrm{f}} F^{*}_{\mathrm{f}\to\mathrm{p}||}\left(\alpha_{\mathrm{f}}, Re_{\mathrm{p}}\right) \boldsymbol{v}_r \tag{3.53}$$

Where $\boldsymbol{v}_r$ is the relative velocity of the particle with respect to that of the fluid, and the particle Reynolds number is used in this formula is the one shown by Figure 3.53. In our simulations, as discussed in the section 3.3.4, the fluctuating scales of the fluid flow are confined between the particles and, in some sense, the particles sees an integrated fluid velocity. We can thus neglect the fluid fluctuations, for that reason we consider the relative velocity as being the relative velocity of the particles to the average fluid macroscopic velocity: $\boldsymbol{v}_r = \boldsymbol{u}_{\mathrm{p}} - \boldsymbol{U}_{\mathrm{f}}$. Since this relative velocity can be decomposed as $\boldsymbol{v}_{\mathrm{r}} = \boldsymbol{V}_r + \boldsymbol{u}'_{\mathrm{p}}$, it can be readily seen that the fluctuating part of force is written as:

$$\boldsymbol{F}'_{\mathrm{f}\to\mathrm{p}} = \quad -3\pi\mu_{\mathrm{f}} d_{\mathrm{p}} \alpha_{\mathrm{f}} F^{*}_{\mathrm{f}\to\mathrm{p}||}\left(\alpha_{\mathrm{f}}, Re_{\mathrm{p}}\right) \boldsymbol{u}'_{\mathrm{p}} \tag{3.54}$$

It follows from the equation above that the linear force tensor is given by the expression below, and the drift component is null.

$$A_{F,ij} = 3\pi\mu_{\mathrm{f}} d_{\mathrm{p}} \alpha_{\mathrm{f}} F^{*}_{\mathrm{f}\to\mathrm{p}||}\left(\alpha_{\mathrm{f}}, Re_{\mathrm{p}}\right) \delta_{ij} \tag{3.55}$$

The force velocity fluctuation correlation can then be written as:

$$\left\langle F_{\mathrm{f}\to\mathrm{p},i} u'_{\mathrm{p},j} \right\rangle = -3\pi\mu_{\mathrm{f}} d_{\mathrm{p}} \alpha_{\mathrm{f}} F^{*}_{\mathrm{f}\to\mathrm{p}||}\left(\alpha_{\mathrm{f}}, Re_{\mathrm{p}}\right) \delta_{im} R_{\mathrm{p},mj} \tag{3.56}$$

Tests with the data have shown that $F^{*}_{\mathrm{f}\to\mathrm{p}||} = 1$ seem to be enough to model the cases with low inertia, whereas the Tenneti et al. correlation, using the average of the Reynolds number that takes into account the particle fluctuating kinetic energy, is the one that approaches most the data, we thus use those correlations in the following comparisons.

All the non-null components of $\left\langle F_{\mathrm{f}\to\mathrm{p},i} u'_{\mathrm{p},j} \right\rangle$ are compared to the right-hand side of Eq. (3.56) for the cases M1, M2 and M3, in Figure 3.57. The results are given in the centre of the core flow for sake of visualization. We note that the model seem to be in accordance with the order of magnitude of the simulation data for all three cases. Regarding the case M1, Figure 3.57(a), the component with indexes xx agrees well with the results. We note that even though the model predicts the same values for the components xy and yx, the results for those components are different $\left\langle F_{\mathrm{f}\to\mathrm{p},x} u'_{\mathrm{p},y} \right\rangle \neq \left\langle F_{\mathrm{f}\to\mathrm{p},y} u'_{\mathrm{p},x} \right\rangle$, in fact, only the component xy agrees with the model, whereas the other one is much smaller. Components yy and zz are relatively smaller in magnitude. Similar results are found for the case M2. Finally for the case M3, we note that the difference between components xy and yx are not significant as the other cases. In addition, still on the case M3, we note that the predictions using this

analysis tend to overestimate the component xx and underestimate the other components.

A similar comparison for the cases with higher inertia, M4, M5 an M6, using the non-dimensional force function proposed by Tenneti et al. with the Reynolds computed with the, is shown by Figure 3.58. We note that all the predictions underestimate the results from the simulations. A posteriori analysis of the data have shown that even if the non-dimensional force function is multiplied by a given value to match one of the force velocity fluctuation component, the other components do not actually match with the same value, indicating that either a drift component is missing or the tensor $A_{F,ij}$ should be anisotropic. Those two options are investigated further in the following sections.

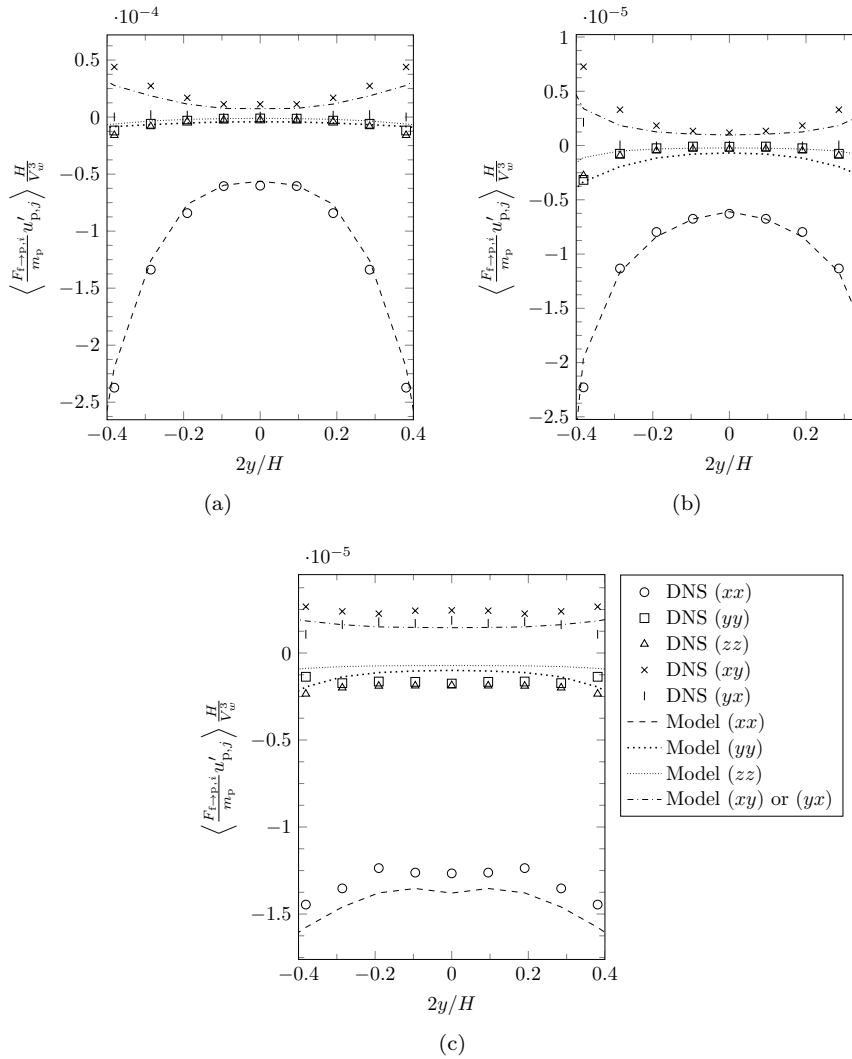

Figure 3.57: Comparison of the model, using $F^*_{\mathrm{f}\to\mathrm{p}||} = 1$, for the cases (a) M1, (b) M2 and (c) M3.

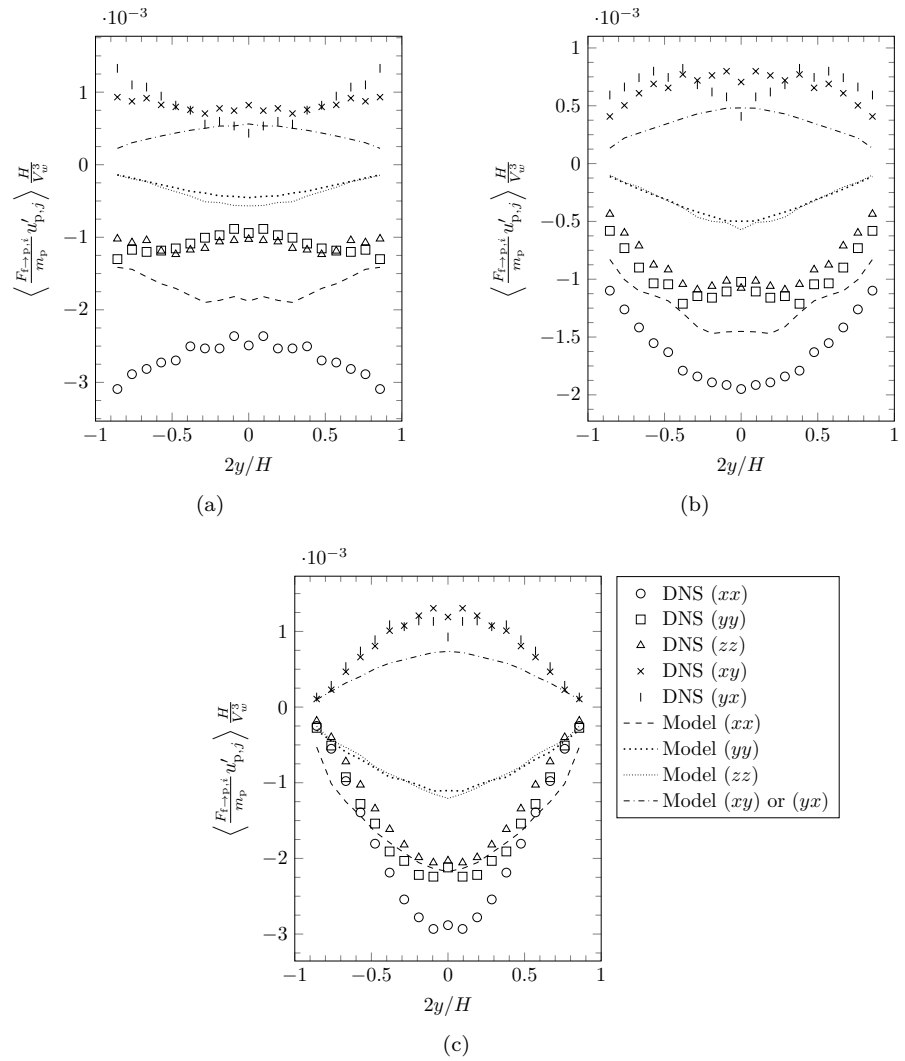

Figure 3.58: Comparison of the model, using the non-dimensional force function given by Tenneti et al. for the cases (a) M4, (b) M5 and (c) M6.

Non-null linear force and dispersion coefficients

In the previous section, we evaluated a model, which corresponds to a particular case of Eq. 3.51 where the linear force tensor is known, and the drift coefficient is null. In this section, we suppose that both $A_{F,ij} = A_F\delta_{ij}$ and $B_{F,ij} = B_F\delta_{ij}$ are isotropic and non-null, which is explored as a first approximation in [38], and we evaluate whether such a model would work with our data set, without making any pre-assumption on the value of the parameters.

Within the framework of the discussed condition, the force velocity fluctuation correlation would be described by

$$n_\mathrm{p}\left\langle F_{\mathrm{f}\to\mathrm{p},i}u'_{\mathrm{p},j}\right\rangle = -n_\mathrm{p}A_F R_{\mathrm{p},ij} - n_\mathrm{p}B_F\delta_{ij} \tag{3.57}$$

In order to test such a model, first we take the traceless version of the equation above, reads:

$$\widehat{\left\langle F_{\mathrm{f}\to\mathrm{p},i}u'_{\mathrm{p},j}\right\rangle} = -A_F\widehat{R}_{\mathrm{p},ij} \tag{3.58}$$

Where $\widehat{\left\langle F_{\mathrm{f}\to\mathrm{p},i}u'_{\mathrm{p},j}\right\rangle} = \left\langle F_{\mathrm{f}\to\mathrm{p},i}u'_{\mathrm{p},j}\right\rangle - \left\langle F_{\mathrm{f}\to\mathrm{p},m}u'_{\mathrm{p},m}\right\rangle\delta_{ij}/3$ is the traceless correlation between the force and the velocity fluctuation and, similarly, the traceless particle kinetic stress $\widehat{R}_{\mathrm{p},ij} = R_{\mathrm{p},ij} - R_{\mathrm{p},mm}\delta_{ij}/3$. The values of A_F, computed through Eq. (3.58) for all the non-null index combinations for the cases M2 and M5 are shown by Figure 3.59, we observe that all the values do not fall into a single curve, indicating that such an isotropic coefficient is not enough to describe our results. Similar results are obtained for the other cases as well.

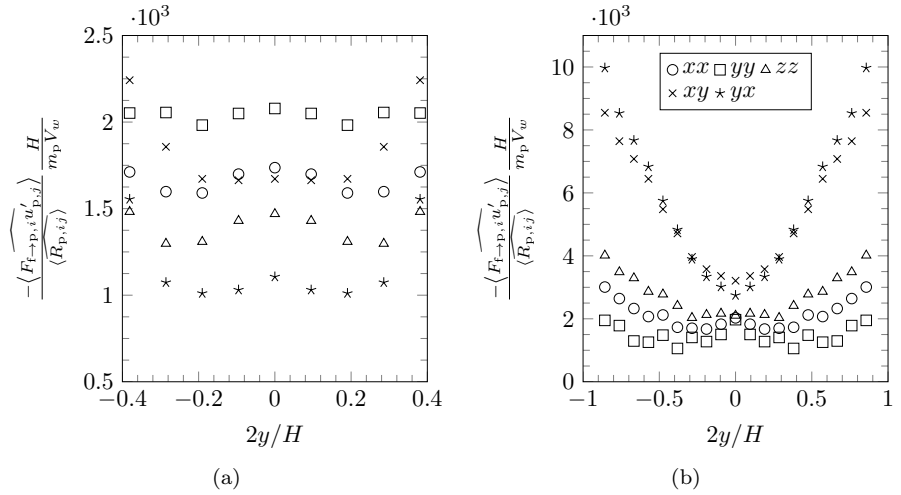

Figure 3.59: Sensibility of the linear force coefficient for the case (a) M2 and (b) M5.

Besides, the differences in the values of A_F when evaluated with different index combinations, a problem arising with such a model is that, as seen on the

previous subsection, in some cases $\left\langle F_{\mathrm{f}\to\mathrm{p},x} u'_{\mathrm{p},y} \right\rangle$ is different from $\left\langle F_{\mathrm{f}\to\mathrm{p},y} u'_{\mathrm{p},x} \right\rangle$, which imply that the matrix on the left-hand side of the equation above is not symmetric. All the terms on the right-hand side of the equation above, are symmetric, since $R_{\mathrm{p},ij}$ is symmetric. For that reason, both sides of the equation would never be completely satisfied regardless of the values of the coefficients.

Anisotropic linear force tensor and a null drift coefficient

Analogously to the last section, we presuppose a version of the model, and evaluate the implication of such hypothesis. In this section we assume an anisotropic linear force tensor $A_{F,ij}$, and a null drift or dispersion coefficient. Within this frame, the equation for the force velocity correlation, see Eq. (3.51), gives:

$$\left\langle F_{\mathrm{f}\to\mathrm{p},i} u'_{\mathrm{p},j} \right\rangle = -A_{F,ik} R_{\mathrm{p},kj} \tag{3.59}$$

In order to test the consistency of the model, the linear force tensor $A_{F,ik}$ can be isolated in the equation above, by multiplying the equation both sides to right by the inverse of the particle kinetic stress matrix $R^{-1}_{\mathrm{p},nj}$. The expression for the linear force tensors then, reads:

$$A_{F,ij} = -\left\langle F_{\mathrm{f}\to\mathrm{p},i} u'_{\mathrm{p},n} \right\rangle R^{-1}_{\mathrm{p},nj} \tag{3.60}$$

With $A_{F,ij}$ computed in this manner, then, a comparison with third order results is performed to verify the consistency of the model. For that purpose Eq. (3.52) is used. In fact, noticing that: $\left\langle F'_{\mathrm{f}\to\mathrm{p},i} u'_{\mathrm{p},j} u'_{\mathrm{p},k} \right\rangle = \left\langle F_{\mathrm{f}\to\mathrm{p},i} u'_{\mathrm{p},j} u'_{\mathrm{p},k} \right\rangle - \left\langle F_{\mathrm{f}\to\mathrm{p},i} \right\rangle R_{\mathrm{p},jk}$, the relationship to be tested with the previously calculated linear force tensor, reads:

$$\left\langle F'_{\mathrm{f}\to\mathrm{p},i} u'_{\mathrm{p},j} u'_{\mathrm{p},k} \right\rangle = -A_{F,im} S_{\mathrm{p},mjk} \tag{3.61}$$

All non-null components of the linear force tensor, calculated by Eq. (3.60), for the cases of low and high inertia are respectively shown by Figures 3.60 and 3.61. We note that for all the cases, the component $A_{F,xy}$ is negative, whereas all the diagonal components are positive. The term $A_{F,yx}$ on the other hand is either positive or negative depending on the case and coordinate in the domain. All the other extra-diagonal components are null. It can be observed a very similar shape for all the terms for the cases of high inertia.

The comparisons for the third order fluid force velocity correlations, using the linear force tensor previously shown, precisely calculated through the Eq. (3.61), are given for the cases with low and high inertia, respectively by Figures 3.62 and 3.63.

Regarding the results for the cases of low inertia, they are given in a log scale for sake of visualization, also only a part of the domain is shown, since near the centre of the domain the values are closer to zero. We compare the absolute values of some of the relevant triple force velocity correlations. It can be observed a good agreement between the tendency of the data and the model, and similar results can be found for the other non-null components as well.

With respect to the cases of high inertia, all the non-null triple force velocity correlations are shown. We note a good overall agreement for all the components. This seem to indicate that a Langevin equation, in the form of Eq. (3.49), containing a second rank anisotropic linear force tensor and a null drift coefficient is enough to correctly describe the force velocity correlations in the Couette domain. Which opens the question on how to model such a tensor.

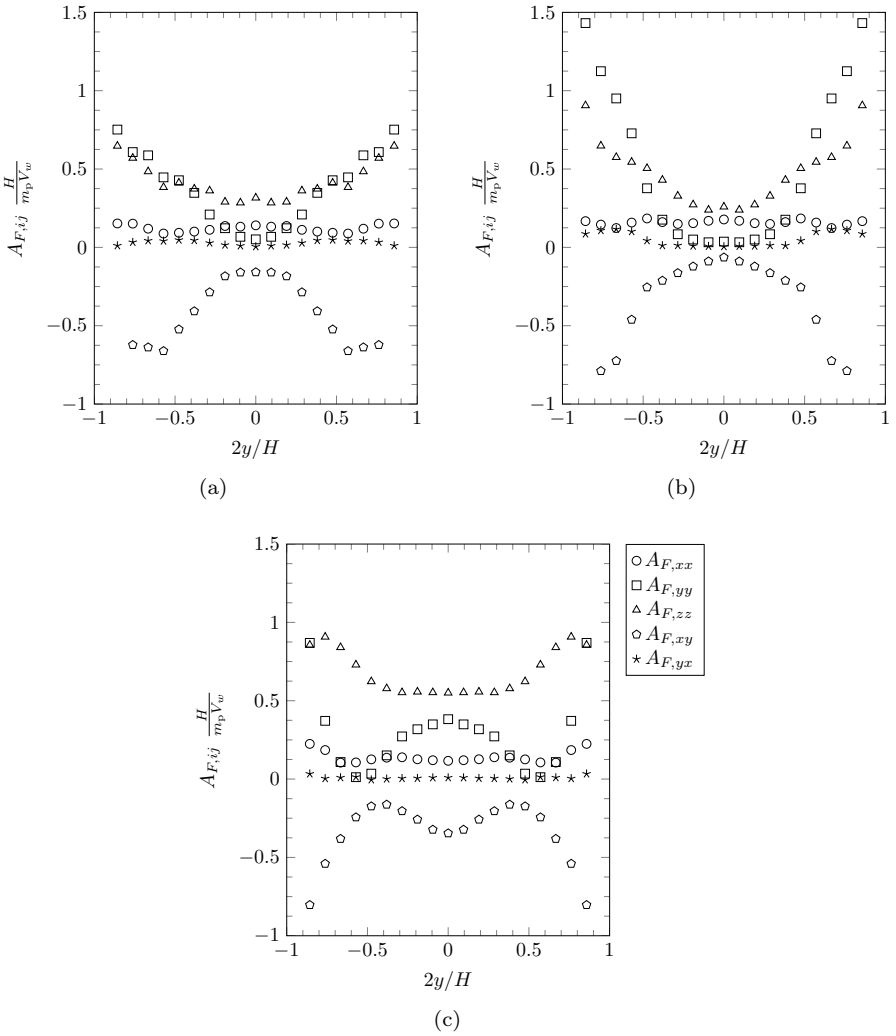

Figure 3.60: Coefficient $A_{F,ij}$ for the cases (a) M1 (b) M2 and (c) M3.

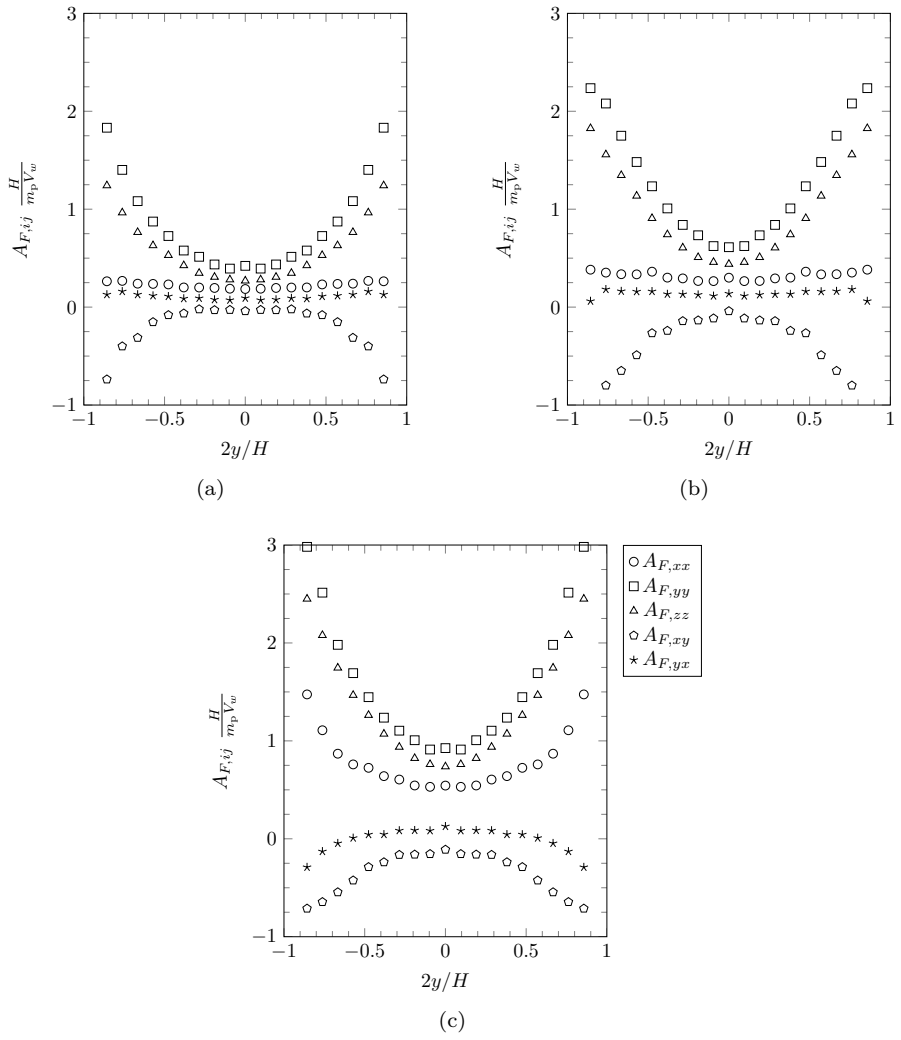

Figure 3.61: Coefficient $A_{F,ij}$ for the cases (a) M4 (b) M5 and (c) M6.

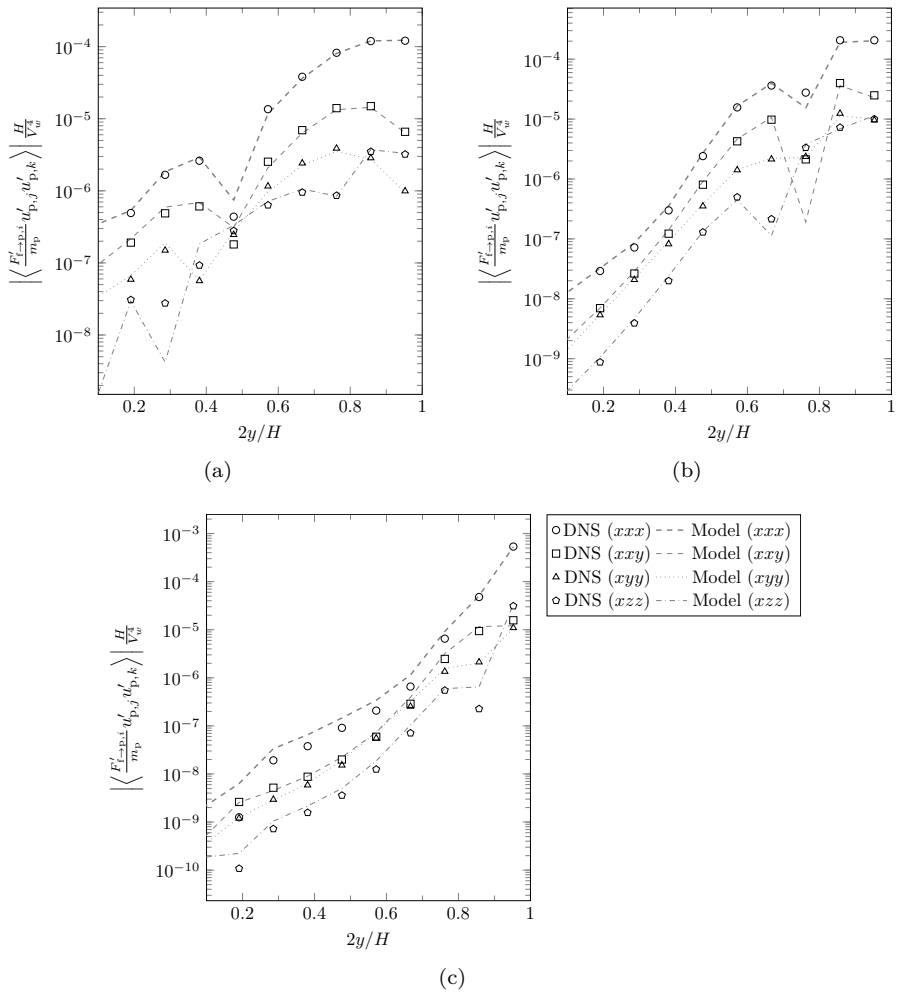

Figure 3.62: Comparison of the third order results, using the linear force tensor computed from second order statistics for the cases (a) M1 (b) M2 and (c) M3.

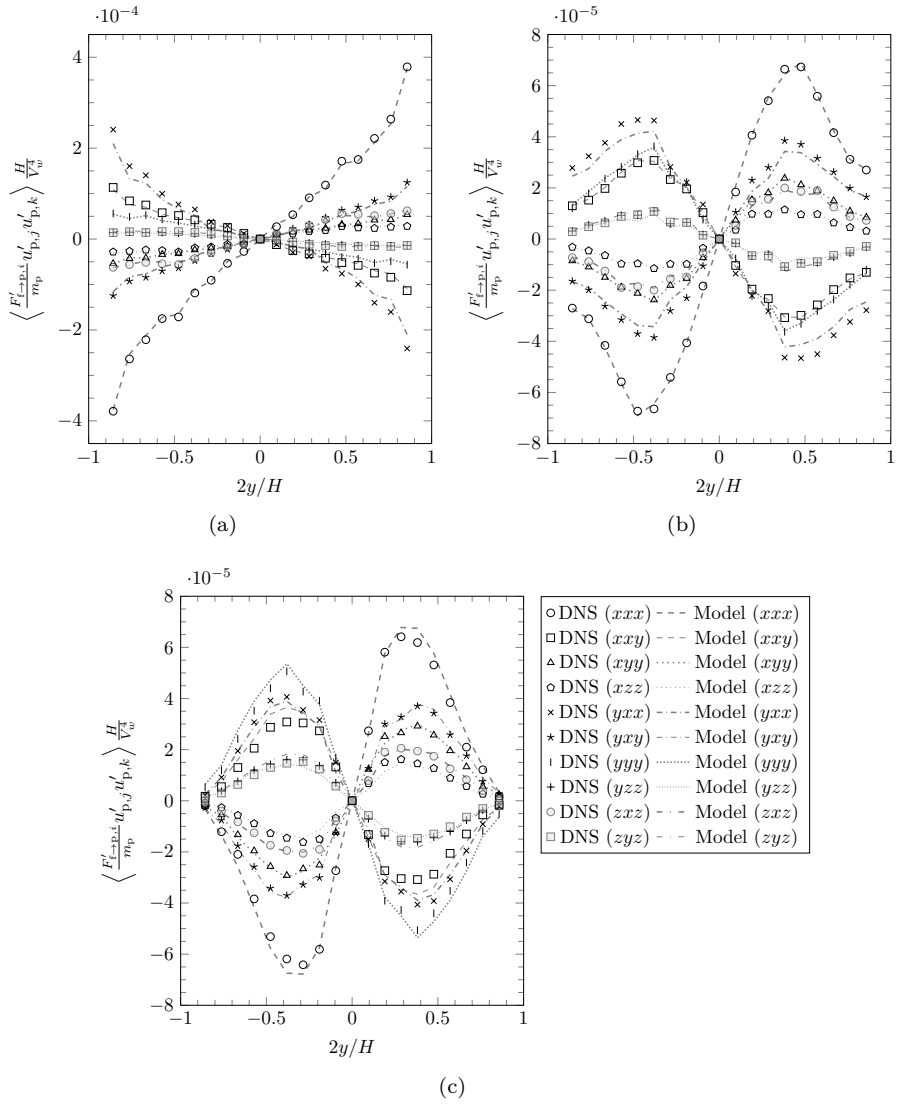

Figure 3.63: Comparison of the third order results, using the linear force tensor computed from second order statistics for the cases (a) M4 (b) M5 and (c) M6.

Chapter 4

Bi-disperse Flow

Contents

4.1 Introduction

In this chapter, bi-disperse fluid-particle numerical simulations in a Couette configuration are investigated. Bi-dispersion is achieved by changing the density of the particles, consequently producing sets of heavier and lighter particles with the same diameter. The physical and numerical description of the cases are provided in the section 1.4.2.

An appropriate definition for the Stokes number taking into account the bi-dispersion is presented, and the influence of this factor on the statistics of the bi-disperse cases, such as the particle number density and particle fluctuating kinetic energy are investigated. In addition to that, the transport equations of both particle phases are shown in the form of a budget, similarly to what has been presented in the mono-disperse chapter. The difference being the terms taking into account the transfer due one class of particle to another. Showing for instance, transfer of random kinetic energy from the heavier to the lighter particle phase.

Next, we focus on the particle-particle interaction terms of the budget. The collision terms presented in the previous cited budgets are decomposed into collision flux and redistribution related tensors, using the procedure presented in the section 2.7, unveiling interesting mechanisms related to inter-particle interaction. Modeling of the collision flux and redistribution tensor for the bi-disperse particle flow is presented and next tested against the data of our resolved simulations.

4.2 Macroscopic behavior and statistics

In the mono-disperse cases, it was observed that a macroscopic transition takes place depending on the bulk Stokes number. For low bulk Stokes number, particles accumulate near the center of the domain, whereas for higher Stokes number particles accumulates more towards the walls. That motivated us to inquiry the macroscopic behavior of a mixture of both particles that would alone have that low bulk Stokes number with another class of particles that would instead have the bigger bulk Stokes number. This is performed in the cases B1, B2 and B3, see Table 1.4, which are characterized by a mixture of particles with $\mathrm{St}_b = 15$ and 30, corresponding respectively to the low and high Stokes numbers of the mono-disperse cases. In addition to that, in order to further deepen our analysis, we studied a mixture of particles with very low bulk Stokes number, case B0, and another one with very high bulk Stokes number, case B4. Regarding B0, we have $\mathrm{St}_b = 7.5$ and 15 and for B4, we have $\mathrm{St}_b = 30$ and 60.

A frontal snapshot of those simulations at steady-state are given by Figure 4.1, with the heavier particles in brown and the lighter particles in white. Also, a view on perspective is given by Figure 4.2.

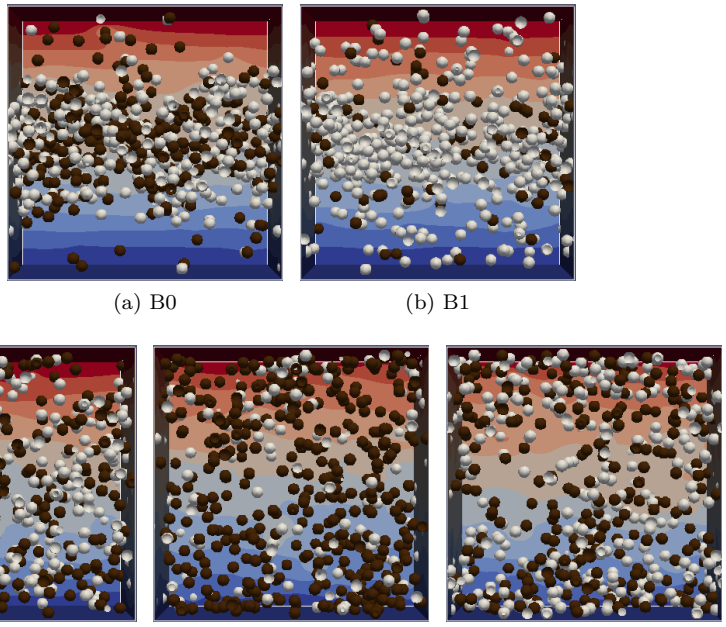

(a) B0 (b) B1

(c) B2 (d) B3 (e) B4

Figure 4.1: Snapshot of the bi-disperse cases, frontal view. Heavier particles are brown and lighter particles are white.

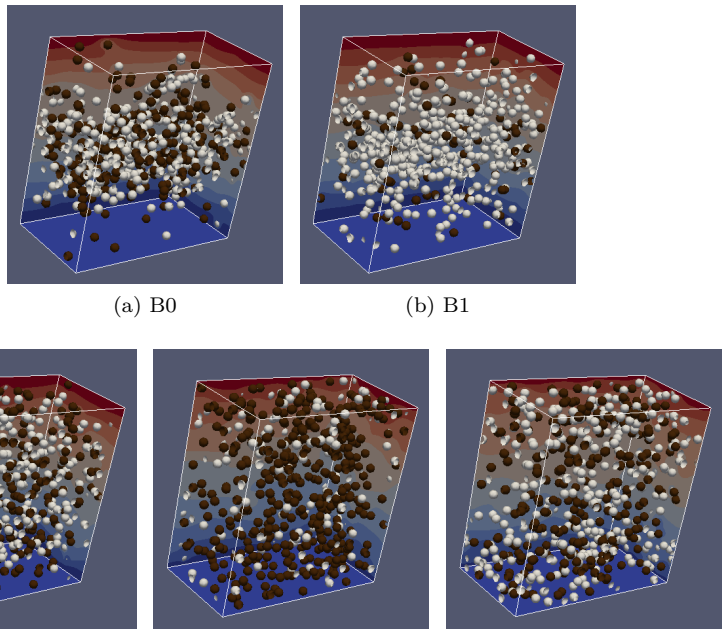

(a) B0 (b) B1

(c) B2 (d) B3 (e) B4

Figure 4.2: Snapshot of the bi-disperse cases in perspective. Heavier particles are brown and lighter particles are white.

4.2.1 Bi-disperse Stokes number

The bulk Stokes number for the mono-disperse cases was defined by Eq. (1.20), as the a global measure of the ratio of the particle inertia to the viscous effects in the domain. This non-dimensional number, turned out to be a good indicator into predicting the macroscopic transition occurring for the mono-disperse cases, being an import tool for analyzing the fluid-particle flow in the Couette configuration.

To analyze the bi-disperse cases however, one has to consider mixture effects. To do so, an equivalent bi-disperse Stokes number St^* is defined as the ratio of the inertial to the hydrodynamic effects in the mixture, in the following form:

$$St^* = \frac{\left(n_\mathrm{p} m_\mathrm{p} \frac{U^2}{L} + n_\mathrm{q} m_\mathrm{q} \frac{U^2}{L}\right)}{\left(\frac{n_\mathrm{p} m_\mathrm{p} U}{\tau_\mathrm{p}} + \frac{n_\mathrm{q} m_\mathrm{q} U}{\tau_\mathrm{q}}\right)} \tag{4.1}$$

Where U, L, τ_p and τ_q are respectively the characteristic velocity, characteristic length scale and characteristic fluid-particle drag scale of the particles of type p and q. An equivalent bi-disperse fluid particle characteristic relaxation time-scale τ^* can be defined as follows:

$$\frac{n_\mathrm{p} m_\mathrm{p} + n_\mathrm{q} m_\mathrm{q}}{\tau^*} \quad = \quad \frac{n_\mathrm{p} m_\mathrm{p}}{\tau_\mathrm{p}} + \frac{n_\mathrm{q} m_\mathrm{q}}{\tau_\mathrm{q}} \tag{4.2}$$

Substituting Eq. (4.2) into Eq. (4.1), we obtain the general expression for the bi-disperse Stokes number:

$$St^* = \tau^* \frac{U}{L} \tag{4.3}$$

Specifically in our bi-disperse simulations, where both particle species share the same diameter, the equivalent bulk bi-disperse fluid particle characteristic time-scale, can be written as follows: $\tau^* = \rho^* d_\mathrm{p}^2 / 18\mu_f$, where ρ^* is the equivalent bi-disperse specific mass, is: $\rho^* = (n_\mathrm{p}\rho_\mathrm{p} + n_\mathrm{q}\rho_\mathrm{q})/(n_\mathrm{p} + n_\mathrm{q})$. Also, considering the fact that the particles share the same velocity gradient, the ratio U/L in Eq. (4.3), can be replaced by the mean particle stream-wise velocity gradient. The resulting formula, for the local bi-disperse Stokes number, reads:

$$St^* = \frac{\rho^* d_\mathrm{p}^2}{18\mu_f} \frac{\partial U_{\mathrm{p},x}}{\partial y} \tag{4.4}$$

A global, or bulk version of the bi-disperse Stokes number, can be computed using the wall velocity, domain dimension and bulk values of particle number density, similarly to what to the calculation of the bulk Stokes number for the mono-disperse cases. In that manner, the bulk bi-disperse Stokes can be written as: $St^*_\mathrm{b} = \frac{\rho^*_\mathrm{b} d_\mathrm{p}^2}{18\mu_f} \frac{2V_w}{H}$, with ρ^*_b, being the bulk bi-disperse specific mass, calculated notably using the bulk particle number density.

Computed values of the St^*_b are given in Table 4.1. The cases are actually enumerated in increasing order of bulk bi-disperse Stokes number. It can be

noticed in Figure 4.1, that the St_b^* have an influence on the macroscopic behavior of the fluid-particle flow, since the particles on the cases B0 and B1 are located near the centre whereas the opposite seems to happens for the cases B2 to B4.

This is in fact, similar to what happens for the mono-disperse cases, where a macroscopic transition happens when the value of bulk Stokes number changes from 15 to 30, indicating that the transition must lie within that range. For the bi-disperse cases, using this appropriate definition presented in this section, the transition seem to happen from the case B1 to B2, hence within the following range: $17.5 < \mathrm{St}_\mathrm{b}^* < 22.5$. Interestingly being consistent to what has been previously observed for the mono-dispersed cases.

Table 4.1: Equivalent bi-disperse bulk Stokes number

CASE	B0	B1	B2	B3	B4
St_b^*	11.2	17.5	22.5	27.5	45.0

Local values of the bi-disperse Stokes number are given by Figure 4.3. The influence of this value in the statistics is studied in this chapter.

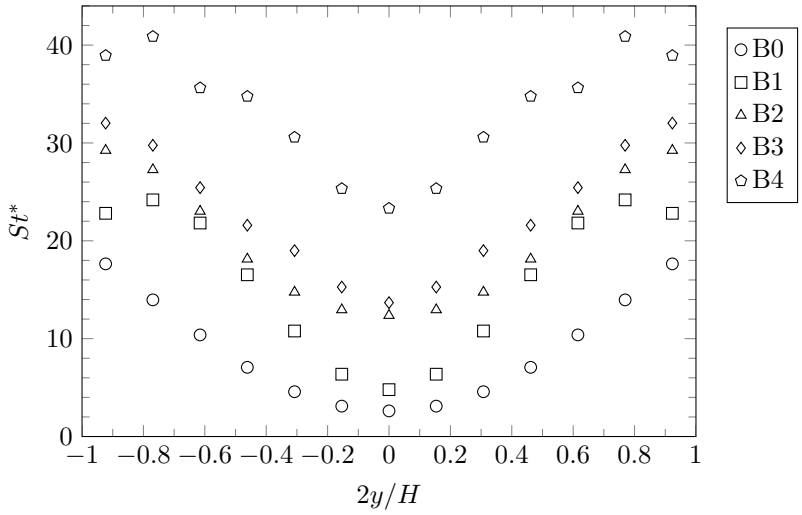

Figure 4.3: Local equivalent bi-disperse Stokes number.

4.2.2 Particle number density

The particle number density for all the bi-disperse cases is given by Figure 4.4. Values are normalized using the bulk particle number density $n_{\mathrm{p,b}}$. Normalized values for the q-species are approximately the same. Hence $n_{\mathrm{p}}/n_{\mathrm{p,b}} \simeq n_{\mathrm{q}}/n_{\mathrm{q,b}}$. Concerning the graph, clearly as the bulk bi-disperse Stokes number augments, the shape of the curve gradually changes from a concave shape to a convex one. In other words, the second derivative of the particle number density with respect to the wall normal direction augments from case B0 to B4, in the centre of the domain.

This evidence on the bulk Stokes number impact on the transition, further corroborates the hypothesis that the Stokes number in fact controls the observed transition. Further pointing out the fact that the formula given by Eq. (4.4) is in reality the relevant non-dimensional number in this study.

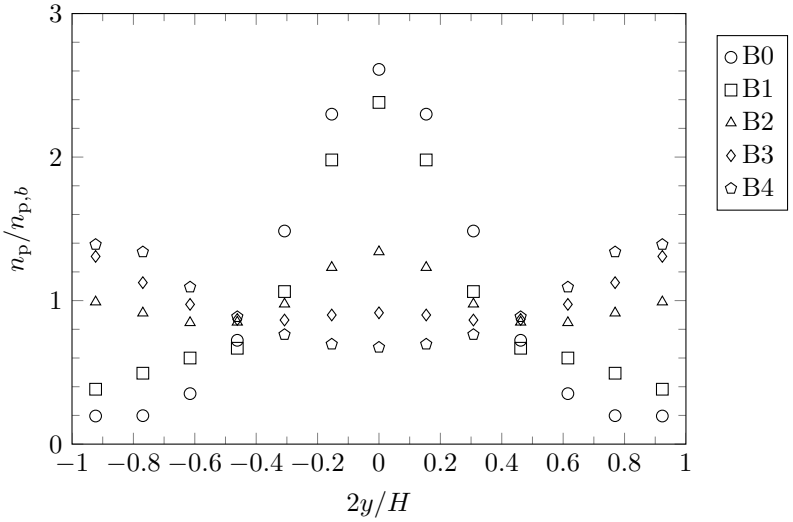

Figure 4.4: Particle number density.

Values of the particle volume fraction for both particle species, α_{p} and α_{q}, can be calculated by multiplying the particle number density by the volume of a single particle. Computed values for the bi-disperse cases are shown by Figure 4.5. Cases B0, B2 and B4, shown by Figure 4.5(a,c,e), have the same number of particles in p and q species therefore the graphs of α_{p} and α_{p} are close to one another. The case B1 and B3, have a different number of particles of p and q species, see Figure. 4.5(b,d).

The bi-disperse cases are indeed dense, reaching up to approximately 15% of total particle volume fraction in centre for the case B0, which is the sum of the α_{p} and α_{q}. Even in the region with lesser particles, in centre of case B4, the sum of particle volume fraction is about 4.8% which is also considered dense.

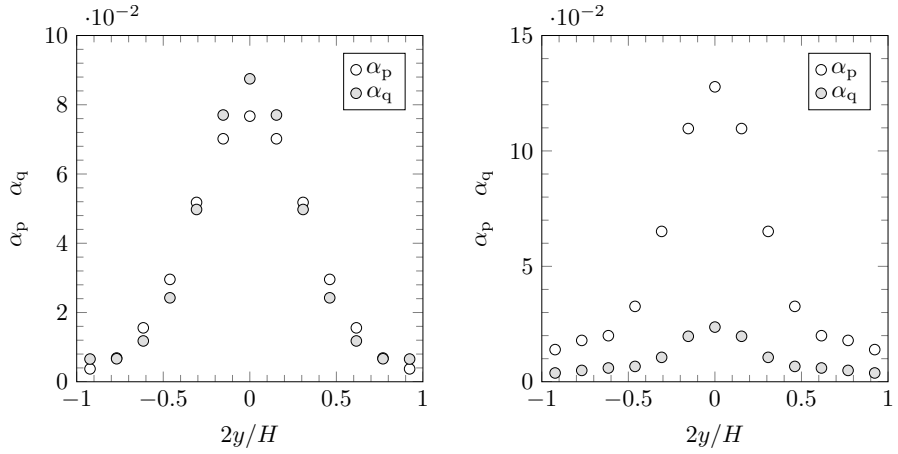

(a) B0

(b) B1

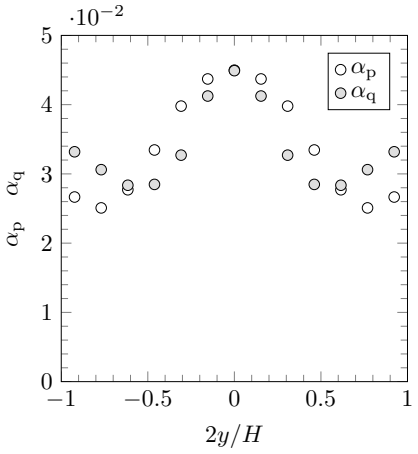

(c) B2

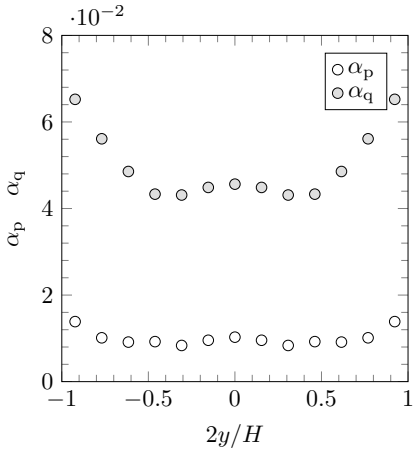

(d) B3

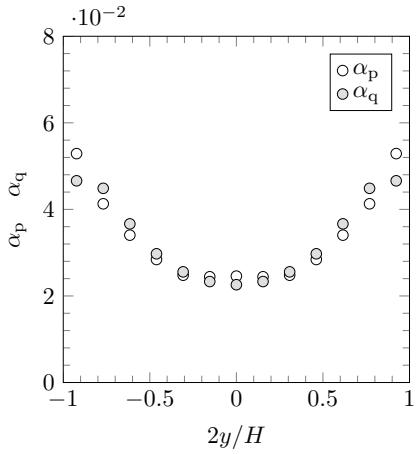

(e) B4

Figure 4.5: Particle volume fraction.

4.2.3 Fluid and particle mean velocities

The mean particle and fluid stream-wise velocity for all the bi-disperse cases are given by Figure 4.7. We observe that the mean velocity of both particle species are very close to one another. The mean fluid velocity is very close to the mean particle velocity as well. The only exception being the case with the smaller inertia, B0, in which, a slightly mean slip between the phases is observed, with the fluid velocity being larger that of particles in absolute values.

Furthermore, analogously to the mono-disperse cases, as the particle inertia augments the profiles of mean velocity change from a "S"-shape curve towards a straight line in the graph. Also, similarly to the mono-disperse cases, mean velocities in the wall normal and span-wise direction are null.

The fore-mentioned influence of the bi-disperse Stokes number on the shape of the mean velocity can be clearly seen on the profiles given by Figure 4.6 for the centre of the core flow. In such a region of interest, the slope of the mean particle velocity seem to have a direct relationship with the particle inertia, or the bi-disperse Stokes number.

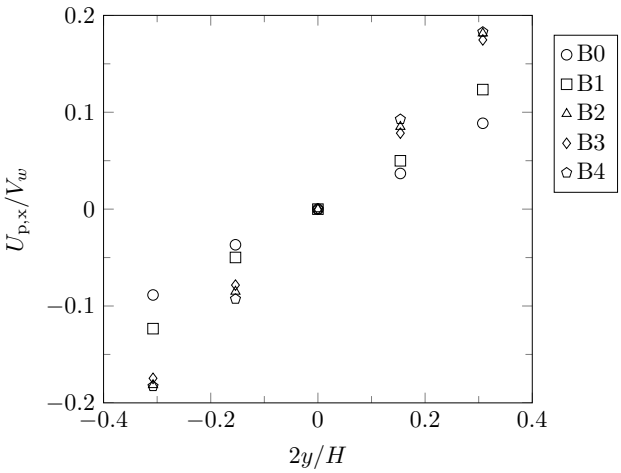

Figure 4.6: Mean particle velocity in the centre of the core flow.

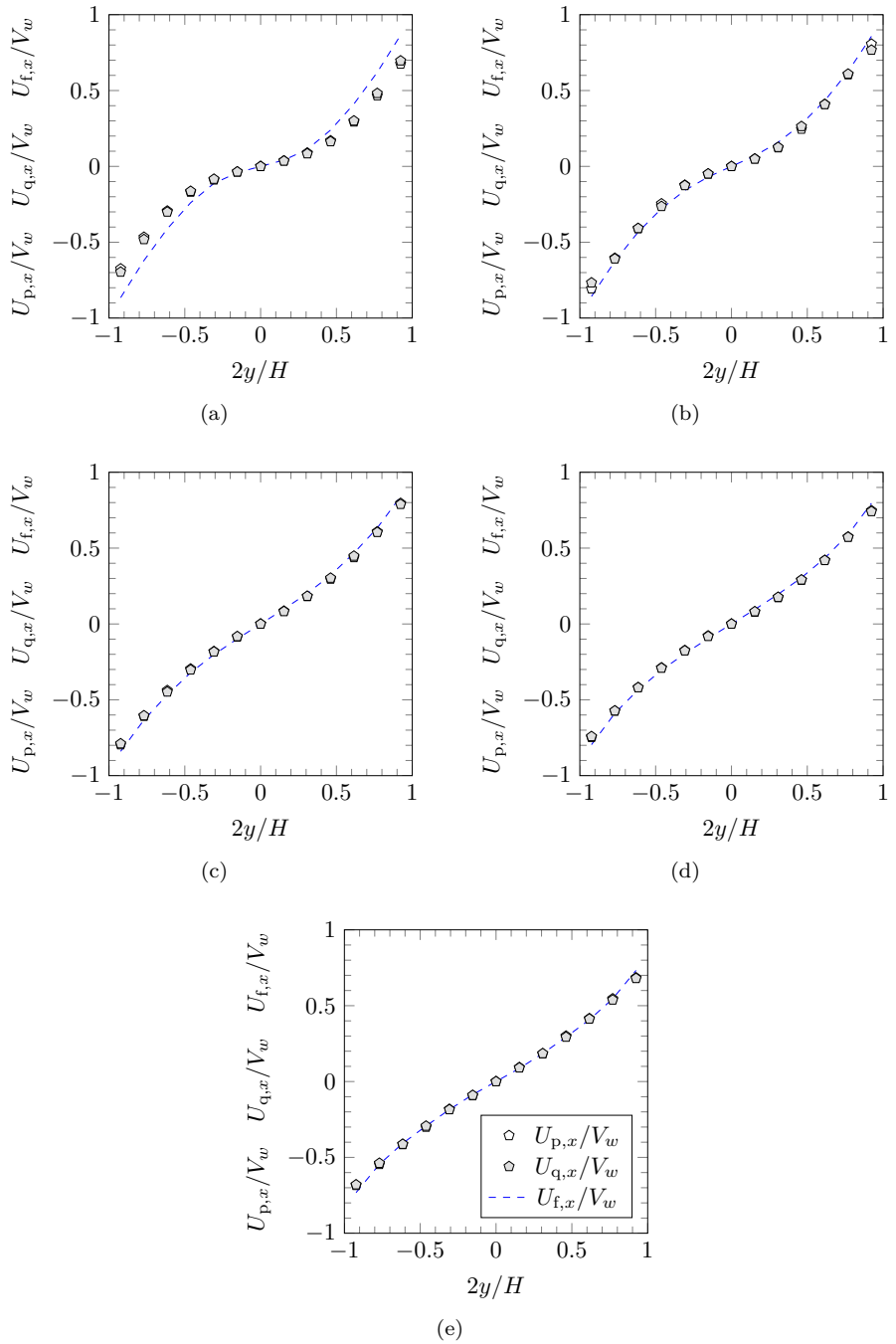

Figure 4.7: Mean fluid and particle velocity for the case (a) B0, (b) B1, (c) B2, (d) B3 and (d) B4.

4.2.4 Particle fluctuating kinetic energies

Particle fluctuating kinetic energy is given by Figure 4.8. A clear augmentation of the normalized fluctuating kinetic energy is observed in the centre with the augmentation of the bi-disperse Stokes number. As opposed to the particle number density, values for both particle species are not always equal. A comparison of the fluctuating kinetic energies of both particle species, for all the bi-disperse cases, are shown by Figure 4.9.

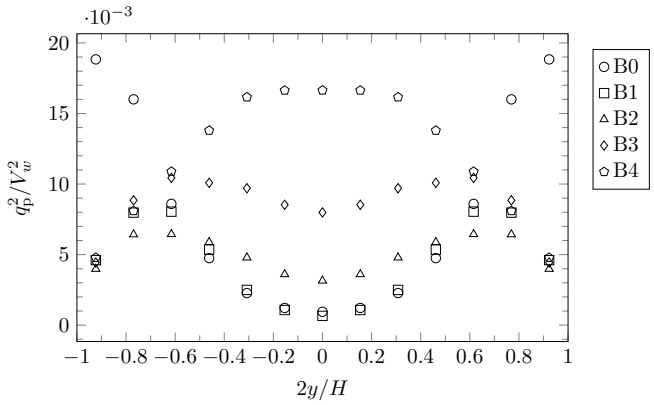

Figure 4.8: Fluctuating kinetic energy of the particles.

A major dissimilarity related to the fluctuating kinetic energy of the particles is found for the case of high Stokes, B4. In fact, the fluctuating kinetic energy for the lighter phase, or p-species, is found to be larger in these regions, that is $q_\mathrm{p}^2 > q_\mathrm{q}^2$. A similar effect happens in some types of plasma systems, where the temperature, or the fluctuating kinetic energy of the electrons, are found to be higher than those of the ions, which is the case in [41].

This effect in our case is related to the relationship between the collision time scale: $\tau^*_\mathrm{coll} \propto 1/\sqrt{q_\mathrm{p}^2 + q_\mathrm{q}^2}$, and the relaxation time scale: τ^*. The latter was presented in the section 4.2.1 and the former can be found in [35].

For the case B4, since the values of $q_\mathrm{p}^2 + q_\mathrm{q}^2$ are relatively high, the collision time scale is relatively smaller, and also its ratio to the relaxation time scale. This means that particles transfer fluctuating kinetic energy faster through collisions relatively to the relaxation time, and since collisions between heavier and lighter particle, tend to transfer more momentum to the lighter particles, combined with the fact that at higher Stokes numbers, collision are more powerful, this contributes to a higher fluctuating kinetic energy for the phase p, or the lighter particles, in this case. One also might argue that this effect is a result of the solution of the transport equations of particle fluctuating kinetic energy of both species where the factors explained above are already implicitly taken into account.

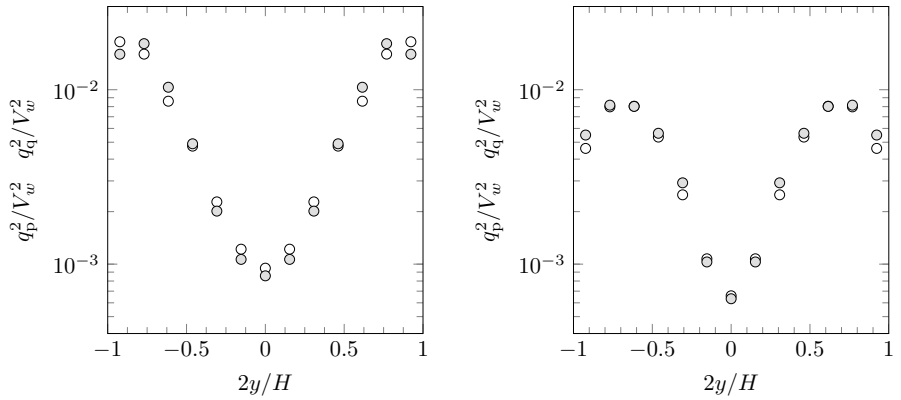

(a) B0

(b) B1

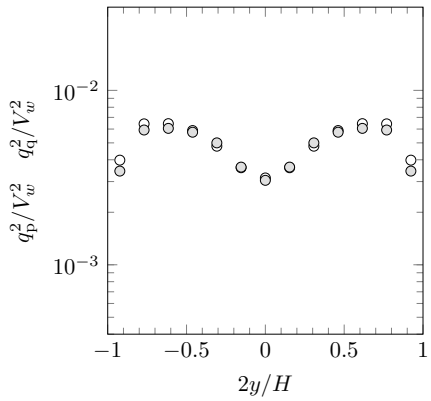

(c) B2

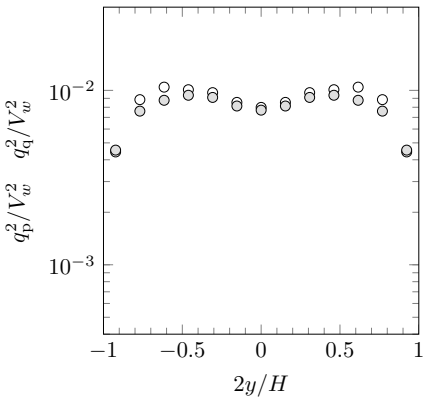

(d) B3

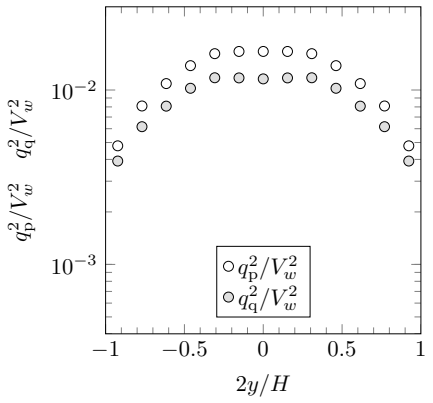

(e) B4

Figure 4.9: Comparison of the particle fluctuating kinetic energy of the p and q species.

4.2.5 Particle kinetic stress

The diagonal components of the particle kinetic stresses of both the lighter and heavier particles, respectively p and q species, are given by Figure 4.11. First of all, we observe that the kinetic stresses for the lighter particles are very close to that of the heavier particles, with the exception of the of the case B4, corresponding to the case with the higher inertia, where the kinetic stresses for the p-particles, are higher than that of the q-particles. Which is due to the same reasons as exposed in the previous section.

It is interesting to observe that as the bulk bi-disperse augments, the shape of the kinetic stresses change from a convex to a more concave shape, similarly to what has been observed for the mono-disperse cases with the increase of the particle inertia.

With respect to shear kinetic stresses, analogously to the mono-disperse cases, the only non-null extra-diagonal component is the one related to the xy indexes. Since all the values for this component are negative, they are given by Figure 4.10 multiplied by minus one for sake of visualizing it into a log scale. In the centre of the core flow, we note that the module of the shear kinetic stress directly augments with the bi-disperse Stokes number for both the lighter and heavier particle species.

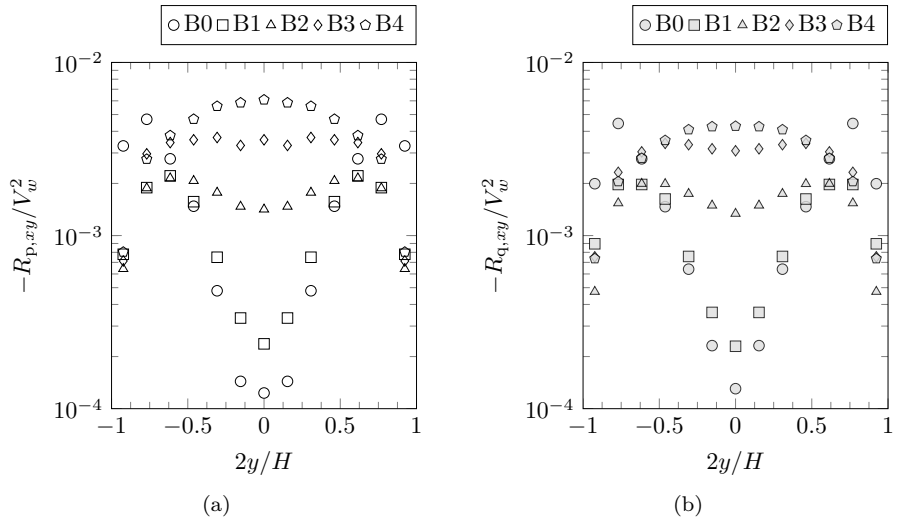

Figure 4.10: Particle shear kinetic stress for (a) p-particles and (b) q-particles.

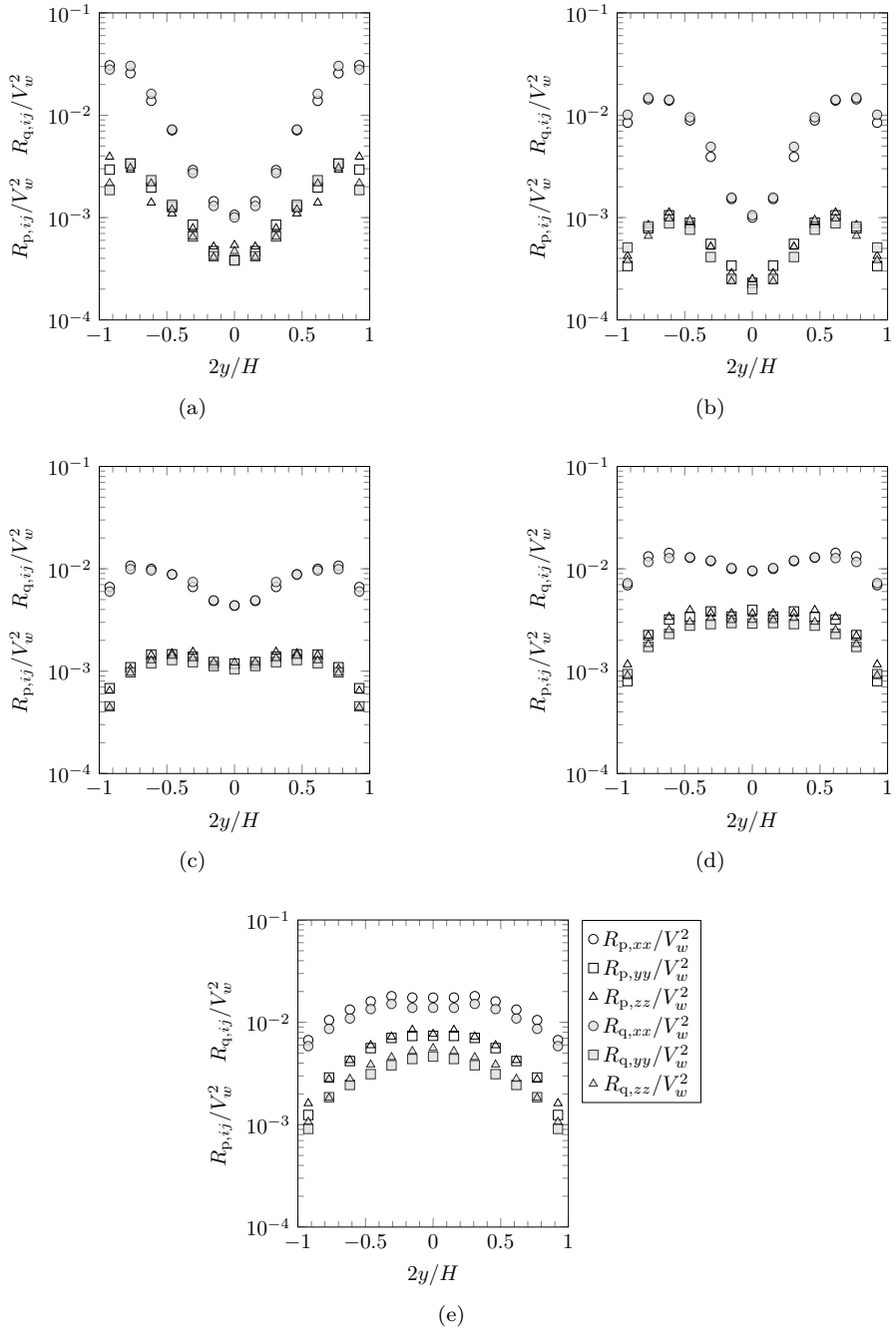

Figure 4.11: Diagonal components of the particle kinetic stresses for the lighter and heaver particles for the cases (a) B0, (b) B1, (c) B2, (d) B3 and (e) B4.

4.3 Particle fluctuating kinetic energy budget

4.3.1 Transport equation budget

In this section, similarly to analysis presented in the section 3.5.3 for the mono-disperse case, the budgets of the particle fluctuating kinetic energy, for both the lighter and heavier particle species are presented. The budget is based on Eq. (2.41), and for the specific case of our configuration can be written for the p-particles as follows:

$$\frac{\partial q_{\mathrm{p}}^2}{\partial t} = \underbrace{-\frac{1}{2n_{\mathrm{p}}}\frac{\partial\left(n_{\mathrm{p}}S_{\mathrm{p},iiy}\right)}{\partial y}}_{D} \underbrace{-R_{\mathrm{p},xy}\frac{\partial U_{\mathrm{p},x}}{\partial y}}_{P} + \underbrace{\left\langle \frac{F_{\mathrm{f}\to\mathrm{p},i}}{m_{\mathrm{p}}}u'_{\mathrm{p},i}\right\rangle}_{F} + \underbrace{\left\langle \frac{F_{\mathrm{p}'\to\mathrm{p},i}}{m_{\mathrm{p}}}u'_{\mathrm{p},i}\right\rangle}_{C_{\mathrm{pp}}} + \underbrace{\left\langle \frac{F_{\mathrm{q}\to\mathrm{p},i}}{m_{\mathrm{p}}}u'_{\mathrm{p},i}\right\rangle}_{C_{\mathrm{qp}}} \tag{4.5}$$

Analogously to the transport equation for the mono-disperse a diffusive, D, a production term due to the velocity gradient, P, and a fluid term, F, are found. In addition, two particle-particle interaction terms intervene in the budget: one due to the interaction with the lighter particles, C_{pp}, and another one due to the heavier particles C_{qp}. They are respectively equal to $\mathbb{C}_{\mathrm{p}\to\mathrm{p}}\left(\frac{m_{\mathrm{p}}u'_{\mathrm{p},i}u'_{\mathrm{p},i}}{2}\right)/n_{\mathrm{p}}$ and $\mathbb{C}_{\mathrm{q}\to\mathrm{p}}\left(\frac{m_{\mathrm{p}}u'_{\mathrm{p},i}u'_{\mathrm{p},i}}{2}\right)/n_{\mathrm{p}}$. The first one in reality accounts for the interaction of the phase p with itself and the second one may be considered as a coupling term between the particle species, or the one that accounts for the inter-species transfer. The transport equation for the fluctuating kinetic energy of the q-species is analogous and contains the following particle-particle interaction terms C_{pq} and C_{qq}.

The budgets for q_{p}^2 and q_{q}^2, for the cases with higher inertia, B2, B3 and B4 are similar and are respectively given by Figures 4.12, 4.13 and 4.14. The cases with low inertia have a very poor signal to noise ratio. For that reason we mainly focus on the budgets of the cases with high inertia. Regarding those cases, we observe that for both particle species, the principal mechanism of fluctuating kinetic energy creation is the production by the mean velocity gradient P. Also, as expected, the fluid term is negative due to the fluid-friction, being the dominant mechanism of fluctuating energy destruction.

Regarding the particle-particle interaction terms, an interesting behavior is found. We observe that for all the presented cases, while the C_{qp} is positive in the lighter particles budget, the term C_{pq} is negative in the budget of the heavier particles. This consistently indicates on the budget of the lighter particles that fluctuating kinetic energy is transferred through interaction with the heavier particles. Also, it indicates that fluctuating kinetic energy is destroyed on the budget of the heavier particles via interaction with the lighter particles. This is a clear quantitative indication of the transfer of energy from the heavier particles to the lighter particles via particle-particle interaction. In addition, we observe that both C_{pp} and C_{qq} are small compared to the other terms.

A decomposition of the collision term into production and source related terms are further investigated in the next section.

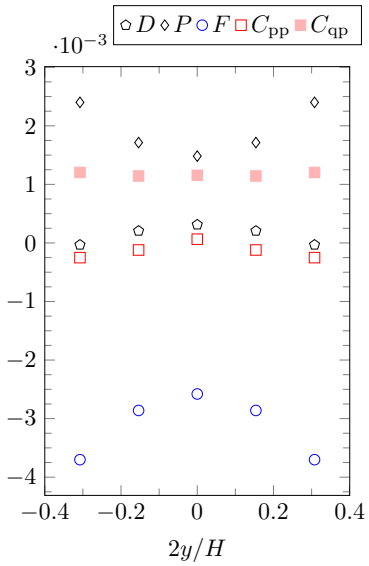

(a) q_p^2 budget

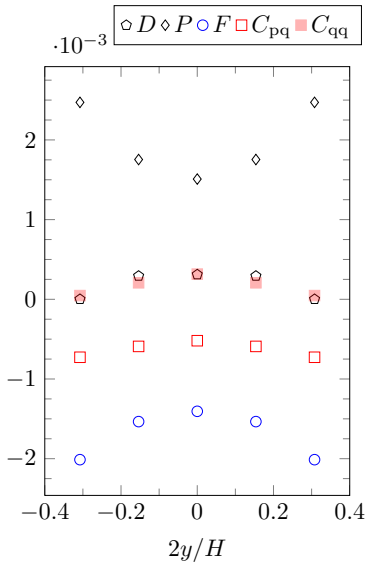

(b) q_q^2 budget

Figure 4.12: Particle fluctuating kinetic energy budget for the case B2. All terms are normalized by H/Vw^2.

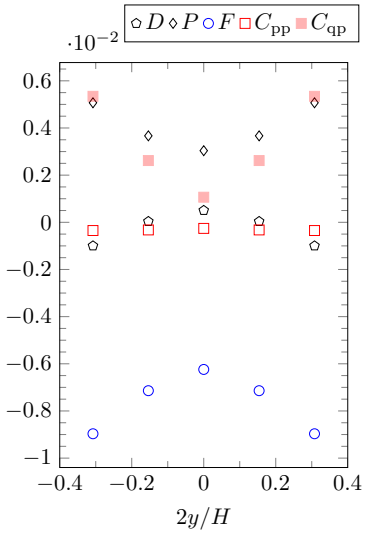

(a) q_p^2 budget

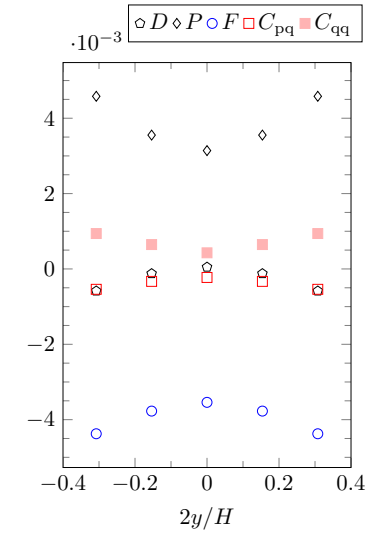

(b) q_q^2 budget

Figure 4.13: Particle fluctuating kinetic energy budget for the case B3. All terms are normalized by H/Vw^2.

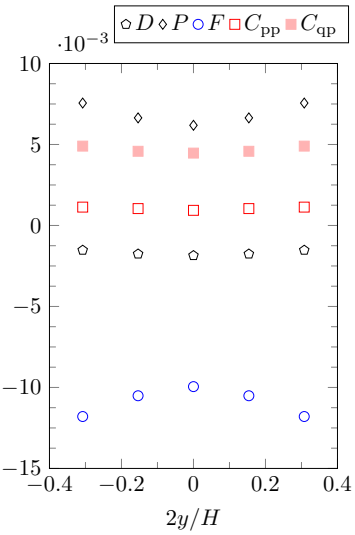

(a) q_{p}^2 budget

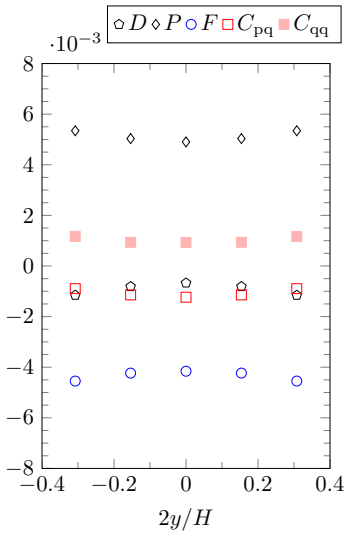

(b) q_{q}^2 budget

Figure 4.14: Particle fluctuating kinetic energy budget for the case B4. All terms are normalized by H/Vw^2.

4.3.2 Particle-Particle interaction term decomposition

The particle-particle interaction terms present in the budgets of the previous section can be further decomposed according to Eq. (2.76), in fact, contracting the indexes, the resulting equation presents as follows:

$$\underbrace{\mathbb{C}_{\mathrm{q}\to\mathrm{p}}\left(m_{\mathrm{p}}u'_{\mathrm{p},i}u'_{\mathrm{p},i}\right)}_{2n_{\mathrm{p}}\left\langle F_{\mathrm{q}\to\mathrm{p},i}u'_{\mathrm{p},j}\right\rangle} = \underbrace{\chi_{\mathrm{qp},ii}}_{\text{source term}} + \underbrace{\frac{\Delta\theta_{\mathrm{qp},iiy}}{\Delta y}}_{\text{collision transport}} + \underbrace{2\theta_{\mathrm{qp},xy}\frac{\Delta U_{\mathrm{p},x}}{\Delta y}}_{\text{collision production}} \tag{4.6}$$

The decomposition of the term on the left-hand side of the equation above, associated to the particle-particle interaction term of the particle fluctuating kinetic energy equation, into the terms of the right-hand side are given by Figures 4.15 to 4.20. It is interesting to note that, even tough the total particle-particle interaction term may seem to have an arbitrary sign, a precise pattern related to the signs of the decomposed terms is found for the shown cases. They are summarized in Table 4.2.

Table 4.2: Sign of the decomposed terms

term	source	transport	production
p → p	-	+	+
p → q	-	+	+
q → p	+	+	+
q → q	-	+	+

Both the collision production and the collision transport terms are positive, while the source term is either negative or positive depending on the specific term. In fact, both the source terms related to the interaction of p with itself and q with itself are negative, which is related to the dissipation of fluctuating kinetic energy through collisions. With respect to the inter-species terms, or coupling terms, we consistently observe that while the source term linked to p → q is negative, the q → p is positive, which indicates that the heavier particles transfer energy to the lighter particles through the source term.

In dilute cases, the collision fluxes tend to be negligible in comparison with the source terms, and the opposite is true as well. This is precisely what happens in the fluctuating kinetic energy budgets as the particle volume fraction augments. As the cases are more dense, the collision fluxes augments and consequently the mechanisms that produce fluctuating kinetic energy through particle-particle interactions, the proportion to the dissipation mechanisms massive overloads it, see Figure 3.42, thus the positive terms in the mono-disperse budgets.

In the bi-disperse cases, as shown in the previous section, the sign of the particle-particle interaction is in fact the result of the proportions of the precisely defined source and flux terms.

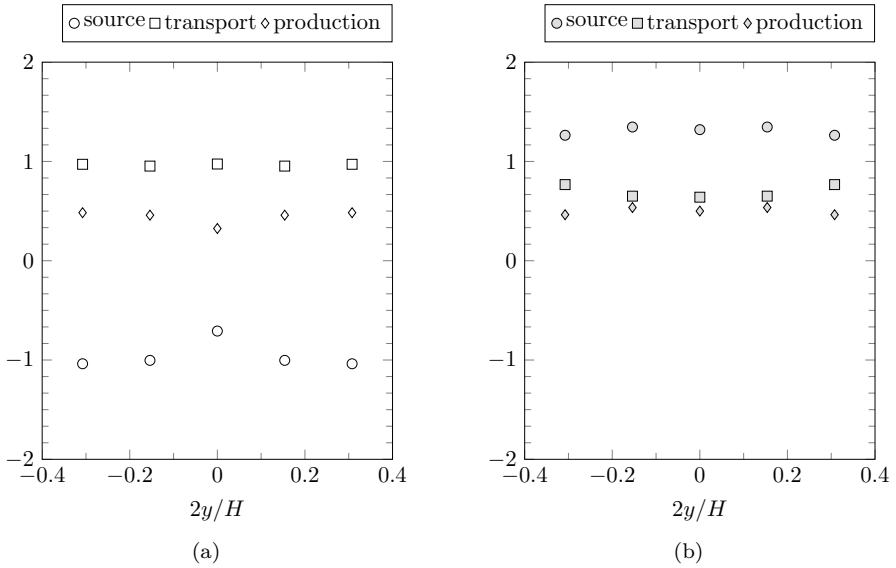

Figure 4.15: Decomposition of the collision terms present in the q_{p}^2 transport equation, into: source, transport and production for the case B2.

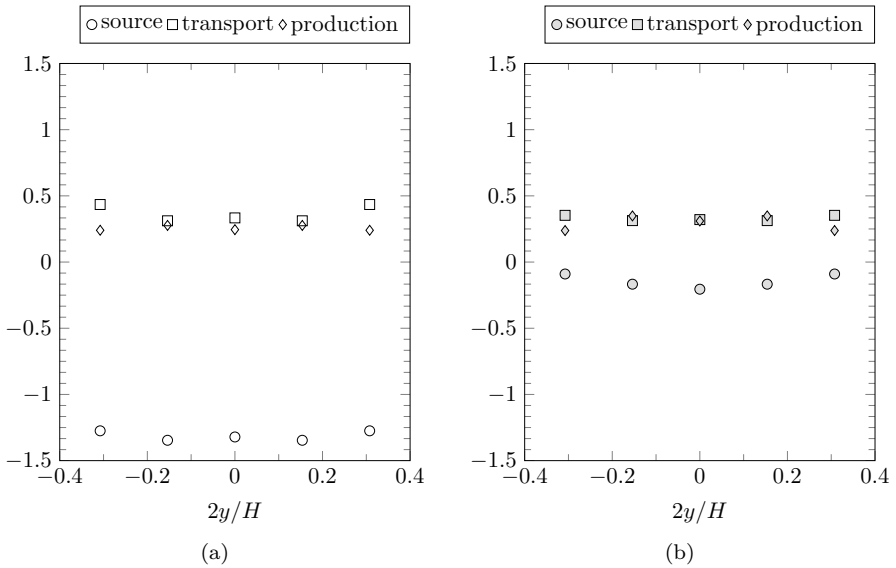

Figure 4.16: Decomposition of the collision terms present in the q_{q}^2 transport equation, into: source, transport and production for the case B2.

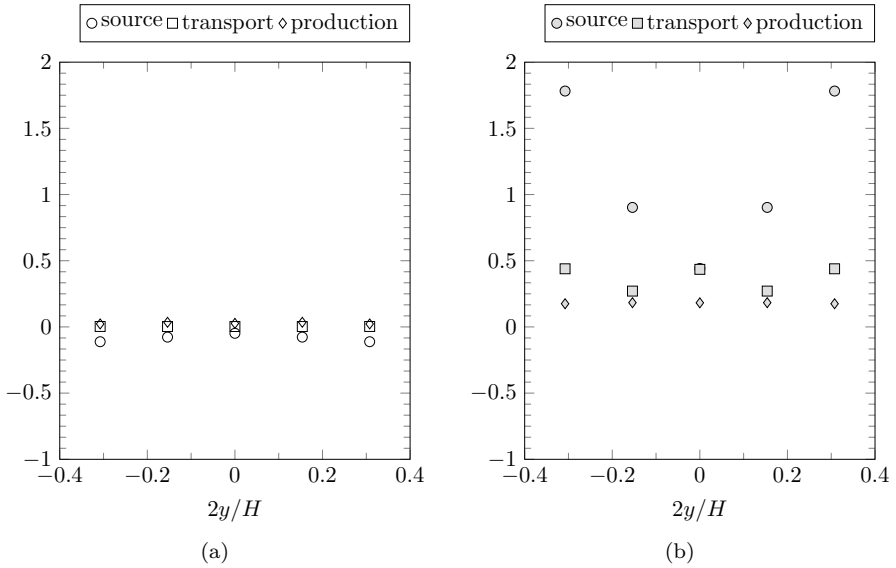

Figure 4.17: Decomposition of the collision terms present in the q_{p}^2 transport equation, into: source, transport and production for the case B3.

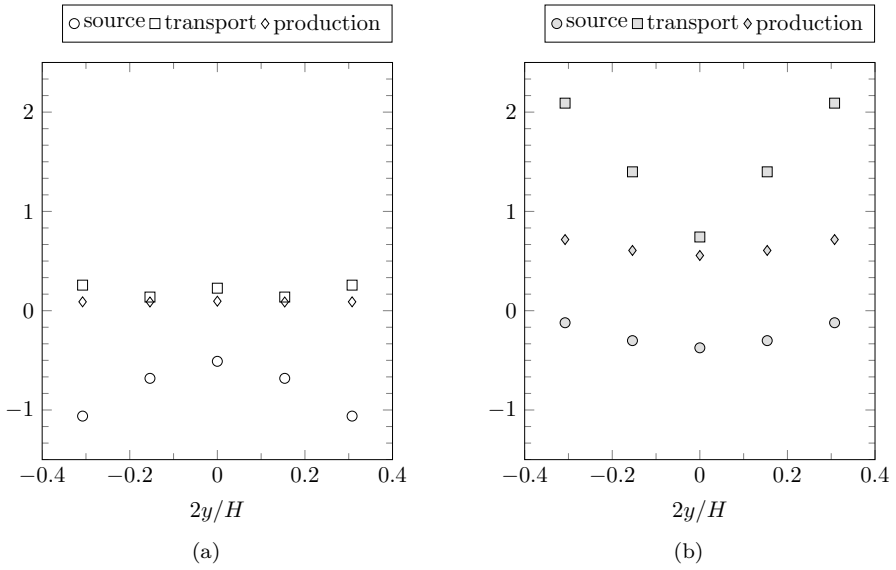

Figure 4.18: Decomposition of the collision terms present in the q_{q}^2 transport equation, into: source, transport and production for the case B3.

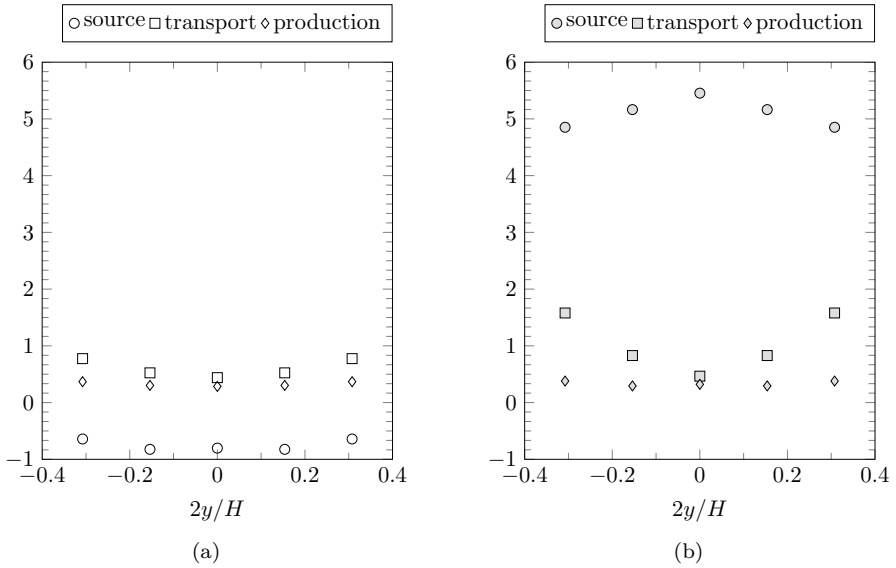

Figure 4.19: Decomposition of the collision terms present in the q_{p}^2 transport equation, into: source, transport and production for the case B4.

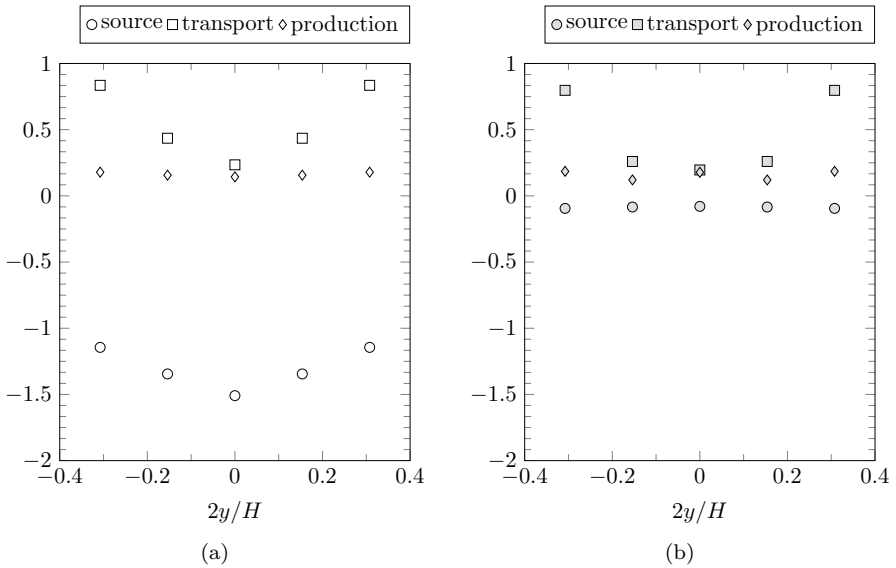

Figure 4.20: Decomposition of the collision terms present in the q_{q}^2 transport equation, into: source, transport and production for the case B4.

4.3.3 Kinetic versus collisional terms

From the particle fluctuating kinetic energy equation, Eq. (4.5), and the decomposition of the particle-particle interaction term, Eq. (2.76), it can be seen that there are two mechanisms of fluctuating kinetic energy production, a purely kinetic P^k_{qp}, and one to the particle-particle interaction: P^c_{qp} . The ratio of the collisional to the kinetic production, is: $P^c_{\mathrm{qp}}/P^k_{\mathrm{qp}} = -\theta_{\mathrm{qp},xy}/n_{\mathrm{p}}m_{\mathrm{p}}R_{\mathrm{p},xy}$.

Normally this ratio tend to zero for very dilute cases, and increase as the particle volume fraction increases. In our bi-disperse cases, the total particle volume fraction does not greatly vary from one case to another. What actually varies is the overall inertia, that augments from case B0 to B4. The ratios of the collisional to the kinetic production are given by Figure 4.21, we note a tendency of diminution of the collisional production with respect to the kinetic one as the particle inertia augments, indicating that the purely kinetic production grows faster with the particle inertia in comparison with the collisional one.

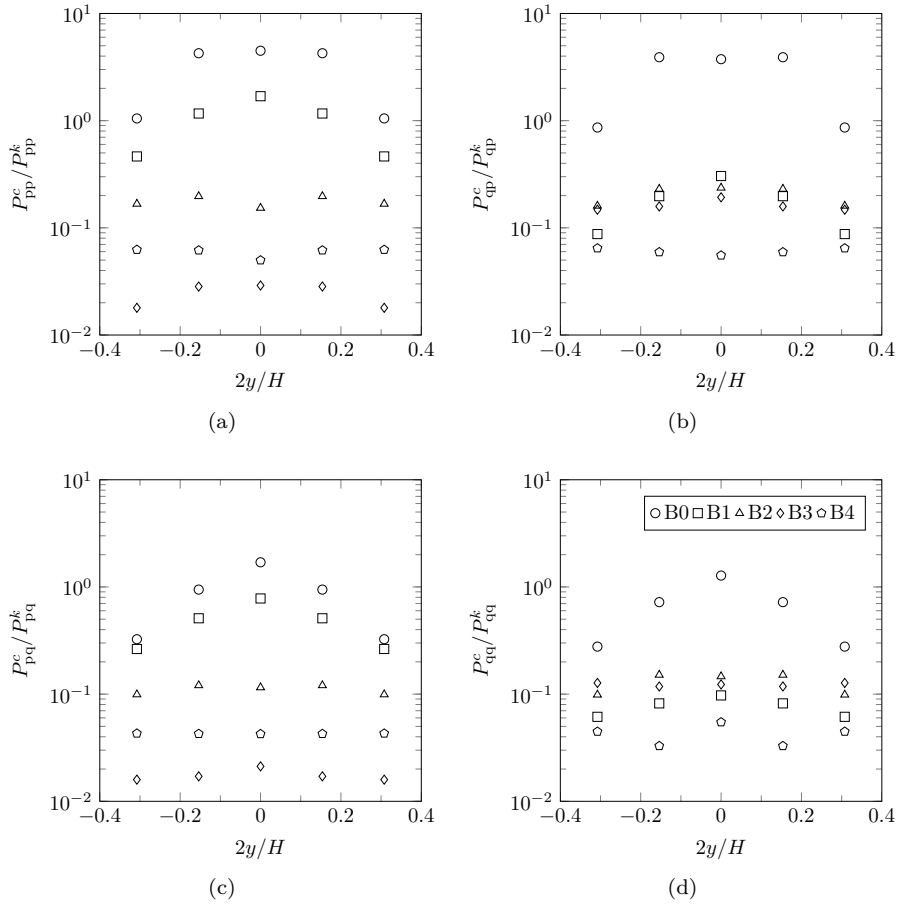

Figure 4.21: Collisional to Kinetic production ratio.

4.4 Particle-Particle interaction modeling

4.4.1 Kinetic theory based collision modeling

In the previous section, the global particle-particle interaction terms were decomposed into flux and source like terms according to the formalism presented in section 2.7. In this section we present a kinetic theory modeling approach, that can be associated to such decomposition formalism.

In the framework of the kinetic theory, the expected rate of change of a given transported variable can be equated in the form a integral over the velocity space, see [18]. This collision integral can be expanded through a Taylor series, into source and flux like terms, see [26]. Notably [10] explored this decomposition for the mono-disperse case, and then [35] extended the methodology for the bi-disperse case. The equations derived by Fede and Simonin. are given in the Apendix A. Specifically, the collision flux is given by Eq. (A.1), and the source, or redistribution term, by Eq (A.2).

Although the formalism shown in section 2.7 is not constrained by any hypothesis of the kinetic theory approach still its methodology can be applied in our case.

Restitution Coefficient

The equations presented in Apendix A require a value for the collision restitution coefficient. In our simulations, even though the dry collision restitution coefficient is set to one, due to lubrication effects, the effective restitution coefficient is in reality different for each interaction, notably depending on the impact conditions.

A formula for the average restitution coefficient $\langle e \rangle$ that takes into account the lubrication effect in a mono-disperse flow has been proposed by [1], and it is given by Eq. (4.7). The formula depends on the values of T_β and V_β, which are respectively given by Eq. (4.8) and Eq. (4.9). Where β is an experimental parameter, and the authors suggest to use the following value: $\beta = 35$.

$$\langle e \rangle = 2e_0 \int_0^\infty u e^{-u^2} e^{-1/\left(2T_\beta^{1/2} u\right)} du \tag{4.7}$$

$$T_\beta = \frac{2}{3} q_\mathrm{p}^2 / V_\beta^2 \tag{4.8}$$

$$V_\beta = \frac{\beta}{4} \frac{d_\mathrm{p}}{\tau_\mathrm{p}} \tag{4.9}$$

The solution to the average restitution coefficient, using $e_0 = 1$, as a function of the parameter T_β is plotted on Figure 4.22. We note that as the value of T_β tends to zero, so the value of the average restitution coefficient tends to zero as well. At the opposite when T_β is very large, then $\langle e \rangle$ tends to e_0. The authors propose the following approximation for $\langle e \rangle$ when $T_\beta \gg 1$, reads:

$$\langle e \rangle \simeq e_0 \left(1 - \frac{1}{2}\sqrt{\frac{\pi}{T_\beta}}\right) \tag{4.10}$$

That approximation, is showed in a red dashed line in Figure 4.22 as well. We note that this formula present a very good approximation for values of $T_\beta > 10^3$.

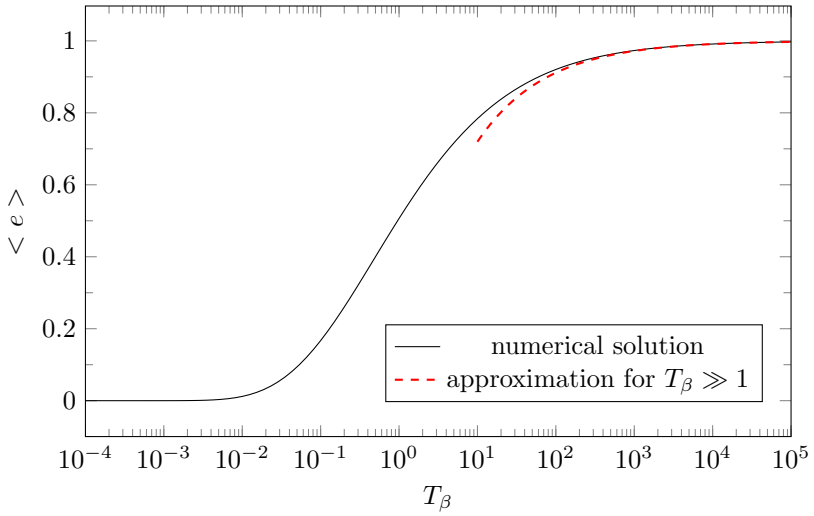

Figure 4.22: Solid line: numerical solution of the mean restitution coefficient, given by Eq. (4.7) which takes into account the lubrication effect for $e_0 = 1$. Dashed line: approximate formula for $T_\beta \gg 1$.

In order to account for the bi-dispersion, the bi-disperse relaxation time, τ^*, is used at Eq. (4.9). In addition to that, the fluctuating kinetic energy is pondered by the product of the particle number density times the particle density, in the formula of T_β, thus yielding the following variables for the collision pair pq:

$$T^*_{\beta,\mathrm{pq}} = \frac{2}{3}\frac{1}{V^{*2}_\beta}\left(\frac{n_\mathrm{p}\rho_\mathrm{p}q^2_\mathrm{p} + n_\mathrm{q}\rho_\mathrm{q}q^2_\mathrm{q}}{n_\mathrm{p}\rho_\mathrm{p} + n_\mathrm{q}\rho_\mathrm{q}}\right) \tag{4.11}$$

$$V^*_\beta = \frac{\beta}{4} d_\mathrm{p}/\tau^*_\mathrm{p} \tag{4.12}$$

Substituting the variable $T^*_{\beta,\mathrm{pq}}$ on Eq. (4.7), would then yield the effective restitution coefficient related to the collision pair pq: $\langle e_\mathrm{pq}\rangle$. Which is used to compute the collision fluxes and restitution terms presented in the next sections. The other restitution coefficients related to the other collision pairs can be easily found in an analogous manner.

For our simulated cases, we obtain values of T^*_β in the order of magnitude of $\sim 10^0$. Indicating that the approximation formula given by Eq. (4.10) cannot be used. Hence, the integral of Eq. (4.7) is numerically solved.

Computed values of the mean restitution coefficient for all the cases are given by Figure 4.23. We note that as the overall particle inertia, or bi-disperse Stokes number, of the cases augment the computed mean restitution coefficient augment as well. Furthermore, we observe that the order of magnitude of the coefficients $< e_{\mathrm{pp}} >$, $< e_{\mathrm{qq}} >$ and $< e_{\mathrm{pq}} >$ are close to one another. Those values are going to be used in the next sections withing the frame of the comparison of our resolved data with available models.

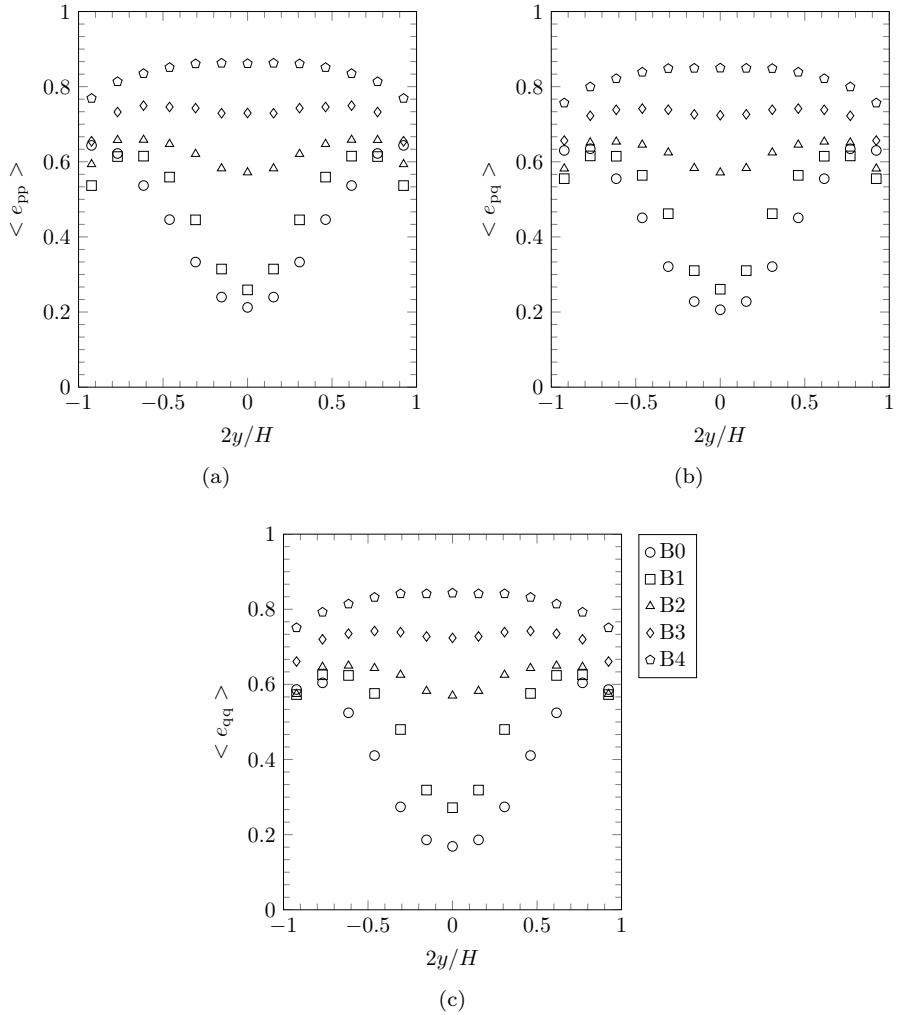

Figure 4.23: Mean restitution coefficient computed for all the cases: (a) $< e_{\mathrm{pp}} >$, (b) $< e_{\mathrm{qq}} >$ and (c) $< e_{\mathrm{pq}} >$.

4.4.2 Momentum collision flux term

A sensibility test for the collision flux model, given in Appendix A, is performed by varying the restitution coefficient and the parameter g_0 also discussed in the Appendix A. Specifically for the bi-disperse case, the parameter g_0 can be computed by Eq. (A.9), yielding $g_0 = g_0^{\mathrm{pq}}$. The sensibility test, for a component of the collision flux, of the case B2, is presented by Figure. 4.24.

The proposed formula for the restitution coefficient given in the last section, as well as two other constant restitution coefficients are tested. In addition to that, the parameter g_0^{pq} is either computed through the formula or set to one.

For this specific case, we note that the parameter pair $(g_0, e) = (1, 1)$, seems to have a good agreement compared with the data. If the value of the restitution coefficient is set to one and g_0^{pq} is used, the model overestimate the results. Maintaining however g_0 equals to one and computing the average restitution coefficient either through the formula or setting it to 0.5, the model underestimates the collision flux. Interestingly, when both parameters are used, $(g_0, e) = (g_0^{\mathrm{pq}}, < e >)$, then the curve seem to fall into tendency of the results from the our simulations. Even tough in this case both the simple combination $(g_0, e) = (1, 1)$ and $(g_0, e) = (g_0^{\mathrm{pq}}, < e >)$ give comparable good results, in other cases, the latter combination is the one that best fits our data, and for that reason it is the retained one.

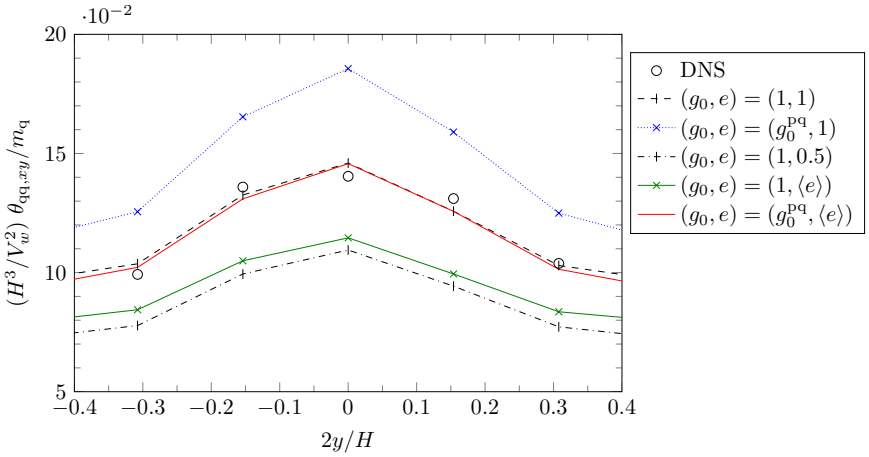

Figure 4.24: Collision flux measured in DNS for the case B2 and the model prediction for several radial distribution function and restitution coefficient.

Using the retained parameters, all the components of the other cases are compared. In Figure 4.25, 4.26 and 4.27 are respectively given the terms of the collision flux tensor for the cases B2, B3 and B4, corresponding to the cases with relatively higher inertia. We note that there is an overall agreement with the results.

Regarding the other cases, B0 and B1, the comparison are respectively given by Figures 4.28 and 4.29. For those cases however, we note that the model seem to underestimate the value of the collision flux in the stream-wise direction, while maintaining a good prediction of the other components related to other components of the tensor.

Higher Stokes

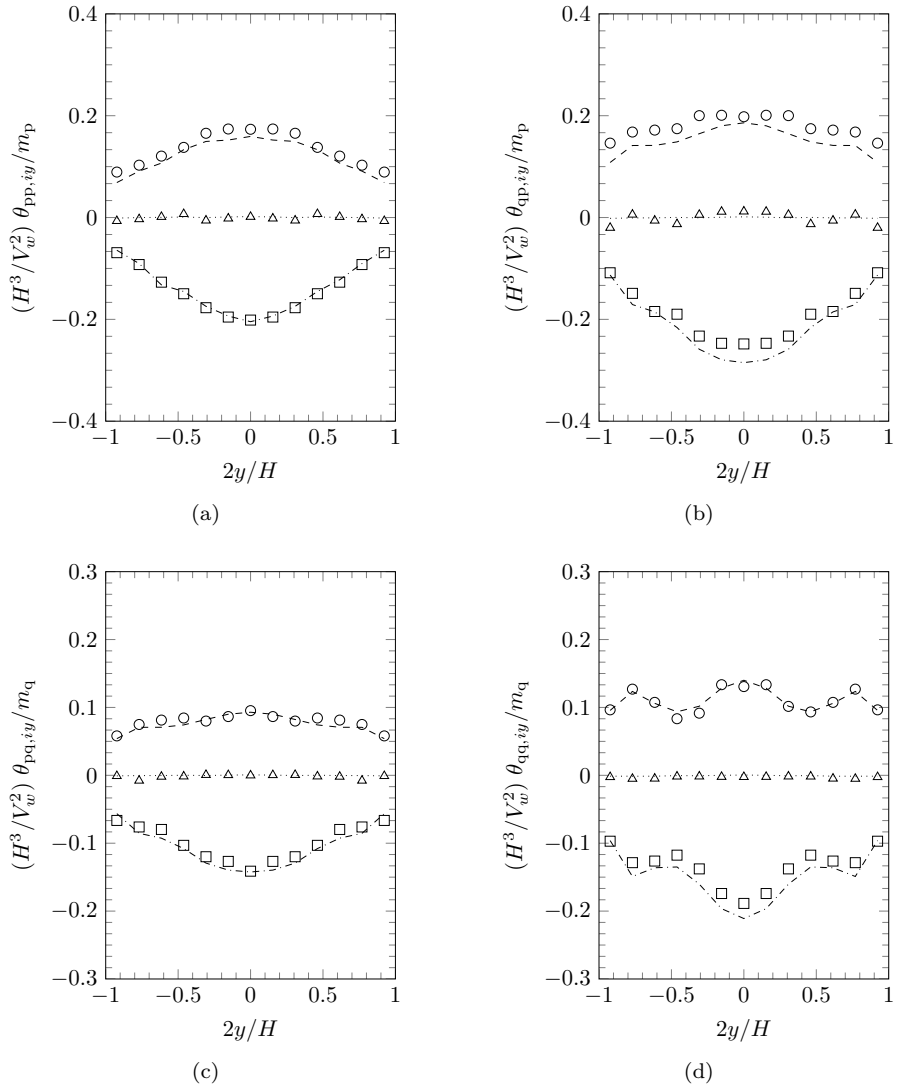

Figure 4.25: Comparison of the collision flux with the available model for the case B2. The symbols are: DNS (xy) (○); DNS (yy) (□); DNS (zy) (△); model (xy) (_ _); model (xy) (_ . _); model (xy) (.....).

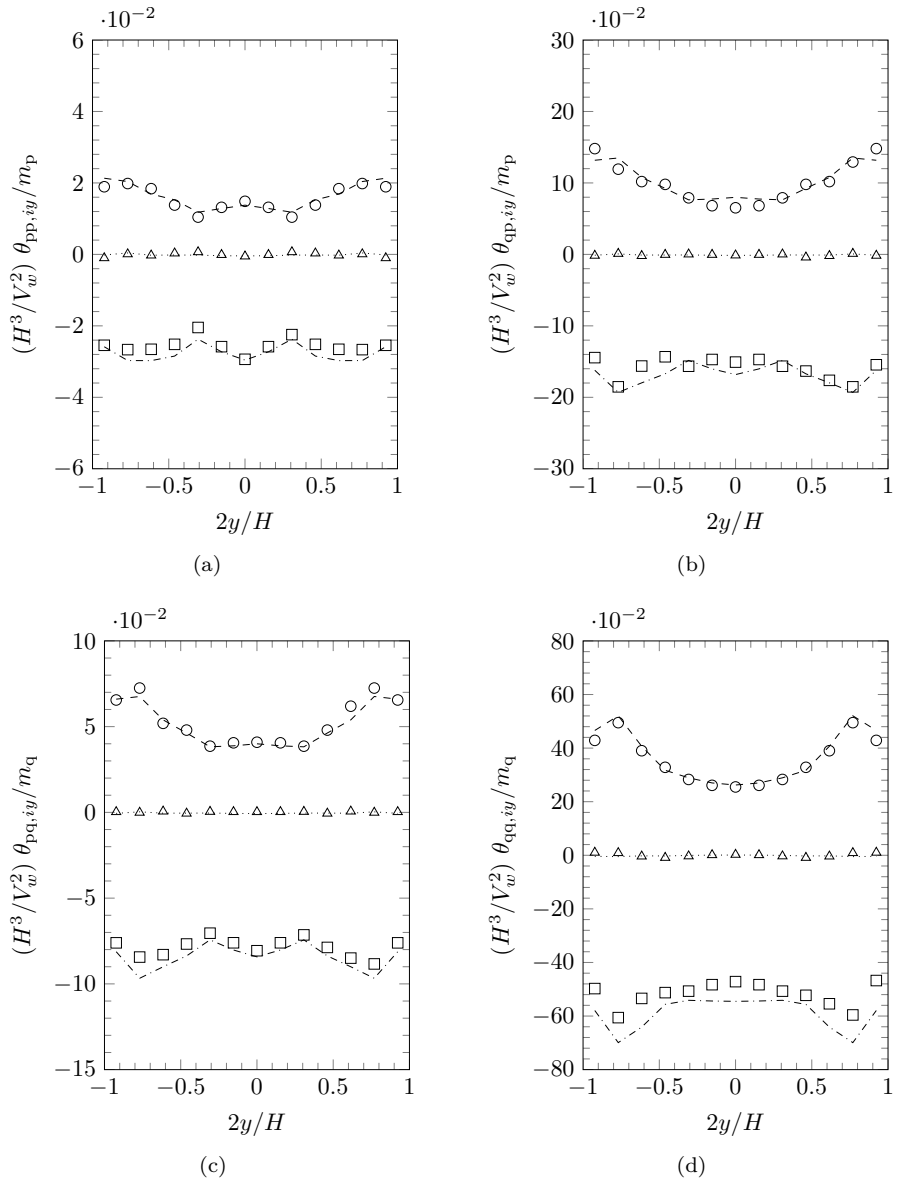

Figure 4.26: Comparison of the collision flux with the available model for the case B3. The symbols are: DNS (xy) (○); DNS (yy) (□); DNS (zy) (△); model (xy) (- - -); model (xy) (- · -); model (xy) (·····).

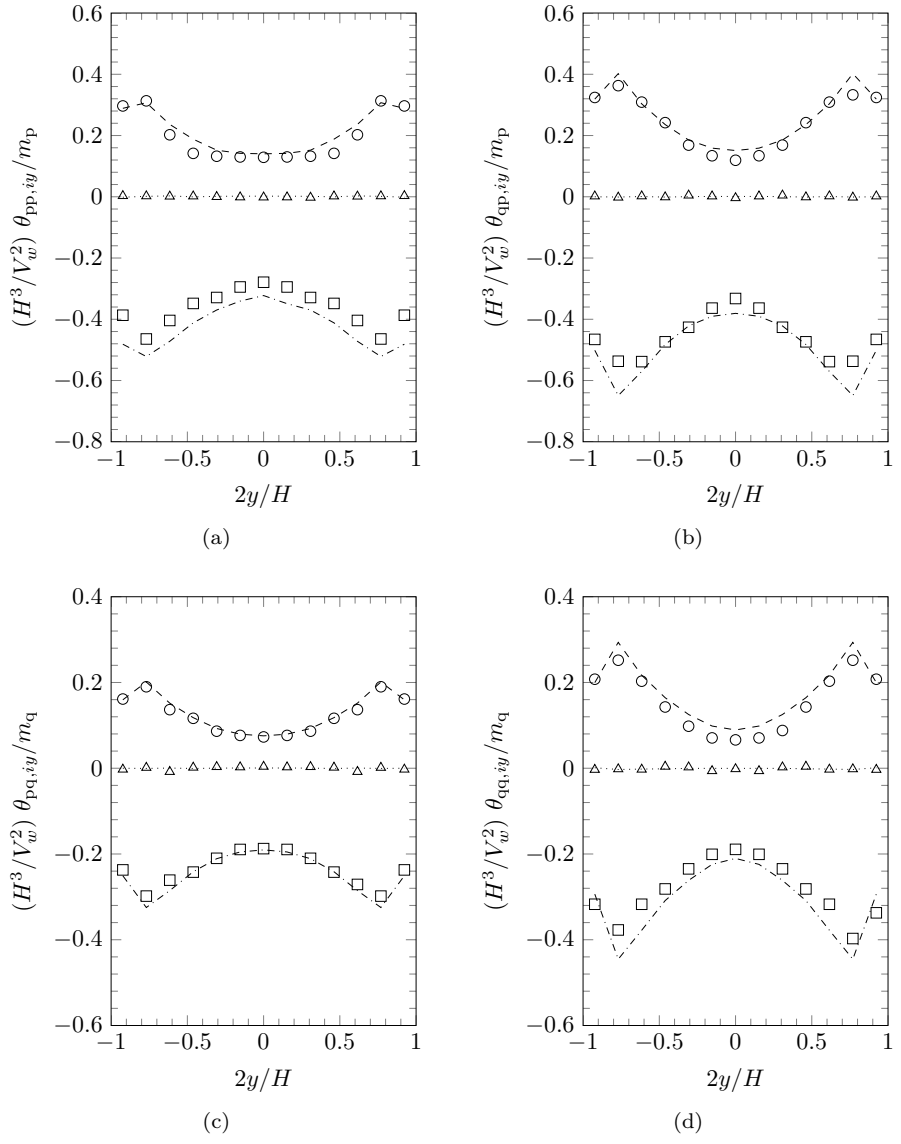

Figure 4.27: Comparison of the collision flux with the available model for the case B4. The symbols are: DNS (xy) (○); DNS (yy) (□); DNS (zy) (△); model (xy) (_ _); model (xy) (_ . _); model (xy) (.....).

Lower Stokes

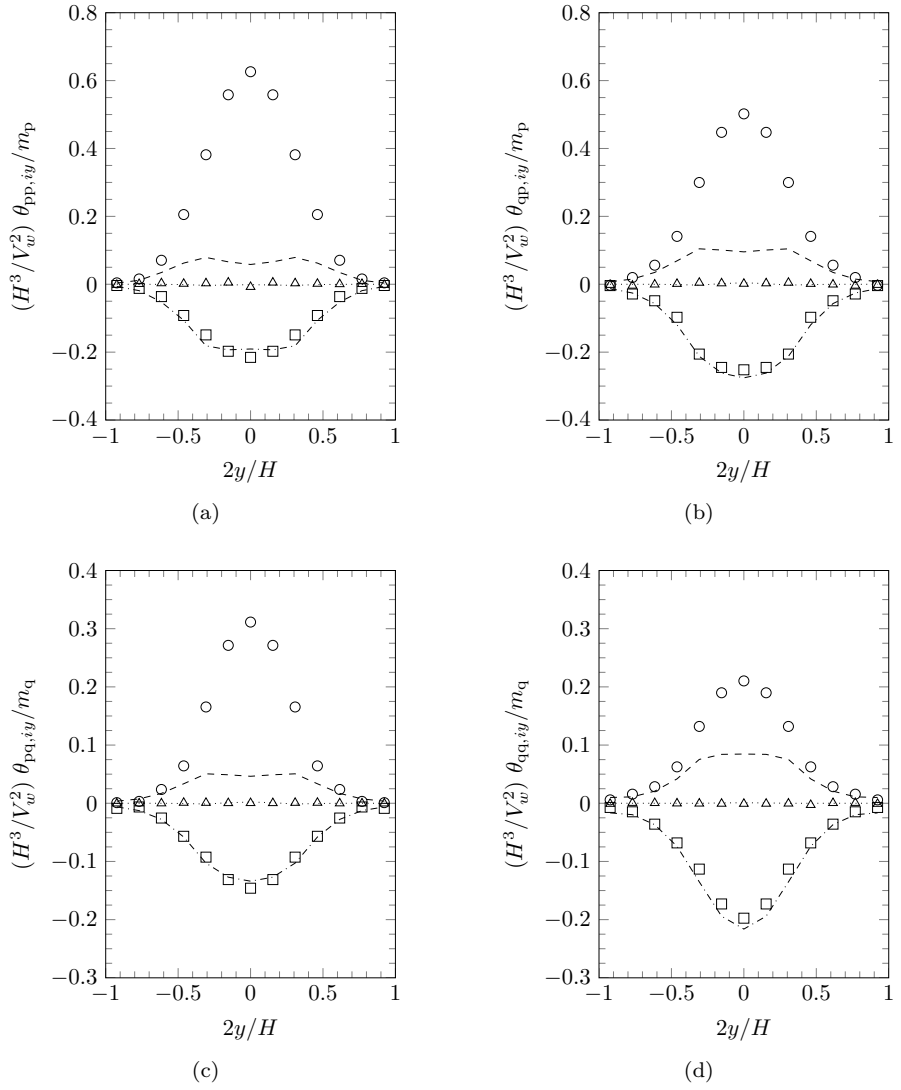

Figure 4.28: Comparison of the collision flux with the available model for the case B0. The symbols are: DNS (xy) (○); DNS (yy) (□); DNS (zy) (△); model (xy) (- - -); model (xy) (-·-·-); model (xy) (·····).

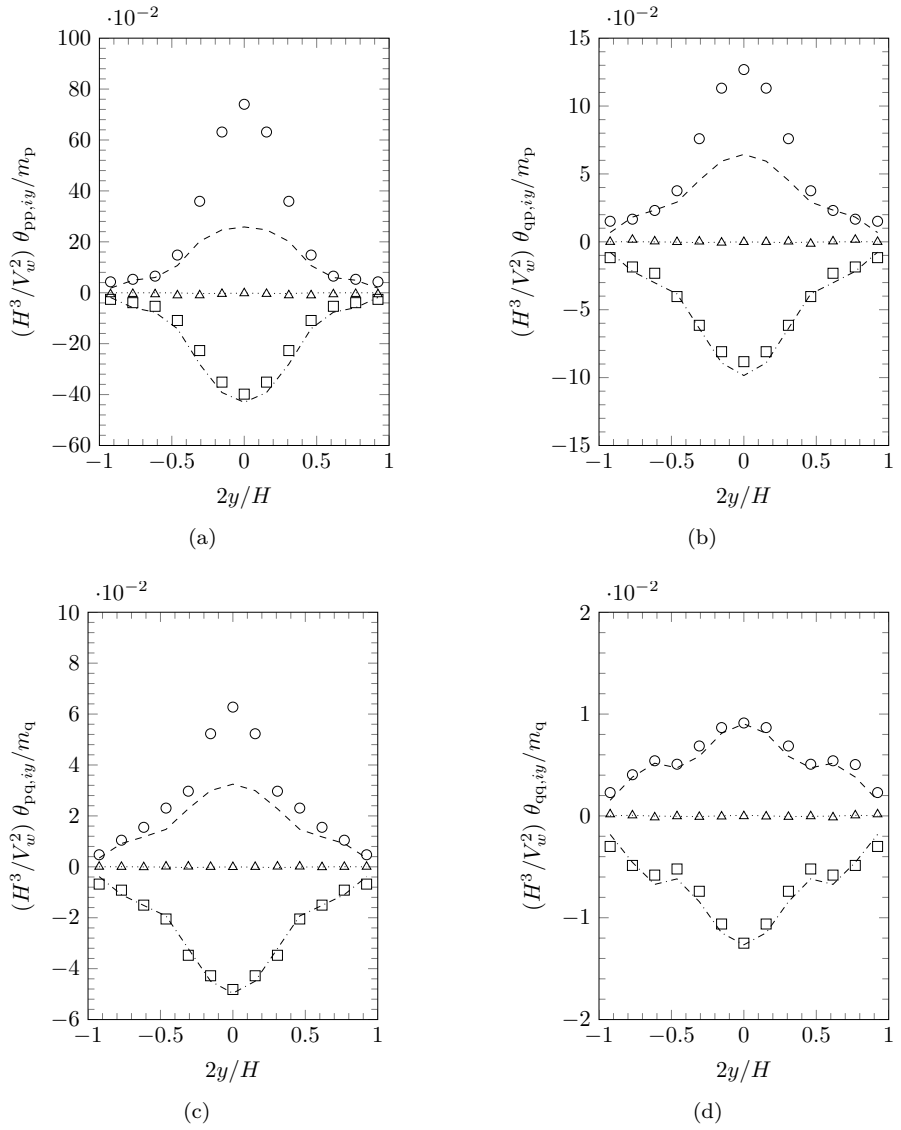

Figure 4.29: Comparison of the collision flux with the available model for the case B1. The symbols are: DNS (xy) (○); DNS (yy) (□); DNS (zy) (△); model (xy) (- -); model (xy) (-.-); model (xy) (.....).

4.4.3 Kinetic stress source term

Using the same parameters for the average restitution coefficient and g_0 parameter (see Figure 4.23 and 4.24), the kinetic stress source term for the cases B2, B3 and B4 are compared with our results, using Eq. (A.2), in Figures 4.30, 4.31 and 4.32. We observe that the model predicts the good order of magnitude of the results. As opposed to the results for the momentum collision flux, the results for the kinetic source term seem to need more significative statistical events to properly converge.

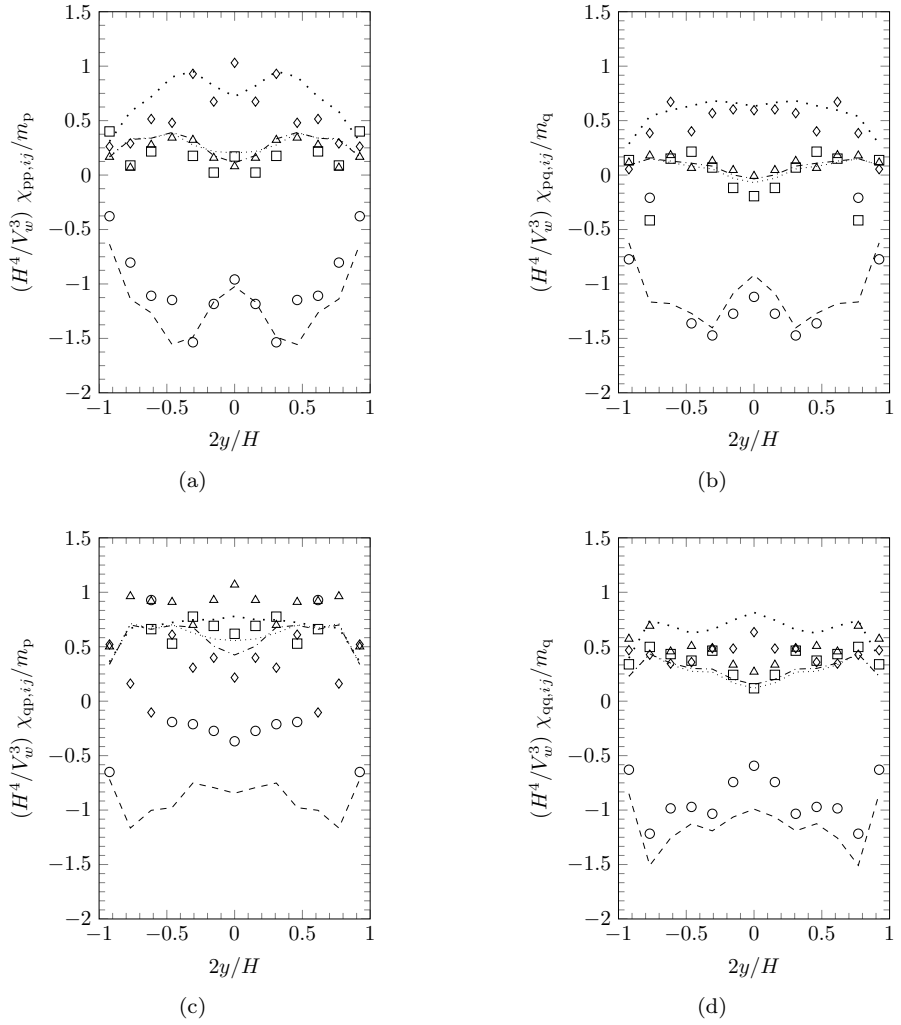

Figure 4.30: Comparison of the source term with the available model for the case B2. The symbols are: DNS (xx) (○); DNS (yy) (□); DNS (zz) (△); DNS (zy) (◇); model (xx) (_ _); model (yy) (_ . _); model (zz) (. . . . .); model (xy) (. . .).

For all the cases, we observe that the kinetic stress source term associated with the stream-wise variance is negative while the other two related to the orthogonal directions are positive. This is the isotropization effect through

the source term, where variance is taken from the stream-wise direction and redistributed to the wall-normal and span-wise directions. A similar effect have been observed in the mono-dispersed cases in [11].

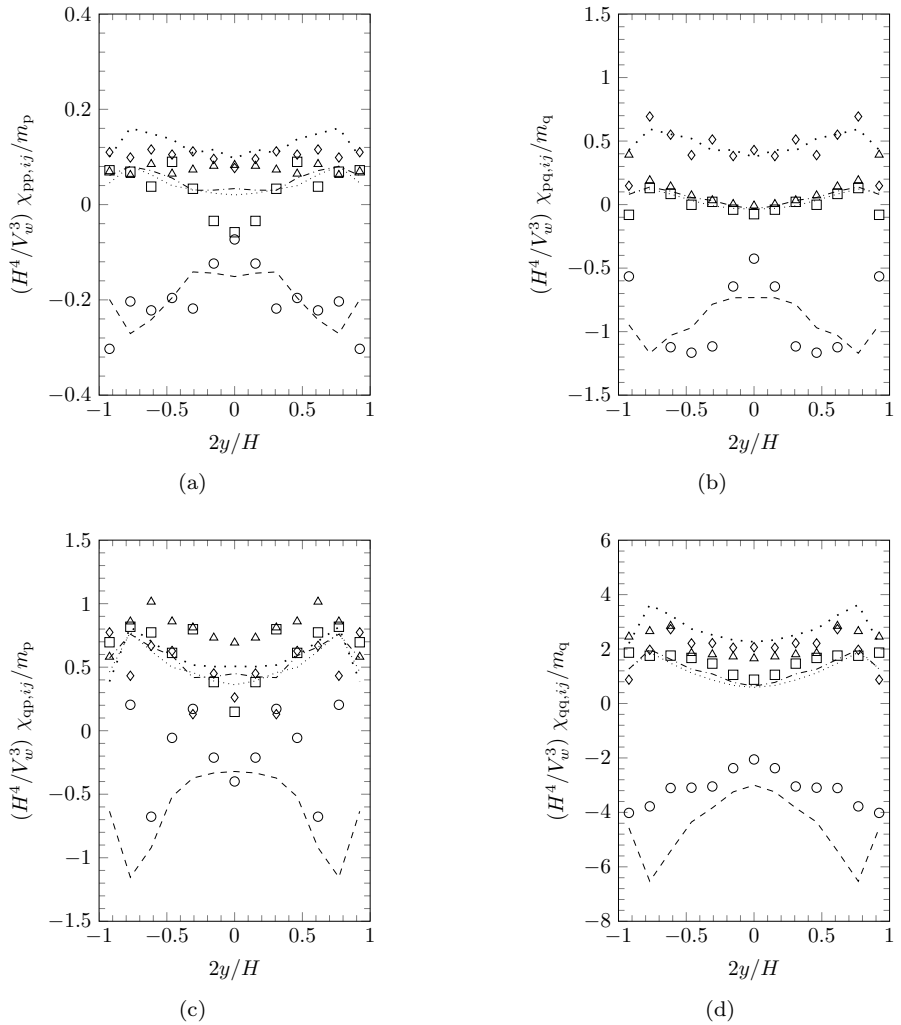

Figure 4.31: Comparison of the source term with the available model for the case B3. The symbols are: DNS (xx) (○); DNS (yy) (□); DNS (zz) (△); DNS (zy) (◇); model (xx) (- - -); model (yy) (-.-.-); model (zz) (.....); model (xy) (. . .).

Since there is almost no-slip between the lighter and heavier phases, the results related to the momentum source term are unusable. The results are close to zero, and therefore a comparison of zero equals to zero yields no significant value, for that reason only the kinetic stress source term is analyzed.

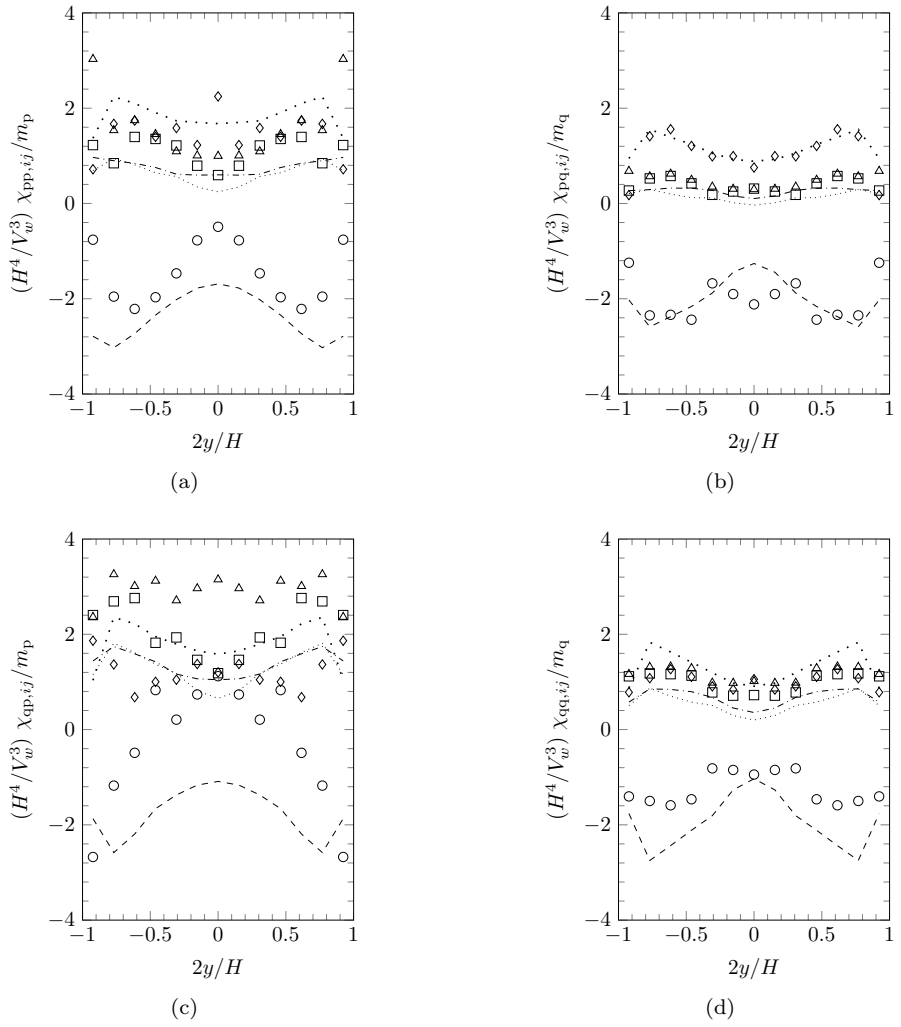

Figure 4.32: Comparison of the source term with the available model for the case B4. The symbols are: DNS (xx) (○); DNS (yy) (□); DNS (zz) (△); DNS (zy) (◇); model (xx) (- -); model (yy) (-·-); model (zz) (·····); model (xy) (. . .).

4.4.4 Kinetic stress collision flux term

We have also, measured the kinetic stress collision flux for the cases B2, B3 and B4. They are given by Figures 4.33, 4.34 and 4.35. Similarly to the momentum collision flux shown in section 4.4.2, the kinetic stress collision flux coverges quicker than the source terms with results having a high signal to noise ratio.

For the cases B2 and B3, we observe that the only non-null kinetic stress collision fluxes are those related to the stream-wise variance and the principal shear kinetic stress, that is θ_{xxy} and θ_{xyy}, with a positive slope for the first and negative one for the second.

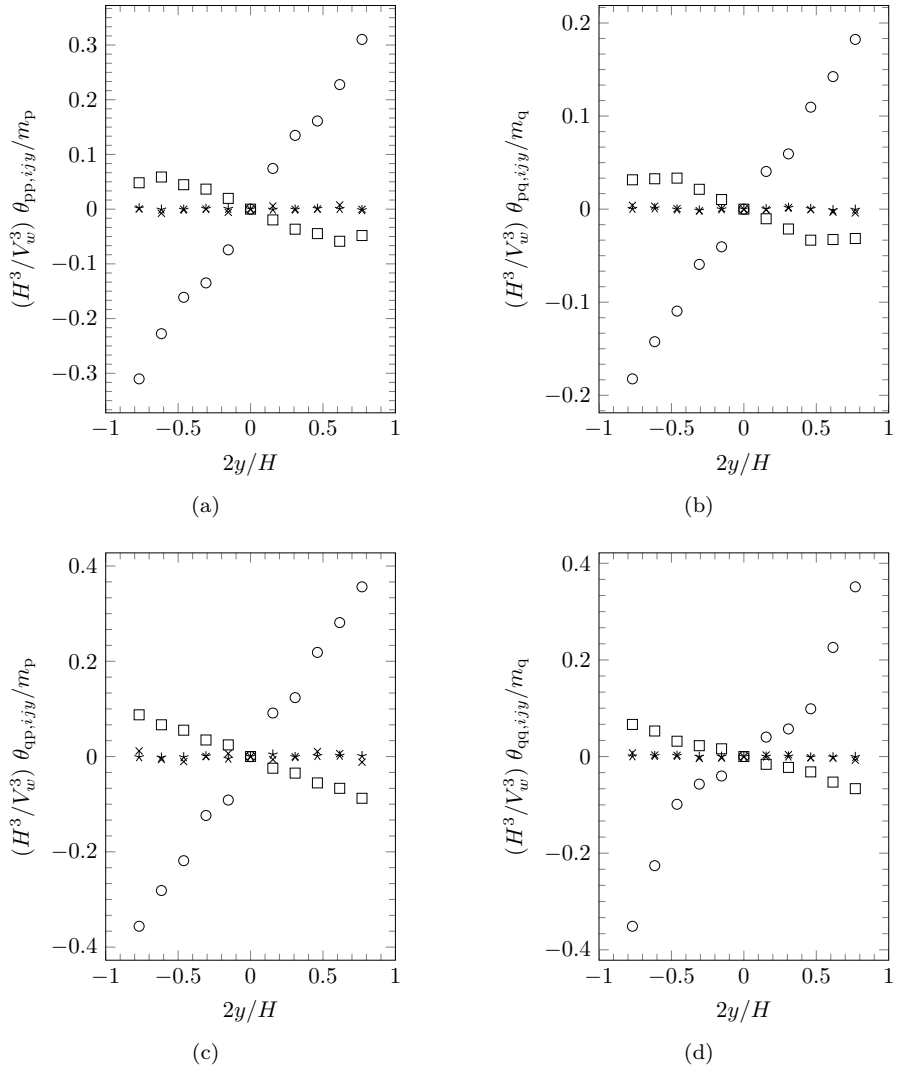

Figure 4.33: Comparison of the kinetic stress collision flux with the available model for the case B2. The symbols are: DNS (xxy) (○); DNS (yyy) (×); DNS (zzy) (⋆); DNS (xyy) (□).

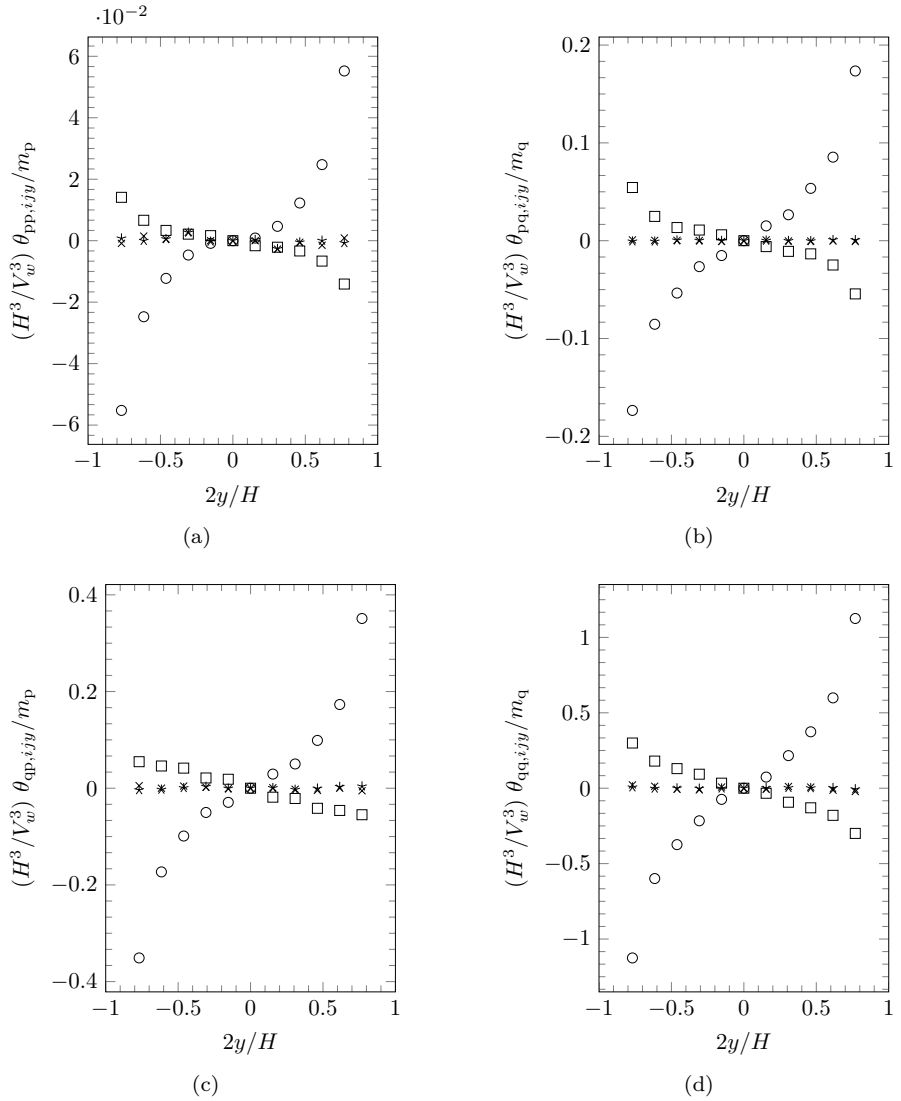

Figure 4.34: Comparison of the kinetic stress collision flux with the available model for the case B3. The symbols are: DNS (xxy) (○); DNS (yyy) (×); DNS (zzy) (⋆); DNS (xyy) (□).

Similar results are found for the case B4 as well with the exception that in this case a slightly negative slope for the kinetic stress collision flux related to the wall-normal direction is found.

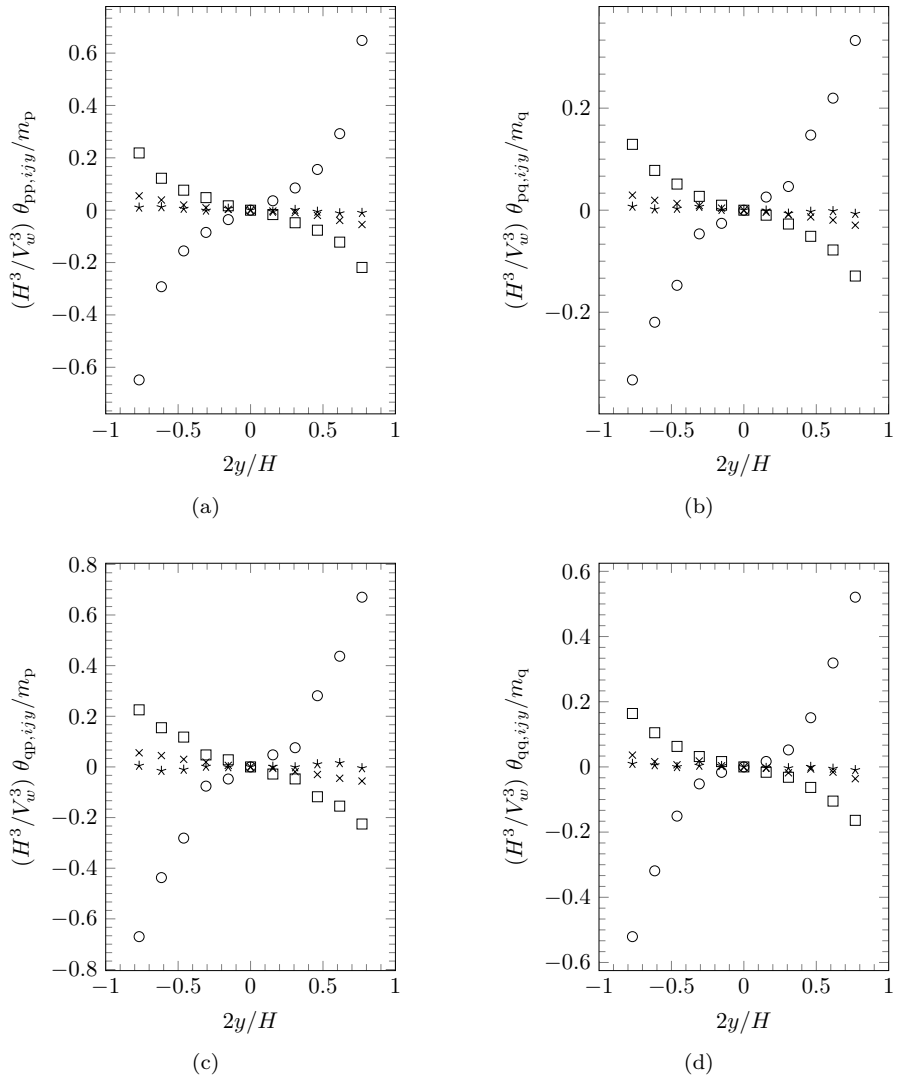

Figure 4.35: Comparison of the kinetic stress collision flux with the available model for the case B4. The symbols are: DNS (xxy) (○); DNS (yyy) (×); DNS (zzy) (⋆); DNS (xyy) (□). model (xy) (- - -); model (xy) (- · -); model (xy) (·····).

Conclusion and Perspectives

Concluding remarks

A particle resolved numerical simulation tool, based on the tensorial viscous penalty method, that allows the resolution of the fluid-flow around the moving particles was used to investigate both mono and bi-disperse fluid-particle flow in a Couette configuration. The aim is to comprehend, test, improve and develop macroscopic models in the frame of the kinetic theory of granular flow, notably leveraging the level of detail contained in the resolved simulations.

Related to the code, an optimization of the parallelism was performed, which greatly improved the performance of the code, allowing for the cases investigated in this thesis to be computed with much less computational cost.

A hybrid Eulerian-Lagrangian statistical approach was introduced, consisting in two different formalisms, one associated to Eulerian averaging for the fluid phase and another Lagrangian averaging for the particle phase. The first one is based upon the characteristic phase operator, and with that, transport equations for the fluid taking into account the exchanges occurring in the fluid-particle interfaces are obtained, and associated with it, average transport equations such as the fluid fluctuating kinetic energy transport equations are derived.

The Lagrangian averaging for the particles, is primarily based upon a fine-grained probability density function and the Liouville's formalism. Transport of equation of average particle quantities such as the mean particle velocity and particle kinetic stress equations were derived. An original aspect about such equations is that they allow for the precise separation of the particle-particle and fluid-particle interaction terms. Also, no assumption of instantaneous collisions are presupposed, indeed, long duration contacts are allowed. As a matter of fact, the formalism presented in this thesis could be easily applied to electric fields, or other types of forces as well. A link between the two statistical formalism's is explored with a discussion about the exchange terms, occurring at the fluid-particle interfaces. It is also shown how such terms can be extracted from our numerical simulations.

We also show an original decomposition of the particle-particle interaction terms into source and flux terms. Such a decomposition allows for the better comprehension of the physical mechanisms playing a role in the transport equations, clearly separating production, dissipation and inter-particle-species transfer of energy, or more precisely in our case, how particles generate fluctuating kinetic energy as they collide or how they transfer variance of velocity

from a direction to another. Moreover, with such a separation one can perceive the fact that the collisional flux related terms become more important as the particle volume fraction augments, while source related terms are dominant in very dilute flow, thus clearly separating the mechanisms associated to the dilute and dense particle flows. Further, a link with such a decomposition and a decomposition linked to the kinetic theory of granular flow was also discussed during the analysis.

Six mono-disperse cases in moderately dense regimes were investigated, with the particle volume fraction varying from 5% to 30% and the bulk Stokes number, which is a non-dimensional number that characterizes the particle inertia in a given fluid environment, ranging from 15 to 30. We observe that a macroscopic transition occurs in that range, with the particles accumulating more near the centre for low bulk Stokes numbers, and the opposite, with particles accumulating more near the walls for the higher Stokes number. This transition was latter explained in the thesis by the action of two opposite physical mechanisms, in fact, on one hand, the fluid pushes the particles to the centre of the core flow and on the other hand, particle pressure, associated with particle variance and collisions between the particles, expels the particles from the centre. In order for the particle flow win the fluid action pushing it toward the centre, it has to produce enough fluctuating kinetic energy, and since the mechanisms of production are proportional to the gradient of mean particle velocity, the Stokes number is thus the good parameter to characterize such a transition, indeed, it is directly proportional to particle velocity gradient and inversely proportional to the fluid-particle response time, which is associated to the fluid-particle force.

As a first analysis, macroscopic parameters such as the local particle number density, particle volume fraction and mean fluid and particle velocities were extracted from resolved simulations. As a result from the fore-mentioned transition, the shape of the volume fraction profiles change from concave to convex as the Stokes number augments. Also, we observe that both the particles and the fluid have approximately the same mean velocity, hence with a very small mean slip between the phases. Based on such slip, the particle Reynolds number is found to be ranging between $10^{-3} \sim 10^{0}$, thus relatively small.

In addition, particle and fluid fluctuating kinetic energies are measured, and similarly, due to the transition, the shape of such curves change, but this time, from convex to concave. As a matter of fact, a inverse relationship is found between the particle number density and the particle fluctuating kinetic energy, which has its explanation roots into the so-called particle pressure effect, where regions of higher variance are accompanied by regions of lower particle number density. This can be easily demonstrated as result of the transport equations. Additionally, we also found that the fluctuating kinetic energy of the fluid phase is systematically smaller than that of the particles. This was latter explained in the thesis to be related to the fact that the particles actually pilot the flow and not the other way around, which is different from gravity driven flows, where fluid fluctuations drive the particle fluctuations.

Statistics of the fluid flow are investigated, such as pressure, Reynolds stresses and viscous dissipation are given. Related to the diagonal terms of the Reynolds stresses, we observe that for all the cases the component associated to the stream-wise direction are systematically larger than the other ones, which is related to the fact that the mechanisms of variance productions are primarily linked to this direction. Concerning the Reynolds shear stresses we observe that

the only non-null term is the one related to the shearing plane.

Further, both the viscous dissipation associated to the transport equation of the mean kinetic energy and that of the fluctuating kinetic energy are measured from our resolved simulations, and, as expected, the order of magnitude of the dissipation is larger for the cases with high Stokes number, as those cases are more energetic. Based upon those values, spatial and temporal scales associated to the fluid fluctuating kinetic energy are evaluated and compared to other relevant scales. With respect to the spatial scales, they are compared to the particle diameter and the average interstice length between the particles, this showed that those scales are in fact confined between the particles. Also, a similar analysis with temporal scales showed that those scales are smaller than the particle response time. This bespeaks to the fact that the fluid fluctuations are probably wakes, confined between the particles, generated as the fluid passes through. Such analysis is also backed up by the budget analysis of the fluid fluctuating kinetic energy, which shows that mainly fluid variance is created by the particles.

With respect to the particle statistics, we first evaluate the local Stokes based on the local mean velocity gradient and compare it to the bulk Stokes number. For the cases with bulk Stokes number equal 15, or the cases with smaller inertia, the local Stokes number in the center of the core flow is found to be much smaller, being close to 1, whereas for the cases with bulk Stokes number equal to 30, values of about 25 are found in the center of the core flow. This occurs due to the fact that the mean velocity gradient for the cases of small inertia are greatly diminished in the center of the core flow.

Particle velocity fluctuations such as the particle kinetic stress, third and fourth order correlations are shown and analyzed in the context of the fluid-particle flow. The overall profiles of particle kinetic stresses are very similar to those of the Reynolds shear stresses, with the velocity variance related to the stream-wise being the larger one among the principal directions, and the shear stress related to the applied shear being the only non-null one. The fact that the particle kinetic stress is similar to the Reynolds stress is thoroughly explained latter by the analysis of the budgets of the transport equations.

Still related to the particle kinetic stress, we also studied the anisotropy coefficient and an inverse relationship with the particle volume fraction is found, which is associated with the fact that more particles promote more particle-particle interactions and consequently more the mechanisms of energy redistribution, or isotropization, through collisions. The Boussinesq approximation with a standard eddy-viscosity-like, or kinetic viscosity closure, in this case, is investigated. Related to such viscosity, a direct relationship with the particle inertia and and an inverse relationship with the particle volume fraction is found. Further, a Knudsen number related to such viscosity is computed and it is found to be very small, in the order of magnitude of 10^{-4}, showing that the cases are in fact close to a local equilibrium. We also examined the predicted values of the kinetic viscosity against available modeling in order to comprehend the trend of the data.

Regarding the third order correlations, we tested the consistency of the so-called Grad approximation and the gradient model. In such inquiry, we calculate whether such equations predict the correct correlation given the data of other correlations. And indeed, those correlations were consistent with the data. Another Knudsen number, based on the gradient model coefficient is computed,

and again, it also indicated a system close to the equilibrium. With respect to the forth order correlations, we tested the Grad and Gaussian approximation, and we found that the Gaussian approach is more consistent with out data set. The fact that the models of third and fourth order correlations are nicely consistent with the models is related to the fact that the systems are close to a equilibrium, which were indicated by the Knudsen numbers.

The budgets of the transport equations related to the fluid-particle flow were computed from our resolved simulations and investigated to understand local physics of the fluid-particle flow. In the mean wall-normal particle velocity budget for instance we noticed that the fluid pushes the particles towards the centre of the core flow. In the budget of the fluid fluctuating kinetic energy we noted that nearly all the production of it comes from the interaction with the particles. This in conjunction with analysis of the its scales, as already stated, indicates that fluid variance comes mainly through the direct interaction with the particles and, as the fluid passes through it, it creates wakes that remain confined in between the interstices of the particles.

In the budget of the particle fluctuating kinetic energy, we observed that the fluid only destructs particle variance through fluid friction, in that sense, consistent with the previously discussed budget since in both of them there is an indication of energy transfer from the particles to the fluid. We also noticed that the main mechanisms of particle variance creation are due to the production terms, which can be traced to the gradient of mean particle velocity. One due to the kinetic production, and another due to collisional production. With respect to the global particle-particle interaction term, we clearly observe a direct relationship of it with the particle volume fraction, which is due to the fact that the collisional flux terms becomes more dominant as the particle flow becomes denser.

Related to the particle kinetic stresses, we note that the production terms only occur in the stream-wise direction, hence the larger values of particle kinetic stress in that direction. In the other orthogonal directions, velocity variance is only generated through redistribution through particle-particle interactions. This, in conjunction with the previous analysis, also explains why the Reynolds stresses are larger in the stream-wise direction as well, which is ultimately related to the fact that variance in the fluid comes from the particles, and the particles, generate more in this direction. Concerning the shear-stresses, the only non-null production occurs in the xy plane, which is the only-non null one.

The instantaneous fluid force in a isolated particle and the mean force of in the frame of an ensemble of spheres is discussed. We discussed the available modeling and the relationship with the data obtained with simulations of the flow past a fixed array of particles. After a discussion and a original analysis of the force-velocity fluctuation is performed using a stochastic Langevin-type impulse model.

Related to the mean transverse force, a correlation analysis is performed to verify with which variables the mean force most correlates with, to investigate the origin of such force. For the cases with small inertia, only the one with the smaller volume fraction highly correlates with variables related to traditional lift expressions, such as the Saffman lift. Even tough such force predicts the correct order of magnitude it does not however predict the right sign. We also compared it with other candidates, such as the force due to pressure gradient and a Magnus-type force and none of them seem to be appropriate in this case.

Regarding the cases with high inertia, on the other hand, a high correlation is observed with the gradient of particle volume fraction, indicating that possibly a phenomenon related to that is taking place. Associated with such high correlation, we computed a linear coefficient and plotted against the data, which gave a good fit with just a linear coefficient. Again, such a force is compared against other candidates, and all of them were much smaller than the order of magnitude of the data.

Based on a stochastic formulation of the particle impulse due to the environing fluid, with a Langevin-type equation, we derived expressions for the force velocity fluctuations correlations which are to be used in the transport equations of first, second and third order. Such expressions are dependent on a linear force tensor and a dispersion tensor. We then framed this set of equations in a particular case corresponding to the modeling approach used by Simonin (which was originally developed for dilute flows) and tested against our data (consisting in moderately dense flows), which finally, nonetheless, gave a good prediction of the order of magnitude of the data, as well as good insights into the modeling aspects of the drag. Within this analysis we noted however that more degrees of freedom would be needed to accurately describe the results, with that in mind, we then assumed other versions of such a model and then verified whether such a form would be consistent.

Still related to that, first we assumed a version of such model with two non-null coefficients, one linear force coefficient and another dispersion coefficient. The results showed that such a model was not able to reproduced the data. After that we tested whether a version of such model with a fully anisotropic linear force tensor and a null dispersion coefficient would consistently reproduce the data. The results showed that indeed such a form is compatible with our particle-resolved simulation data (And the fact that this model works, may be related to the fact that the anisotropic linear force tensor captures the effects of neighboring particles in our moderately dense flow). This opens the question into how to model such a tensor.

Next on the last chapter, five bi-disperse simulations are then analyzed. A method for computing the equivalent bi-disperse Stokes number is derived and then analyzed in the frame of our data, which indeed seemed to be coherent, in fact, most of the statistics either grow or decrease according to the augmentation of this parameter. The values of the mean velocity for all the phases are very close to one another, hence with a negligible slip between all the phases. Analogously to the mono-disperse cases the particle fluctuating kinetic energy is larger than the fluid fluctuating kinetic energy, regarding the difference between the fluctuating kinetic energy of the lighter versus the heavier phase, we observed that they are very close for all the cases, with the exception of the most inertial case, which was explained by the relationship of time-scales in this case.

The budget of the fluctuating kinetic energy is then presented with the particle-particle interaction term separated into one due to the effect of the lighter phase and another due to the heavier phase, clearly showing the coupling effect between the phases. Next, these global particle-particle interaction terms are separated into the source and flux related terms. This analysis showed that even though the global particle-particle interaction terms may assume any arbitrary value, those separated terms had a clear sign related to a physical mechanism, for instance, the collisional production is, as expected, always pos-

itive, whereas the source term assume negative or positive values depending on whether the there is a transfer from on particle phase to the other, with respect to the dissipation through particle-particle interactions. We also compared the effects of kinetic versus collisional production, which, within our parameter range, as the inertia augments, the ratio of the collisional to the kinetic production shrinks.

An extension of the mean restitution coefficient for the bi-disperse case is presented and then computed for all the cases. Such values are then used to compare the momentum collisional flux and the kinetic stress source term, yielding interesting results.

One could say that, the avant-garde aspect of this thesis work, is to provide a comprehensive methodology for the analysis of fluid-solid flows through particle-resolved simulations, including suitable statistical procedures based on a powerful formalism in which the high level of microscopic detail contained in the simulations are leveraged to provide useful macroscopic statistics. Furthermore, fluid-particle and particle-particle interactions are exhaustively analyzed providing interesting mathematical modeling insights that ultimately deepen the comprehension of the fluid-particle flow physics.

Perspectives

With the accomplishment of this thesis work, some questions that would deserve the attention of a future study appeared. In this section, we aim to cite and describe some of those ideas that would certainly contribute to a progress in the field.

As a first perspective, it would be interesting to study the effects of particle rotation in the Couette configuration. This could be done by the computation of the mean angular velocity and its fluctuating correlations, such as the fluctuating kinetic energy associated to the rotation. And that, followed by an investigation of the budgets of the transport equations of those variables. Which would serve to characterize the transfers between particle rotation and translation, and the possible implications of that in the fluid-particle flow.

Pseudo-turbulence could be further studied to test whether its values could be predicted by modeling. As a first step in this direction, a correlation analysis of the Reynolds stresses as well as the fluctuating kinetic energy with other variables could be performed to check with which parameter those pseudo-turbulence related variables are correlated most. Additionally, it could be tested against available models in the literature as well.

Regarding the transfer of momentum from the fluid to the particles. It would be interesting to further investigate the role of the local micro-structure, or more precisely, how the local organization of an ensemble of neighboring particles affects the fluid force applied to a given particle. Indeed, what motivates this investigation is the strong correlation between the mean transverse force and the gradient of particle volume fraction in our configuration. The work in this direction could be tackled at two possible fronts: the first, to look qualitatively at the fluid flow around the particle to examine more in detail why this happens, and the second, to verify whether it is possible to derive through first-principles, a lift coefficient that would take into account such effect.

Related to force-velocity fluctuation correlations, it has been demonstrated that for our Couette configuration, an anisotropic force tensor stemming form an Stochastic based approach is enough to model the data extracted from our resolved simulations. It would be useful to further inspect into the possibilities of modeling such a tensor.

Another beneficial perspective would be to perform the numerical integration of Eq. (2.51). With those results, then the divergence term present in Eq. 2.53, could be further studied. In a similar fashion, the other divergence terms associated to other coupling terms, such as the one associated to the fluctuating kinetic energy could be also studied by using a similar procedure. Such computations would make possible to further dive into the analysis of the budgets of the fluid transport equations.

With respect to particle-particle interactions, it would be interesting to derive a formula for the bi-disperse kinetic stress flux term, using the same approach as the one for the derivation of the formulas in the Appendix A, and compare it with the data extracted from our resolved simulations, given in the form of graphs in this thesis. Additionally, the study of the decomposition of the particle-particle interaction terms into source and flux terms could be also performed for the mono-disperse cases as well.

With enough high performance computation resources available, it would be helpful to perform more "simulations points", broadening the range of particle volume fractions and Stokes numbers. This would permit to further extend the range of validity of the models shown in this manuscript, as well as to deepen the comprehension of the involved phenomena. Indeed, increasing the number of particle volume fraction "simulation points", with very dilute and super dense cases, would for instance permit to further inquire into the influence of neighboring particles and the role of particle-particle interactions versus fluid-particle interactions in those different limiting cases.

Furthermore, increasing the range of particle inertia, would allow for the investigation of possible new mechanisms occurring at either very high of very low Stokes numbers, as well as to better characterize the competing mechanisms, described in this thesis, related to the transition. Besides, with respect to bi-disperse cases, other combinations of cases could be tested as well, including for instance other combinations of particle density ratio, and other combinations of particle volume fractions as well.

Moreover, the same methodology of analysis used in this thesis could be used for other configurations, such as a channel flow or gravity driven flow. This could provide other useful insights into the fluid-particle flow dynamics.

Performing a benchmark test against other comparable codes to see whether similar results could be obtained, would be of value as well. Additionally, it would be interesting to try engineer a experimental apparatus, within the same range of Stokes numbers and particle volume fractions to further study the flow.

Finally, last but not least, the authors of this study firmly believe that the results of this thesis could be used to provide content for scientific communications, such as articles in journals, or presentations in international conferences.

Appendix A

Bi-disperse source and flux terms formulas

In this appendix, we give the formulas for the bi-disperse collision flux. The collision flux for mono-disperse particle laden-flow have been investigated by [10], and then extended to the bi-dispersed case by [35, 36]. Eq. (A.1) is the formula of the collision flux for the bi-disperse case, derived by the former author:

$$\begin{aligned} -\frac{\theta_{\mathrm{pq},ij}}{m_{\mathrm{q}}} &= +M_{\mathrm{qp}}\frac{1}{12}\nu^{c}_{\mathrm{pq}}\mathcal{L}_{\mathrm{pq}}\frac{1+e_c}{2}\delta_{ij} \\ &\quad -M_{\mathrm{qp}}\frac{1}{30}\nu^{c}_{\mathrm{pq}}d^{2}_{\mathrm{pq}}\frac{1+e_c}{2}\left(D_{\mathrm{p},kk}+D_{\mathrm{q},kk}\right)\delta_{ij} \\ &\quad -M_{\mathrm{qp}}\frac{1}{15}\nu^{c}_{\mathrm{pq}}d^{2}_{\mathrm{pq}}\frac{1+e_c}{2}\left(D_{\mathrm{p},ij}+D_{\mathrm{q},ij}\right) \\ &\quad +M_{\mathrm{qp}}\frac{1}{30}\nu^{c}_{\mathrm{pq}}\mathcal{L}_{\mathrm{pq}}\frac{1+e_c}{2}\left(T_{\mathrm{p}}+T_{\mathrm{q}}\right)^{-1}\left(\hat{R}_{\mathrm{p},ij}+\hat{R}_{\mathrm{q},ij}\right) \end{aligned} \tag{A.1}$$

The formula for the bi-disperse redistribution tensor, or source term, is given by the Eq. (A.2):

$$
\begin{aligned}
\frac{\chi_{\mathrm{pq},ij}}{m_\mathrm{q}} \;=\;& -M_\mathrm{qp}^2\frac{1-e_c^2}{4}\nu_\mathrm{pq}^c\frac{2}{3}\left(T_\mathrm{p}+T_\mathrm{q}\right)\delta_{ij} \\
& -M_\mathrm{qp}\frac{1+e_c}{2}\nu_\mathrm{pq}^c\frac{4}{3}\left(\frac{m_\mathrm{p}T_\mathrm{p}-m_\mathrm{q}T_\mathrm{q}}{m_\mathrm{p}+m_\mathrm{q}}\right)\delta_{ij} \\
& -M_\mathrm{qp}\frac{1+e_c}{2}\nu_\mathrm{pq}^c\frac{2}{3}\left(M_\mathrm{pq}\hat{R}_{\mathrm{p},ij}-M_\mathrm{qp}\hat{R}_{\mathrm{q},ij}\right) \\
& -M_\mathrm{qp}^2\nu_\mathrm{pq}^c\frac{\left(1+e_c\right)\left(3-e_c\right)}{5}\frac{1}{2}\left(\hat{R}_{\mathrm{p},ij}+\hat{R}_{\mathrm{q},ij}\right) \\
& -M_\mathrm{qp}\frac{1+e_c}{2}\nu_\mathrm{pq}^c\frac{4}{15}\left(T_\mathrm{p}+T_\mathrm{p}\right)^{-1}\left(\frac{m_\mathrm{p}T_\mathrm{p}-m_\mathrm{q}T_\mathrm{q}}{m_\mathrm{p}+m_\mathrm{q}}\right)\left(\hat{R}_{\mathrm{p},ij}+\hat{R}_{\mathrm{q},ij}\right) \\
& -\frac{1}{60}\nu_\mathrm{pq}^c\mathcal{L}_\mathrm{pq}M_\mathrm{qp}^2\frac{\left(1+e_c\right)\left(3e_c-1\right)}{4}\left(D_{\mathrm{p},kk}+D_{\mathrm{q},kk}\right)\delta_{ij} \\
& +\frac{1}{30}\nu_\mathrm{pq}^c\mathcal{L}_\mathrm{pq}M_\mathrm{qp}\left(1+e_c\right)\left(T_\mathrm{p}+T_\mathrm{p}\right)^{-1}\left(\frac{m_\mathrm{p}T_\mathrm{p}-m_\mathrm{q}T_\mathrm{q}}{m_\mathrm{p}+m_\mathrm{q}}\right)\left(D_{\mathrm{p},kk}+D_{\mathrm{q},kk}\right)\delta_{ij} \\
& +\frac{1}{12}\nu_\mathrm{pq}^c\mathcal{L}_\mathrm{pq}M_\mathrm{qp}\frac{\left(1+e_c\right)}{2}\left(M_\mathrm{pq}\hat{D}_{\mathrm{p},ij}-M_\mathrm{qp}\hat{D}_{\mathrm{q},ij}\right) \\
& +\frac{1}{10}\nu_\mathrm{pq}^c\mathcal{L}_\mathrm{pq}M_\mathrm{qp}^2\frac{\left(1+e_c\right)\left(2-e_c\right)}{4}\left(D_{\mathrm{p},ij}+D_{\mathrm{q},ij}\right) \\
& +\frac{2}{15}\nu_\mathrm{pq}^c\mathcal{L}_\mathrm{pq}M_\mathrm{qp}\frac{\left(1+e_c\right)}{2}\left(T_\mathrm{p}+T_\mathrm{p}\right)^{-1}\left(\frac{m_\mathrm{p}T_\mathrm{p}-m_\mathrm{q}T_\mathrm{q}}{m_\mathrm{p}+m_\mathrm{q}}\right)\left(D_{\mathrm{p},ij}+D_{\mathrm{q},ij}\right)
\end{aligned}
\tag{A.2}
$$

Where the values of $D_{\mathrm{p},ij}$, M_pq, M_qp, $\mathcal{L}_\mathrm{pq}$, ν_pq^c and $\hat{R}_{\mathrm{p},ij}$ are respectively given by the following set of equations:

$$D_{\mathrm{p},ij} = \frac{1}{2}\left(\frac{\partial U_{\mathrm{p},i}}{\partial x_j}+\frac{\partial U_{\mathrm{p},j}}{\partial x_i}\right) \tag{A.3}$$

$$M_\mathrm{pq} = \frac{2m_\mathrm{p}}{m_\mathrm{p}+m_\mathrm{q}} \tag{A.4}$$

$$M_\mathrm{qp} = \frac{2m_\mathrm{q}}{m_\mathrm{p}+m_\mathrm{q}} \tag{A.5}$$

$$\mathcal{L}_\mathrm{pq} = d_\mathrm{pq}\sqrt{2\pi\left(T_\mathrm{p}+T_\mathrm{q}\right)} \tag{A.6}$$

$$\nu_\mathrm{pq}^c = g_0^\mathrm{pq}n_\mathrm{p}n_\mathrm{q}d_\mathrm{pq}^2\pi\sqrt{\frac{16}{3\pi}\left(q_\mathrm{p}^2+q_\mathrm{q}^2\right)} \tag{A.7}$$

$$\hat{R}_{\mathrm{p},ij} = R_{\mathrm{p},ij}-T_\mathrm{p}\delta_{ij} \tag{A.8}$$

For more details on the derivation of that equation, see the original document [35]. Concerning the value of g_0, which comes from the molecular chaos assumption [18], for bi-disperse particle flow, we use the formula proposed by [80]. It is given by the set of equations below:

$$g_0^{pq}(\alpha_m) = \left(1 - \frac{\alpha_m}{\alpha_{\max}}\right)^{-\gamma_{\mathrm{pq}}\alpha_{\max}} \tag{A.9}$$

$$\gamma_{\mathrm{pq}} = 1 + \frac{3}{2}\left(\frac{d_{\mathrm{p}}d_{\mathrm{q}}}{d_{\mathrm{p}} + d_{\mathrm{q}}}\right)\frac{\xi_m}{\alpha_m} \tag{A.10}$$

$$\xi_m = 2\left(\frac{d_{\mathrm{p}}}{\alpha_{\mathrm{p}}} + \frac{d_{\mathrm{q}}}{\alpha_{\mathrm{q}}}\right) \tag{A.11}$$

$$\alpha_m = \alpha_{\mathrm{p}} + \alpha_{\mathrm{q}} \tag{A.12}$$

Bibliography

[1] Abbas, M., Climent, E., Parmentier, J.-F., & Simonin, O. (2010). Flow of particles suspended in a sheared viscous fluid: Effects of finite inertia and inelastic collisions. *AIChE journal*, 56(10):2523–2538.

[2] Aidun, C. K. & Clausen, J. R. (2010). Lattice-boltzmann method for complex flows. *Annual Review of Fluid Mechanics*, 42:439–472.

[3] Alméras, É., Masbernat, O., Risso, F., & Fox, R. O. (2019). Fluctuations in inertial dense homogeneous suspensions. *Physical Review Fluids*, 4(10):102301.

[4] Balzer, G., Boelle, A., & Simonin, O. (1995). Eulerian gas-solid flow modelling of dense fluidized bed. *Fluidization*, 8:1125.

[5] Barkla, H. & Auchterlonie, L. (1971). The magnus or robins effect on rotating spheres. *Journal of Fluid Mechanics*, 47(3):437–447.

[6] Basset, A. B. (1888). On the motion of a sphere in a viscous liquid. *Philosophical Transactions of the Royal Society of London. A*, 179:43–63.

[7] Beetstra, R., van der Hoef, M. A., & Kuipers, J. (2007). Drag force of intermediate reynolds number flow past mono-and bidisperse arrays of spheres. *AIChE journal*, 53(2):489–501.

[8] Berger, M. J. & Oliger, J. (1984). Adaptive mesh refinement for hyperbolic partial differential equations. *Journal of computational Physics*, 53(3):484–512.

[9] Bernard, M. (2014). *Approche multi-échelle pour les écoulements fluide-particules*. PhD thesis, INP Toulouse.

[10] Boelle, A. (1997). *Validation d'un modèle à deux fluides appliqué à la simulation des lits fluidisés denses*. PhD thesis, Paris 6.

[11] Boelle, A., Balzer, G., & Simonin, O. (1995). Second-order prediction of the particle-phase stress tensor of inelastic spheres in simple shear dense suspensions. *ASME-Publications-Fed*, 228:9–18.

[12] Boussinesq, J. (1885). Sur la resistance qu'oppose un fluide indefini en repos, sans pesanteur, au mouvement varie d'une sphere solide qu'il mouille sur toute sa surface, quand les vitesses restent bien continues et assez faibles pour que leurs carres et produits soient negligiables. *Compte Rendu de l'Académie de Sciences de Paris*, 100:935–937.

[13] Brändle de Motta, J. (2013). *Simulation des écoulements turbulents avec des particules de taille finie en régime dense*. PhD thesis, Toulouse, ISAE.

[14] Brändle de Motta, J., Breugem, W.-P., Gazanion, B., Estivalezes, J.-L., Vincent, S., & Climent, E. (2013). Numerical modelling of finite-size particle collisions in a viscous fluid. *Physics of Fluids*, 25(8):083302.

[15] Breugem, W.-P. (2010). A combined soft-sphere collision/immersed boundary method for resolved simulations of particulate flows. In: *ASME 2010 3rd Joint US-European Fluids Engineering Summer Meeting collocated with 8th International Conference on Nanochannels, Microchannels, and Minichannels*, pages 2381–2392. American Society of Mechanical Engineers.

[16] Buyevich, Y. A. & Shchelchkova, I. (1979). Flow of dense suspensions. *Progress in Aerospace Sciences*, 18:121–150.

[17] Caltagirone, J. & Vincent, S. (2001). Tensorial penalisation method for solving navier-stokes equations. *Comptes Rendus de l'Academie des Sciences Series IIB Mechanics*, 329(8):607–613.

[18] Chapman, S., Cowling, T. G., & Burnett, D. (1990). *The mathematical theory of non-uniform gases: an account of the kinetic theory of viscosity, thermal conduction and diffusion in gases*. Cambridge university press.

[19] Cheremisinoff, N. P. (1986). Review of experimental methods for studying the hydrodynamics of gas-solid fluidized beds. *Industrial & Engineering Chemistry Process Design and Development*, 25(2):329–351.

[20] Chevrier, S. (2017). *Development of subgrid models for a periodic circulating fluidized bed of binary mixture of particles*. PhD thesis.

[21] Climent, E. & Maxey, M. (2003). Numerical simulations of random suspensions at finite reynolds numbers. *International Journal of Multiphase Flow*, 29(4):579–601.

[22] Climent, E. & Maxey, M. R. (2009). The force coupling method: A flexible approach for the simulation of particulate flows. In: *Theoretical Methods for Micro Scale Viscous Flows*. F. Feuillebois and A. Sellier.

[23] Corona, A. A. (2008). *Agitation of particles in a liquid fluidized bed. Experimental study*. PhD thesis, Toulouse University.

[24] Corrsin, S. & Lumley, J. (1956). On the equation of motion for a particle in turbulent fluid. *Applied Scientific Research, Section A*, 6(2):114–116.

[25] Crowe, C. T., Schwarzkopf, J. D., Sommerfeld, M., & Tsuji, Y. (2011). *Multiphase flows with droplets and particles*. CRC press.

[26] Dahler, J. S. & Sather, N. F. (1963). Kinetic theory of loaded spheres. i. *The Journal of Chemical Physics*, 38(10):2363–2382.

[27] Daly, B. J. & Harlow, F. H. (1970). Transport equations in turbulence. *The Physics of Fluids*, 13(11):2634–2649.

[28] Dance, S. & Maxey, M. (2003). Incorporation of lubrication effects into the force-coupling method for particulate two-phase flow. *Journal of computational Physics*, 189(1):212–238.

[29] Delhaye, J.-M. (1974). Jump conditions and entropy sources in two-phase systems. local instant formulation. *International Journal of Multiphase Flow*, 1(3):395–409.

[30] Derksen, J. J. (2007). The lattice-boltzmann method for multiphase fluid flow simulations and euler-lagrange large-eddy simulations. In: *Multiphase reacting flows: modelling and simulation*, pages 181–228. Springer.

[31] Elhimer, M., Praud, O., Marchal, M., Cazin, S., & Bazile, R. (2017). Simultaneous piv/ptv velocimetry technique in a turbulent particle-laden flow. *Journal of Visualization*, 20(2):289–304.

[32] Ergun, S. (1952). Fluid flow through packed columns. *Chem. Eng. Prog.*, 48:89–94.

[33] Eshghinejadfard, A., Abdelsamie, A., Hosseini, S. A., & Thevenin, D. (2017). Immersed boundary lattice boltzmann simulation of turbulent channel flows in the presence of spherical particles. *International Journal of Multiphase Flow*, 96:161–172.

[34] Esteghamatian, A., Hammouti, A., Lance, M., & Wachs, A. (2017). Particle resolved simulations of liquid/solid and gas/solid fluidized beds. *Physics of Fluids*, 29(3):033302.

[35] Fede, P. (2004). *Modélisation et simulation de l'influence de la turbulence sur les collisions dans les écoulements mono-et bi-solides*. PhD thesis, Toulouse, INPT.

[36] Fede, P. & Simonin, O. (2005). Application of a perturbated two-maxwellian approach for the modelling of kinetic stress transfer by collision in nonequilibrium binary mixture of inelastic particles. *ASME*.

[37] Fortin, M. & Glowinski, R. (1983). Méthodes de lagrangien augmenté: applications à la résolution numérique de problèmes aux limites. *Journal of Applied Mathematics and Mechanics*, 63(11):583–584.

[38] Garzó, V., Tenneti, S., Subramaniam, S., & Hrenya, C. (2012). Enskog kinetic theory for monodisperse gas–solid flows. *Journal of Fluid Mechanics*, 712:129–168.

[39] Gatignol, R. (1983). The faxén formulae for a rigid particle in an unsteady non-uniform stokes flow. *Journal de Mécanique theorique et appliquée*, 1, N.2:143–160.

[40] Grad, H. (1949). On the kinetic theory of rarefied gases. *Communications on pure and applied mathematics*, 2(4):331–407.

[41] Graham, D., Cairns, I. H., Skjaeraasen, O., & Robinson, P. (2012). Three-dimensional electromagnetic strong turbulence: Dependence of the statistics and dynamics of strong turbulence on the electron to ion temperature ratio. *Physics of Plasmas*, 19(2):022306.

[42] Hanjalic, K., Launder, B., et al. (1972). A reynolds stress model of turbulence and its application to thin shear flows. *Journal of Fluid Mechanics*, 52(4):609–638.

[43] Hatano, H. & Ishida, M. (1983). Study on the entrainment of fcc particles from a fluidized bed. *Powder Technology*, 35(2):201–209.

[44] He, J. & Simonin, O. (1993). Non-equilibrium prediction of the particle-phase stress tensor in vertical pneumatic conveying. *ASME*, 166:253–253.

[45] Hill, R. J., Koch, D. L., & Ladd, A. J. (2001a). The first effects of fluid inertia on flows in ordered and random arrays of spheres. *Journal of Fluid Mechanics*, 448:213–241.

[46] Hill, R. J., Koch, D. L., & Ladd, A. J. (2001b). Moderate reynolds number flows in ordered and random arrays of spheres. *Journal of Fluid Mechanics*, 448:243–278.

[47] Hölzer, A. & Sommerfeld, M. (2009). Lattice boltzmann simulations to determine drag, lift and torque acting on non-spherical particles. *Computers & Fluids*, 38(3):572–589.

[48] Hu, H. H. (1996). Direct simulation of flows of solid-liquid mixtures. *International Journal of Multiphase Flow*, 22(2):335–352.

[49] Hu, H. H., Patankar, N. A., & Zhu, M. (2001). Direct numerical simulations of fluid–solid systems using the arbitrary lagrangian–eulerian technique. *Journal of Computational Physics*, 169(2):427–462.

[50] Ishii, M. (1975). Thermo-fluid dynamic theory of two-phase flow. *NASA Sti/recon Technical Report A*, 75:29657.

[51] Kataoka, I., Ishii, M., & Serizawa, A. (1986). Local formulation and measurements of interfacial area concentration in two-phase flow. *International Journal of Multiphase Flow*, 12(4):505–529.

[52] Kuerten, J. G. (2016). Point-particle dns and les of particle-laden turbulent flow-a state-of-the-art review. *Flow, Turbulence and Combustion*, 97(3):689–713.

[53] Kunii, D. & Levenspiel, O. (2013). *Fluidization engineering*. Elsevier.

[54] Kurose, R. & Komori, S. (1999). Drag and lift forces on a rotating sphere in a linear shear flow. *Journal of Fluid Mechanics*, 384:183–206.

[55] Ladd, A. & Verberg, R. (2001). Lattice-boltzmann simulations of particle-fluid suspensions. *Journal of Statistical Physics*, 104(5-6):1191–1251.

[56] Ladd, A. J. (1994a). Numerical simulations of particulate suspensions via a discretized boltzmann equation. part 1. theoretical foundation. *Journal of Fluid Mechanics*, 271:285–309.

[57] Ladd, A. J. (1994b). Numerical simulations of particulate suspensions via a discretized boltzmann equation. part 2. numerical results. *Journal of Fluid Mechanics*, 271:311–339.

[58] Lapeyre, B., Pardoux, É., & Sentis, R. (1998). *Méthodes de Monte-Carlo pour les équations de transport et de diffusion, Mathématiques et Applications 29*. Springer.

[59] Lavieville, J. (1997). *Simulations numeriques et modelisation des interactions entre l'entrainement par la turbulence et les collisions interparticulaires en ecoulements gaz-solide*. PhD thesis, Rouen.

[60] Lefebvre, A. & Maury, B. (2005). Apparent viscosity of a mixture of a newtonian fluid and interacting particles. *Comptes rendus mécanique*, 333(12):923–933.

[61] Leveque, R. J. & Li, Z. (1994). The immersed interface method for elliptic equations with discontinuous coefficients and singular sources. *SIAM Journal on Numerical Analysis*, 31(4):1019–1044.

[62] LeVeque, R. J. & Li, Z. (1997). Immersed interface methods for stokes flow with elastic boundaries or surface tension. *SIAM Journal on Scientific Computing*, 18(3):709–735.

[63] Li, Z. & Lai, M.-C. (2001). The immersed interface method for the navier–stokes equations with singular forces. *Journal of Computational Physics*, 171(2):822–842.

[64] Manneville, P. (2015). On the transition to turbulence of wall-bounded flows in general, and plane couette flow in particular. *European Journal of Mechanics-B/Fluids*, 49:345–362.

[65] Maury, B. (1999). Direct simulations of 2d fluid-particle flows in biperiodic domains. *Journal of Computational Physics*, 156(2):325–351.

[66] Maxey, M. (2017). Simulation methods for particulate flows and concentrated suspensions. *Annual Review of Fluid Mechanics*, 49:171–193.

[67] Maxey, M. R. & Riley, J. J. (1983). Equation of motion for a small rigid sphere in a nonuniform flow. *The Physics of Fluids*, 26(4):883–889.

[68] Mehta, Y., Jackson, T., & Balachandar, S. (2020). Pseudo-turbulence in inviscid simulations of shock interacting with a bed of randomly distributed particles. *Shock Waves*, 30(1):49–62.

[69] Mittal, R. & Iaccarino, G. (2005). Immersed boundary methods. *Annual Review of Fluid Mechanics*, 37:239–261.

[70] Monin, A. S. & Yaglom, A. M. (2013). *Statistical fluid mechanics, mechanics of turbulence*, volume 2. Courier Corporation.

[71] Morioka, S. & Nakajima, T. (1987). Modeling of gas and solid particles 2-phase flow and application to fluidized-bed. *Journal de Mécanique Théorique et Appliquée*, 6(1):77–88.

[72] Moslemian, D. (1988). *Study of solids motion, mixing, and heat transfer in gas-fluidized beds.* PhD thesis.

[73] Neau, H., Pigou, M., Fede, P., Ansart, R., Baudry, C., Mérigoux, N., Laviéville, J., Fournier, Y., Renon, N., & Simonin, O. (2020). Massively parallel numerical simulation using up to 36,000 cpu cores of an industrial-scale polydispersed reactive pressurized fluidized bed with a mesh of one billion cells. *Powder Technology*.

[74] Nigmetova, A. (2019). *DEM-CFD simulation of dilute and dense particle laden flows: application to a lab-scale pressurized dense fluidized bed*. PhD thesis.

[75] Odar, F. & Hamilton, W. S. (1964). Forces on a sphere accelerating in a viscous fluid. *Journal of Fluid Mechanics*, 18(2):302–314.

[76] Oseen, C. W. (1927). Neuere methoden und ergebnisse in der hydrodynamik. *Leipzig: Akademische Verlagsgesellschaft mb H.*

[77] Özel, A. (2011). *Simulation aux grandes échelles des lits fluidisés circulants gaz-particule*. PhD thesis.

[78] Özel, A., Brändle de Motta, J., Abbas, M., Fede, P., Masbernat, O., Vincent, S., Estivalezes, J.-L., & Simonin, O. (2017). Particle resolved direct numerical simulation of a liquid–solid fluidized bed: Comparison with experimental data. *International Journal of Multiphase Flow*, 89:228–240.

[79] Parmentier, J.-F. & Simonin, O. (2012). Transition models from the quenched to ignited states for flows of inertial particles suspended in a simple sheared viscous fluid. *Journal of Fluid Mechanics*, 711:147–160.

[80] Patiño-Palacios, G. (2007). *Modélisation numérique eulérienne des écoulements gaz-solide avec plusieurs espèces de particules*. PhD thesis, Institut National Polytechnique de Toulouse.

[81] Peskin, C. S. (1972). Flow patterns around heart valves: a numerical method. *Journal of Computational Physics*, 10(2):252–271.

[82] Peskin, C. S. (1977). Numerical analysis of blood flow in the heart. *Journal of Computational Physics*, 25(3):220–252.

[83] Pialat, X. (2007). *Développement d'une méthode hybride eulérienne-lagrangienne pour la modélisation numérique de la phase particulaire dans les écoulements turbulents gaz-particules*. PhD thesis, Ecole nationale supérieure de l'aéronautique et de l'espace.

[84] Pope, S. B. (2000). *Turbulent flows*. Cambridge university press.

[85] Rahmani, M., Hammouti, A., & Wachs, A. (2018). Momentum balance and stresses in a suspension of spherical particles in a plane couette flow. *Physics of Fluids*, 30(4):043301.

[86] Randrianarivelo, T. N. (2005). *Etude numérique des interactions hydrodynamiques fluides/solides: application aux lits fluidisés*. PhD thesis, Bordeaux 1.

[87] Reeks, M. (1991). On a kinetic equation for the transport of particles in turbulent flows. *Physics of Fluids A: Fluid Dynamics*, 3(3):446–456.

[88] Rettinger, C. & Rüde, U. (2018). A coupled lattice boltzmann method and discrete element method for discrete particle simulations of particulate flows. *Computers & Fluids*.

[89] Romanov, V. A. (1973). Stability of plane-parallel couette flow. *Functional analysis and its applications*, 7(2):137–146.

[90] Rubinow, S. I. & Keller, J. B. (1961). The transverse force on a spinning sphere moving in a viscous fluid. *Journal of Fluid Mechanics*, 11(3):447–459.

[91] Rubinstein, G. J., Derksen, J., & Sundaresan, S. (2016). Lattice boltzmann simulations of low-reynolds-number flow past fluidized spheres: effect of stokes number on drag force. *Journal of Fluid Mechanics*, 788:576–601.

[92] Saffman, P. (1965). The lift on a small sphere in a slow shear flow. *Journal of Fluid Mechanics*, 22(2):385–400.

[93] Saha, S. & Alam, M. (2017). Revisiting ignited-quenched transition and the non-newtonian rheology of a sheared dilute gas-solid suspension. *arXiv preprint arXiv:1706.04457*.

[94] Sakiz, M. & Simonin, O. (1998). Continuum modelling and lagrangian simulation of the turbulent transport of particle kinetic stresses in a vertical gas-solid channel flow. In: *3rd International Conference on Multiphase Flows, Lyon, France*.

[95] Sakiz, M. & Simonin, O. (1999). Numerical experiments and modelling of non-equilibrium effects in dilute granular flows. In: *RGD: rarefied gas dynamics (Marseille, 26-31 July 1998)*.

[96] Schiller, L. & Naumann, A. (1935). A drag coefficient correlation. vdi zeitung, 77: 318–320, 1935. *Cité page*, 38.

[97] Sheen, S. & Raptis, A. (1983). Active acoustic cross-correlation technique applied to flow velocity measurement in a coal/liquid slurry. In: *1983 Ultrasonics Symposium*, pages 591–594. IEEE.

[98] Shi, P. (2021). *Hydrodynamic forces on a sphere translating steadily in a wall-bounded linear shear flow*. PhD thesis, TU Dresden.

[99] Simonin, O. (1991a). Prediction of the dispersed phase turbulence in particle-laden jets. *Gas-Solid Flows ASME-FED*, 121:197–206.

[100] Simonin, O. (1991b). Second-moment prediction of dispersed phase turbulence in particle-laden flows. In: *8th Symposium on Turbulent Shear Flows, Volume 1*, volume 1, pages 7–4.

[101] Simonin, O. (1991c). Third-moment closure in second-moment prediction of dispersed phase turbulence in particle-laden flows. In: *Annexe 3, EDF Report HE-44/91.24, LNH, Chatou, France*.

[102] Simonin, O. (1996). Combustion and turbulence in two-phase flows. In: *The von Karman Institute for Fluid Dynamics*, volume 2, page 37.

[103] Simonin, O. (2000). Statistical and continuum modelling of turbulent reactive particulate flows, part i: Theoretical derivation of dispersed phase eulerian modelling from probability density function kinetic equation. In: *The von Karman Institute for Fluid Dynamics*, volume 6.

[104] Simonin, O. (2021a). Private Communication.

[105] Simonin, O. (2021b). Modélisation de la dispersion turbulente des particules dans le cadre de l'approche pdf. In: *Seminar at Commissariat a l'Energie Atomique et aux Energies Alternatives*.

[106] Simonin, O. & Squires, K. D. (2003). On two-way coupling in gas-solid turbulent flows. In: *Fluids Engineering Division Summer Meeting*, volume 36967, pages 515–523.

[107] Sommerfeld, M. & Tropea, C. (1999). Single-point laser measurement. In: *Instrumentation for Fluid Particle Flow*, pages 252–317. Elsevier.

[108] Soo, S. L. (1999). *Instrumentation for fluid particle flow*. Elsevier.

[109] Stokes, G. G. (1851). *On the effect of the internal friction of fluids on the motion of pendulums*, volume 9. Pitt Press Cambridge.

[110] Sun, J. & Yan, Y. (2016). Non-intrusive measurement and hydrodynamics characterization of gas–solid fluidized beds: a review. *Measurement Science and Technology*, 27(11):112001.

[111] Tenneti, S., Garg, R., & Subramaniam, S. (2011). Drag law for monodisperse gas–solid systems using particle-resolved direct numerical simulation of flow past fixed assemblies of spheres. *International Journal of Multiphase Flow*, 37(9):1072–1092.

[112] Tenneti, S. & Subramaniam, S. (2014). Particle-resolved direct numerical simulation for gas-solid flow model development. *Annual review of fluid mechanics*, 46:199–230.

[113] Thiam, E. I. (2018). *Analysis of heat transfer in dense particle-laden flows by fully-resolved-particle direct numerical simulations*. PhD thesis, Université Paul Sabatier de Toulouse.

[114] Thiam, E. I., Masi, E., Climent, É., Simonin, O., & Vincent, S. (2019). Particle-resolved numerical simulations of the gas–solid heat transfer in arrays of random motionless particles. *Acta Mechanica*, 230(2):541–567.

[115] Tsao, H.-K. & Koch, D. L. (1995). Simple shear flows of dilute gas–solid suspensions. *Journal of Fluid Mechanics*, 296:211–245.

[116] Tsuji, Y., Kawaguchi, T., & Tanaka, T. (1993). Discrete particle simulation of two-dimensional fluidized bed. *Powder technology*, 77(1):79–87.

[117] Uhlmann, M. (2005a). An immersed boundary method with direct forcing for the simulation of particulate flows. *Journal of Computational Physics*, 209(2):448–476.

[118] Uhlmann, M. (2005b). An improved fluid-solid coupling method for dns of particulate flow on a fixed mesh. In: *Proc. 11th Workshop Two-Phase Flow Predictions, Merseburg, Germany.*

[119] Uhlmann, M. (2006). Experience with dns of particulate flow using a variant of the immersed boundary method. In: *ECCOMAS CFD 2006: Proceedings of the European Conference on Computational Fluid Dynamics, Egmond aan Zee, The Netherlands, September 5-8, 2006*. Delft University of Technology; European Community on Computational Methods in Applied Sciences (ECCOMAS).

[120] Uzawa, H. (1958). Iterative methods for concave programming. *Studies in linear and nonlinear programming*, 6:154–165.

[121] Vincent, S., Brändle de Motta, J., Sarthou, A., Estivalezes, J.-L., Simonin, O., & Climent, E. (2014). A lagrangian vof tensorial penalty method for the dns of resolved particle-laden flows. *Journal of Computational Physics*, 256:582–614.

[122] Vincent, S., Caltagirone, J.-P., Lubin, P., & Randrianarivelo, T. N. (2004). An adaptative augmented lagrangian method for three-dimensional multimaterial flows. *Computers & fluids*, 33(10):1273–1289.

[123] Vincent, S., Randrianarivelo, T. N., Pianet, G., & Caltagirone, J.-P. (2007). Local penalty methods for flows interacting with moving solids at high reynolds numbers. *Computers & fluids*, 36(5):902–913.

[124] Vogel, G., Sandus, O., Steunenberg, R., & Mecham, W. (1958). Fluidized-bed techniques in producing uranium hexafluoride from ore concentrates. *Industrial & Engineering Chemistry*, 50(12):1744–1747.

[125] Wachs, A. (2011). Peligriff, a parallel dem-dlm/fd direct numerical simulation tool for 3d particulate flows. *Journal of Engineering Mathematics*, 71(1):131–155.

[126] Wang, Q., Squires, K., Chen, M., & McLaughlin, J. (1997). On the role of the lift force in turbulence simulations of particle deposition. *International Journal of Multiphase Flow*, 23(4):749–763.

[127] Wen, C. Y. (1966). Mechanics of fluidization. In: *Chem. Eng. Prog. Symp. Ser.*, volume 6, pages 100–101.

[128] Yan, Y. (1996). Mass flow measurement of bulk solids in pneumatic pipelines. *Measurement Science and Technology*, 7(12):1687.

[129] Zaichik, L. & Vinberg, A. (1991). Modeling of particle dynamics and heat transfer in turbulent flows using equations for first and second moments of velocity and temperature fluctuations. In: *8th Symposium on Turbulent Shear Flows, Volume 1*, volume 1, pages 10_2_1–10_2_6.

[130] Zhang, D. & Prosperetti, A. (1994). Averaged equations for inviscid disperse two-phase flow. *Journal of Fluid Mechanics*, 267:185–219.

[131] Zhou, Q. & Fan, L.-S. (2015). Direct numerical simulation of low-reynolds-number flow past arrays of rotating spheres. *Journal of Fluid Mechanics*, 765:396.